CRANFIELD INSTITUTE OF TECHNOLOGY

Xiangcheng ZHANG

Fracture of Modified Urethane-Methacrylate Resins

School of Industrial and Manufacturing Science

PhD Thesis

CRANFIELD INSTITUTE OF TECHNOLOGY

School of Industrial and Manufacturing Science

PhD Thesis

1989 - 1992

Xiangcheng ZHANG

Fracture of Modified Urethane - Methacrylate Resins

Supervisor: Professor Clive B Bucknall

March 1993

ABSTRACT

Fracture and toughening mechanisms in rubber modified and hybridized urethane-methacrylate resins have been investigated. Fracture mechanisms are defect-dominated in the unmodified resin. The relationships between defect size and fracture strength are characterized through the critical stress intensity factor K_{IC}. Low fracture toughness and high crack sensitivity of the unmodified resin is due to lack of plastic deformation at the crack tip. A 10-fold increase in fracture resistance in the resin has been achieved through rubber modification. The main reason for the improvement is due to occurring of intensive plastic deformation in the presence of rubber, which effectively eases stress concentrations and spreads them away from the crack tip. Deformation mechanisms in rubber-modified resins are shear-dominated. Cavitation of rubber plays a key role in inducing shear deformation in the matrix. Fracture processes in rubber-modified resins start from coalescence and linkage of voids initiated inside rubber particles within rubber domains, which leads to final fracture in the resin matrix. Further increase in K_{IC} was also obtained by incorporation of filler in a matrix toughened with rubber. This increase is not due to the effect of crack front pinning but due to increase in Young's modulus in the presence of rigid filler. The same deformation and fracture mechanisms operate in the hybrid resins as in the rubber-modified ones.

CONTENTS

NOMENCLATURES

α_ϕ	concentration shift factor
α_σ	stress shift factor
β	a constant which defines the shape of relaxation spectrum
γ_e	surface energy
γ_p	plastic work ahead of the crack tip
$\dot{\gamma}$	shear strain rate
Γ	stress concentration factor
ε	strain
$\dot{\varepsilon}$	strain rate
λ	extension ratio
μ	shear modulus
ν	Poisson's ratio
ν_e	entanglement density (in Kramer's theory)
ρ	crack tip radius
σ	stress
σ_h	hydrostatic stress
σ_i	principal stress when i = 1, 2 or 3
σ_c	fracture strength
σ_s	shear stress
σ_{tc}	critical stress ahead of the crack tip
σ_{yield}	yield stress in uniaxial tension
τ	relaxation time
ϕ	volume fraction
Ω	activation free volume (holes) (in Chow's yield theory)
ω	rotation angle of polymer chain (in Argon's yield theory)
Υ	total surface work required to develop crazes (in Kramer's theory)

a^*	effective radius of polymer segment (in Argon's yield theory)
B_P	Pukanszky constant
D	diffusion coefficient
E	Young's modulus
f	free volume fraction
G	energy release rate; G_{IC} the critical energy release rate under plane strain conditions
h	Plank constant
k	Boltzmann constant
K	stress intensity factor; K_{IC} the critical stress intensity factor under plane strain conditions (also called fracture toughness)
l_e	chain contour of polymer network
r_P	plastic zone size ahead of the crack tip
r_{Irwin}	Irwin's plastic zone diameter ahead of the crack tip
$r_{Dugdale}$	Dugdale plastic zone length ahead of the crack tip
r_c	critical distance ahead of the crack tip (in crack tip blunting theory)
r_h	cavitation zone size ahead of the crack tip
V^*	activation volume
z^*	effective length of polymer segment (in Argon's yield theory)

CHAPTER 1

INTRODUCTION

At present, 7 to 10 % of all plastics are used in automobiles and a proportion of 12 to 14 % consumption is anticipated for the next few years in western countries (Weber 1990). The production of high-grade engineering plastics is predicted to grow at 5 % annually for the next few years. In terms of tonnage, the most important materials in this area will be those used in production of car bodies. The amount of plastics used in this field is expected to more than double between now and the year 2000 (Wood 1990). Therefore, development of these high grade engineering plastics and composites for this particular area is important.

The ICI products, Modar resins, which were developed in 1985, have demonstrated some advantages in the applications such as body panels, bonnet, boot and hard top roofs of cars. Good dimensional stability and surface finish are the main advantages. However, low fracture toughness and high crack sensitivity are the main problems with these materials. In order to explore new applications of Modar resins for the car industry, more research is needed.

As a joint research programme between ICI and Cranfield Institute of Technology (CIT), the work involved in this thesis is based on the patented publication of C B Bucknall(CIT), M Orton(ICI) and G. Jackson(ICI): Paraloid BTA 753 toughened Modar resins (European Patent Application No. 91309647.5). The main purpose of this research is to understand the factors that affect the fracture resistance of the materials, with particular reference to additives used in commercial resins and to aggressive environments likely to be encountered in service.

Theoretical aspects of yield and fracture are summarized in Chapter 2. Some applications of these theories are reviewed in Chapter 3. The functions of matrices, rubber particles and rigid fillers are discussed respectively, with respect to deformation and toughening mechanisms of rubber toughened plastics, particulate and hybrid thermosetting composites. This includes the roles of matrix deformation and rubber cavitation.

Experimental work is collected in Chapter 4. Chapter 5 contains results from investigating water diffusion properties of Modar resins, with reference to Fick's diffusion theory in conditions where water environments are mainly concerned. One interesting phenomenon - internal fracture in Modar matrix - is noted. The internal cracks look like discs and have been termed as disc-like cracks in this thesis. Further discussion about the water induced cracking in Modar matrix will be given in Chapter 7.

Deformation and fracture of rubber toughened Modar resins, particulate filled and hybrid

Modar composites are discussed in Chapters 6 and 7, with and without reference to liquid environments. Comparisons of experimental results with some theories are made.

Some discussion about relationships between theoretical prediction and results obtained in this research will be detailed in these two Chapters too. By using Eyring's and Argon's theories, characterization of yielding behaviour has been made for unmodified Modar resin, the rubber toughened and the rubber/filler hybridized composites. Eyring's activation volume and Argon's microstructure parameters of polymer deformation at yielding have been obtained for these three systems, following some discussions about the physical meaning.

By using fracture mechanics theories, quantitative measurement of fracture toughness has also been made for these three systems. Good agreement between the theories and experimental results has been obtained in correlation of internal disc-like crack, which was induced by water, using the critical stress intensity factor K_{IC}. Other theories such as crack tip blunting and crack tip pinning will be discused in these two Chapters too.

Finally, discussions about mechanisms of toughening in plastics and hybridized composites are presented in Chapter 8, with particular reference to the materials used in the research. Based on the observations of deformed microstructure and fracture toughness measurement, the main factors that affect fracture toughness are discussed. These factors include (a) the roles of big rubber domains and small rubber particles, (b) the mechanisms of matrix deformation, (c) the morphology of plastic zones under different conditions, and (d) matrix coatings above the poles of hard filler particles. Conclusions about toughening mechanisms will be drawn in this Chapter and Chapter 9 for these particular Modar resins.

CHAPTER 2

BASIC THEORIES OF FRACTURE MECHANICS AND YIELD

Materials failure can take place in different ways. They are normally classified into two modes: brittle failure and ductile failure. Prediction of failure in materials is of great importance to designers, engineers and materials scientists. This chapter will cover some theoretical aspects of fracture and yield, which will be used in the following chapters.

2.1 Introduction to Elastic Fracture Mechanics

The objective of fracture mechanics is to give quantitative answers to specific questions concerning the relationship between defect size and failure strength of materials. The first important breakthrough was made by Griffith in 1920. Griffith theory was based on the energy balance approach which enabled him to define unstable conditions under which cracks would grow. His experimental results on glass specimens agreed well with his theory. Since then linear elastic fracture mechanics (LEFM) has been well developed. A cracked body can be loaded in different ways. Only one loading mode which causes crack opening will be considered in this Chapter. It is normally termed Mode I loading.

2.1.1 Energy Approach

Griffith Theory

Consider an infinite plate with unit thickness which contains a through-thickness crack of length 2a. A uniform stress σ is applied at infinity perpendicular to the crack as shown in Figure 2.1. The total energy U_t of the cracked plate can be expressed as:

$$U_t = U_0 + U_a + U_\gamma - F \tag{2.1}$$

where

U_o = elastic energy stored in the loaded uncracked system (U_o is a constant),
U_a = elastic energy change after introducing the crack,
U_γ = elastic surface energy change introduced by formation of the crack surfaces,
F = the work performed by external forces.

Now, consider the case of fixed grip conditions, i.e. there is no external work done on the

system and the grip remains stationary when the crack spreads (F=0). The change of elastic surface energy is equal to the product of the surface energy of the material, γ_e, and the new area of the crack, i.e. $dU_\gamma = 2(2\gamma_e da)$. Griffith used Inglis' analysis of elastic energy change after introducing the crack. It is given by:

$$U_a = -\frac{\pi a^2 \sigma^2}{E} \tag{2.2a}$$

where E is Young's modulus, and the negative sign means that the system potential energy decreases. Figure 2.2 shows the total potential energy change. It can be seen that the system will become unstable when 'a', the crack length approaches a_m as the total energy will decrease after $a > a_m$. This situation can be treated mathematically at $a = a_m$ by differentiating equation (2.1) and setting $dU_t/da = 0$. The result is given by:

$$\sigma_c = \sqrt{\frac{2\gamma_e E}{\pi a}} \tag{2.3a}$$

where σ_c is the fracture stress. Equation (2.3a) can be applied to a thin wide sheet. For a thick plate, the corresponding equations are:

$$U_a = -(1-\nu^2)\frac{\pi a^2 \sigma^2}{E} \tag{2.2b}$$

$$\sigma_c = \sqrt{\frac{2\gamma_e E}{(1-\nu^2)\pi a}} \tag{2.3b}$$

where ν is Poisson's ratio.

Equations (2.3a) and (2.3b) establish the basic relationship between defect size and fracture strength for an ideal elastic material.

Irwin's Modification to the Griffith Theory

The Griffith theory was modified in 1948 by Irwin, who extended the theory to materials which perform limited plastic deformation at the crack tip.

Equation (2.3a) can be rearranged:

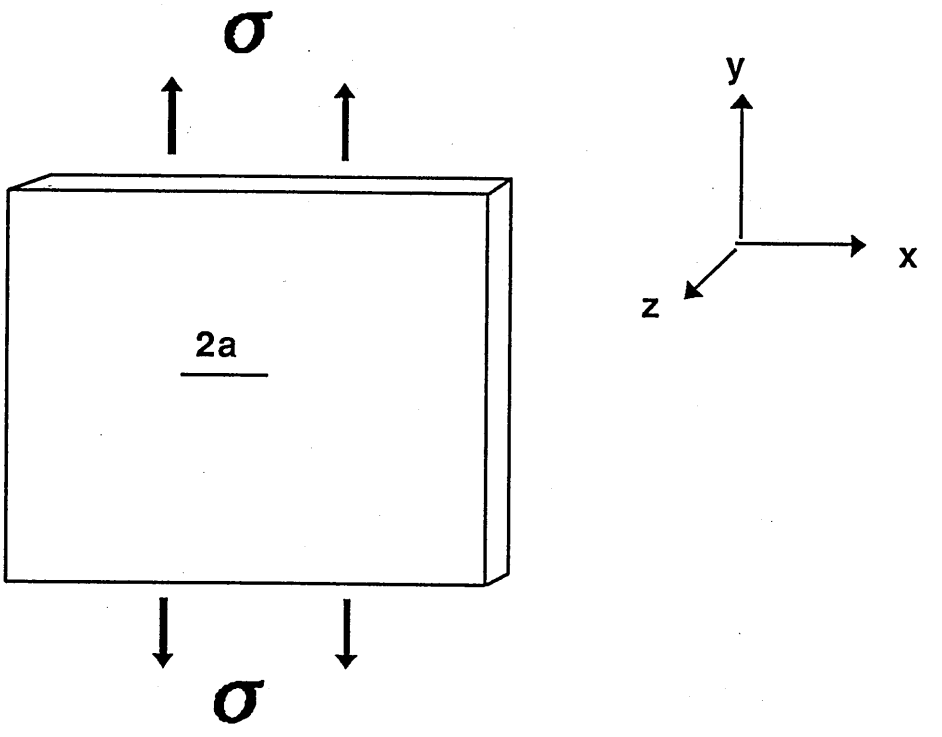

Figure 2.1 Through thickness crack in an infinite plate.

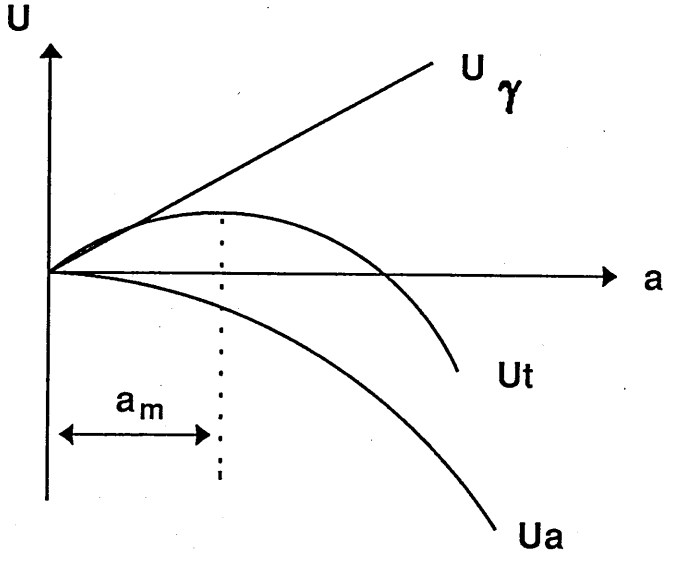

Figure 2.2 Energy change as a function of crack length.

$$\frac{\sigma_c^2 \pi a}{E} = 2\gamma_e \tag{2.4a}$$

The left side of equation (2.4a) is defined as the critical energy release rate 'G_C', which represents the elastic energy per unit crack surface area that is available for infinitesimal crack extension. The right side of the equation stands for the crack resistance 'R'. The energy release rate G must be greater than or at least equal to R in order to make the crack grow. This can be expressed as:

$$\sigma^2\pi a/E = G \geq \sigma_c^2\pi a/E = G_c = R = 2\gamma_e$$

The modification to the equation is made by introducing another crack resistance term γ_p, which represents the extra work required to cause plastic flow at the crack tip. Now, the crack resistance R is contributed by both elastic surface work γ_e and plastic work γ_p. It can be generally written as:

$$\frac{\sigma_c^2 \pi a}{E} = G_C = 2(\gamma_e + \gamma_p) \tag{2.5a}$$

Equation (2.5a) can be applied to a thin wide sheet. For a thick plate, following the same procedure and using Equation (2.3b), the corresponding equation is:

$$(1-\nu^2)\frac{\sigma_c^2 \pi a}{E} = G_{IC} = 2(\gamma_e + \gamma_p) \tag{2.5b}$$

In order to have a better understanding, two specific stress conditions which are often used in fracture mechanics are introduced now. Consider a thin wide sheet with a central through-thickness crack as shown in Figure 2.1. When a uniform stress σ acts on the sheet in the direction parallel to the plane of the sheet, the stress at the crack tip in the direction perpendicular to the plane is considered to be zero, where the thickness decreases because of the Poisson contraction. Under these conditions is termed plane stress. For a very thick plate and for the same applied stress considered above, through-thickness stresses are generated at the crack tip by the materials surrounding the crack, where the thickness does not decrease as in the case of a thin sheet. Through-thickness strain is considered to be zero. Under these conditions is termed plane strain.

The subscripts 'C' and 'IC' of G in Equations (2.5a) and (2.5b) are considered to stand for critical situations in plane stress and plane strain conditions respectively.

Griffith theory and its modified forms give a quantitative solution to the problem of crack size and fracture strength. However, from a practical application point of view, it is not convenient to define the conditions at which an ideally elastic sharp crack will become unstable. It is also difficult to use the theory to predict subcritical crack growth such as fatigue. To overcome these difficulties, one important achievement of LEFM was made by Irwin in 1950.

2.1.2 The Stress Intensity Approach

In 1950, Irwin applied elastic analysis to describe the magnitude of the stress field about the crack tip by means of a stress intensity factor. In general, the stresses at the crack tip can be expressed by

$$\sigma_{ij} = [K/(2\pi r)^{1/2}]f(\theta)$$

where K is the stress intensity factor, 'r' and θ are the distance from the crack tip and the angle corresponding to r, using cylindrical coordinates as indicated in Figure 2.3. Most commonly quoted solutions to the equation are based on Westergaard's analysis (1939), with reference to Mode I loading. For an infinite plate with unit thickness which contains a central sharp crack of length 2a, the stresses in the vicinity of the crack tip under biaxial tension can be expressed by the following equations (Ref: Ewalds 1986):

$$\sigma_x = \frac{\sigma\sqrt{\pi a}}{\sqrt{2\pi r}}\cos\frac{\theta}{2}\left(1-\sin\frac{\theta}{2}\sin\frac{3\theta}{2}\right)$$

$$\sigma_y = \frac{\sigma\sqrt{\pi a}}{\sqrt{2\pi r}}\cos\frac{\theta}{2}\left(1+\sin\frac{\theta}{2}\sin\frac{3\theta}{2}\right) \qquad (2.6)$$

$$\tau_{xy} = \frac{\sigma\sqrt{\pi a}}{\sqrt{2\pi r}}\sin\frac{\theta}{2}\cos\frac{\theta}{2}\cos\frac{3\theta}{2}$$

It can be seen that all the stresses in the equation are the product of two terms: one is determined by the factor $(2\pi r)^{-1/2}f(\theta)$, and another is determined by the magnitude of elastic stress, which is a function of remote stress and crack size, the factor $\sigma(\pi a)^{1/2}$. This last factor is defined as the mode I stress intensity factor for the defined stress field above:

$$K = \sigma\sqrt{\pi a} \qquad (2.7)$$

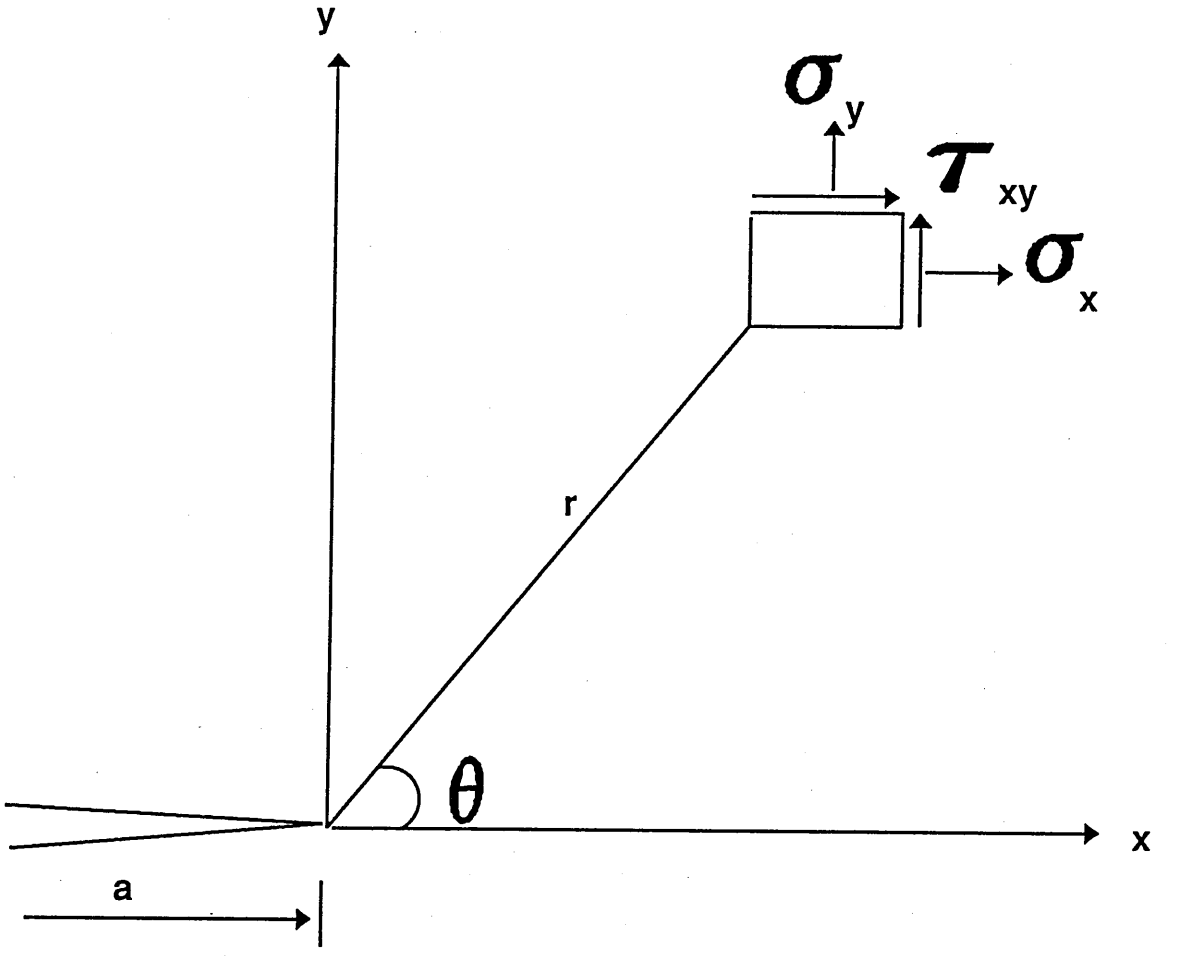

Figure 2.3 Stresses ahead of the crack tip under plane stress conditions.

Here is considered plane stress conditions. For plane strain conditions where a thick plate is considered, through-thickness elastic stress σ_z will be generated ahead of the crack tip. This stress can be obtained through Equation (2.6) by the relation $\sigma_z = \nu(\sigma_x + \sigma_z)$, where ν is Poisson's ratio.

When remote stress σ approaches its critical value σ_c, the left hand term in Equation (2.7) will approach its critical value too, i.e. K_C, which represents the critical stress intensity factor in plane stress conditions. In plane strain conditions, it is termed K_{IC}. Because materials show minimum toughness under plane strain conditions and K_{IC} is a material constant, K_{IC} is also called fracture toughness.

Both the energy approach (Section 2.1.1) and the stress intensity approach are used to establish the relationships between fracture stress and critical defect size. There should be a fundamental relation between these two methods. By definition, the energy release rate is the energy change per unit crack surface for infinitesimal crack extension. Recall equation (2.2a), the left side is the elastic energy change created by introducing the crack 2a with two equal crack surfaces. Therefore, differentiating this equation gives:

$$\frac{\partial U_a}{\partial a} = -2G = -\frac{2\sigma^2 \pi a}{E} \tag{2.8}$$

$$G = \frac{\sigma^2 \pi a}{E} \tag{2.9}$$

where negative sign means decreasing energy and 2 represents two unit crack surfaces. A combination of Equations (2.7) and (2.9) gives:

$$K = \sqrt{GE} \tag{2.10a}$$

Equation (2.10a) is for the plane stress conditions. For plane strain conditions, differentiating Equation (2.2b) and following the same procedure as above gives

$$K = \sqrt{\frac{GE}{(1-\nu^2)}} \tag{2.10b}$$

It is emphasized here that $K = \sigma(\pi a)^{1/2}$ is true only for a centrally cracked infinite plate under Mode I loading. For other geometries, it takes the general form $K = Y\sigma(\pi a)^{1/2}$, where Y is geometric factor. In addition, since both K and G can be used to characterize crack growth and fracture, they are equivalent in nature under linear elastic fracture mechanics. When G

approaches G_C or G_{IC}, K equally approaches K_C or K_{IC} respectively.

2.1.3 Crack Tip Plasticity

The stress intensity approach was used to describe the stress field in the vicinity of the crack tip as expressed by equation (2.6), which indicates that all the stresses become infinite at the crack tip, i.e. $\sigma_{ij} \rightarrow \infty$ as $r \rightarrow 0$. Normally, materials will yield in the vicinity of the crack tip after the stresses approach the yield stress. As a result, a plastic deformation zone will be generated about the crack tip, where plastic deformation has taken place.

Before further discussion on the subject, it will be helpful if stress field is expressed in terms of principal stresses when yield criteria are considered in the evaluation of plasticity. This can be done by using Mohr's circle construction as indicated in Figure 2.4. The principal stresses can be expressed by:

$$\sigma_{1,2}=\frac{\sigma_x+\sigma_y}{2}\pm R \tag{2.11}$$

where

$$R=\sqrt{(\frac{\sigma_y-\sigma_x}{2})^2+\tau_{xy}^2}$$

Substituting Equation (2.6) into (2.11) and using K instead of $\sigma(\pi a)^{1/2}$ gives:

$$\sigma_1=\frac{K}{\sqrt{2\pi r}}\cos\frac{\theta}{2}(1+\sin\frac{\theta}{2}) \tag{2.12a}$$

$$\sigma_2=\frac{K}{\sqrt{2\pi r}}\cos\frac{\theta}{2}(1-\sin\frac{\theta}{2}) \tag{2.12b}$$

The third principal stress σ_3 is either zero, under plane stress conditions, or equal to $\nu(\sigma_1+\sigma_2)$, under plane strain conditions. For the latter case, σ_3 is:

$$\sigma_3=\frac{2\nu K}{\sqrt{2\pi r}}\cos\frac{\theta}{2} \tag{2.12c}$$

As far as the crack tip plasticity is concerned, two problems need to be resolved. First is the size of plastic zone and second the shape. In fact, no accurate solutions to the problems have

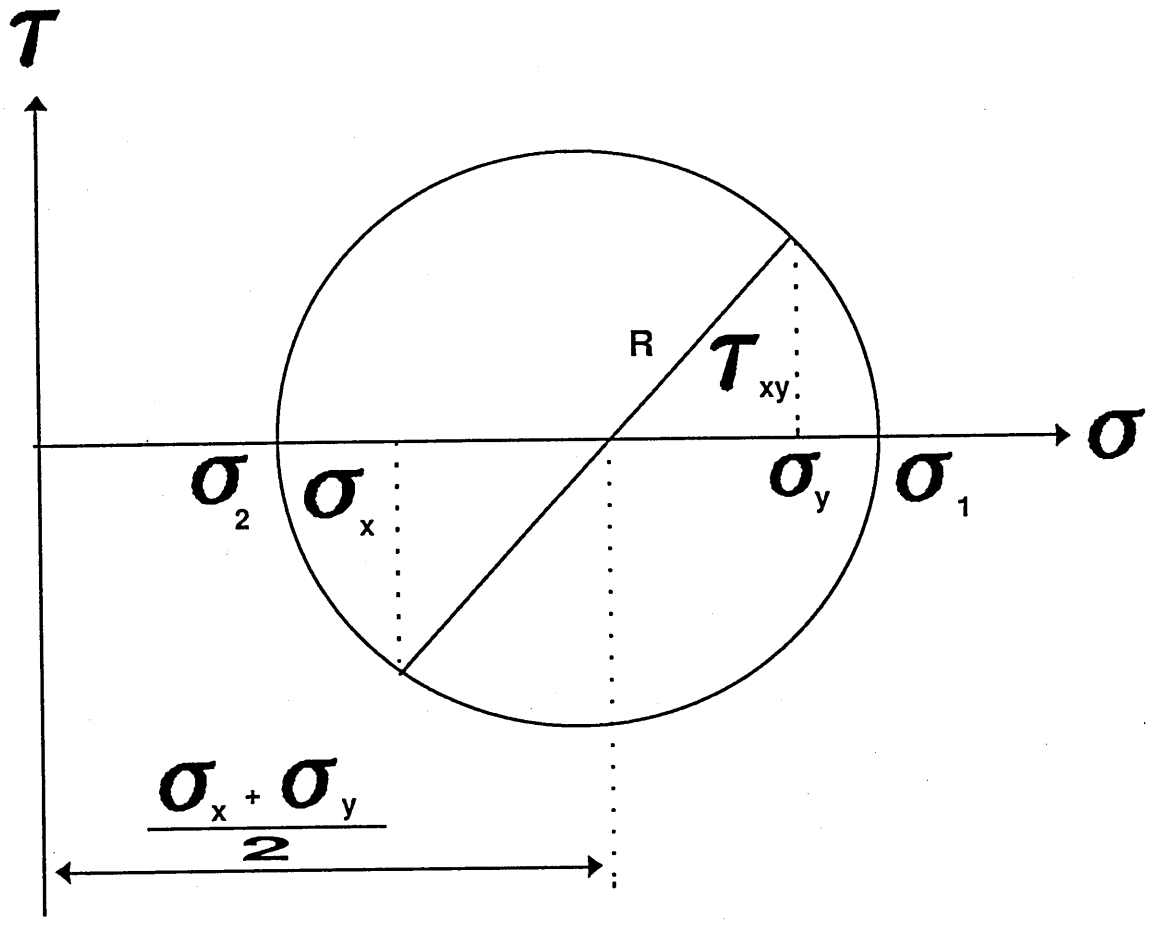

Figure 2.4 Mohr's circle of stress.

been obtained. All attempts that have been made follows one of the two approaches. One approach can give a better approximation of the size but for an assumed shape, e.g. the analysis conducted by Irwin and Dugdale . Another one can give a better description of the shape but with compromising the accuracy of the size. Besides these two, which are going to be discussed soon, the plasticity induced by the cavitation of rubber particles in toughened plastics gives a different view on both the size and the shape. This will be discussed separately in Chapter 8.

Plastic Zone Size

Now consider the stress field as defined above for plane stress conditions ($\sigma_3=0$) and at $\theta=0$. Equation (2.12) becomes:

$$\sigma_1=\sigma_2=\frac{K}{\sqrt{2\pi r}} \tag{2.13}$$

Under this circumstance, $\sigma_1=\sigma_y$ and $\sigma_2=\sigma_x$ (see Equation (2.6)).

By using Von Mises yield criterion which states that yielding will occur when:

$$(\sigma_1-\sigma_2)^2+(\sigma_2-\sigma_3)^2+(\sigma_3-\sigma_1)^2 = 2\sigma_{yield}^2 \tag{2.14}$$

where σ_{yield} is the yield stress under simple tension, it is given $\sigma_1=\sigma_{yield}$, i.e. the material will yield when the principal stress approaches the yield stress. If it is assumed that all the stresses will level off after they are greater than σ_{yield}, as a first approximation, an estimate of the plastic zone size r_p can be obtained simply substituting σ_{yield} for σ_1 in Equation (2.13):

$$r_p=\frac{1}{2\pi}\left(\frac{K}{\sigma_{yield}}\right)^2 \tag{2.15}$$

This is illustrated in Figure 2.5, where circular plastic zone is assumed. It can be seen that all the stresses above σ_{yield} have been simply cut off without further contributions to the plasticity. This hypothesis is not accurate. It has been corrected by Irwin.

Irwin's circular zone model

Irwin considered the same stress field above but took all the stresses above σ_{yield} into account

in the evaluation of plastic zone size. It was assumed that the zone is circular and the material is elastic - perfectly plastic. Under the latter condition, no strain hardening exists in plastic deformation. So the occurrence of plasticity makes the crack appear longer than its physical size. So a notional crack tip with a notional crack increment Δa_n are defined by Irwin as shown in Figure 2.6. The effective crack length a_{effect} and the corresponding stress intensity factor become:

$$a_{effect} = a + \Delta a_n$$

$$K=\sigma\sqrt{\pi(a+\Delta a_n)} \tag{2.16}$$

The question is Δa_n = ? Irwin argued that Δa_n must be related to the redistribution of the stresses which are above σ_{yield}. The shadow area A in Figure 2.6, which accounts for the work of the redistribution of these elastic stresses, should be equal to the area $\sigma_{yield}\Delta a_n$, which accounts for plastic work done by the redistribution, i.e.:

$$\sigma_{yield}\Delta a_n=\int_0^{r_p}\sigma_1 dr-\sigma_{yield}r_p \tag{2.17}$$

$$\Delta a_n+r_p=\frac{1}{\sigma_{yield}}\int_0^{r_p}\sigma_1 dr=\frac{1}{\sigma_{yield}}\int_0^{r_p}\frac{K}{\sqrt{2\pi r}}dr$$

$$\Delta a_n+r_p=\frac{2K}{\sigma_{yield}\sqrt{2\pi}}\sqrt{r_p}=2\sqrt{r_p}\sqrt{r_p}=2r_p \tag{2.18}$$

where the plastic size r_p ahead of the notional crack tip is expressed in the same way as in Equation (2.15) except that the crack length is (a + Δa_n) rather than 'a'. Irwin's analysis results in a plastic zone diameter twice that obtained from Equation (2.15) and the notional crack tip locates at the centre of the assumed circular zone, i.e.

$$r_{Irwin}=2r_p=\frac{1}{\pi}\left(\frac{K}{\sigma_{yield}}\right)^2 \tag{2.19}$$

Dugdale's line-zone model

Instead of Irwin's circular plastic zone, Dugdale chose another shape of the zone for the evaluation of plastic zone size. His analysis is based on the hypothesis that all plastic

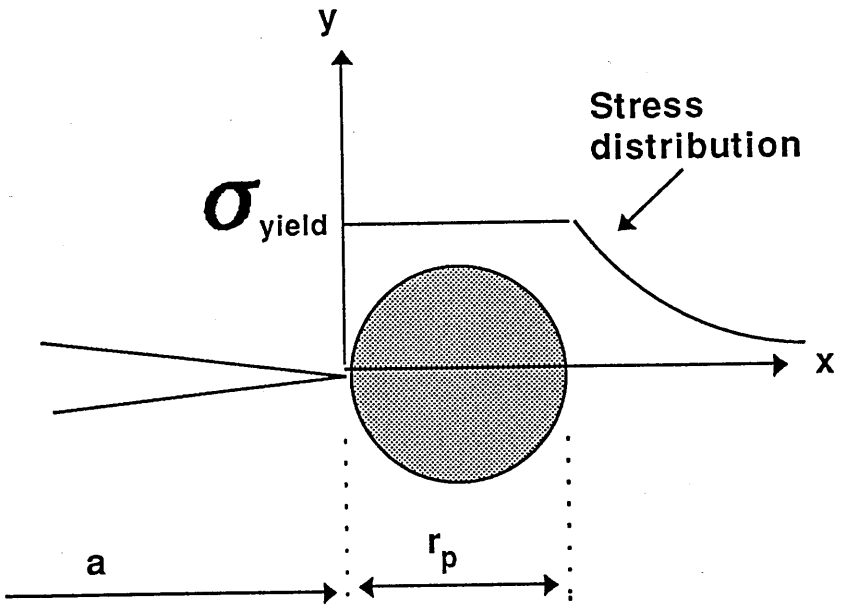

Figure 2.5 Schematic diagram of plastic zone ahead of the crack tip.

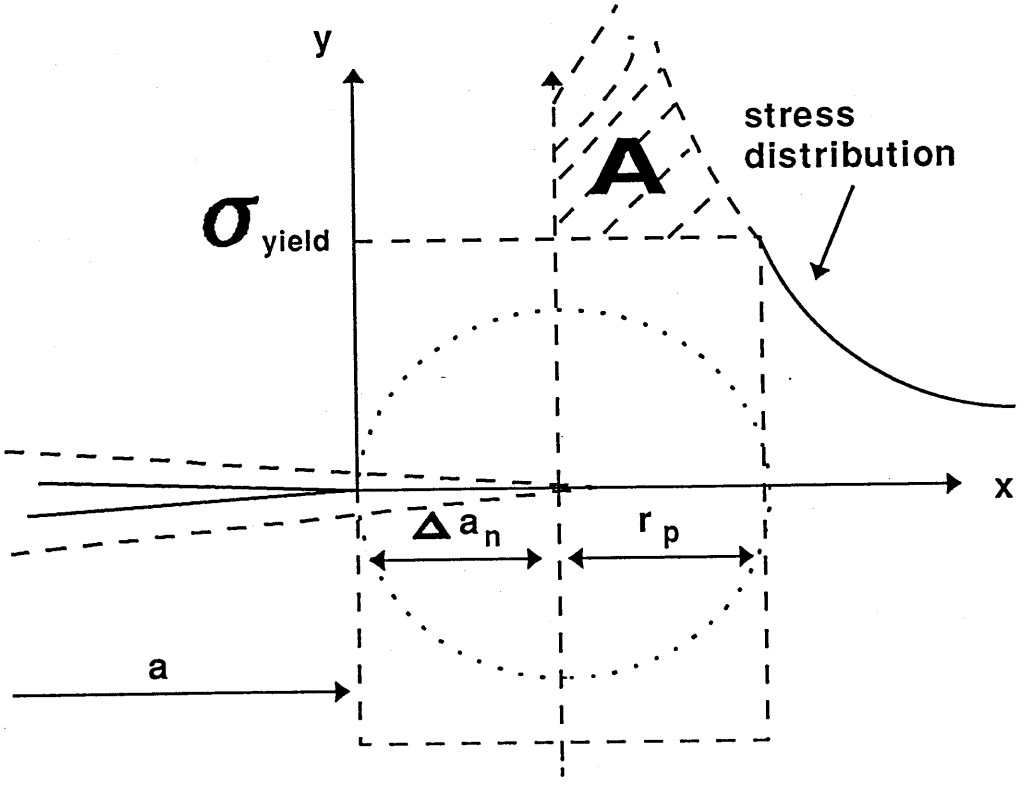

Figure 2.6 Irwin's plastic zone and schematic diagram of stress redistribution.

deformation is concentrated in a strip ahead of the crack tip, which is assumed to carry the yield stress. This is schematically shown in Figure 2.7. The general equation from Dugdale's analysis is:

$$\frac{a}{a+r_{Dugdale}} = \cos\left(\frac{\sigma}{\sigma_{yield}}\frac{\pi}{2}\right) \tag{2.20}$$

Expanding $\cos(\sigma\pi/2\sigma_{yield})$ as a series, Equation (2.20) becomes:

$$\frac{a}{a+r_{Dugdale}} = 1-\frac{1}{2!}\left(\frac{\sigma}{\sigma_{yield}}\frac{\pi}{2}\right)^2+\ldots+(-1)^n\frac{1}{(2n)!}\left(\frac{\sigma}{\sigma_{yield}}\frac{\pi}{2}\right)^{2n}\ldots$$

For the small stress which is less than a third of the yield stress, i.e. $\sigma \le \sigma_{yield}/3$, the equation can be written as:

$$\frac{a}{a+r_{Dugdale}} = 1-\frac{\pi^2}{8}\left(\frac{\sigma}{\sigma_{yield}}\right)^2$$

$$\frac{r_{Dugdale}}{a+r_{Dugdale}} = \frac{\pi^2}{8}\left(\frac{\sigma}{\sigma_{yield}}\right)^2 \tag{2.21}$$

with an error < 0.1 %. Assuming a >> $r_{Dugdale}$, it is given:

$$r_{Dugdale} = \frac{\pi}{8}\frac{\sigma^2\pi a}{\sigma_{yield}^2} = \frac{\pi}{8}\left(\frac{K}{\sigma_{yield}}\right)^2 \tag{2.22}$$

Comparison of this equation with Equation (2.19), it is found that $r_{Dugdale}=1.2r_{Irwin}$. The difference is in the shape of plastic zone. One assumes a strip plastic zone and the other a circular one. Some materials show Dugdale's line-zone model ahead of the crack tip but others Irwin circular plastic zone. This will be discussed in the following chapter.

It should be noted that the analysis discussed above is considered only under plane stress conditions. When the specimen thickness is taken into account, the plastic constraint factor is expected to affect plastic zone size at the crack tip.

Through-thickness Plastic Zone Size and Shape

As discussed in the beginning of this section, evaluation of plastic zone in the vicinity of the crack tip can be given either a better approximation of the size but for an assumed shape or a better description of the shape but with compromising the accuracy of the size. The first subject has been discussed above. Now consider the second one the shape of plastic zone.

If the first approximation of plastic zone size is acceptable [Equation (2.15)], the plastic zone size under other conditions can also be obtained following the same principle. Substituting all the principle stresses of Equation (2.12) into Equation (2.14) - the Von Mises yielding criterion - and using $r_p(\theta)$ instead of 'r' results in:

$$\frac{r_p(\theta)}{r_p} = \frac{3}{4}\sin^2(\theta)+\frac{1}{2}(1-2\nu)^2(1+\cos\theta) \qquad (2.23)$$

$$r_p = \frac{1}{2\pi}\left(\frac{K}{\sigma_{yield}}\right)^2$$

where r_p is plane stress plastic zone size at $\theta = 0$ and ν Poisson's ratio.

Figure 2.8 is drawn according to equation (2.23) at Poisson's ratios 0, 0.3 and 0.5 respectively. When $\nu = 0$, Equation (2.23) reduces to plane stress conditions. It can be seen that plastic zone size is much bigger under these conditions than that under plane strain conditions because of additional constraint for the latter. Therefore, thick specimens will form a 'sandwich'-like plastic zone shape, with a big plastic zone at surfaces and a small one towards the centre at the crack tip as indicated schematically in Figure 2.9. This is because plane stress conditions occur in the surfaces.

When $\theta = 0$, plastic zone size under plane strain conditions is given by equation (2.23):

$$r_p'(0) = \frac{1}{2\pi}\left(\frac{K}{\sigma_{yield}}\right)^2 (1-2\nu)^2 \tag{2.24a}$$

$$r_p'(0) = \frac{1}{2\pi}\left(\frac{K_I}{C\sigma_{yield}}\right)^2 \tag{2.24b}$$

where C = 1/(1-2ν) and it is called plastic constraint factor.

It is emphasized that these plastic zones described by Equation (2.23) apply only to the materials which obey the Von Mises yielding criterion. Further discussions on the subject will be followed in Chapter 8 when the effect of cavitation of rubber particles on plastic deformation is discussed.

2.1.4 Crack Tip Blunting Theory

In the previous discussion, a sharp crack was assumed. When a crack tip has a tip radius ρ, local stress along Y-direction can be expressed by (Williams 1980):

$$\sigma_y = \sigma + \sigma\sqrt{a}\frac{2\rho + 2r}{(\rho + 2r)^{3/2}} \tag{2.25}$$

where 'a' is half crack length (a >> ρ), 'r' is the distance ahead of the crack tip and σ is remote stress as indicated in Figure 2.10. When a >> r, equation (2.25) can be written as:

$$\sigma_y = \frac{\sigma\sqrt{a}}{\sqrt{2r}}\frac{1+\frac{\rho}{r}}{\left(1+\frac{\rho}{2r}\right)^{3/2}} \tag{2.26}$$

It is assumed that failure will occur when stress σ_y approaches a critical value σ_{tc} at critical distance r_c ahead of the crack tip, i.e.:

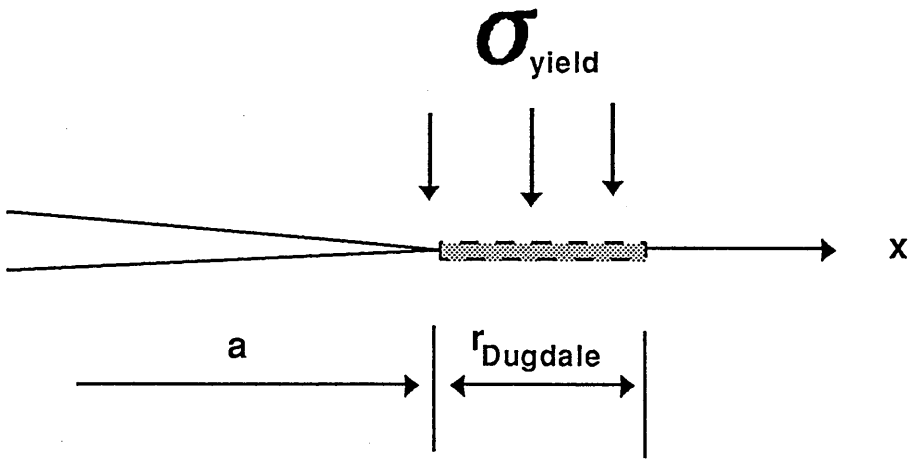

Figure 2.7 Dugdale's line-zone model.

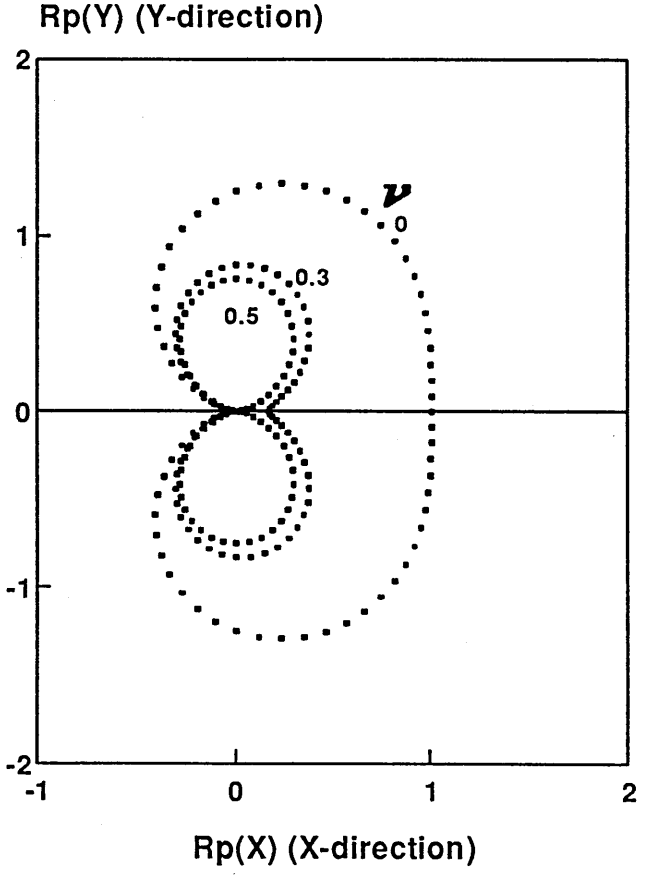

Figure 2.8 Von Mises plastic zone.

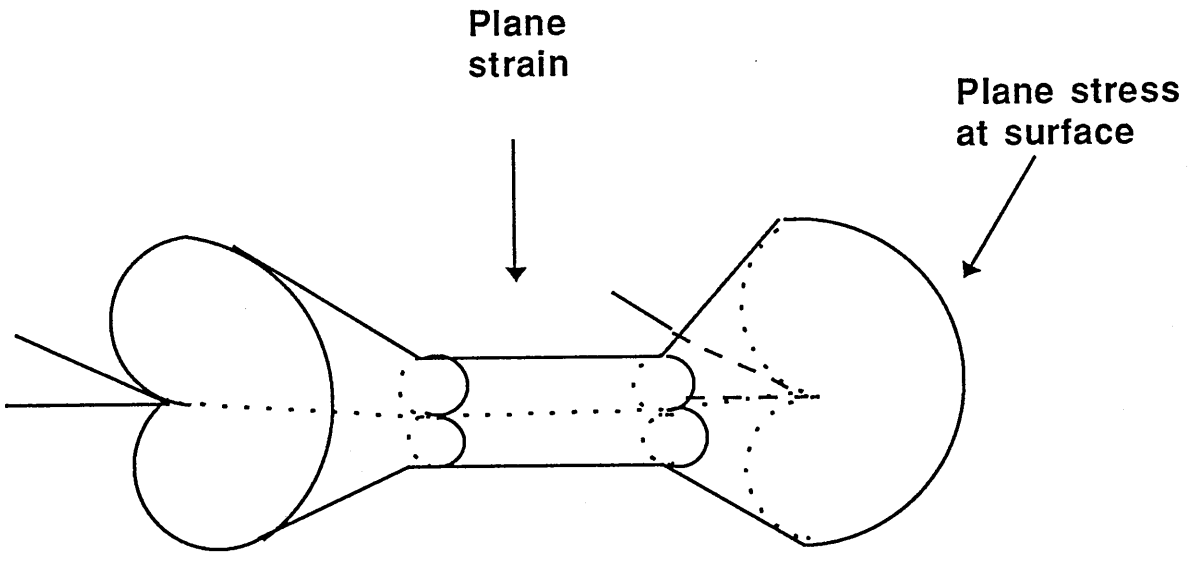

Figure 2.9 Through thickness plastic zone.

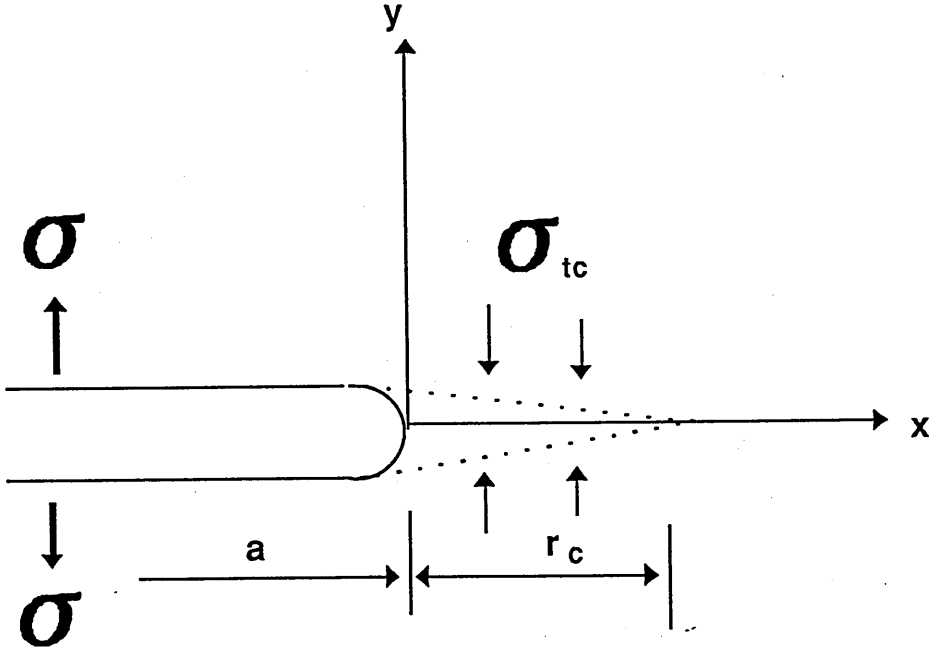

Figure 2.10 Schematic diagram of blunt crack tip.

$$\sigma_{tc} = \frac{\sigma\sqrt{a}}{\sqrt{2r_c}} \frac{1+\frac{\rho}{r_c}}{\left(1+\frac{\rho}{2r_c}\right)^{3/2}} \tag{2.27}$$

The critical stress intensity factor at the 'sharp' crack r_c can be expressed by (Kinloch 1983):

$$K_{tc} = \sigma_{tc}\sqrt{2\pi r_c} \tag{2.28}$$

On the other hand, when remote stress $\sigma = \sigma_c$, the critical stress intensity factor for the blunted crack tip K_{IB} is given by:

$$K_{IB} = \sigma\sqrt{\pi a} \tag{2.29}$$

Combination of equations (2.27), (2.28) and (2.29) gives:

$$K_{IB}=K_{tc}\frac{\left(1+\frac{\rho}{2r}\right)^{3/2}}{\left(1+\frac{\rho}{r}\right)} \tag{2.30}$$

For the case where $\rho >> r_c$, i.e. $\rho/r_c >>1$, equation (2.30) becomes $K_{IB}=½K_{tc}(\rho/2r)^{1/2}$. Linear relationship between K_{IB} and $(\rho/r)^{1/2}$ will be expected as crack tip radius increases. Equation (2.30) is a version of crack tip blunting theory.

2.1.5 Subcritical Crack Growth - Fatigue

As discussed in section 2.1.2, stress intensity factor K determines the local stress magnitude of a cracked system. No matter if the system is in the critical state or below it, K is still applicable. As far as material fatigue properties are concerned, the main question is, under repeated alternative stresses, how long will it take from an initial crack size to a maximum permissible crack size.

In the 1960s, Paris answered the question by using the stress intensity factor to characterize fatigue behaviour quantitatively. He postulated that the fatigue crack propagation (FCP) process was mainly controlled by the stress intensity factor (Paris 1963). By using stress

intensity range ΔK, the relationship between FCP and ΔK was given by:

$$\frac{da}{dn} = A\Delta K^4 \tag{2.31a}$$

where da/dn stands for crack growth per cycle, 'A' is constant and $\Delta K = K_{max} - K_{min} = \sigma_{max}(\pi a)^{1/2} - \sigma_{min}(\pi a)^{1/2}$, here σ_{max} and σ_{min} are maximum and minimum values of repeated alternative tensile stresses. This perhaps is the first time when Paris suggested that fatigue crack growth rate was proportional to ΔK raised to the fourth power. This relationship agreed well with crack growth data of aluminum alloy (Paris 1963). A more general Paris equation is usually written as:

$$\frac{da}{dn} = A\Delta K^m \tag{2.31b}$$

where 'm' is constant, which can vary from 2 to 12 (Kocanda 1978). Equation (2.31) is known as Paris Law. It is the basic FCP theory from which many other theories have been developed.

2.1.6 Geometry Effect on Fracture Toughness

The ideas of LEFM discussed in the previous sections can be expressed theoretically by critical energy release rate G_C or critical stress intensity factor K_C. These parameters must be measured by experiment before they can be used for engineering purposes. In this section, a general equation which is used for caculation of G_C and K_C will be introduced considering geometric factor.

Consider a crack of length 2a in a plate with a thickness B and a width W as shown in Figure 2.11. When the crack grows from 'a' to a+δa at constant load P, the energy change of the process is given by:

$$GB\delta a = \frac{1}{2}P\delta u \tag{2.32}$$

which is the shadowed area in Figure 2.11. By definition, specimen compliance C is given by C=u/P, then $\delta u = P\delta C$. Equation (2.32) becomes:

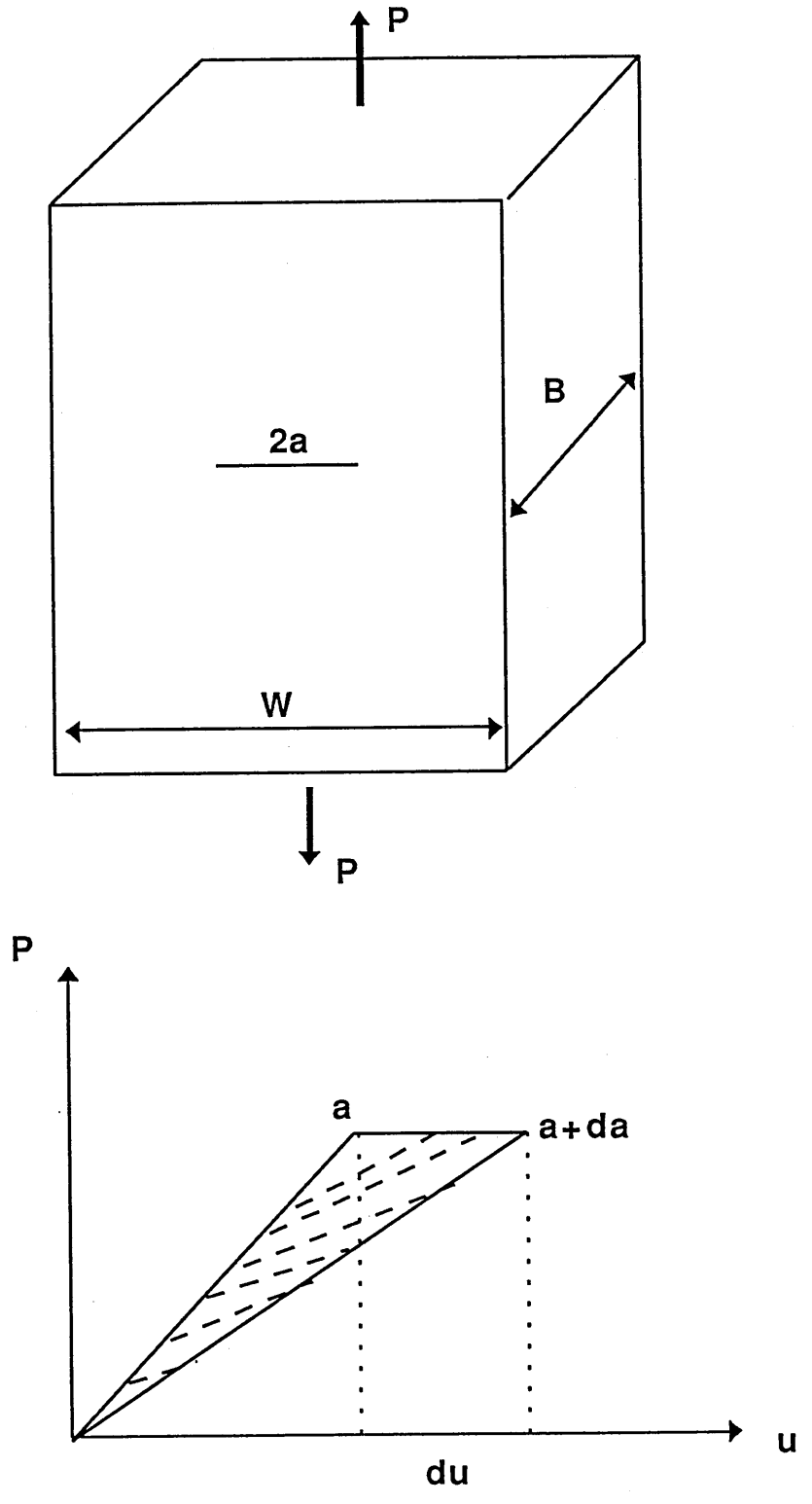

Figure 2.11 Energy change at crack growth (constant load P).

$$G = \frac{1}{2}\frac{P^2}{B}\frac{dC}{da} \tag{2.33}$$

This equation can be transformed to a dimensionless form by introducing modulus E and specimen width W. It is given by:

$$\frac{GEWB^2}{P^2} = \frac{EB}{2}\frac{dC}{d\left(\frac{a}{W}\right)} \tag{2.34}$$

The right hand term in Equation (2.34) is independent of the size scale of the specimens and elastic properties of the materials. Once a calibration is made for a certain specimen configuration, it can be used for any material provided that the specimens have the same configuration. Normally the right hand term is expressed as a polynominal form. Then equation (2.34) becomes:

$$\frac{GEWB^2}{P^2} = A_1\left(\frac{a}{W}\right) + A_2\left(\frac{a}{W}\right)^2 + \ldots\ldots$$

$$K = \sqrt{GE} = \frac{P}{\sqrt{WB}}\left[D_1\left(\frac{a}{W}\right) + D_2\left(\frac{a}{W}\right)^2 + \ldots\ldots\right]$$

$$K = \frac{P}{\sqrt{WB}}Y \tag{2.35}$$

where Y is a function of (a/W), which depends only on specimen geometry. Equation (2.35) is a general form which can be used to calculate fracture toughness through experiment. Y values are available for certain standard specimen configurations.

2.2 The Yielding Behaviour of Polymers

In section 2.1, the relationships between fracture strength and maximum permissible defect size have been discussed. All the theories are based on the assumption that materials are linear elastic in nature. They can be applied under conditions in which materials are perfectly elastic with very limited plastic deformation at the crack tip. Polymer yielding is another important research area which is of significance in theory and in application of polymer materials. One of the most important yielding characteristics of polymers is time/temperature

dependence. In order to establish the relationships between yield stress and strain rate/temperature, three theories will be considered in this section. They are the Eyring, Argon and Chow theories. The former two theories are based on the model of plastic flow in the glassy state. The later one is based on the assumption of a non-equilibrium state defined by free volume.

2.2.1 Eyring's Theory

Eyring's theory (1936) is based on the activation energy concept, which has been used to obtain absolute rates of chemical reaction. For a segment movement of long polymer chain in the glassy state, activation energy theory can also be used if it is assumed that the movement of a segment of polymer chain must overcome an energy barrier in order to jump from one equilibrium state to another. The peak point of energy barrier acts as intermediate stage in the moving process. This is schematically shown in Figure 2.12. (Reference: McCrum et al 1988)

According to the theory, activation free energy ΔG^*, determines the rate of this transformation process at a given temperature. Mathematically, it can be expressed as:

$$R_{ta} = \frac{kT}{h}\exp\left(-\frac{\Delta G^*}{RT}\right) \tag{2.36}$$

$$R_{ta} = \frac{kT}{h}\exp\left(\frac{\Delta S^*}{R}\right)\exp\left(-\frac{\Delta H^*}{RT}\right)$$

where, R_{ta} is the rate of one segment of polymer chain jumping from one equilibrium position 'A' to another equilibrium position 'B', and k, h and R are the Boltzmann, the Planck and the molar gas constants respectively; ΔG^*, ΔS^* and ΔH^* are the differences in Gibbs free energy, entropy and enthalpy between the equilibrium state and the activated state respectively.

It is expected, from Figure 2.12(a), that the reverse rate of movement of a segment from B to A, R_{tb}, will be equal to that from A to B, i.e. $R_{ta} = R_{tb}$. However, when a shear stress σ_s is applied to a segment at position A, which is assumed to promote the movement from position A to position B, the work done by the force could be expressed by the product of the shear stress σ_s, the effective shearing area of the segment and the distance from A to the activated state, x^*, i.e. $(\sigma_s A^*)x^* = \sigma_s v^*$. Here v^* is normally termed the activation volume.

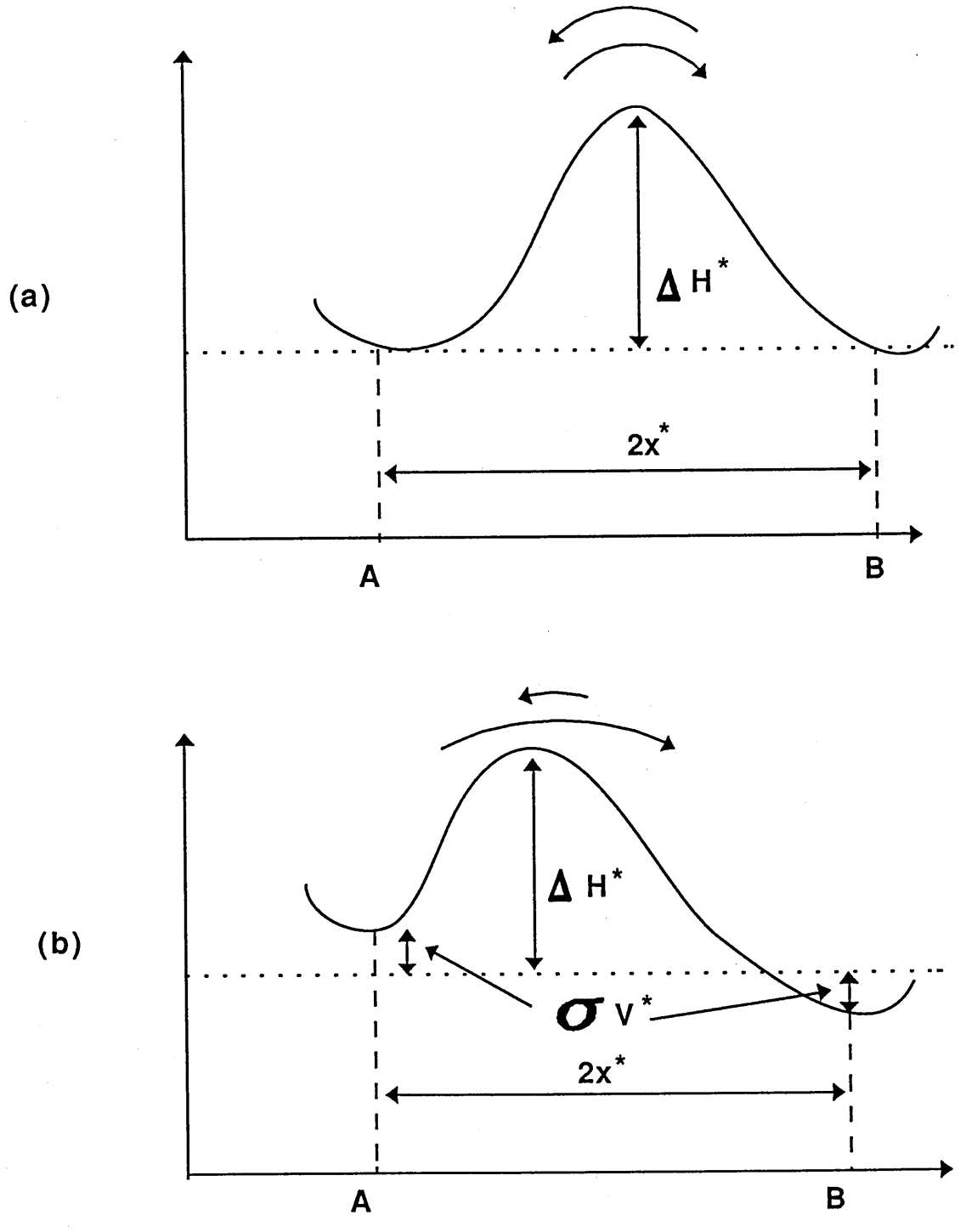

Figure 2.12 Schematic diagram of energy barrier: (a) before stress applied; (b) after stress applied.

The energy barrier has been changed by this shear force as indicated in Figure 2.12(b). The net jumping speed from A to B is then expressed as $R_t = R_{ta}-R_{tb}$. It is given by:

$$R_t = \frac{kT}{h}\exp\left(\frac{\Delta S^*}{RT}\right)\exp\left(-\frac{\Delta H^*}{RT}\right)2\sinh\left(\frac{\sigma_s V^*}{RT}\right) \tag{2.37}$$

where V^* is molar activation volume, resulting from v^* multiplied by Avogadro's constant.

It is assumed that σ_s is the deviatoric shear stress and the material obeys Von Mises yielding criterion:

$$(\sigma_1-\sigma_2)^2+(\sigma_2-\sigma_3)^2+(\sigma_3-\sigma_1)^2 = 6\sigma_{sy}^2 \tag{2.38}$$

Combination of this equation and Equation (2.14) gives:

$$\sigma_{sy} = \frac{1}{\sqrt{3}}\sigma_{yield} \tag{2.39}$$

As mentioned before, σ_{yield} is the yield stress under simple tension. So Equation (2.39) established the relationship between shear yield stress and tensile yield stress under simple tension.

In order to make equation (2.37) applicable, two assumptions are made here: (a) the dominant mechanisms of deformation is shearing and it will occur when $\sigma_{sy} = 3^{-½}\sigma_{yield}$ under simple tension; (b) the total strain is the summation of strains of each individual segment,i.e. $\varepsilon_y = \Sigma\varepsilon_i$, here ε_i is the strain of one moving segment. Consider a number of segments N and each of them has average strain ε_a moving from A to B at yield, the total strain would be equal to $N\varepsilon_a$. Therefore, the total strain rate $\dot{\varepsilon}_y$ can be expressed by $\dot{\varepsilon}_y = N\varepsilon_a R_t$. Substituting Equation (2.37) for R_t and using $3^{½}\sigma_{yield}$ instead of σ_{sy} in the equation, it is given by:

$$\dot{\varepsilon}_y = \dot{\varepsilon}_0\exp\left(-\frac{\Delta H^*}{RT}\right)2\sinh\left(\frac{\sigma_{yield}V^*}{\sqrt{3}RT}\right) \tag{2.40}$$

where $\dot{\varepsilon}_0 = (N\varepsilon_a kT/h)\exp(\Delta S^*/R)$. When $\sigma_{yield}V^* >> 3^{½}RT$, $2\sinh[(\sigma_{yield}V^*)/(3^{½}RT)] \approx \exp[(\sigma_{yield}V^*)/(3^{½}RT)]$ and equation (2.40) becomes:

$$\dot{\varepsilon}_y = \dot{\varepsilon}_0\exp\left(-\frac{\Delta H^*}{RT}\right)\exp\left(\frac{\sigma_{yield}V^*}{\sqrt{3}RT}\right)$$

$$\frac{\sigma_{yield}}{T} = \frac{\sqrt{3}}{V^*}\left(\frac{\Delta H^*}{T} + 2.303R\log\frac{\dot{\varepsilon}_y}{\dot{\varepsilon}_0}\right) \tag{2.41}$$

Equation (2.41) is a version of Eyring's basic equation. The dependence of yield stress on temperature and strain rate is now quantitatively described by the equation. At a given temperature, a linear relationship will be expected between yield stress σ_{yield} and logarithm yield strain rate $\dot{\varepsilon}_y$. Increasing strain rate will give rise to a higher yield stress. On the other hand, increasing temperature will reduce yield stress at a given strain rate.

2.2.2 Argon's Theory

Argon (1973) developed Eyring's theory. He modeled polymer yielding as a chain alignment process through a series of local rotations along the chain. The significant aspect of the theory is that the effective radius of the polymer chain and its segment length at yield can be obtained on the basis of actual molecular structure. It is impossible to get these structural parameters through Eyring's theory.

The essential idea of the theory is to work out the energy change during a polymer chain alignment at yield, on the basis of polymer chain conformation. It would be expected that there should be some resistance against the alignment. It may come from two parts: (a) the entropic resistance, and (b) the elastic resistance which comes from the neighbourhood of each segment. It is known that the entropic resistance will dominate the chain alignment when the temperature is above the glass transition temperature T_g under loading. The polymer will recover to its original state as soon as the stress is released. However, the second factor will be the main resistance which dominates the alignment process when temperature is below T_g. The aligned chain will not recover to its original state even after the stress has been released unless it is reheated to a temperature above T_g. Based on these facts, Argon took the second factor into account in order to calculate the free energy change (the Gibbs free energy) for a polymer chain aligning in the glassy state, ignoring the entropic resistance.

Argon assumed that a polymer chain consists of a number of segments in a zig-zag formation. These segments are initially in a random distribution and each segment has a pair of kinks at the two ends. It is also assumed that each segment alignment step would eliminate a pair of kinks along the polymer chain. The Gibbs energy can be obtained if the energy needed to reduce a pair of kinks can be calculated. This energy should be the same as that needed to form a pair of kinks. Fortunately, this problem was solved by Li and Gilman (1970).

The formation of a pair of kinks from an aligned segment would be equivalent to the process modeled by Li and Gilman as shown in Figure 2.13. It was assumed that two circular wedges separated by a distance 'z' were cut from an aligned polymer chain of radius 'a'. The two pieces with a wedge angle 'ω' were then inserted at the positions just opposite where they were cut out. Then a pair of kinks was formed along the polymer chain. These are known as wedge disclination loops, as defined by Li and Gilman (1970).

It is worth noticing that only elastic stress field, both within and outside the wedge loops, was considered by Li and Gilman in the model and it was based on the atomic dimensions of polymer chain.

The Gibbs energy has changed during the formation of two wedge disclination loops (Figure 2.13). The components of the change are:

(a) the strain energy $2\Delta F_s$. ΔF_s is the energy of formation of one wedge loop, which accounts for all the contributions in the elastic field outside the wedge loop. Here '2' means a pair of loops (or kinks in polymer chain) which are considered at the same time as mentioned above.

(b) the interaction energy ΔF_i. This is the energy that accounts for the energy change of interaction between the two neighbouring loops and within the stress field of the two loops.

(c) the work done by external force ΔW_σ. This is the energy needed to make the newly-formed loops stable.

The energy changes in (a) and (b) were calculated by Li and Gilman. The energy in (c) by Argon (1973). The total energy change is given by:

$$\Delta G = 2\Delta F_s + \Delta F_i - \Delta W_\sigma \tag{2.42}$$

where

$$2\Delta F_s = \frac{3\pi\mu\omega^2 a^3}{16(1-\nu)}$$

$$\Delta F_i = -\frac{9\pi\mu\omega^2 a^3}{8(1-\nu)}\left(\frac{a}{z}\right)^5$$

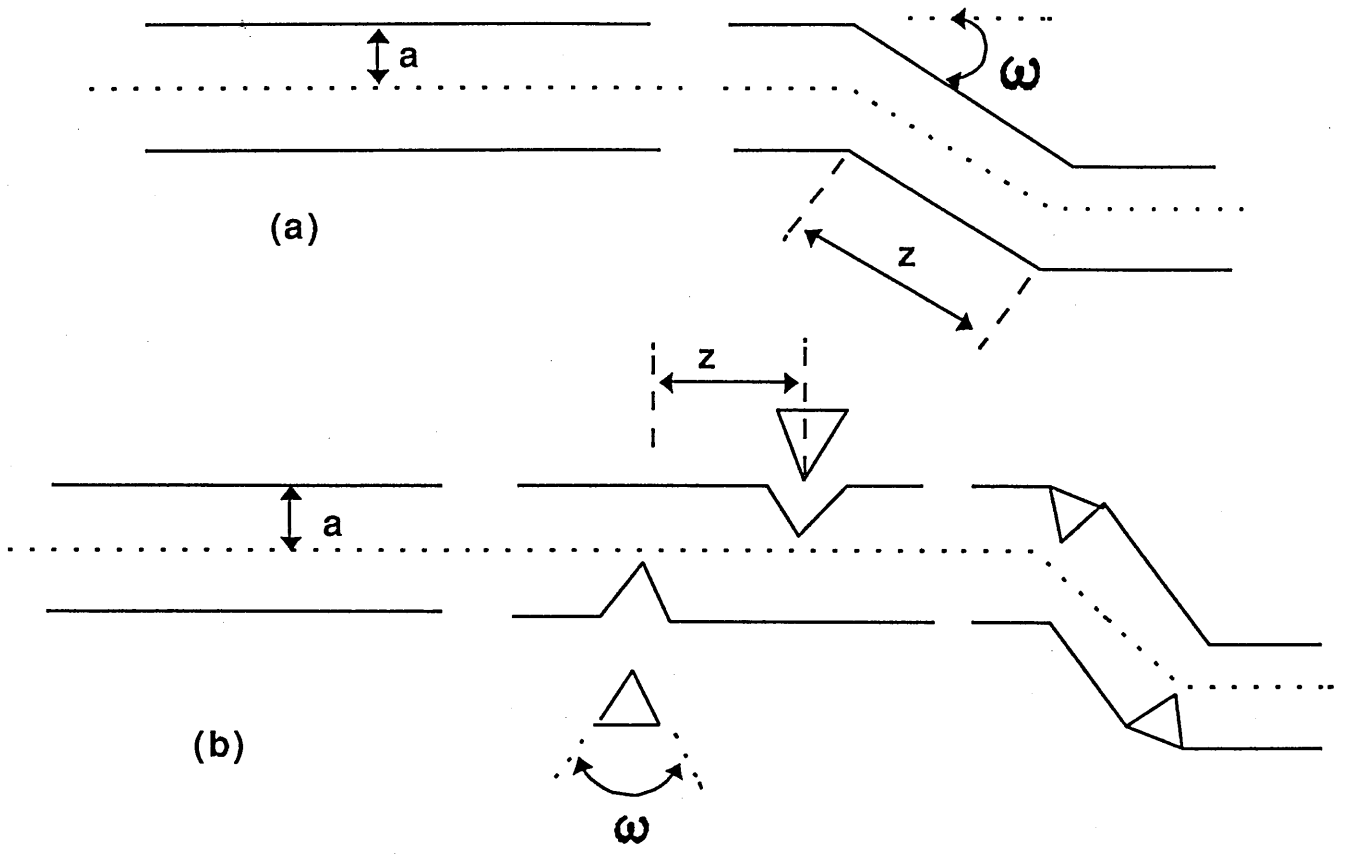

Figure 2.13 (a) Schematic of formation of a pair of kinks along a polymer chain; (b) modelling of (a) by using a pair of wedge disclination loops.

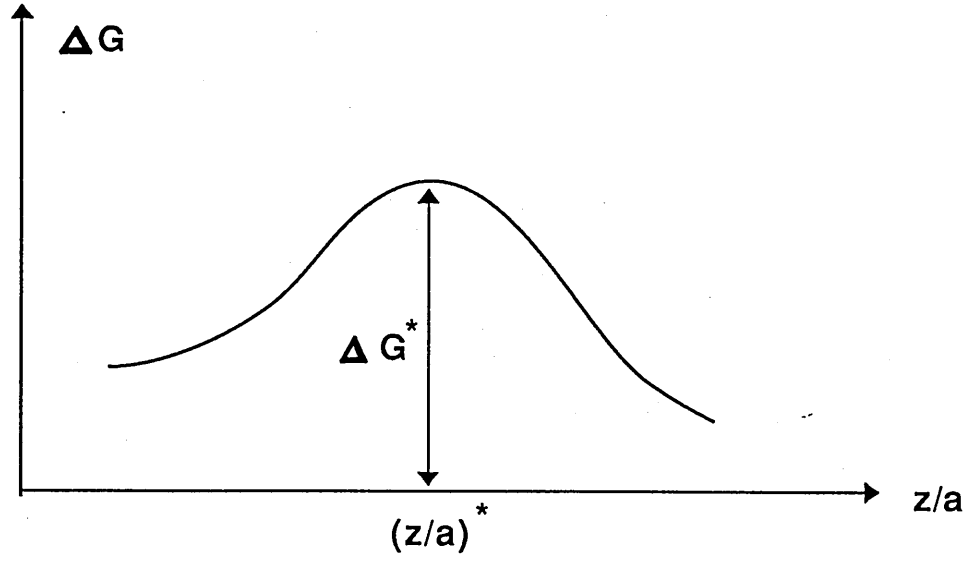

Figure 2.14 Schematic of Gibbs energy change as a function of distance (z/a) separated by two neighbour kinks.

$$\Delta W_\sigma = \pi \mu \omega^2 a^3 \left(\frac{z}{a}\right)\left(\frac{\sigma_s}{\mu}\right)$$

where μ is shear modulus, ω rotation angle, 'a' effective radius of polymer chains, z the distance between kinks, σ_s shear stress, and ν Poisson's ratio.

The energy change ΔG at a given shear stress σ_s as a function of dimensionless distance (z/a) is schematically shown in Figure 2.14. It is clearly indicated that there is a peak point at which $\partial(\Delta G)/\partial(z/a)_{\omega,\sigma} = 0$. At this point, equation (2.42) gives:

$$\Delta G^* = \frac{3\pi \mu \omega^2 a^3}{16(1-\nu)}\left[1 - 8.5(1-\nu)^{5/6}\left(\frac{\sigma_s}{\mu}\right)^{5/6}\right] \tag{2.43}$$

with a critical activation distance $(z/a)^*$ given by:

$$\left(\frac{z}{a}\right)^* = \left(\frac{45}{8(1-\nu)}\frac{\mu}{\sigma_s}\right)^{1/6} \tag{2.44}$$

ΔG^* is known as activation free energy. By using the absolute rate theory, substituting Equation (2.43) for ΔG^* into Equation (2.36) gives:

$$R_{ta} = \frac{kT}{h}\exp\left\{\frac{3\pi \mu \omega^2 a^3}{kT16(1-\nu)}\left[1 - 8.5(1-\nu)^{5/6}\left(\frac{\sigma_s}{\mu}\right)^{5/6}\right]\right\} \tag{2.45}$$

where Boltzmann's constant k was used instead of the molar gas constant R.

Follow the same principle as that in deriving Equation (2.41) in Section 2.2.1 but (a) use shear yield stress σ_{sy} and shear strain rate $\dot{\gamma}$ rather than tensile ones (for adhering to Argon's original expressions) and (b) ignore the reverse rate because shear stress has applied to the system. The relationships between σ_{sy} and $\dot{\gamma}$ can be expressed by:

$$\dot{\gamma} = \dot{\gamma}_0 \exp\left\{\frac{3\pi \mu \omega^2 a^3}{16kT(1-\nu)}\left[1 - 8.5(1-\nu)^{5/6}\left(\frac{\sigma_s}{\mu}\right)^{5/6}\right]\right\} \tag{2.46}$$

$$\left(\frac{\sigma_{sy}}{\mu}\right)^{5/6} = \frac{1}{8.5(1-\nu)^{5/6}}\left[1+\frac{36.8kT(1-\nu)}{3\pi\mu\omega^2 a^3}\log\frac{\dot{\gamma}}{\dot{\gamma}_0}\right] \qquad (2.47)$$

where $\dot{\gamma}$ is shear strain rate with pre-exponential factor $\dot{\gamma}_0$. The rest of the parameters have the same meanings as defined before. Equation (2.47) is a basic equation of Argon.

There is one interesting conclusion which can drawn from Equation (2.47), i.e. yield stress is dependent only on modulus and Poisson's ratio at absolute zero temperature 0(K).

Comparing Argon's Equation (2.47) with Eyring's (2.41), it will be seen that these two equations have a similar form. Instead of Eyring's activation volume, microstructure parameters 'a' and 'z' for polymer chain segment movement involved at yield have been clearly defined in the Argon theory. Another two material constants, shear modulus and Poisson's ratio ν, are also taken into account.

Nevertheless, both Eyring's and Argon's theories are based on the assumption that polymer chains must overcome an energy barrier in order to move from one equilibrium state to another by using absolute rate theory. External shear force plays an important role which changes the energy barrier and promotes the chain movement along a certain direction. In addition to these two theories, another different view on polymer yielding behaviour in the glassy state was advanced by Chow. He emphasized that it is the change of free volume that determines the yield stress of polymer materials.

2.2.3 Chow's Theory

Chow's theory is based on the assumption that amorphous polymers are not in a state of thermodynamic equilibrium. The structure of the materials does not freeze at temperatures below T_g and will change by redistribution of holes (free volume) in a non-equilibrium state. These holes have set up a series of energy barriers during their formation. The redistribution of these holes involves overcoming these energy barriers.

Chow's theory also assumes that a polymer material will yield when applied strain rate $\dot{\varepsilon}$ approaches the order of apparent relaxation time τ of the system. This means $\dot{\varepsilon}\tau \approx 1$. Therefore, the relationship between yield stress and strain rate and temperature could be established if a suitable τ expression could be found.

For a given material at a given temperature, the relaxation time τ can be generally expressed by:

$$\tau = \tau_r \alpha(T,\delta)\alpha_\sigma \tag{2.48}$$

where τ_r is relaxation time at a reference temperature T_r, $\alpha(T,\delta)$ is a shift factor for the non-equilibrium state δ at temperature T and α_σ is stress shift factor. Under simple tension, α_σ is given by (Chow 1988):

$$\alpha_\sigma = \exp\left(-\frac{\Delta w}{2\beta RT}\right) \tag{2.49}$$

$$\Delta w = \sigma_{11}\Omega_{11}\left(\frac{N}{n}\right) = \frac{\sigma_{11}\Omega_{11}}{f} \tag{2.50}$$

where Δw is the work done by external stress σ_{11} on each of the holes in an assumed lattice, Ω_{11} the molar pressure activation volume of the hole, ß a constant which defines the shape of material relaxation spectrum, R the gas constant. In Equation (2.50), N is the total number of lattice cells including n holes, which gives free volume fraction f by f=n/N.

Combination of equations (2.48), (2.49) and (2.50) gives τ as:

$$\tau = \tau_0 \exp\left(-\frac{\sigma_{11}\Omega_{11}}{2f\beta RT}\right) \tag{2.51}$$

where $\tau_0 = \tau_r\alpha(T,\delta)$. By setting $\dot{\varepsilon}\tau \approx 1$, $\sigma_{11} = \sigma_{yield}$ and $\dot{\varepsilon} = \dot{\varepsilon}_y$ at yield, the relationship between yield stress and strain rate is given by:

$$\sigma_{yield} = \frac{4.606f\beta RT}{\Omega_{11}}(\log\tau_0 + \log\dot{\varepsilon}_y) \tag{2.52}$$

Equation (2.52) has a similar form to Eyring's equation (2.41) and Argon's equation (2.47). However, the meaning of activation volume is different. Here, Ω_{11} is the pressure activation volume of holes rather than Eyring's effective activation volume in shear deformation as assumed in the previous section. The hole shear activation volume which characterizes the deviatoric part of activation volume Ω_{12} can be obtained by the relation $\Omega_{12} \approx 1.41\Omega_{11}$ (Chow 1984). Physically, Ω_{11}/f and Ω_{12}/f represents the volume of polymer segments undergoing deformation. More discussions about the meanings on activation volume will be followed in Chapter 6.

One advantage of Chow's theory is that it can be used for composite materials. The relationships between yield stress, strain rate and concentration of filler can be expressed in one equation after introducing another concentration dependent shift factor α_ϕ in equation (2.48).

It is assumed that the relaxation time τ of a polymer can be expressed by Doolittle equation:

$$\ln\tau = \frac{B}{f} \tag{2.53}$$

where B is Doolittle constant and f is free volume of the polymer. After incorporation of rigid filler into the polymer, the total free volume of the composite f_c is:

$$f_c = \phi f_i + (1-\phi)f$$

where ϕ is the volume fraction of filler and f_i is the free volume of the filler. Assuming the filler has no free volume contributable, i.e. $f_i = 0$, it is given:

$$f_c = f(1-\phi) \tag{2.54}$$

The corresponding Doolittle equation is:

$$\ln\tau_c = \frac{B_c}{f_c} = \frac{B_c}{f(1-\phi)} \tag{2.55}$$

Combination of Equations (2.53) and (2.55) gives:

$$\ln\frac{\tau_c}{\tau} = \frac{B_c}{f(1-\phi)} - \frac{B}{f} \tag{2.56}$$

When $\phi = 0$, $\tau_c = \tau$. This leads to $B_c = B$ and Equation (2.56) becomes:

$$\tau_c = \tau\alpha_\phi \tag{2.57}$$

$$\alpha_\phi = \exp\left[\frac{B\phi}{f(1-\phi)}\right]$$

α_ϕ is the concentration dependent shift factor. Substituting Equation (2.48) for τ into (2.57) gives:

$$\tau_c = \tau_r \alpha(T,\delta)\alpha_\sigma \alpha_\phi \tag{2.58}$$

Following the same procedure as mentioned above, another equation similar to (2.52) but for particulate composites can be expressed by:

$$\sigma_{yield} = \frac{4.606 f \beta RT}{\Omega_{11}}\left[\log\tau_0 + \log\dot{\varepsilon}_y + \frac{B\phi}{2.303 f(1-\phi)}\right] \tag{2.59}$$

All the parameters have the same meanings as defined above.

The significance of Equation (2.59) is that the influence of filler on yield stress is quantitatively described, relating to the filler concentration. Further discussion will be followed in Chapter 6 when experimental results are presented.

CHAPTER 3

FRACTURE AND YIELD OF RUBBER TOUGHENED THERMOSETS,PARTICULATE AND HYBRID COMPOSITES

In the previous chapter, some important theories about fracture and yield have been covered to a certain extent. This chapter will review some applications of these theories. As most materials concerned in the thesis are composites, stress analysis for these materials will be reviewed in the first instance before further discussion about yield and fracture of these materials.

3.1 Stress Analysis Around Soft/Hard Inclusions

Dispersed inclusions will locally alter the stress field around them if they have different elastic properties from the matrix. A complete analysis of the stress field around a cylindrical or spherical inclusion was conducted by Goodier (1933). In order to make the analysis easier, here is considered the two dimensional case as indicated in Figure 3.1, where σ is applied stress acting at infinity; R is radius of inclusion; 'r' and θ are the cylindrical coordinates of a point away from the inclusion; σ_θ and σ_r are tangential and radial stresses at the point defined by the coordinates (r,θ) respectively. The purpose of chosing this simple model is to outline stress concentrations around a soft inclusion, such as rubber, and a hard one, such as filler, to find out the differences between them.

Here it is assumed that the inclusion is subjected to an uniform tensile stress at infinity and the matrix is ideally elastic, isotropic and homogeneous. The stresses around the inclusion are given by (Evans 1974):

$$\sigma_r=\frac{\sigma}{2}(1+\cos 2\theta)+2\sigma\left\{-A\left(\frac{R}{r}\right)^2+B\left[3\left(\frac{R}{r}\right)^4-4\left(\frac{R}{r}\right)^2\right]\cos 2\theta\right\} \tag{3.1a}$$

$$\sigma_\theta=\frac{\sigma}{2}(1-\cos 2\theta)+2\sigma\left[A\left(\frac{R}{r}\right)^2-3B\left(\frac{R}{r}\right)^4\cos 2\theta\right] \tag{3.1b}$$

$$A=\frac{(1-2\nu_i)\mu_m-(1-2\nu_m)\mu_i}{4[(1-2\nu_i)\mu_m+\mu_i]}$$

$$B=\frac{\mu_m-\mu_i}{4[\mu_m+(3-4\nu_m)\mu_i]}$$

where ν_i and ν_m are Poisson's ratio of inclusion and matrix, and μ_i and μ_m are shear modulus of inclusion and matrix respectively.

Consider three special cases:

(a) at the interface (R = r);
(b) at $\theta = 0$ and $r \geq R$;
(c) at $\theta = \pi/2$ and $r \geq R$.

The stress distributions around an inclusion are shown in Figure 3.1. It is assumed that $\mu_i >> \mu_m$ for hard inclusion (H) and $\mu_i << \mu_m$ for soft inclusion (S). Under these conditions, the constant A is equal to 0.25 and $-0.25(1-2\nu_m)$ and B 0.25 and $-0.25/(3-4\nu_m)$ for soft and hard inclusion respectively. $\nu_m = 0.34$ is used in the caculation. The stress distributions for each special case are as follows:

(a) At interface (Figure 3.1(b)): Both radial stress and tangential stress for a hard inclusion are tensile except at angles θ=72° to 90° where they are slightly compressive. For a soft inclusion, however, tangential stress is compressive at angles θ=0° to 30°. After that, the tangential stress is tensile. Radial stress, on the other hand, is zero along the boundary.

(b) At at $\theta = 0$ and $r \geq R$ (Figure 3.1(c)): For a hard inclusion, radial stress increases from the interface into the matrix then, at a distance about 0.2R (0.2 radius of the inclusion) away from the inclusion, it decreases gradually until approaching the applied stress. Tangential stress is below the applied stress and decreases to zero at a distance about one inclusion radius R away. For a soft inclusion, on the other hand, radial stress is less than the applied stress, approaching zero then a little compressive stress towards the interface. Tangential stress is mainly in compression.

(c) At at $\theta = \pi/2$ and $r \geq R$ (Figure 3.1(d)): The radial stress for a hard inclusion is compressive while tangential stress is tensile. However, both of them are considerably smaller than applied stress in the region adjacent to the inclusion. For a soft inclusion, tangential stress approaches the maximum at the interface, where stress concentration factor equals to 3, and it decreases from there into the matrix gradually. Radial stress increases, however, is much less than the radial stress and less than the applied stress.

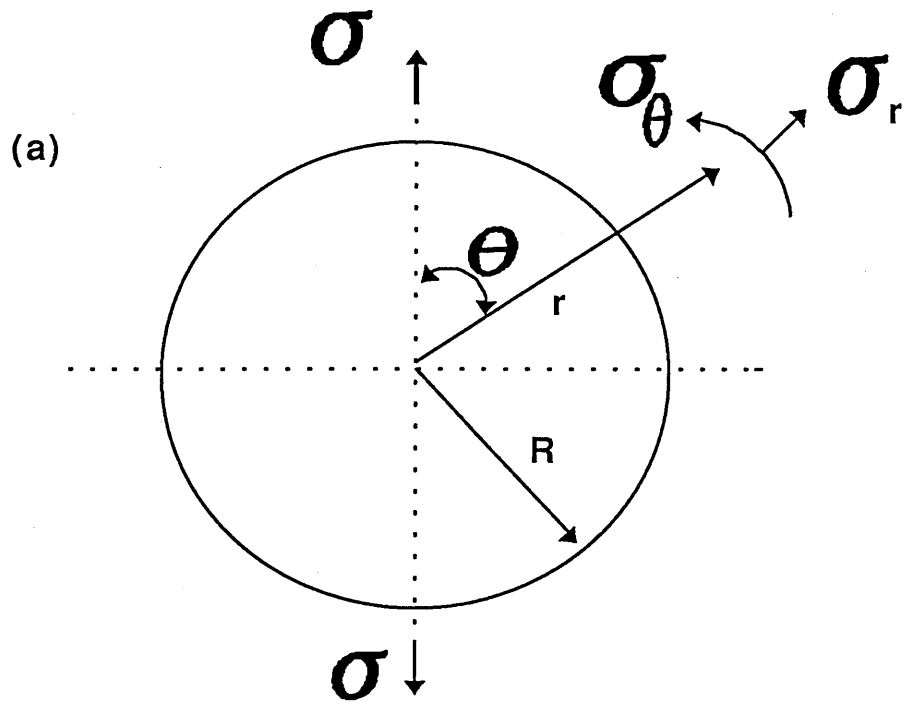

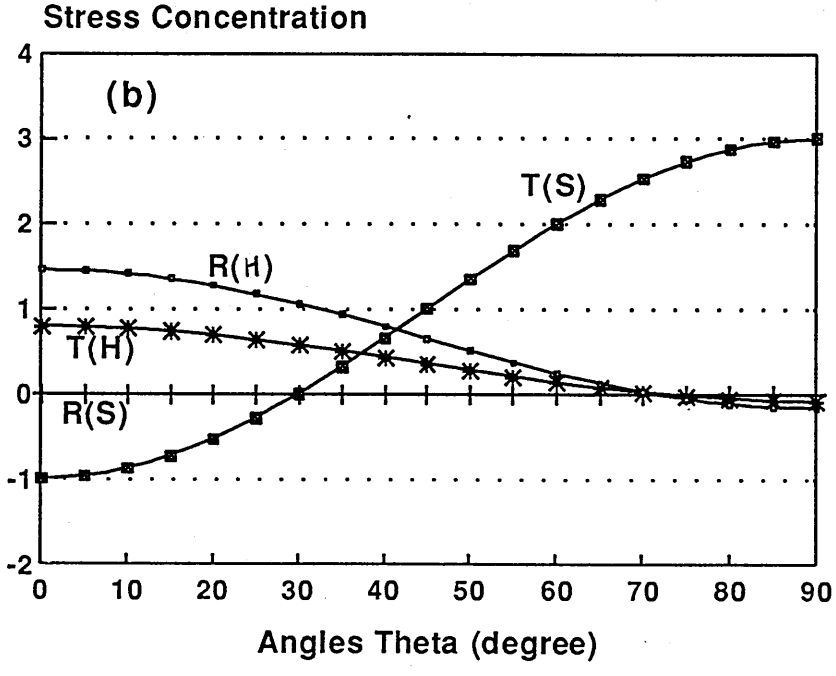

Figure 3.1 Schematic diagram of stress field around an inclusion (a); and radial (R) and tangential (T) stress concentrations around hard (H) and soft (S) inclusions at r = R (a), $\theta = 0$ (c) and $\theta = 90^{\circ}$(d).

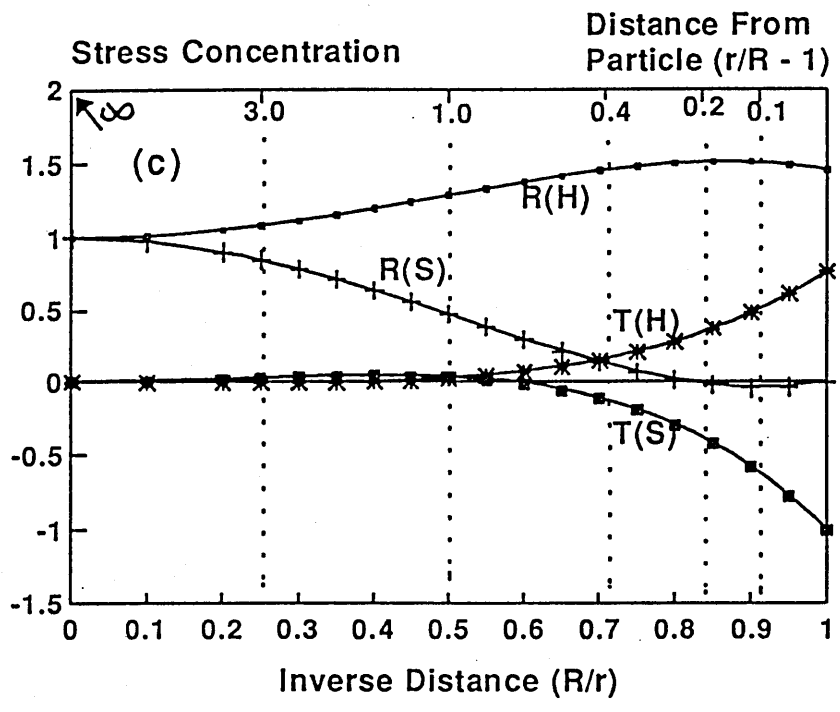

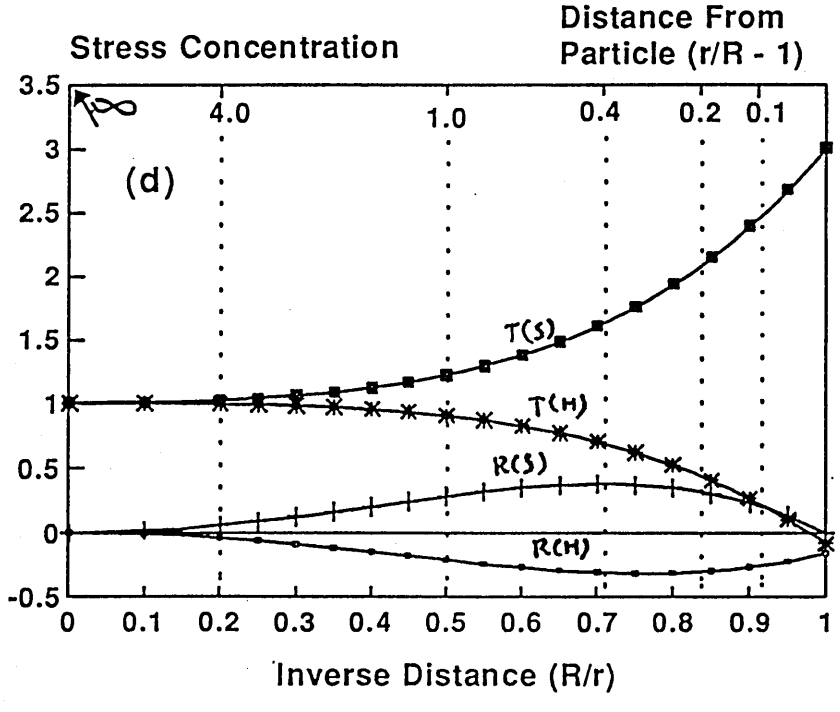

Figure 3.1 (continued).

A few conclusions can be drawn from this analysis as indicated in Figure 3.1:

(1) Soft inclusions give rise to greater disturbance to the elastic field than hard ones (Figure 3.1(b))

(2) The considerable influence of both hard and soft inclusions on the elastic field is confined to its neighbourhood (Figure 3.1 (c) and (d)).

(3) The greatest stress concentration is at the interface at $\theta = \pi/2$ to applied load direction for soft inclusions (Figure 3.1 (b) and (d)) but in matrix adjacent to a hard inclusion at $\theta = 0$ to the loading direction (Figure 3.1 (b) and (c)).

This analysis considers only one isolated inclusion. For most rubber toughened and particulate reinforced plastics, dispersed inclusions are too close together to be treated as isolated inclusions. There is no analytical solution available to solve the problem. The other methods commonly used are numerical ones.

Finite element analysis has been used to analyze stress around inclusions for rubber toughened and particulate plastics. One analysis considered here was developed by Guild and Young (1989). The model of primary grid for this finite analysis is shown in Figure 3.2. Uniform diameter of spherical particles was assumed here. All the analysis was based on a resin cylinder with radius equal to its half-height (Figure 3.2(a)) which contains a single spherical inclusion. Some conclusions relevant to this thesis are collected here:

(1) Stress concentration caused by soft inclusions (rubber particles) is higher than that caused by hard inclusions (filler particles) at the same concentrations. The higher the concentration of inclusions, the higher the stress concentration.

(2) The greatest stress concentration is at the equator for soft inclusions but in the matrix above the pole for hard inclusions.

(3) By using Mises octahedral shear stress in the finite analysis, two maximum stress concentrations were observed for hard inclusions as indicated in Figure 3.3. The first one is in the matrix above the pole and the second is at interface at angle $\theta = 42°$. These two maximum octahedral stresses, however, vary with concentrations of the hard inclusions. The first one is higher than the second at concentrations above 12 vol % and smaller than the second at concentrations below that level.

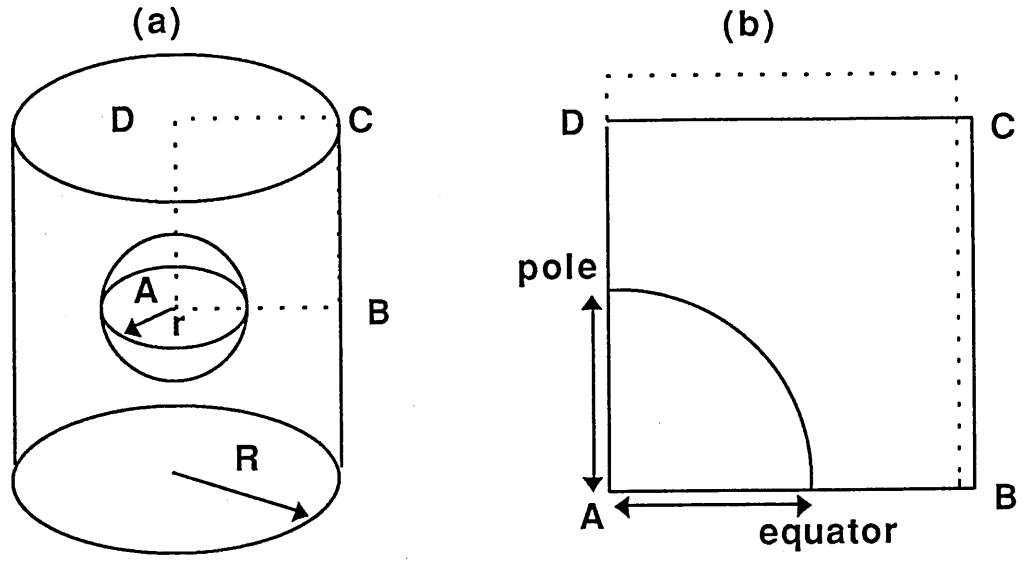

Figure 3.2 The model of primary grid.

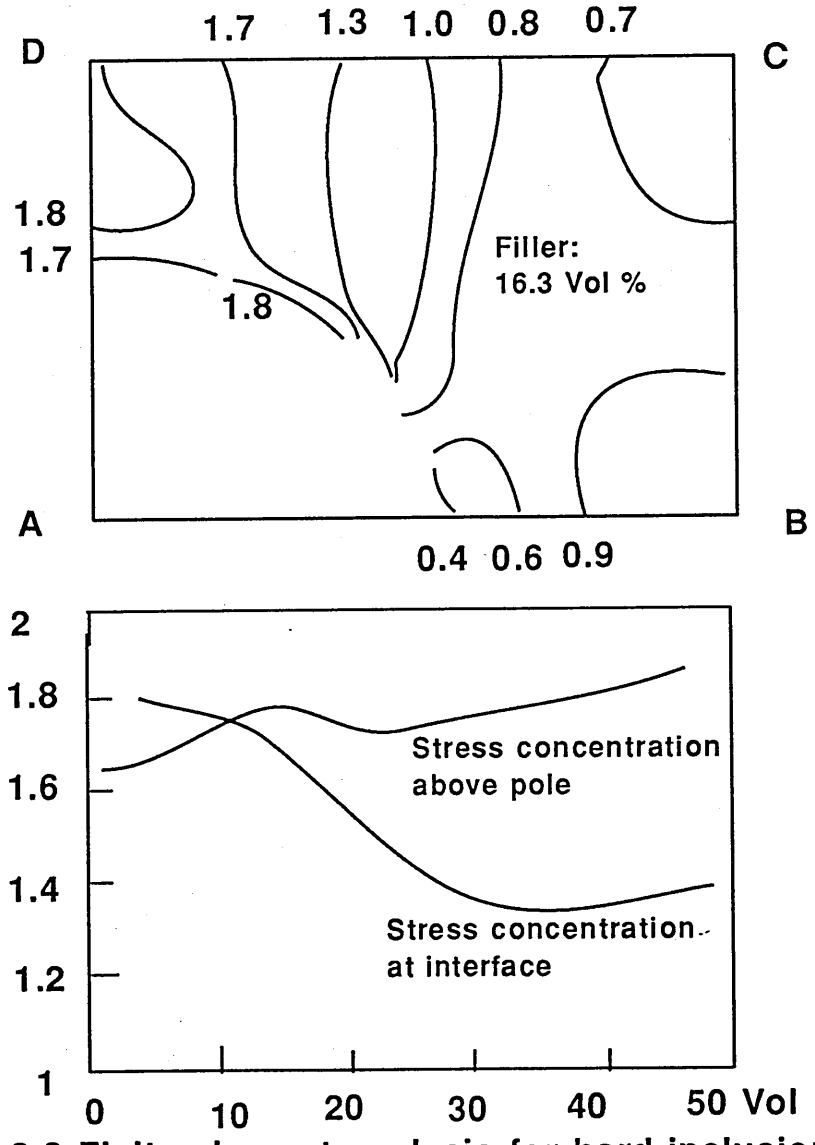

Figure 3.3 Finite element analysis for hard inclusions: stress concentration factors of Von Mises stress (after Guild 1989).

Both the finite element analysis conducted by Guild and Young and the analysis discussed previously come to almost the same conclusions on these points where stress concentrations around hard/soft inclusions are concerned. It seems that soft inclusions are more effective than hard inclusions as stress concentrators for the situation considered here.

3.2 Mechanisms of Fracture Resistance

In general, two main deformation mechanisms may be involved in toughened plastics (Bucknall 1977). One process is shearing. Diffuse shear zones and localized shear bands will be developed during plastic deformation but volume is kept unchanged. Another process is that plastic deformation will create extra volume in the forms of craze and voids/cavitation. No matter which mechanism plays a role, the functions of rubber particles and of polymer matrix should be clearly understood. Before further discussion on the subject, failure behaviour of rubber toughened and unmodified plastics will be reviewed in the first instance.

3.2.1 Failure Modes

Different crack propagation behaviour has been observed in both thermoplastics and thermosets. Broutman and McGarry (1965) reported two different failure modes - continuous (stable) and discontinuous (stick-slip) - in the glassy polymers PMMA and PS. The double-cantilever-beam (DCB) specimens were used at low cross head speed and at temperatures between -40°C and 50°C. Based on instrumented impact tests, Bucknall (1977, 1988) described three distinguishable types of fracture behaviour in rubber toughened glassy polymers: unstable crack propagation with and without plastic deformation and stable ductile propagation. Temperature and rubber concentration have a strong influence on these failure modes.

Kinloch and co-workers (1983) observed three different types of crack propagation behaviour in cross-linked epoxy and rubber toughened epoxies. They defined the three crack propagation modes as stable ductile (Type A), unstable brittle (Type B) and stable brittle (Type C). All these modes were also observed in particulate and hybrid epoxy composites (Kinloch 1985). Temperature again is a key factor that affects these failure modes. Besides the influence of temperature, Truong (1990) found both strain rate and rubber concentration could change crack propagation mode from one to another at a given temperature.

In general, low temperature, low rubber loading and high strain rate lead to more brittle failure. High temperature, high rubber loading and low strain rate cause more ductile failure. The dependence of temperature and deformation rate (strain rate) on material failure behaviour is similar to that predicted by the theories of Eyring, Argon and Chow (Section 2.2) for the polymer yield process. Low temperature and high strain rate give rise to high yield stress. High temperature and low strain rate reduce yield stress. The fact is that all the findings mentioned above have strong linkage with plastic deformation accompanying each failure mode. Little plastic deformation indicates more brittle failure and extensive plastic deformation means more ductile failure. As discussed in Section 2.1.3, the results from theoretical analysis have established this relationship between the scale of plastic deformation and the yield stress (Equations (2.19), (2.22) and (2.23)). Lower yield stress means greater plastic deformation. This implies that yield stress is one important factor that controls material failure mode as well as fracture resistance.

Besides temperature and strain rate, both soft inclusions (rubbers) and hard inclusions (rigid fillers) have significant influence on yield stress and fracture resistance of polymer matrices. The applications of rubbers and fillers as modifiers have made great contributions to the plastics industry. However, the question of how many mechanisms are involved in yield and fracture processes, and which one controls fracture resistance in these materials are still controversial issues.

3.2.2 Functions of Polymer Matrix

It is generally recognized that two kinds of deformation mechanisms are essentially involved in toughened plastics. The first type is crazing and the second type is shear. Rubber particles will act as 'catalysts', altering the stress distribution within the matrix and accelerating plastic deformation. The basic deformation mechanisms of the matrix cannot be changed simply by incorporation of rubber particles (Bucknall 1977). They should be the same mechanism as in homogeneous polymers. Based on this understanding, the key factor is what controls the mechanisms in the matrix: crazing, shearing or both of them ?

Henkee and Kramer (1984) concluded that the chain contour length l_e between entanglements is the key factor which determines the deformation mechanism of glassy polymers. Low l_e prefers shear yield and high l_e prefers craze yield.

A model based on the role of chain entanglement in controlling resistance to crazing is given by Kramer (1984):

$$\Upsilon = \gamma + \frac{1}{4} d_e \nu_e U \tag{3.2}$$

where, Υ is the total surface work, γ van der Waals surface work, d_e the vector between the endpoints of chain contour l_e, ν_e the entanglement density and U the energy required to break a single bond. Equation (3.2) implies that creation of the fibril surface in a craze requires to overcome (a) the van der Waals surface work γ and (b) the work for chain scission $¼ d_e \nu_e U$. In Kramer's theory, chain disentanglement caused by chain scission is essential for creation of crazes. Otherwise shear deformation occurs.

In order to make the role of chain contour l_e clear in determination whether material deforms in shear or crazing, Equation (3.2) can be transformed into another form as follows.

The relationship between chain contour l_e, end to end distance d_e and maximum extension ratio of a single strand λ_{max} can be expressed by:

$$\lambda_{max} = \frac{l_e}{d_e} \tag{3.3}$$

Substituting this equation into Equation (3.2) for d_e gives:

$$\Upsilon = \gamma + \nu_e U \frac{l_e}{\lambda_{max}} \tag{3.4}$$

To make the scission of a single entangled strand possible, theoretically, the extension ratio λ should approach λ_{max}. For an extremely rigid polymer chain which, presumably, has high l_e and d_e and the ratio l_e/d_e is approximately equal to 1, λ is much easier to approach λ_{max} by extension of the strand. For a flexible polymer chain, on the other hand, which, presumably, has a high ratio $l_e/d_e >> 1$, i.e. $\lambda_{max} >> 1$, high extension is required for λ approaching λ_{max}.

For bulk polymers rather than a single entangled strand, strain hardening is an important feature during polymer chain orientation because of polymer chain orientation. What is recognized is that strain hardening is easily set up at low strain for low l_e for high entanglements but it is difficult for high l_e for lack of entanglements. For the latter case, continuous chain scission followed by fibrillation would take place, forming void-fibril network - craze, and strain hardening would take place later within craze fibrils through molecular orientation. By changing PPO/PS blend ratio, l_e is adjustable. The transition from craze deformation to shear deformation has been observed by the same authors. More recently, a modified model for matured crazes in PS was proposed by Miller and co-workers

(1991). A certain number of cross-tie fibrils which were generated periodically during craze formation was detected. These cross-tie fibrils link the main fibrils and pull them away from the tensile axis at a certain angle, which is dependent on temperature. Mesh-like array microstructures - crazes - were developed.

As far as toughening in thermosets is concerned, the question is whether the two deformation mechanisms, craze and shear, which are the dominating mechanisms in toughened thermoplastics, both function or only one of them plays a role. The answer to the question was given by Glad and Kramer (1991) for the case of plane stress conditions. They worked on thin films of epoxy resin with varying cross-link densities and using uncross-linked epoxy as the extreme case. Their results confirmed that deformation mechanisms were dominated by shearing in these thermosetting materials. No craze was observed and only plastic deformation zones were formed at the crack tip for all the resins investigated. The interesting thing is the shape of the deformation zone.

Plastic deformation zones, which look like Dugdale line-zones (Section 2.1.3), were created ahead of the crack tip in the lightly cross-linked resins. There is a clear boundary between bulk material and the material which was drawn from it. This process appears like that of craze formation which has clear boundaries between deformed and non-deformed material, but occurs without fibrillation. However, for highly cross-linked resins, only Irwin circular plastic zones (Section 2.1.3) were generated at the crack tip and there are no clear boundaries between deformed and non-deformed materials. In the transition from Dugdale line-zone to Irwin circular zone, the controlling factor is cross-link density.

It was also observed that localized and limited plastic deformation (shear) occurs in highly cross linked epoxies. This localized deformation zone is confined to the area ahead of the crack tip, forming a circular zone. For lightly cross-linked epoxies, however, both the form and the scale of plastic deformation are different from what is observed in highly cross-linked epoxies. Strain softening followed by strain hardening leads to the formation of interfaces between bulk material and shear zone. The delay of strain hardening in lightly cross-linked epoxies may be the reason why these materials develop Dugdale line-zones ahead of the crack tip instead of Irwin circular plastic zones. Whether or not these differences need different rubber tougheners will require further research.

Nevertheless, general conclusions may drawn from the above discussion. Both deformation patterns, craze and shear, function for thermoplastics but only shearing dominated deformation mechanisms play a role in thermosets (at least under plane stress conditions!). The two basic deformation patterns provide the fundamental understanding of yield mechanisms for most

thermoplastics and thermosets. The fact is that most thermoplastics and thermosets can be toughened by incorporation of a small amount of rubber particles. What roles are actually played by rubber particles needs further exploration. However, there are no general conclusions that have been drawn on the subject. It is still a controversial issue.

3.2.3 Functions of Rubber Particles

As discussed in section 3.1, rubber particles can locally increase stress at their equators and this effect will be more pronounced with increasing rubber concentration (Guild 1989). As a result, plastic deformation will be expected to take place initially at equators rather than in the other places. Based on this fact, crazing mechanisms will be discussed in the first instance.

The Roles of Rubber in Craze Deformation

Crazing, as one kind of plastic deformation, is very likely be initiated at the equators of rubber particles whenever possible. A typical material is high-impact polystyrene (HIPS). The dominating deformation mechanism in this material is multiple crazing (Bucknall 1977, 1988 and 1990). Rubber particles play important roles in this plastic deformation.

Firstly, a rubber particle initiates one or more crazes at its equator, then grows in the polymer matrix along the direction perpendicular to the loading axis. Secondly, a rubber particle can act as a 'craze stopper'. When a mature craze comes across another rubber particle, the craze cannot grow further and will be arrested by the rubber particle or stopped by shear bands (Bucknall 1977). This could prevent the craze from developing into a crack. Thirdly, a rubber particle can transmit high stress into its centre as a stress 'bearer'. As a result, localized yielding (crazing) at equators of rubber particles will enhance the global plastic deformation by forming multiple crazes and increase fracture resistance. This localized yielding will greatly release stress concentrations, especially at the sharp crack tip. Therefore, the scale of this localized yielding will determine the extent of general plastic deformation. This, in turn, decides the failure mode, whether it is brittle or ductile or something in between, as discussed previously.

From this point of view, the amount of rubber particles which can effectively initiate a craze, develop a craze and stop a craze from turning into crack will determine the fracture resistance in those materials which are toughened through the crazing mechanism. The size of rubber

particles will be decisive for these processes. It has been concluded that both small and big particles have the same function in craze initiation but only big particles can effectively resist crack propagation at high failure speed (Bucknall 1990).

If a matrix cannot deform through crazing, but yields by shearing, what functions are actually played by rubber particles? Why are those materials which can deform through shearing crack sensitive, and lacking resistance to fracture propagation before rubber toughening? There are some questions which have not obtained satisfactory solutions yet. The roles of rubber particles in shear dominated matrixes are less well understood than that in craze dominated matrices. A few theories including rubber particle stretching, critical inter-particle distance and rubber particle cavitation will be discussed. Some comments on each theory are given below.

Rubber Tear Theory

Kunz et al (1978, 1980) supposed that rubber particle stretching and tearing consume most of the energy during fracture. Based on this assumption, rubber stretching and tearing energy can be calculated according to rubber elasticity theory. Although several direct observations of rubber bridging across open cracks were reported (Kunz 1980, Sayre 1984, Yee 1991), many experiments have demonstrated that matrix plastic deformation is the main source of energy dissipation (Bucknall 1977, Kinloch 1983 1985 1986 1987, Yee 1983 1984 1986 1989 1991, Sue 1991). The extent of plastic deformation will determine fracture resistance. As discussed in Section 3.2.1, it is the scale of plastic deformation that controls failure behaviour. It is hard to believe that the transitions between three failure modes, which are common phenomena for both thermoplastics and thermosets, are simply controlled by rubber tearing. There are many other experimental facts which cannot be explained by the rubber tear theory. These criticisms were given by Kinloch el at (1983). If this rubber stretching and tearing does make some contribution to fracture resistance in toughened plastics, it plays a secondary role.

Inter-particle Distance Theory

Wu (1985) is the first researcher who suggested an important factor relating to rubber particles: the critical inter-particle distance ID_c. The inter-particle distance ID should be smaller than ID_c, i.e. $ID < ID_c$ in order to achieve the toughening effect. This could not be achieved when $ID > ID_c$. ID_c was assumed to be a material (matrix) constant and independent

of rubber volume fraction and particle size. According this theory, the brittle-tough transition occurs at ID_c.

It has been supposed that the underlying mechanism with ID is the change in stress state of the matrix, which is affected by the ligaments between rubber particles. The transition from plane strain to plane stress will be set up at ID_c (Borggreve 1988, Margolina 1988, Wu 1988). As a result, shear deformation will easily take place in those ligaments which are smaller than the critical matrix-ligament thickness defined by ID_c.

If ID_c is a constant property of the polymer matrix, it should not be affected by the type of rubber used. However, Borggreve et al (1989) found that the type of rubber used did affect the fracture resistance of rubber toughened nylon, which was the same material used by Wu in his research. Borggreve concluded that inter-particle distance ID_c is not the only parameter which determines impact behaviour of rubber toughened nylon. The properties of the rubber have a strong influence on the fracture resistance and brittle-tough transition temperature. It seems that lower modulus of rubber would produce higher fracture resistance (notched Izod impact testing) when the size of rubber particles were kept almost the same. Borggreve suggested that the ability of the rubber to undergo cavitation is another factor which affects fracture resistance as well as inter-particle distance.

Rubber Cavitation Theory

Rubber particle cavitation was first reported by Breuer et al (1977). After that, more and more evidence of rubber cavitation has been reported (Kinloch 1983,1986; Chan 1984, Shah 1984, Yee 1983, 1986, 1989, 1991, Sue 1991, Borggreve 1989). It is generally believed that the key role of rubber cavitation is to release hydrostatic stresses, which are generated at the crack tip under tension, thereby promoting shear deformation.

A sharp crack, whatever the reason for its presence, will build up stress concentrations at its tip. When the crack has no alternative but to grow under tensile loading, it will fracture through one of the three crack propagation modes (Section 3.2.1). To ease the concentrated stress and spread it away from the crack tip will be a decisive step towards fracture resistance improvement for the cracked body. However, this cannot be easily achieved in neat glassy polymers for lack of 'agents' to do the job. Also it may be difficult for rubber toughened plastics if there is no rubber particle cavitation at all. The reason is that hydrostatic stress resists shear deformation but prefers brittle failure. As the bulk modulus of rubbers is comparable to that of a solid polymer matrix (Bucknall 1977, Yee 1991), it is difficult to

release the hydrostatic stress without rubber cavitation. After rubber cavitation, the cavitated rubber particles can effectively release the constraint stress and nucleate shear deformation (Section 8.2). As a result, fracture becomes so difficult that a major fraction of the cracked part is forced to undergo large plastic deformation through shearing, adjacent to the crack tip. Thus the concentrated stress has been released and spreads away. Therefore, the resistance of the crack propagation is increased.

The importance of rubber cavitation has been questioned by others (Guild 1990, Wu 1988). The essential argument is whether shear deformation is dependent on rubber cavitation or not. Guild and Young (1990), basing on the results of finite element analysis, suggested that shear deformation and rubber particle cavitation may take place independently. Wu (1988) also argued that rubber cavitation may not be necessary. The low rubber modulus (compared to that of glassy matrix) will enable the concentrated stress to be released through shear deformation in thin ligaments, which are defined by critical inter-particle distance ID_c.

There are some other experimental results which may not agree with the rubber cavitation theory. But shear deformation induced by the rubber phase may play an important role (McGarry 1986, Lin 1986) under these circumstances. An interesting experiment was conducted by McGarry and Ming (1986). A thin layer of rubber CTBN, about 0.14 microns, was coated on glass beads which were used as a modifier of one epoxy resin. The fracture resistance G_{IC} increased about 10 times after incorporation of the coated glass beads at concentration 10 vol% (limited rubber involved). It only doubled using non-coated glass beads. A similar experiment conducted by Lin et al (1986) also confirmed that a thin layer of rubber which is coated onto glass beads could considerably increase fracture resistance of epoxy resins. The morphology of fracture surfaces showed that extensive plastic deformation had taken place at the interfaces of rubber coated glass beads. Little plastic deformation could be observed at the non-coated glass beads.

Whether or not rubber cavitation occurred in the thin rubber layer is not clear. The hard inclusions under the rubber coatings may make the cavitation more difficult than in the neat rubber particles. However, shearing processes may possibly be under way at filler/rubber/matrix interfaces at an early stage of crack propagation.

As discussed in Section 3.1, the stress distribution around a hard inclusion is different from that around a soft one. The maximum stress concentration is at the equator for soft inclusions (rubber) but just above the pole for hard inclusions (rigid filler). Uneven stress field created around rubber coated glass beads will promote shear deformation. It is quite possible that this shear deformation will take place at rubber phases (thin rubber layer outside rigid filler) first,

without rubber cavitation, as rubber has much lower shear modulus than the polymer matrix.

Under plane strain compression conditions, rubber cavitation is ruled out. Shear deformation induced by rubber particles has been observed. This will be discussed in Chapter 8.

3.2.4 Functions of Rigid Filler Particles

Rigid filler particles can play many roles in a brittle polymer matrix, forming debonded zones, stepping on fracture surfaces, deflecting/bridging/pinning the crack front, as well as locally altering stress field around the particles. However, Green (1977) concluded that, except for pinning, all these functions play only secondary roles in increasing the fracture resistance of particulate composites.

Crack pinning theory was proposed by Lange (1970,1971) and modified and extended by Evans (1972) and Green (1977, 1979). The theory is based on the findings that rigid particles dispersed in a brittle matrix can increase fracture strength and fracture surface energy (Lange 1971, Evans 1972). This increment is mainly due to the line tension effect. The line tension originates from the crack front bowing between a pair of impenetrable obstacles, where the length of the crack front increases. Therefore, extra energy will be required for crack propagation. This effect is normally described as crack tip pinning (Further discussion on the subject will be in Chapter 8).

Direct observation of crack front pinning between two adjacent rigid particles has been made by Green (1977) and Kinloch (1985). Also Moloney (1983,1987) and Kinloch (1985) have proved that theoretical predictions based on the pinning mechanism and experimental data agreed fairly well when crack propagation was dominated by the brittle failure mode (Section 3.2.1).

Filled materials using rubber toughened resins as matrices have been explored very recently. The advantages of the hybrid composites have been demonstrated by some researchers (Bandyopadhyay 1988, Low 1987 1988 1989, Amar and Mai 1988 (review), Kinloch 1985, and Moloney 1987). Fracture toughness could be further increased without sacrifice of elastic modulus and strength comparing to unmodified and rubber toughened thermosets.

However, toughening mechanisms in hybrid composites are not well understood yet. Whether or not the pinning mechanism exists remains uncertain. If it does play a role, how much contribution to fracture toughness is made by this mechanism? If it has little or no

importance, what mechanisms are functioning and what roles do filler particles actually play? These issues will be discussed further in Chapters 6, 7 and 8, particularly with reference to the materials used in this research.

3.3 Fracture of Thermosets

In the previous section, some important issues about toughening mechanisms were discussed. It is generally recognized that shearing is a dominating mechanism in thermosetting polymers. This section will discuss a few factors that affect fracture toughness of these materials in order to get better understanding of the toughening mechanisms.

3.3.1 Effects of Cross-link Density

Yee and Pearson (1983 1984 1989) reported that cross-link density had a strong influence on fracture toughness of rubber toughened epoxies. This influence was hardly observed in the unmodified parent materials. Fracture toughness did not increase considerably with decreasing cross-link density. However, it increased considerably with decreasing cross-link density after incorporation of rubbers. The concept of toughenability of a resin matrix was then proposed by the authors. It was proposed that cross-link density is a key factor that determines the toughenability, i.e. whether a polymer matrix can be toughened or not at a given cross-link density. The lower the cross-link density, the greater the toughenability. This is shown in Figure 3.4.

The main reason why highly cross-linked thermosets cannot be effectively toughened is the resin microstructure itself. A three dimensional network with small chain contour length l_e (between entanglements) will resist large scale shear deformation and only limited plastic deformation can take place before chain rupture (Section 3.2.2) .

On the other hand, in those thermosets with long l_e, the low fracture resistance is due not to lack of deformation ability but to high constraint stress that is set up at the crack tip. The sharp crack, whenever it is present, will build up hydrostatic stress at the crack tip. This triaxial stress field will limit shear deformation and cause brittle failure. The dispersed rubber particles can effectively release the hydrostatic stress through cavitation (Yee 1986, 1989, 1991; Kinloch 1983, 1986, Sue 1991). This function is believed to be the initial stage before general plastic (shear) deformation occurs in the matrix.

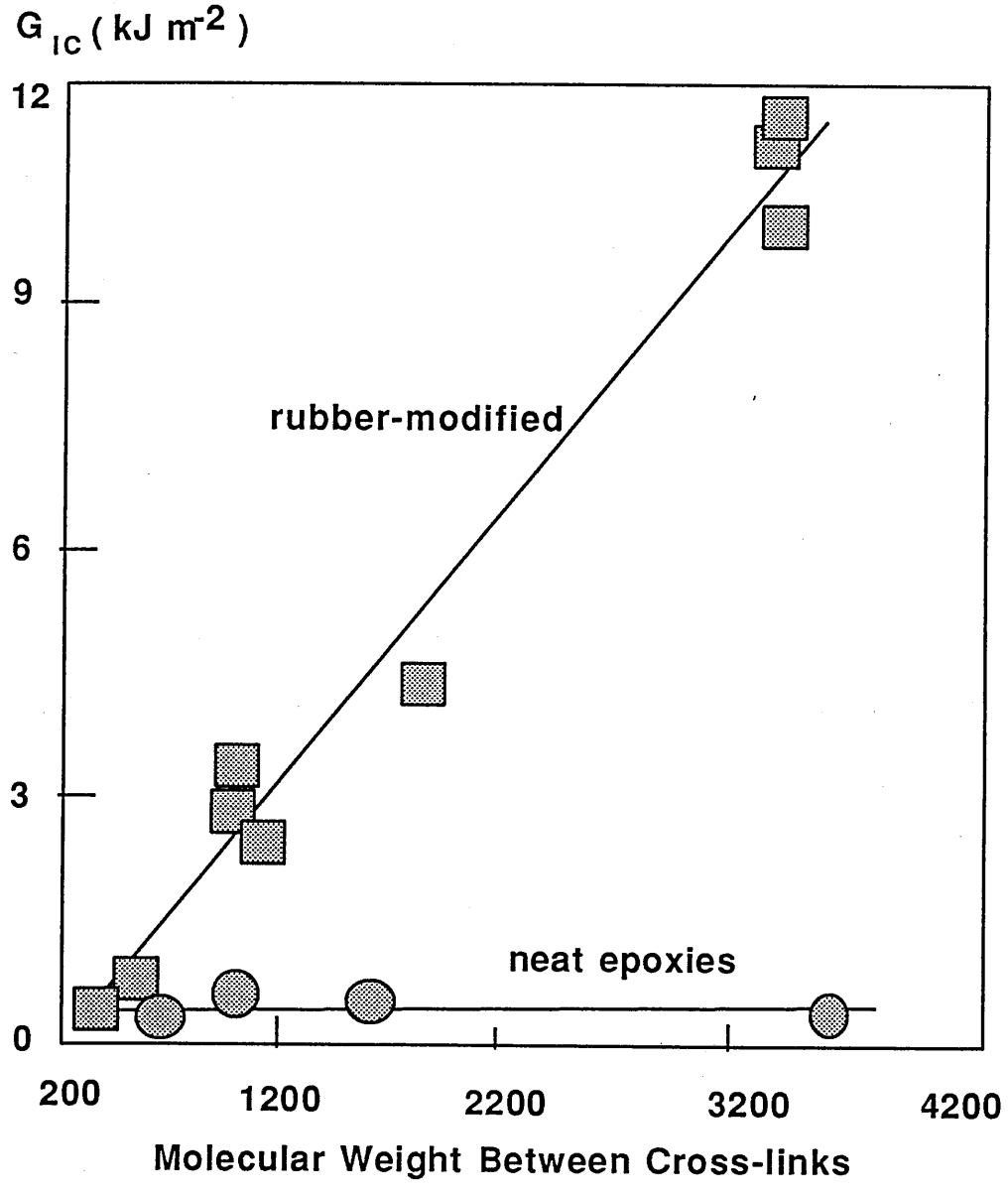

Figure 3.4 Influence of cross-link density on fracture resistance of epoxies (after Yee 1983,1984).

3.3.2 Effects of Rubber Properties

The understanding of the influence of rubber properties on toughening efficiency in rubber toughened thermosets is not as good as that for the matrix. A few important properties of rubber particles need to be well understood in order to develop more effective modifiers. Here are considered two of them - rubber cavitation stress and rubber particle size effects.

Rubber Cavitation Stress

As discussed previously, cavitation of rubber particles plays an important role in rubber toughened thermosets. There are two questions which need to be answered. The first concerns cavitation stress. At what stress level will the cavitation start? The second is what kind of rubber will be a better toughener: the one with high cavitation stress or the one with low cavitation stress?

There are at least two factors that affect rubber cavitation stress under triaxial stresses. One is rubber elastic modulus E and another is 'void' size from which rubber cavitation is induced (Gent and Wang 1991). High modulus of rubber should give rise to high cavitation stress. Also it is true that small voids in the rubber will require high cavitation stress. However, this latter effect seems not so pronounced according to Gent and Wang's analysis. Cavitation stress normally lies in a narrow range from 3E to E, corresponding to void radii from 0.5 to 1000 microns. Below this range, no general conclusions could be drawn according to the authors.

For rubber toughened thermosets, rubber particles with radii as small as 0.05 μm in radius have been used (Yee 1991, Sue 1991 and this research). It is unlikely to contain real 'void' for such small rubber particles. The fact is that those rubber particles do cavitate. A circular cavitation zone ahead of the crack tip has been observed (Yee 1991, Sue 1991 and Chapter 8).

However, at what stress level the small rubber particle will start cavitation is not clear. Based on the results of finite element analysis, Guild and Young (1989) suggested that the matrix yield stress would be enough to initiate cavitation from small voids, which may be the areas not fully polymerized and which could not be observed by conventional microscope techniques. In addition, one quantitative description of rubber cavitation stress was made by Schwier et al (1985). They succeeded in characterization of craze growth for polystyrene/polybutadiene di-block copolymers by choosing PB cavitation stresses of 60 MPa

at temperature 20°C and 73 MPa at -20°C respectively. However, the cavitation stress of the rubber used in this research appears to be less than these values (Chapters 6 and 8).

Another question that needs to be answered is what kind of rubber will be a better toughener, the one with high cavitation stress or the one with low cavitation stress?

Unfortunately, very little investigation has been made on the problem. Borggreve (1991) indicated that the rubber with lower rubber modulus may be a better modifier than the one with higher modulus in his work of toughening nylon. On the other hand, Yee (1991) suggested that the rubber with high cavitation stress may be a more effective modifier. The reason is that higher cavitation stress would allow higher stress to be built up before cavitation and fracture. This would produce higher fracture toughness.

Rubber Particle Size

In addition to rubber cavitation, another factor that affects the fracture toughness of rubber toughened thermosets is rubber particle size. The influence of rubber particle size on fracture toughness of rubber toughened thermosets has been reported by several researchers (Kunz 1978, Rowe 1978, Yee 1983 1991, Sue 1991).

In work on toughening epoxies, Kunz and co-workers (1978) showed that small rubber particles gave rise to high fracture toughness (the underlying mechanisms were not correctly interpreted by the authors). Three groups of particle size in range of (a) 0.1 - 1 μm, (b) 1 - 20 μm, and (c) 20 - 50 μm, show that fracture resistance is in the order: group (a) > (b) > (c).

In their early report, Yee and Pearson (1983) concluded that rubber particle size between 1 to 10 microns had little influence on fracture toughness of rubber toughened epoxies. More recently, a different conclusion was drawn by Yee and Pearson (1991) and Sue (1991) that rubber particle did have considerable influence on the properties. The smaller the rubber particles, the higher the fracture toughness of rubber toughened epoxies. The rubber particle sizes in their investigation was from 0.1 to 500 μm, but those particle sizes less than 5 μm appear to give rise to high fracture resistance.

All the conclusions drawn above about the influence of size have not considered the following factors: inter-particle distance ID, rubber cavitation ability and matrix ductility. Whether or not different thermosetting matrices require different rubbers is not clear now.

3.3.3 Effects of Rigid Fillers

For brittle matrices, a linear relationship between fracture toughness K_{IC} and filler volume fraction has been reported by Moloney and co-workers (1987). A good agreement has been obtained between experimental data and crack pinning theory (Section 3.2.4). However, this kind of agreement has not be observed for ductile matrices or rubber toughened ones (Kinloch et al 1985). Instead of linear relationships, a maximum fracture toughness K_{IC} exists at a certain filler concentration. This optimum filler loading appears to vary with matrix ductility: In rubber toughened matrices, the optimum filler loading is low but, in an unmodified matrix, it is high (Kinloch et al 1985).

Two mechanisms have been suggested to explain the effects of filler on fracture toughness. One is pinning and another is crack tip blunting (Kinloch 1985, Mai 1988). The difficulty is to separate the two effects. Based on the study of particulate and hybrid epoxy composites, Kinloch and co-workers concluded that crack pinning would be a dominating mechanism at low temperature but, at high temperature, crack tip blunting would be a primary toughening mechanism. The underlying deformation mechanism for both systems is shearing (Young 1986). As far as micromechanisms are concerned, further discussion about the effects of rigid fillers on fracture behaviour will be presented in Chapter 8.

3.4 Yielding of Thermosets

As discussed previously, the dominating deformation mechanism in thermosets is shearing (Section 3.2.2). This section will discuss the underlying micromechanisms of the yielding process in general.

3.4.1 Micromechanisms

Eyring's solid flow model (Section 2.1.1) has been successfully used both in thermoplastics (Kramer 1975, Bucknall 1977 (review), 1982, 1984; Ward 1983 (review)) and thermosets (Ishai 1967,1968). Another theory which has been used is Argon's (Section 2.1.2). Also good agreement between the theory and experiments has been obtained (Argon 1973, 1977; Yamini 1980; Young 1986). Activation volume can be obtained from Eyring's theory. Two interesting parameters which represent chain segment length and diameter that are involved in yield movement can be calculated from Argon's theory.

Haward and Thackray (1968) made a comparison of Eyring's activation volume, obtained from yield stress data, with the volume of statistical random chain segment, obtained from solution studies. Some data are collected in Table 3.1. Eyring's activation volume is 5 to 10 times as big as the volume of statistical chain segments for polymers. For example, the Eyring activation volume of PC is 6.4 nm^3 while the statistical volume is 0.48 nm^3 . Also the former is 4.6 nm^3 and 9.6 nm^3 but the latter is 0.91 nm^3 and 1.22 nm^3 for PMMA and PS respectively. This comparison implies that the shear activation volume contains not a single segment but a bundles of chain segments.

For thermosets, Ishai (1967) studied the yield behaviour of plasticized epoxy resin and calculated Eyring activation volumes. The results show that the activation volume is 4.2 nm^3 under uniaxial tension, and 3.8 nm^3 under uniaxial compression. Kinloch et al obtained the activation volumes 2.0 nm^3 and 1.9 nm^3 under compression for epoxy and the rubber toughened epoxy respectively. These data are also collected in Table 3.1.

Table 3.1

	Statistical Volume nm^3	Eyring's Volume nm^3	Argon's Parameters a^* (nm)	z^*
PC	0.48	6.4	0.58	1.16
PMMA	0.91	4.6	0.41	0.82
PS	1.22	9.6	0.37	0.74
Epoxy	-	2.0[a], 3.8[b] (4.2)[b]	0.42	0.88
RT-Epoxy	-	1.9[a]	-	-
Filled-E	-	3.8[b]	0.43	1.03
Hybrid-E	-	-	0.45	1.04
add silane	-	-	0.50	1.15

Notice: RT-Epoxy: Rubber Toughened Epoxy; Filled-E: Particulate Filled Epoxy; Hybrid-E: Toughened/Filled/Epoxy

References: (1) Ward(1983) and Argon (1977): PC, PMMA and PS
(2) Kinloch(1983): (a)
(3) Ishai(1976): (b)
(4) Yamini(1980) and Young(1986): the rest of data

By using Argon's theory, the dimensions of polymer chain segments involved in yielding processes can be calculated (Section 2.2.2). One is the diameter a^*, which represents the number of polymer chain segments involved, and another is the length z^*, which represents the number of monomer units along polymer chain involved. These data for thermosets in Table 3.1 are collected from diverse sources (Argon 1977, Yamini 1980, Young 1986).

It is interesting to notice that all the dimensions a^* and z^* lie in the same order for both thermoplastics and thermosets. This may imply that the fundamental yielding mechanisms of thermosets should be no different from those of thermoplastics. For the latter, it has been worked out that the radius a^* contains 1 to 7 polymer segments and the length z^* contains 1 to 5 monomer units, varying according to different materials (Argon 1977). This conclusion also implies that plastic deformation at yield is a cooperative movement involving several chain segments rather than a single chain segment.

3.4.2 Effects of Soft/Rigid Inclusions

It is generally recognized that incorporation of soft/hard inclusions will change the yield stress of composite materials. For soft inclusions, local stress concentrations at the equators will decrease global yield stress, which is lower than that of the matrices. For hard inclusions, local stress concentrations are at and above the poles. This effect, however, does not lead to the reduction of global yield stress but normally increases it with increasing rigid inclusion concentrations. The reason for the increase has been assumed to be the change of activation energy barrier, which is increased after incorporation of hard inclusions (Ishai 1968), according to Eyring's model (Section 2.2.1). Another different view explaining the increase was given by Chow (1991). The reduction of overall free volume is believed to take the responsibility.

As far as yielding mechanisms are concerned, the study of the influence of soft/hard inclusions on Eyring activation volume will help the understanding of underlying mechanisms of polymer yielding. Ishai (1968) studied the effects of fillers and voids on yield behaviour of one epoxy. He concluded that both rigid fillers and voids had little influence on Eyring activation volume under compression. The effect of local stress concentrations caused by voids could be simply expressed by

$$\Gamma = (1-1.2\phi_v^{2/3})^{-1} \tag{3.5}$$

where, Γ is stress concentration factor and ϕ_v is volume fraction of voids. The decrease of

yield stress was assumed to be due to the effect of this stress concentration factor Equation (3.5). For hard inclusions, however, there was little stress concentration effect that was detectable under compression conditions at filler loadings up to volume 51%. The maximum nominal shear stress acting on the continuous matrix phase was assumed.

Based on investigations of epoxies, particulate and hybrid epoxy composites, Yamini (1980) and Young (1986) found Argon's parameters a^* and z^* measured at yielding were almost independent of filler, in particulate composites, and independent of rubber/filler, in hybrid composites (see Table 3.1).

It is worth noticing that all the results on thermosets mentioned above were obtained under uniaxial compression. This could be one reason why local stress concentrations around fillers have not be detected and the same values of Eyring activation volume v^* and Argon parameters a^* and z^* were obtained from different systems but from the same matrix. However, it would be expected that the stress concentration effect caused by rigid filler/rubber will be more pronounced and such parameters as v^*, a^* and z^* will be different from one system to another if the measurement is conducted under tensile conditions (discussion will follow in Chapter 6). Nevertheless, these conclusions based on data obtained under compression conditions do support the argument that it is matrices that determine deformation mechanisms (Bucknall 1977). The function of additives (such as rubbers) is to facilitate matrix deformation but not alter the deformation mechanisms.

CHAPTER 4

EXPERIMENTAL PROCEDURE

This chapter describes the experimental procedures which are common to all the tests, including specimen preparation, instruments and testing conditions. Further details for each of the corresponding tests will be given separately when experimental results are presented in the following chapters.

4.1 Materials

Base Resin - Modar 8035 prepared by Dr. Jane Stoddart (ICI)
Densities: 1.08 and 1.22 g/cm^3 for the uncured and cured resin respectively.
Rubber - Paraloid BTA 753, modified resin powder, Rohm & Haas
Density: 0.95 g/cm^3
- XC 37 modifier, ICI
Filler - Silica Cristobalite Flour XPF6 (50% below 10 μm and 25% below 4 μm) provided by ICI; Density: 2.34 g/cm^3

Modar 8035 is a urethane-methacrylate resin. It is dissolved in methyl methacrylate monomer and forms a cross-linked network with the monomer during free radical polymerization. The basic chemical structure of Modar resin and the resin network is schematically shown in Figure 4.1.

Two types of rubber have been used in this research. One is Paraloid BTA 753, a core-shell polymer with a PMMA shell and with polybutadiene core. Another is XC 37, a four-layer core-shell polymer. Poly(butylacrylate-co-styrene) acts as the rubbery phase and poly(methyl methacrylate-co-ethyl acrylate) as the glassy phase. Light cross-linking and grafting are made within core-shell particles. The microstructures of these two rubbers are schematically shown in Figure 4.2.

Materials were made as follows. All the plaques were made in a glass plate mould using an initiator system 1% benzoyl peroxide (BPO) (36% active paste) and 0.5% catalyst N,N-dimethylaniline (DMA). These quantities were based on the amount of neat resin in each polymerization.

For rubber toughened systems, the rubber powder was mixed into Modar 8035 resin for 20

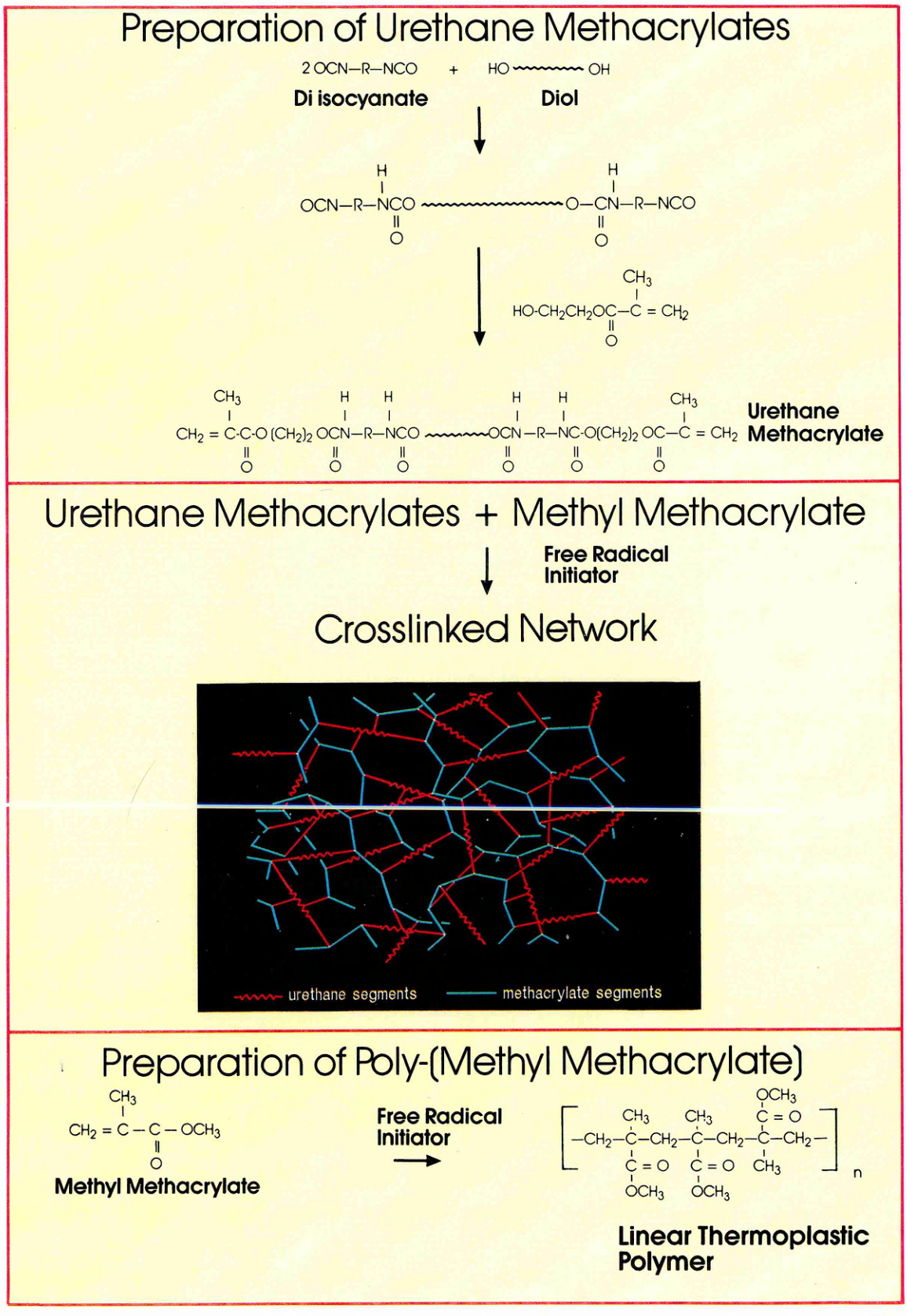

Figure 4.1 Basic chemical structure of Modar 8035 and the resin network.

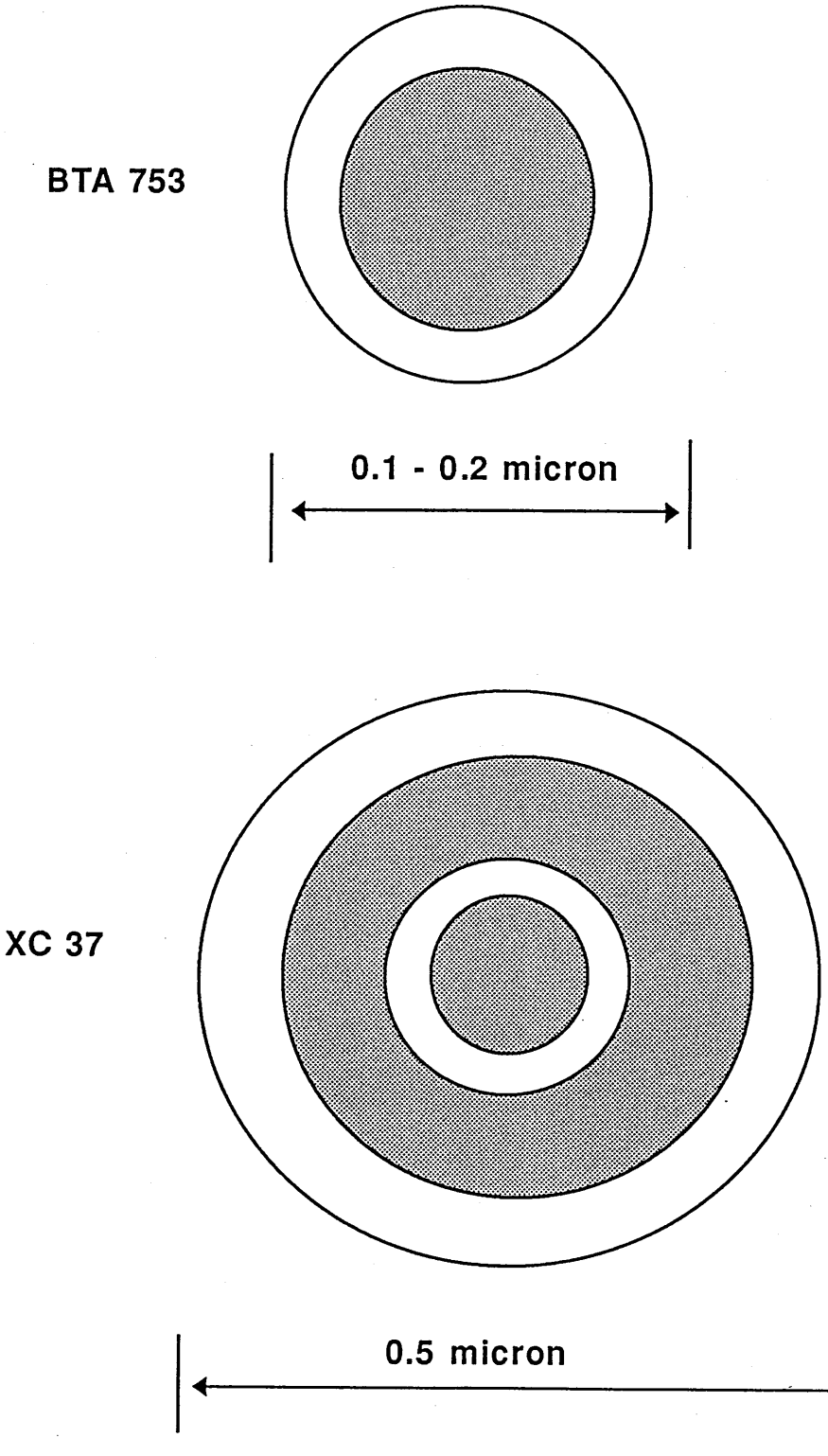

Figure 4.2 2 and 4 layer core-shell rubber modifiers.

mins with the aid of a Silverson mixer. After that, the mixture was divided into two parts, one containing BPO and another DMA, and left to degass under 600 mmHg vacuum at ambient temperature for about 6 mins. The two parts were then mixed together, filled into the glass mould and allowed to stand for curing at ambient temperature.

For hybridized composites, the Modar resin containing 15 wt % rubber was mixed for 15 mins, then filled with varying quantities of silica filler, with mixing for another 5 mins. A coupling agent A174, 3-(trimethoxysilyl)-propylmethacrylate, was added to the systems at a concentration of 0.5% based on weight of filler. The following procedures were the same as

Table 4.1 Formulations of rubber-modified Modar 8035

Materials Code	Modar 8035		BTA 753/XC 37	
T00F00	100[a]	100[b]	0[a]	0[b]
T05F00	95	93.7	5	6.33
T10F00	90	87.5	10	12.5
T15F00	85	81.5	15	18.5

Note: 'a' and 'b' are weight and volume percentages respectively; 'b' calculated from component densities for the materials toughened by rubber Paraloid BTA 753 only.

Table 4.2 Formulations of hydrid Modar 8035

Materials Code	Toughened Matrix*		Filler	
T15F00	100[a]	100[b]	0[a]	0[b]
T15F10	90	94.7	10	5.3
T15F20	80	88.9	20	11.1
T15F30	70	82.3	30	17.7
T15F40	60	75.0	40	25.0
T15F46	54	70.2	46	29.8

Note: 'a' and 'b' are weight and volume percentages respectively; 'b' calculated from component densities.

* constant ratio of 15/85 rubber BTA 753 to Modar resin

these mentioned above except that degassing time varied between 10 and 30 mins, depending on the viscosity of the mixtures. The mixtures were left to stand for approximately 1 hour prior to curing.

After completion of initial polymerization in the glass mould, all the plaques were taken out and post cured in a oven at 115°C for about 40 hours. The materials used in this research are listed in Tables 4.1 and 4.2 as weight and volume percentages.

4.2 Moisture Measurement

The specimens used for these experiments were about 10 x 10 (mm) squares with a thickness between 0.7 mm and 1 mm. In order to provide an initial dry condition for absorption experiments, all specimens were preconditioned in a vacuum oven at 65°C for 4 days. The dried specimens were gradually cooled down then kept in a desiccator. After that, they were placed in distilled water either at 100°C or at 23°C. Water concentration increments were measured with a Mitsubishi Moisture Meter CA-05 at regular intervals during water absorption experiments.

4.3 Tensile Testing

Modulus, yield stress, strength and elongation at break were measured in uniaxial tension, using dog-bone-shaped specimens with 40 mm gauge length, about 5.6 mm width and 2.5 mm thickness. The experiments were conducted on an Instron Model 6025 fitted with a longitudinal extensometer. Volume changes were measured using an additional strain sensor. Cross head speed was 0.5 mm min^{-1} for normal mechanical testing. A range of strain rates covering from 0.00013 s^{-1} to 0.32 s^{-1} was used in investigating relationships between yield stress and strain rate.

4.4 Plane Strain Compression Testing

Plane strain compression tests were conducted on a NENE instrument at a crosshead speed of 0.5 mm min^{-1} at 23°C. The schematic of the experimental diagram is shown in Figure 4.3. A pair of flat parallel dies was placed on opposing sides of a flat specimen. On applying compressive load in direction 1, the material deformed vertically in this direction will be forced to move only along direction 3 providing that the width of the specimen is big enough

to prevent it from increasing under the dies in direction 2. So plane strain conditions are achieved. Two different dies of breadth 3.07 and 6.16 mm were used in the tests. A specimen width 5 times the die breadth was used in order to eliminate end edge effects and to ensure plane strain conditions. The specimen thickness was about 2.5 mm. Also a lubricant ROCOL ASP anti-scuffing paste was used, coated on the surfaces between die and specimen to reduce friction which may be generated during loading.

4.5 Fracture Toughness Testing

Fracture toughness of Modar 8035 resin, the rubber toughened resins and the hybrid composites - Modar/Rubber/Filler - was measured using recommended standard specimens: single edge notched bending (SENB), according to the European Protocol - A Linear Elastic Fracture Mechanics (LEFM) Standard for Testing K_{IC} and G_{IC} for Plastics (October 1989). However, roller pins, as suggested in the Protocol, were not used. Two fixed parallel pins were used instead. The test was conducted on the NENE D.B.30 machine at a crosshead speed of 0.5 mm/min. The schematic diagram of the experiment is shown in Figure 4.4.

An initial 'natural crack' was made in the SENB specimen in Figure 4.4 according to the following instructions. Firstly, machine a sharp notch in the specimen with a V-shaped cutter using a milling machine, then fix the specimen in a vice and place a new razor blade in the notch. After that, tap the razor blade to generate a natural crack into the specimen.

In order to obtain a valid fracture toughness K_{IC}, a candidate value K_Q was calculated first using Equation 2.35 (Chapter 2):

$$K_Q = \frac{P_Q}{B\sqrt{W}} Y \tag{4.1}$$

where

$$Y = 6\left(\frac{a}{W}\right)^{\frac{1}{2}} \frac{\left[1.99 - \frac{a}{W}\left(1 - \frac{a}{W}\right)\left(2.15 - 3.93\frac{a}{W} + 2.7\left(\frac{a}{W}\right)^2\right)\right]}{\left(1 + 2\frac{a}{W}\right)\left(1 - \frac{a}{W}\right)^{\frac{3}{2}}}$$

and P_Q was the load valid for K_Q calculation, which was determined through load - displacement record according the standard mentioned above. As shown in Figure 4.5, a best

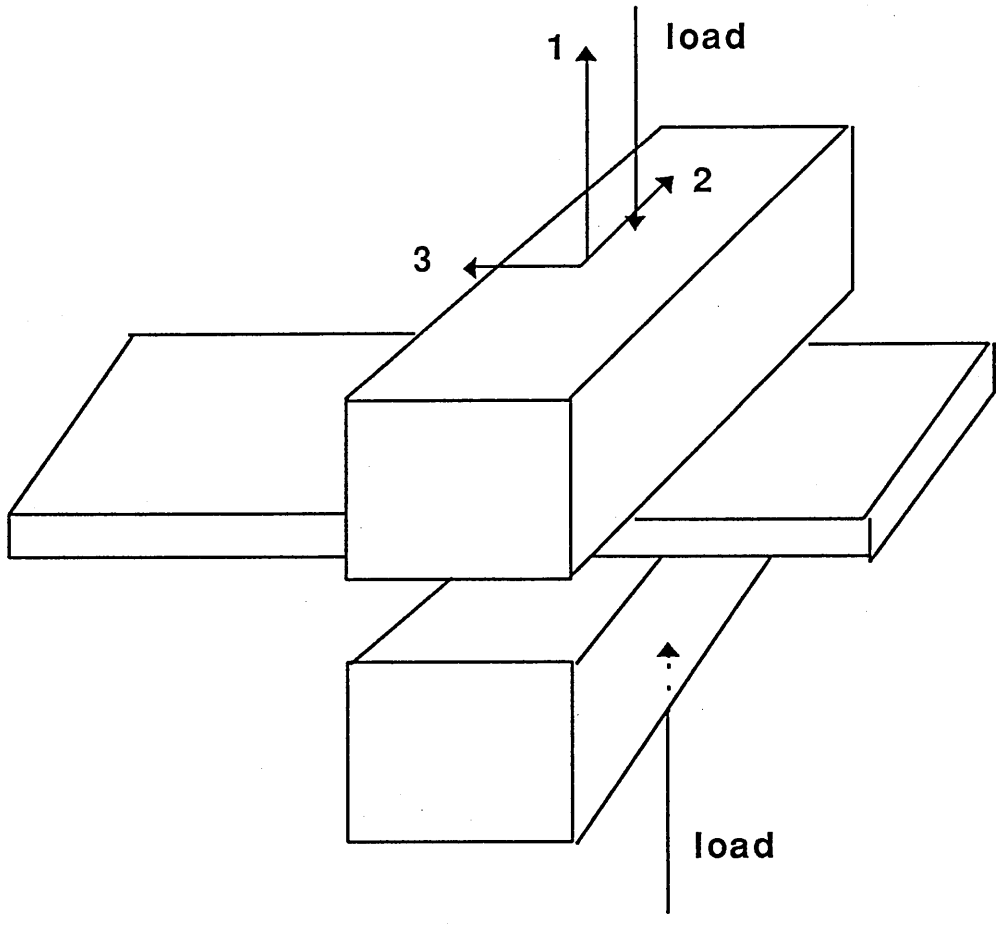

Figure 4.3 Schematic diagram of plane strain compression test.

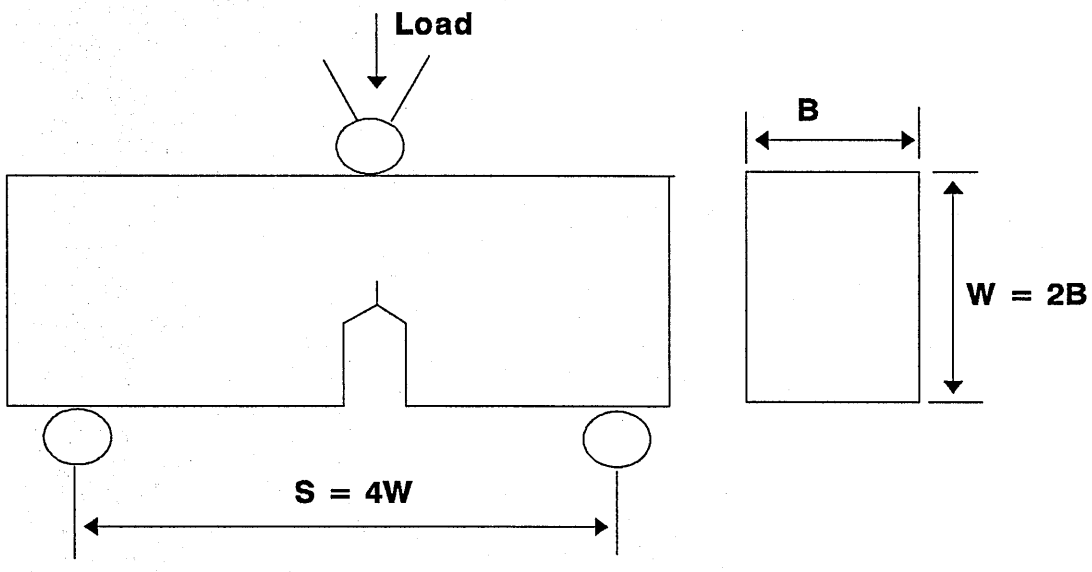

Figure 4.4 Schematic diagram of SENB test.

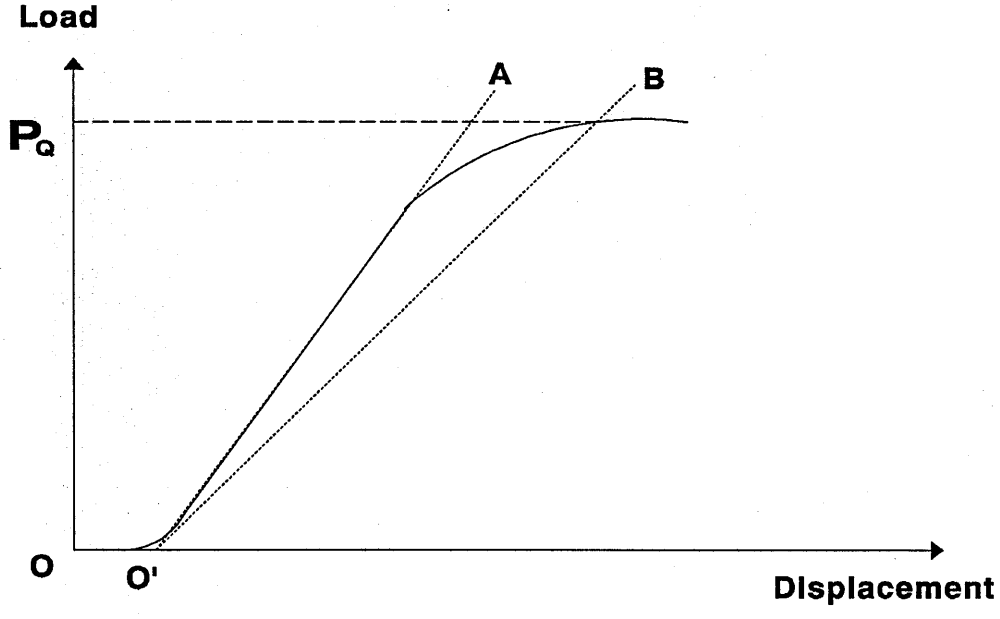

Figure 4.5 Schematic diagram of load - displacement of SENB testing.

straight line O'A was drawn to determine the initial slope of the load - displacement curve, then another straight line O'B is drawn with a slope 5% less than that of line O'A. The load P_Q was determined at the intersection of line O'B with the load - displacement record. If no intersections occurred. i.e. failure load P_C fell between the two lines, P_C was used to calculate K_Q. This was the most common case in these experiments.

The validity of K_Q was checked using the standard according to the size criteria:

$$B,a,(W-a)>2.5\left(\frac{K_Q}{\sigma_{yield}}\right)^2 \tag{4.2}$$

where B, W are thickness and width of the specimen respectively and 'a' is crack length as indicated in Figure 4.4. If these conditions were met then K_Q was taken as K_{IC}.

4.6 Fatigue Testing

Fatigue testing was conducted on the servo-hydraulic fatigue testing machine designed and built at Cranfield Institute of Technology. The standard compact tension (CT) specimens were used, with 75 mm width and 4 mm and 6 mm thickness, referring to ASTM E647. However, an initial natural crack was introduced by a fresh razor blade (the same method as that mentioned above, Section 4.5) rather than through the fatigue procedure as suggested by ASTM E647. The tests were carried out under sinusoidal load control with constant amplitude at ambient temperature and at 2 Hz frequency. The stress ratio R (which is the ratio of minimum load to maximum load) was controlled at R = 0.1. The fatigue crack growth as a function of number of cycles was measured by means of a travelling microscope capable of 10 μm resolution. Reference marks were made on the specimens in order to eliminate potential errors due to accidental movement of the travelling microscope. A schematic diagram of the experimental arrangement is shown in Figure 4.6.

The stress intensity range, $\Delta K = K_{max} - K_{min}$, corresponding to a given crack growth rate was calculated using Equation 2.35 (Chapter 2):

$$\Delta K=K_{max}-K_{min}=\frac{P_{max}-P_{min}}{B\sqrt{W}}Y \tag{4.3}$$

where

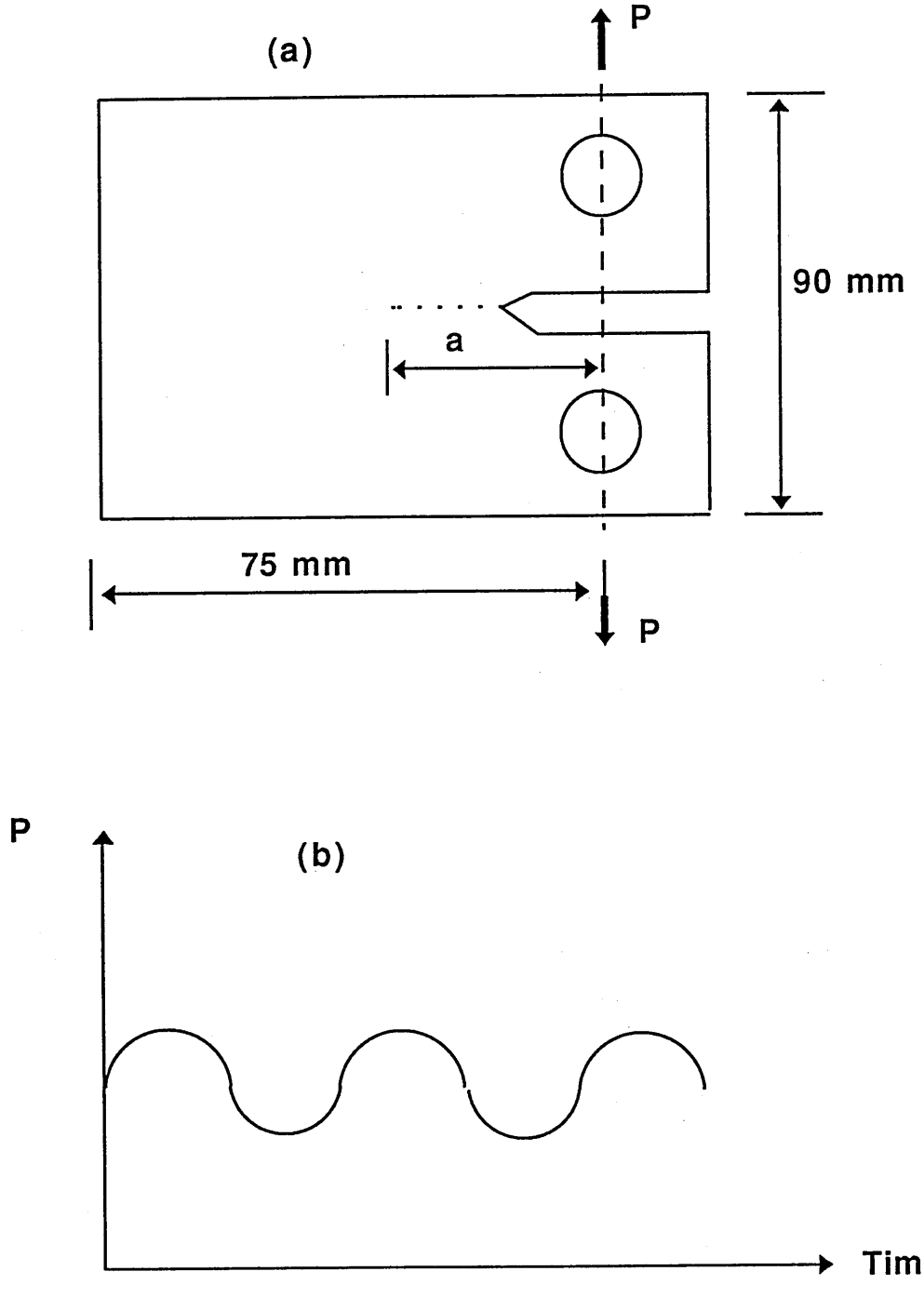

Figure 4.6 Schematic diagrams of compact tension specimen (a); and loading cycles in fatigue testing (b).

$$Y=\frac{2+\frac{a}{W}}{(1-\frac{a}{W})^{3/2}}(0.886+4.64\frac{a}{W}-13.32(\frac{a}{W})^{2}+14.72(\frac{a}{W})^{3}-5.6(\frac{a}{W})^{4})$$

where B, W are specimen dimensions and 'a' the crack length as defined in Figure 4.6. The geometric factor Y was according to ASTM E647.

4.7 Optical Microscopy

1. Reflection Microscopy

Regions ahead of the crack tip on the edge surface of SENB specimens (referring to Figure 4.4, not fracrture surface) were examined directly under microscope Nikon 143650 before and after deformation. These specimens were carefully polished to get rid of surface defects before loading.

2. Transmission Microscopy

Thin sections of deformed SENB and tensile specimens with thickness less than 100 μm were made by the following procedures: a piece of sample containing the area of interest was cut out by fine handsaw first. This was followed by grinding with SiC Papers P500 and P1200 using water as cooling agent. The sample was then polished with Buehler 3.0 μm aluminum oxide powder and 0.3 μm slurries on Buehler polishing cloth. Reflection microscope was used to evaluate the quality of sample preparation during polishing. The fine polished section was examined by transmission microscope Olympus BH-2.

In addition, thin samples about 60 μm, which were made in two micro slides by the same procedure as making the resin plaques (Section 4.1), were used to observe deformation behaviour of the rubber toughened Modar resin. Tensile deformation of the thin samples was controlled by hand and examined under the Olympus BH-2.

4.8 Electron Microscopy

1. Scanning Electron Microscopy

Fracture surfaces were examined using SEM Model ISI ABT-55. The specimens were coated with gold/palladium for morphological investigation. Some specimens which need element analysis were coated with carbon and examined by Cambridge Stereoscan Model 250 MK3.

2. Transmission Electron Microscopy

The specimen containing the area of interest was shaped by glass knife first, making a trim block as indicated in Figure 4.7. This was followed by staining process. The trimmed specimen was placed in a vial containing 0.25 gram osmium tetroxide (OsO_4) for about 2 weeks. After that, thin sections about 60 to 80 nm thick were cut by diamond knife using Ultracut E (Reichert-Jung) at cutting speed 1 mm/min and at angle 45° to the trimmed surface of specimens. TEM Philips Model CM20 was used for the microstructure investigation.

4.9 DMTA and DSC

The dynamic mechanical behaviour was investigated using dynamic mechanical thermal analyzer (PL-DMTA). The specimens were flat strips with thickness either 1.5 mm or 2.5 mm. The thinner one was used to monitor the glass transition of dispersed rubber phase at low temperature. The thicker one was used for matrix glass transition characterization at high temperature. The overall temperatures covered from -90°C to 180°C at heating rate 3°C min^{-1}. The dynamic frequency covered from 0.1 Hz to 30 Hz. The temperature corresponding to the peak point in tanδ in DMTA tests is taken as T_g (see Figure 6.9 later in Chapter 6)

In the investigation of glass transition of water saturated specimens, cellophane film, which was saturated with water, was used to seal the specimens in order to retard the speed of water desorption during DMTA experiments. The error of apparent Tg introduced by the cellophane was corrected as follows. The normal material (not water saturated) was tested under the conditions: one using the sealing procedure and another without it. It was found that apparent T_g reduced about 5.5°C when the sealing method was used. So the difference was taken into account for the values measured for water saturated materials.

Differential scanning calorimeter Perkin-Elmer Model DSC-4 was also used to monitor glass transition of the materials investigated at scanning rate 10°C/min. The middle point between onset and ending points of glass transition on DSC records is taken as the T_g (see Figure 6.10 later in Chapter 6).

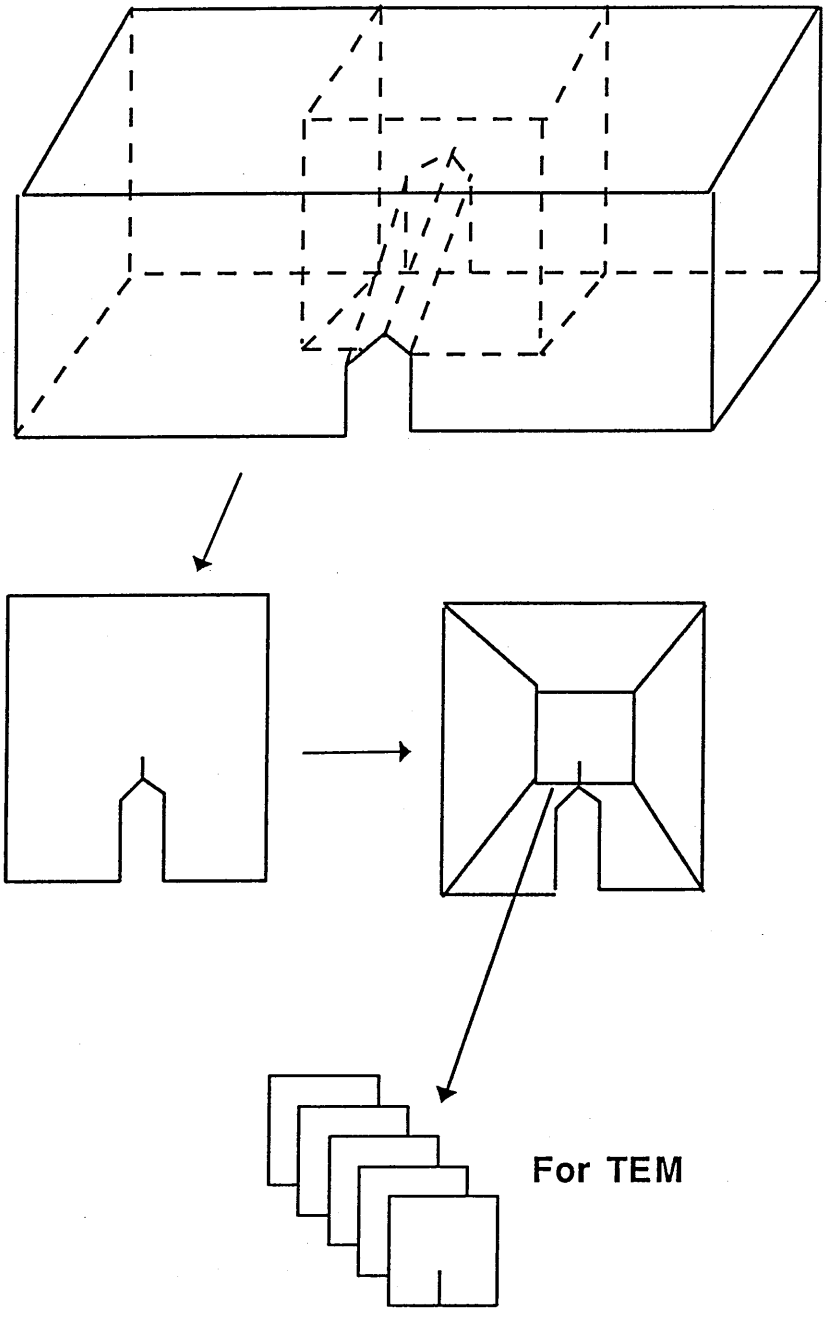

Figure 4.7 Schematic of TEM specimen preparation.

CHAPTER 5

DIFFUSION BEHAVIOUR

5.1 Introduction

Mechanical properties may suffer when materials such as thermosets and thermosetting composites are exposed in aggressive environments. Water is one of the materials most likely to be encountered during service. In this research, two types of damage induced by water have been recognized. One is recoverable damage. Thermodynamic properties, such as glass transition temperature Tg, and mechanical properties, such as modulus and fracture strength, will recover to the values in dry conditions after water has been driven out. Another type of damage is permanent, in the form of disc-like cracks. This damage cannot recover even after water being driven out. Before further discussions about mechanisms involved in these two types of damage (which will be discussed in Chapter 7), the mechanisms of water transportation in the materials used in this research should be understood first. The objective of this chapter is to determine water concentration as a function of time during absorption with reference to Fick's law. Water-induced internal cracking will be presented too.

5.2 Basic Diffusion Equation: Fick's Law

The first quantitative diffusion equation was proposed by Fick (1855). He adopted the mathematical equation of heat conduction derived by Fourier (1822). The basic hypothesis is that the transfer rate of a diffusing substance through unit area of a section is proportional to the concentration gradient normal to the section. This can be expressed by:

$$F = -D\frac{\partial C}{\partial x} \tag{5.1}$$

where F is the transfer rate per unit area, C the concentration of diffusing substance, x the space coordinate normal to the section, and D diffusion coefficient. This is schematically shown in Figure 5.1.

Consider one dimensional diffusion. The change of diffusing substance C within time 'dt' in unit area from 'x' to 'x+dx' can be expressed by:

$$\frac{\partial C}{\partial t} = -\left(\frac{\partial F}{\partial x}\right) \tag{5.2}$$

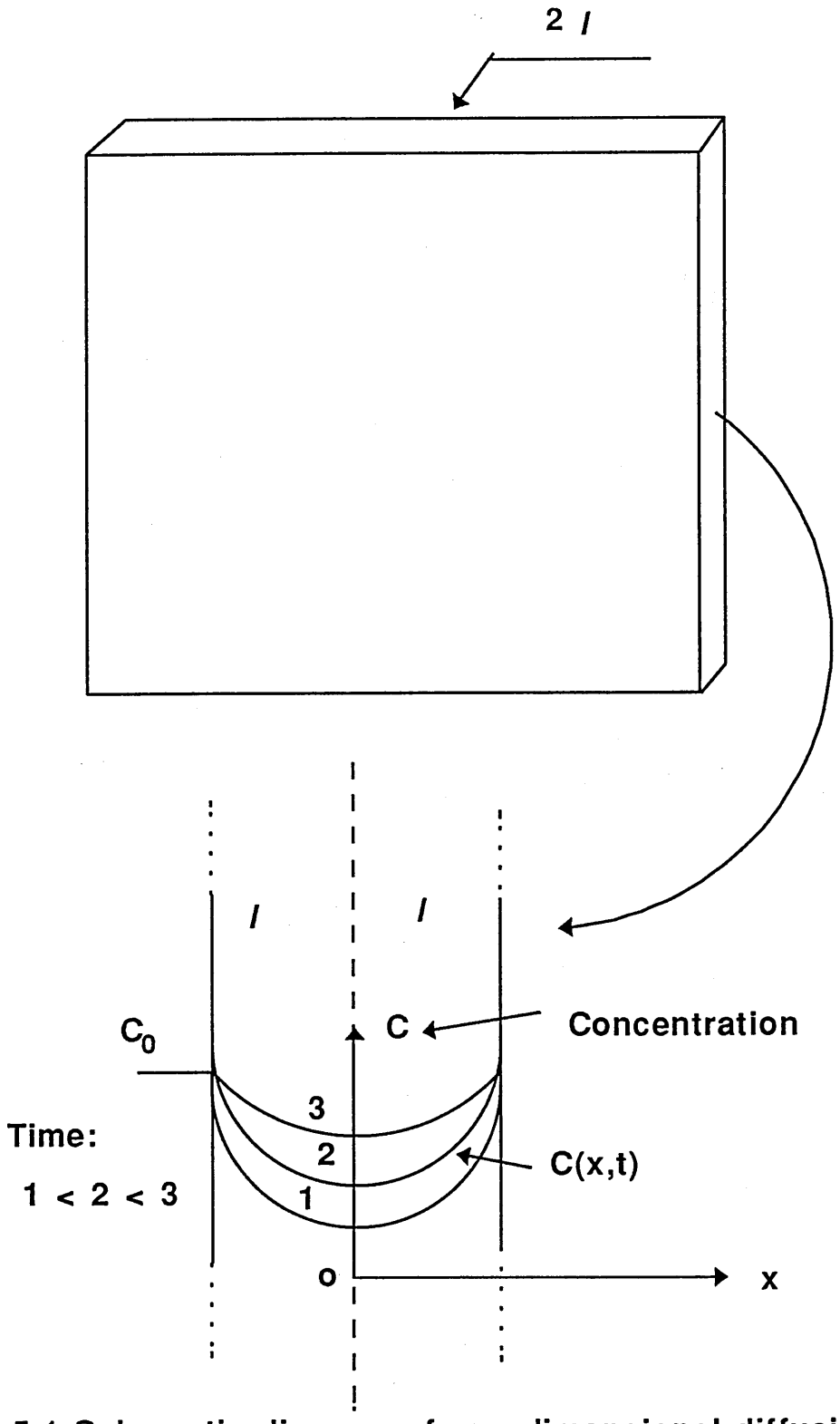

Figure 5.1 Schematic diagram of one dimensional diffusion (absorption).

Assuming a constant diffusion coefficient D and combining equations (5.1) and (5.2) makes:

$$\frac{\partial C}{\partial t} = D\left(\frac{\partial^2 C}{\partial^2 x}\right) \tag{5.3}$$

Equations (5.1) and (5.3) are known as Fick's first and second laws.

One solution of equation (5.3) for the one dimensional case can be expressed by (Crank 1957):

$$\frac{C-C_i}{C_0-C_i} = 1 - \frac{4}{\pi}\sum \frac{(-1)^n}{2n+1} e^{-D(2n+1)^2\pi^2 t/4l^2} \cos\frac{(2n+1)\pi x}{2l} \tag{5.4}$$

where C_i is the initial concentration in region $-l < x < l$ and C_0 the concentration at surfaces. This equation can be applied to both absorption and desorption processes.

For the case of absorption, if it is assumed that $C_i = 0$ and $C_0 = C_s$, where C_s is assumed to be the saturated concentration, integrating equation (5.4) from x = -l to x = l at time 't' makes:

$$\frac{M_t}{M_s} = 1 - \sum \frac{8}{(2n+1)^2\pi^2} e^{-D(2n+1)^2\pi^2 t/4l^2} \tag{5.5a}$$

where M_t is the total amount of diffusing substance which has entered into the sheet at time t, and M_s saturated concentration.

For the case of desorption, if it is assumed that $C_i = C_s$ and $C_0 = 0$, integrating equation (5.4) from x = -l to x = l at time 't' makes:

$$\frac{M_t}{M_s} = \sum \frac{8}{(2n+1)^2\pi^2} e^{-D(2n+1)^2\pi^2 t/4l^2} \tag{5.5b}$$

It can be seen that Equation (5.5b) can be obtained by subtracting Equation (5.5a) from 1.

Other corresponding solutions useful for small times are (Crank 1957):

$$\frac{C-C_0}{C_s-C_0} = \sum (-1)^n erfc\left[\frac{(2n+1)l-x}{2\sqrt{Dt}}\right] + \sum (-1)^n erfc\left[\frac{(2n+1)l+x}{2\sqrt{Dt}}\right] \tag{5.6}$$

$$\frac{M_t}{M_s}=2\left(\frac{Dt}{l^2}\right)^{1/2}\left[\pi^{-1/2}+2\sum(-1)^n erfc\left(\frac{nl}{\sqrt{Dt}}\right)\right] \tag{5.7}$$

where 'erfc' stands for error function and M_t/M_s is for the case of absorption under the conditions defined above. Normally, the first right hand term in Equation (5.7) is used to obtain diffusion coefficient D at the initial stage of absorption/desorption when the rest of the terms in the equation are negligible. This can be expressed by:

$$\frac{M_t}{M_s}\approx 2\left(\frac{Dt}{\pi l^2}\right)^{\frac{1}{2}} \tag{5.8}$$

Theoretically, it is now possible to predict concentrations of diffusing substance within the plane sheet at any time and at any position from equation (5.4) unless diffusion coefficient D is known. As predicted by equation (5.8), the initial period of absorption/desorption will give rise to a straight line by plotting M_t/M_s versus $t^{1/2}$. Diffusion coefficient D can be obtained through this slope experimentally.

In addition to Fickian diffusion, non-Fickian diffusion in polymers has been reported (Thomas 1978). If Equation (5.8) is re-written in a general form:

$$\frac{M_t}{M_s}=Kt^n \tag{5.9}$$

where K and n are constants, three cases of diffusion can be classified as follows (Alfrey 1966, Thomas 1978):

(a) $n = ½$, Case I (Fickian) diffusion;
(b) $½ < n < 1$, anomalous diffusion;
(c) $n = 1$, Case II diffusion.

It was assumed that the rate of small molecule diffusion is much less than that of polymer segment relaxation for Case I diffusion. For Case II diffusion, the former is much greater than the latter. Anomalous diffusion is between these two extremes.

5.3 Experimental Results

In order to obtain absolute rates of water absorption in terms of diffusion coefficients, a series of experiments was designed for the purpose, using the method described in Section 4.1. The experimental results of water absorption for three typical materials Modar 8035 (T00F00), the rubber toughened (T15F00) and the hybridized (T15F46) resins are shown in Figures 5.2 and 5.3. Figures 5.2 contains the results of water absorption at 100°C and Figure 5.3 the results at 23°C. It is clearly shown that reasonable straight lines in initial period of water absorption have been obtained by plotting M_t/M_s versus $t^{1/2}/l$. Diffusion coefficients were obtained through these slopes using Equation (5.8). They are summarised in Table 5.1. In addition, the saturated concentrations of water M_s are also listed in the table for each of the corresponding materials. These data of M_s at 23°C were obtained by extrapolation of curves of water absorption up to 500 days as indicated in Figure 5.4. The measurement was conducted on an analytical balance using 4 x 8 x 16 (mm) block specimens. Each point in the plot is the average of the five measurements.

Table 5.1 Water Absorption Parameters

Materials	T00F00		T15F00		T15F46	
T (°C)	23	100	23	100	23	100
D ($\mu m^2\ s^{-1}$)	0.21	21.7	0.22	20.2	0.18	15.2
M_s (wt %)	2.5	3.2	2.5	3.2	1.4	1.8

It can been noted that diffusion coefficient D is two orders of magnitude higher at 100°C than that at 23°C for each of the corresponding materials. Untoughened and rubber toughened materials (T00F00 and T15F00) have almost the same 'D'. However, for the hybrid material - filled and toughened T15F46, it is lower than the former two materials. Water concentrations at equilibrium follow the same trend.

5.4 Discussions

5.4.1 Comparison with Theory

Comparisons of experimental data with Fick's law are shown in Figures 5.5, 5.6. Solid lines

in these plots are analytical solutions according to Equation (5.5a) and points shown experimental results. These plots are made by drawing normalized water concentration against dimensionless time T^* which is the product of diffusion coefficient and the time divided by the thickness of the sheet raised to power 2, i.e $T^* = Dtl^{-2}$.

In general, good correlation between the data and Fick's solution has been obtained for these three materials. At temperature 100°C, these relationships are followed until the water absorption levels off, suggesting that the system is approaching equilibrium (Figure 5.6). After that, however, water uptake shows a further increase over an extended absorption time. At temperature 23°C, unmodified Modar resin T00F00 obeys Fick's law well. For the rubber toughened T15F00 and the hybrid composite T15F46, however, deviations from the Fickian diffusion occur (Figure 5.5). Water uptake speed is a little higher in the initial period than that predicted by Fick's law but it is slower than that predicted in the times later.

In addition to Fickian diffusion, non-Fickian diffusions were reported by Thomas and Windle (1978) for methanol/PMMA systems. The interesting phenomena are that Fickian diffusion (Case I diffusion) occurred only in the conditions when methanol was heated up to its boiling point, but typical Case II diffusions occurred at ambient temperature. For the latter case, a linear relationship between concentrations of diffusing substance M_t and time 't' (n=1 in Equation 5.9) remains until equilibrium. This can be schematically shown in Figure 5.7.

In this research, however, Fickian diffusion appears to be the best description for the materials investigated in water environments, as compared with anomalous diffusion and Case II diffusion. Figure 5.8 is the plot made for this purpose, where n= 0.5, 0.75 and 1 have been chosen for each of the corresponding materials according to Equation 5.9. Water concentrations in the initial period are chosen up to about 0.6 M_s (M_s is the saturated concentration of water). It can be seen that a reasonable straight line is given only for Case I diffusion when n = 0.5 for all three materials investigated. This implies that the diffusion pattern tends to be Fickian for all three materials investigated.

5.4.2 Factors Affecting Diffusion Behaviour

As mentioned previously, temperature has a strong influence on water diffusion rate. Diffusion coefficient is two orders of magnitude higher at 100°C than that at 23°C for each of the corresponding materials. For example, the absorption diffusion coefficient D is 0.21 $\mu m^2\ s^{-1}$ at 23°C for neat Modar resin T00F00 and 21.7 $\mu m^2\ s^{-1}$ for the same material but at 100°C. For modified Modar resins, it is 0.22 and 0.18 $\mu m^2\ s^{-1}$ at 23°C but 20.2 $\mu m^2\ s^{-1}$ and

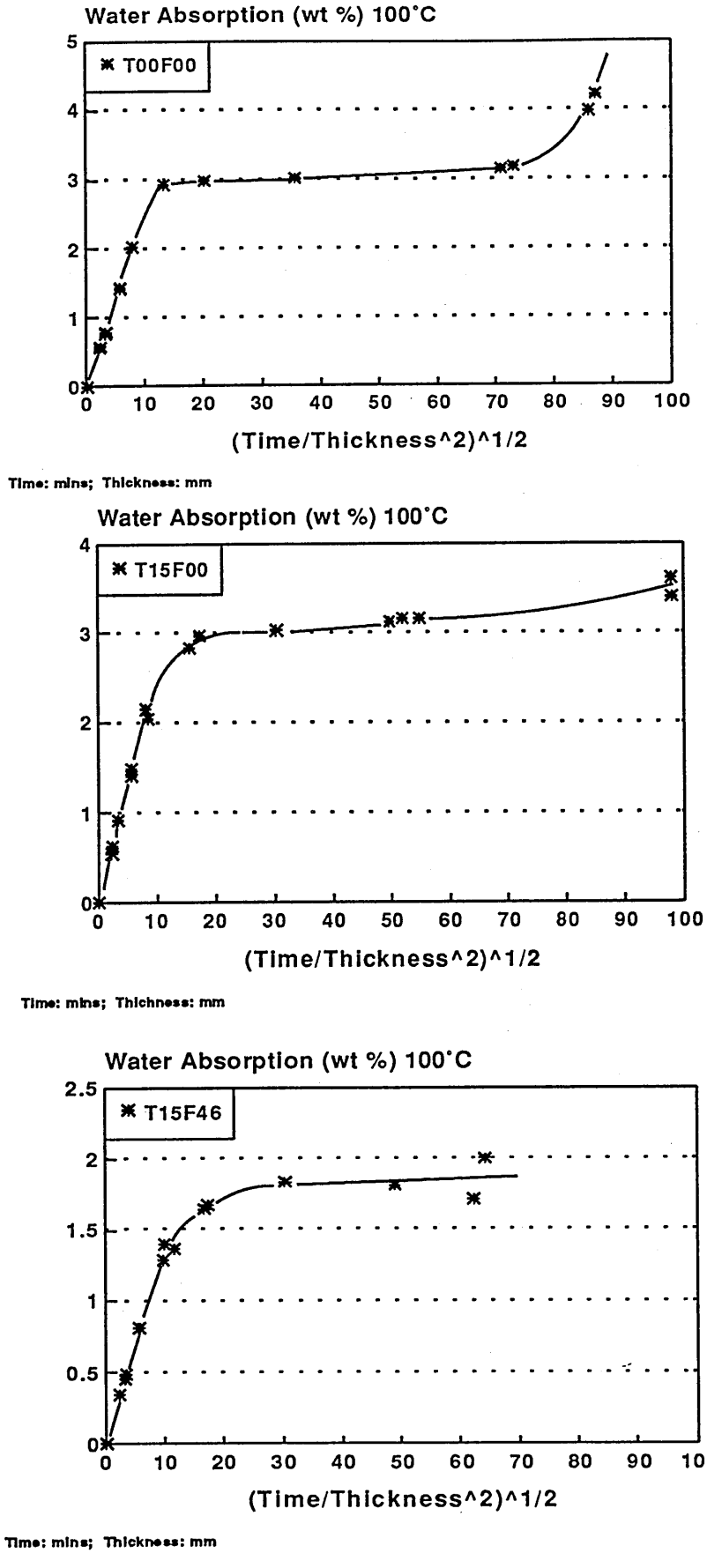

Figure 5.2 Water uptake as a function of time for materials T00F00 (top), T15F00 (middle) and T15F46 (bottom) at 100°C

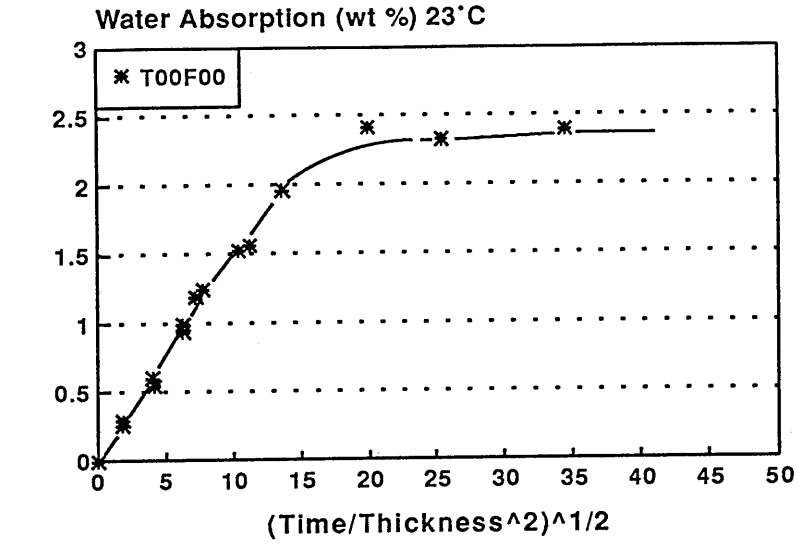

Time: Hours; Thickness: mm

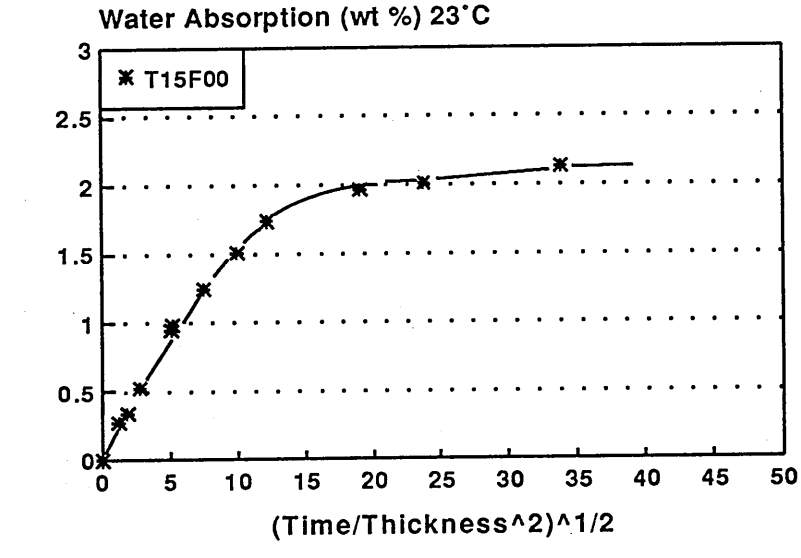

Time: hrs, Thickness: mm

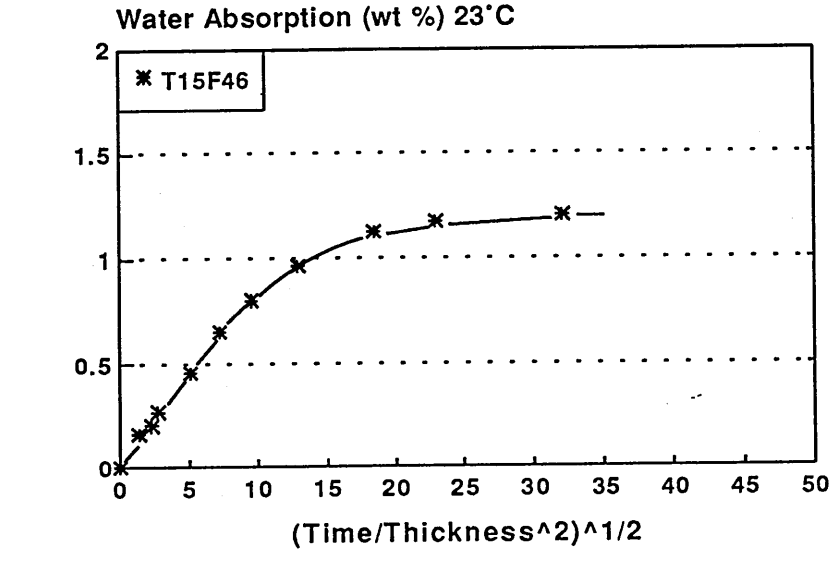

Time: hrs, Thickness: mm

Figure 5.3 Water uptake as a function of time for materials T00F00 (top), T15F00 (middle) and T15F46 (bottom) at 23°C.

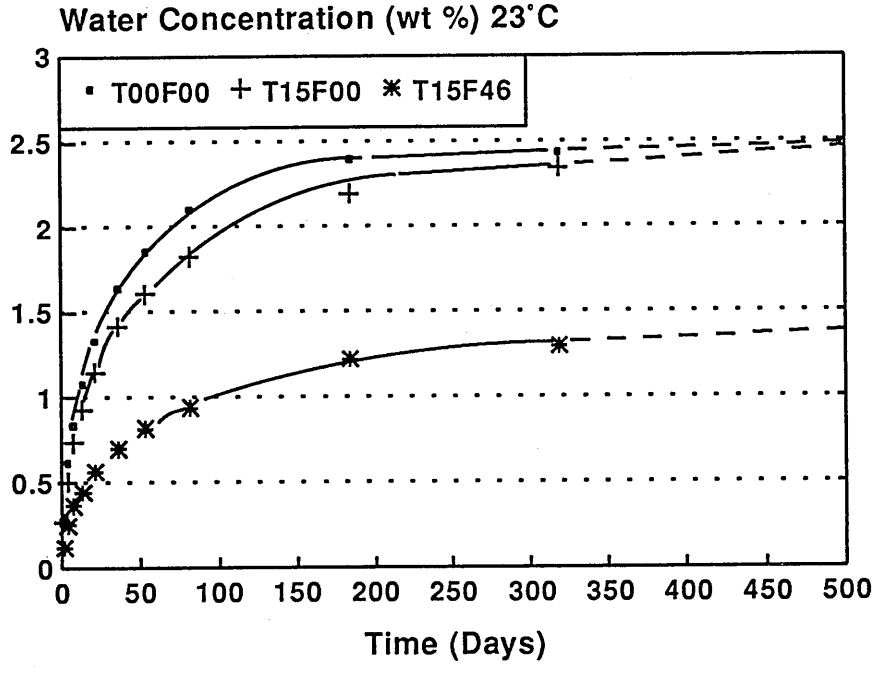

Figure 5.4 Water uptake as a function of time for materials T00F00, T15F00 and T15F46 (23°C).

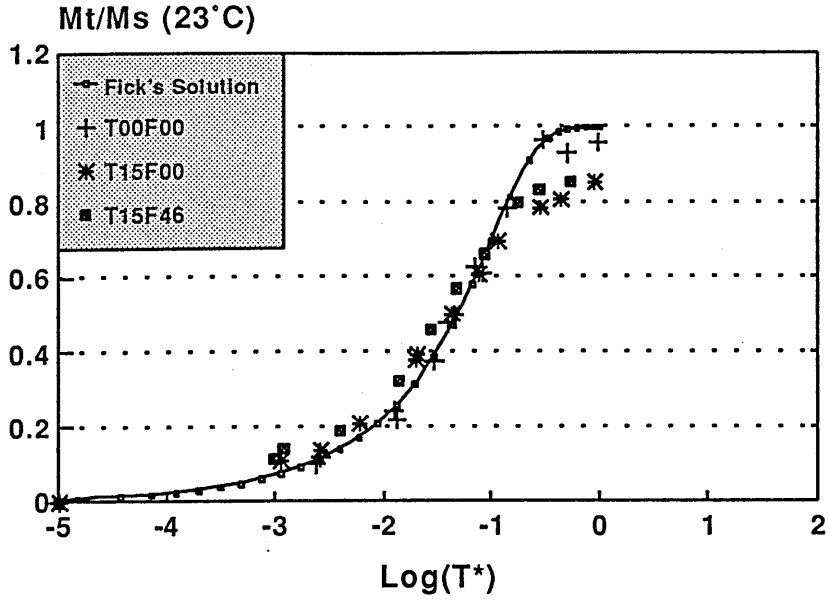

T*: Time*D/Thickness^2
D: Diffusion Coefficient
Ms: Saturated Water Concentration

Figure 5.5 Comparison of Fick's solution with experimental results of modified and unmodified Modar 8035 (23°C)

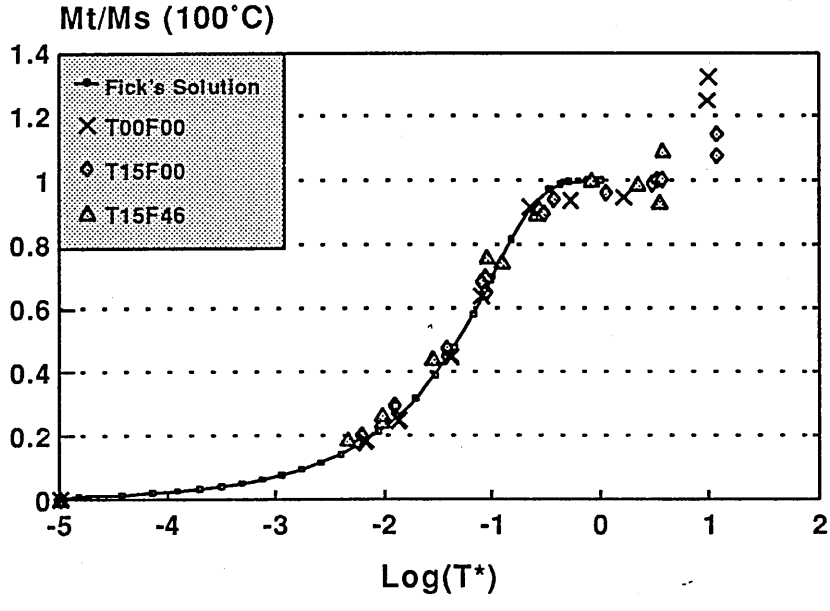

T*: Time*D/Thickness^2
D: Diffusion Coefficient
Ms: Saturated Water Concentration

Figure 5.6 Comparison of Fick's solution with experimental results of modified and unmodified Modar 8035 (100°C)

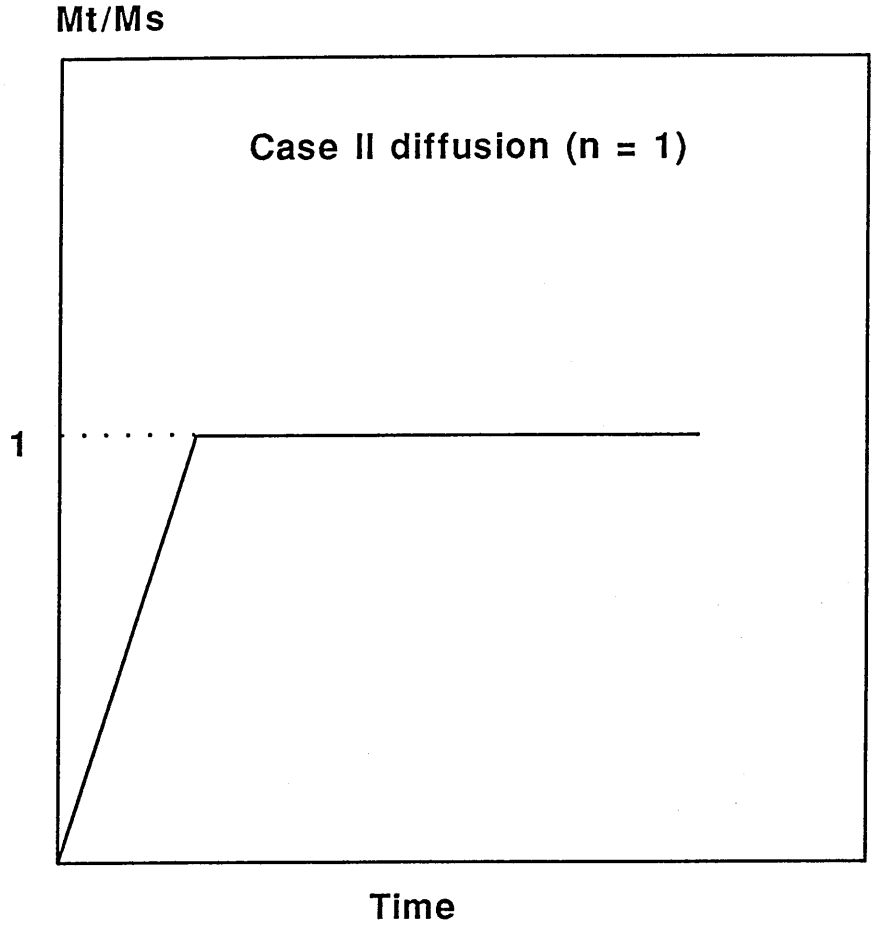

Figure 5.7 The schematic diagram of Case II diffusion (absorption).

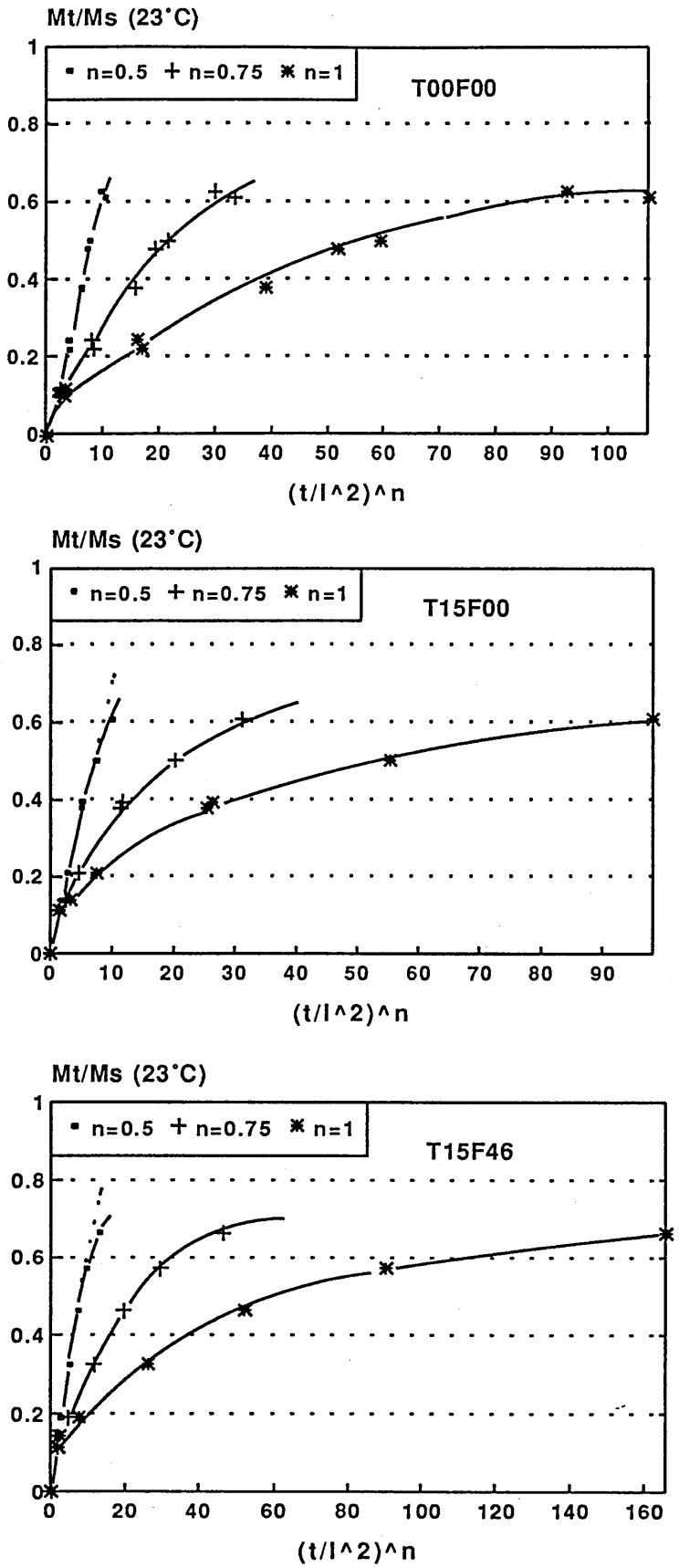

Figure 5.8 Water uptake as a function of time raised to power 'n': T00F00 (top), T15F00 (middle) and T15F46 (bottom).

15.2 $\mu m^2 s^{-1}$ at 100°C for T15F00 and T15F46 respectively. Temperature also affects the saturated concentrations of water. The higher the temperature, the higher the concentration (Table 5.1).

Addition of rubber and filler can affect water diffusion. As indicated in Figure 5.5, experimental data for both the rubber toughened T15F00 and the hybrid composite T15F46 deviate from theoretical prediction to a certain extent at temperature 23°C. The rate of water uptake is systematically higher than that predicted by Fick's law at concentration below 0.6 Ms. After that, it falls off. The reason for the deviation is not well understood.

Three factors may be responsible for the deviation. The first is non-Fickian diffusion, the second the multiple-phase structure of resin composites and the third the internal stresses in the presence of additives.

As discussed previously, the first factor is not important because it appears that Fickian diffusion can give rise to the best fitting curve (straight lines) in the initial period of diffusion (Figure 5.8). Here, Fickian and non-Fickian diffusions are determined by whether a linear relationship exists or not between the concentration of diffusing substance and the time raised to power 'n' as defined by Equation 5.9. It is impossible to draw a straight lines when n=0.75 or 1 but linearity is observed for n = 0.5 for all the materials studied. Therefore, Fickian diffusion appears to be the best one although differences exist between the theoretical prediction and experiments.

For the second factor, it is understood that rubber and filler particles will interfere with diffusion process if diffusion coefficients for rubber and filler are different from that of the resin matrix. Also interfaces formed between different materials will alter the diffusion process. The interesting thing is that the deviation of experimental data from Fickian diffusion at 100°C is less than that at 23°C for these two materials T15F00 and T15F46 (up to apparent equilibrium) as indicated in Figures 5.5 and 5.6. This cannot be well explained simply by what have mentioned above.

The third factor, i.e. the internal stresses, perhaps is the key factor that affects the diffusion mechanisms of the resin composites. Compressive stresses would be generated during the resin curing due to the resin shrinkage. It is estimated that about 11 % volume reduction of Modar 8035 resin will be made during the resin curing[1]. The pressure due to this shrinkage

[1] Calculated according to densities 1.08 and 1.22 g cm^3 for liquid Modar 8035 resin and the cured resin respectively (the data in Chapter 4)

will be exerted on each individual rubber and/or filler particle. With regard to diffusion, those pressures near sheet surfaces are relatively easier to release than those in the centre by the process of water diffusing through a matrix. This is because free surfaces at both sides of the sheet have less resistance to polymer chain swelling caused by small molecules. Therefore, the diffusion resistance is less near the surface than that in the centre. The apparent rate of water transportation is faster in the initial stage than that at latter times (Figure 5.5). Increasing temperature will accelerate polymer chain relaxation process and help to ease the internal stresses. So the deviation from what is predicted by Fick's law will be reduced at high temperature (Figure 5.6), compared to that at relatively lower temperature (Figure 5.5).

In addition, filler seems to have a more pronounced influence on the diffusion process than rubber. This is reflected on the saturated concentrations of water. As indicated in Table 5.1, incorporation of filler particles causes a reduction of the water concentration. For the hybrid composite T15F46, it is 1.4 wt % at 23°C and 1.8 wt % at 100°C, compared to 2.5 % and 3.2 wt % at 23°C and 100°C respectively for both T00F00 and T15F00. The reason for the reduction may be the same as that discussed above - internal compressive stresses in addition to the effect of the filler itself.

Assuming the filler does not absorb water at all and does not affect the water absorption of the rubber toughened matrix (T15F00), the matrix should be able to absorb water up to Ms = 2.5 % at 23°C and 3.2 % at 100°C (Table 5.1). With regard to the presence of filler, the overall concentration at equilibrium should be 0.7 x 2.5 % = 1.75 % for the hybrid composite T15F46 at 23°C, considering that the matrix accounts for about 70 % total volume (Table 4.2 in Chapter 4). For the same reason, this material should be able to absorb water up to 2.2 % (0.7 x 3.2 % = 2.2 %) at 100°C. However, the actual saturated water concentrations are 1.4 % and 1.8 % at 23°C and 100°C respectively. They are considerably smaller than that predicted above. This implies that filler makes a 'negative' contribution to the water absorption.

The reason for the reduction cannot be the change of capacity of water absorption of the matrix itself. Internal stresses are probably the main cause responsible for the reduction. As discussed previously, compressive stresses, which are generated due to the resin shrinkage in the presence of filler, will act on each individual filler particle and create more resistance to the swelling process of the polymer caused by water diffusion. As a result, the amount of water uptake is less than that predicted from the data obtained without the presence of filler. One conclusion at least can be drawn from this analysis: that the water absorption of the matrix is not independent of the filler used. Internal stresses can alter the equilibrium

concentration of the diffusing substance as well as the rate of overall diffusion.

It is interesting to note that, for unmodified and rubber toughened Modar resin, water uptake at high temperatures increases unexpectedly after the time when the equilibrium appears to have been reached as shown in Figure 5.6. It is at this time when disc-like cracks start to develop within the neat Modar resin.

5.4.3 Formation of Disc-like Cracks

Disc-like cracks will develop within unmodified Modar resin if the time of water absorption at 100°C is extended. Sharp increase of water uptake (Figure 5.6) is due to the formation of disc-like cracks for unmodified Modar resin, which is shown in Figure 5.9.

The scale of cracking and the size of cracks can be increased by extending time. It has been found that these disc-like cracks originate from some kind of 'impurity' (detailed in Section 7.4). The bigger the size of the impurity, the bigger the cracks.

Another interesting phenomenon is that these cracks occur only after the time when equilibrium appears to have been reached. The crack can start to develop in a few days for thin sheet and it can form in one month for a thick one. This is because a thin sheet can reach its equilibrium much quicker than a thick one as water uptake is mainly controlled by the term t/l^2 (t is time and l thickness) for a given material for the case of Fickian diffusion. This is indicated in Equations 5.4, 5.5 and 5.8. Reducing thickness can greatly reducing diffusion time for a given water uptake.

However, no evidence has been obtained about the formation of these disc-like cracks within the rubber toughened T15F00 and the hybridized composite T15F46 materials. For the former, only honeycomb-like defects were observed, which are shown in Figure 5.10. For the hybrid composite T15F46, results from tensile fracture experiments have ruled out the existence of disc-like cracks within the material. Fracture strength of the material is not affected by long term water absorption process but it reduces dramatically for the unmodified Modar. The mechanisms of formation of disc-like cracks will be discussed in Chapter 7.

5.5 Conclusions

(1) Fickian diffusion dominates the diffusion behaviour for the systems water/Modar 8035

resin and water/modified resin composites. For the later systems, deviations from Fickian diffusion occur to a certain extent, especially at low temperatures.

(2) Increasing temperature can effectively increase both diffusion rate and equilibrium concentrations of water.

(3) Incorporation of rigid filler reduces the overall capacity for water uptake of the resin matrix, which is probably caused by internal stresses due to shrinkage of the curing resin in the presence of filler.

(4) Disc-like cracks will be generated in the unmodified Modar 8035 resin after the time when equilibrium appears to have been reached, which is responsible for the sharp increase of water uptake observed in the experiments.

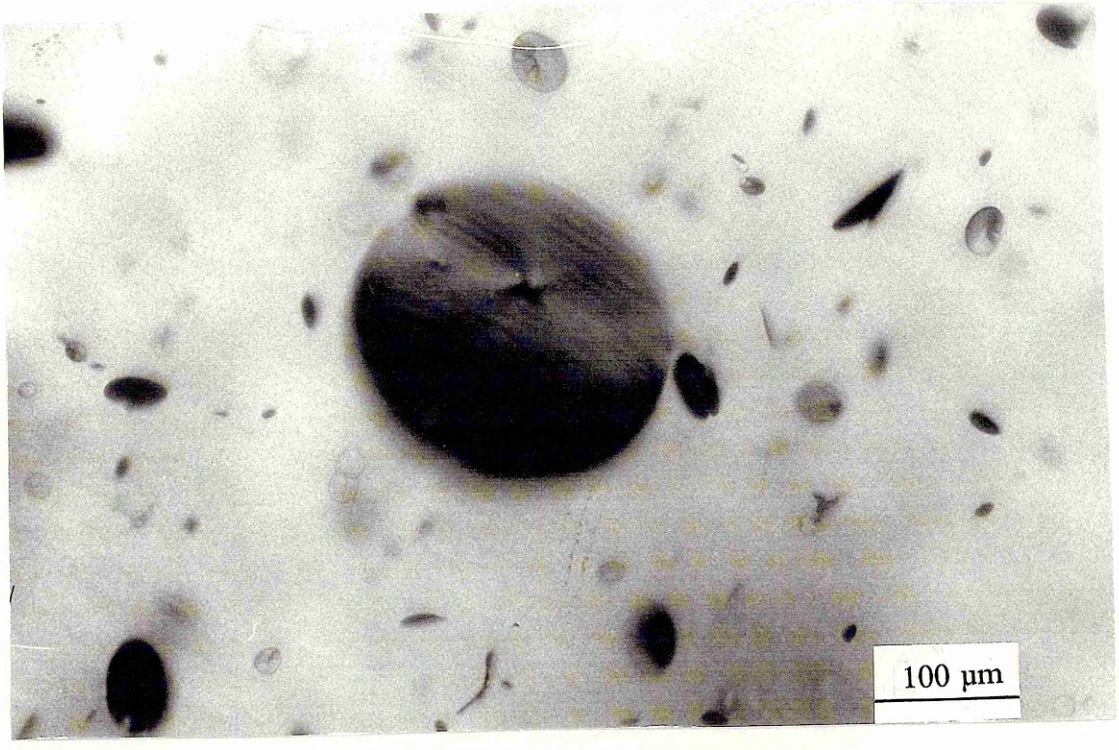

Figure 5.9 Disc-like cracks of Modar 8035 formed in water environment at 100°C.

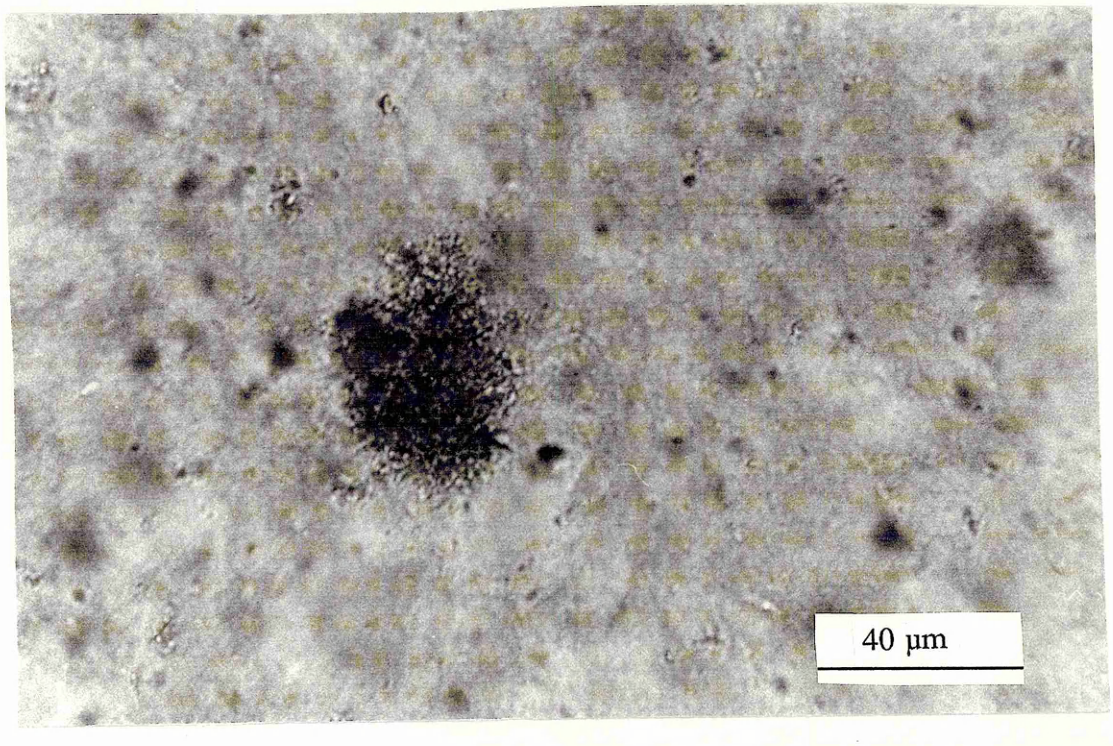

Figure 5.10 Honeycomb-like defects of Modar 8035 modified with 15 wt % rubber in water environment at 100°C.

CHAPTER 6

DEFORMATION BEHAVIOUR

6.1 Introduction

A typical tensile stress - strain relationship of a modified Modar 8035 resin is shown in Figure 6.1. Before further discussions on the deformation behaviour for all the materials investigated, some terms relating to tensile properties and the method used in the tests will be explained first.

Yield Stress:

Yield stress is normally defined through stress (σ) - strain (ε) curves in tensile tests. A typical σ-ε curve for a ductile plastics is shown in Figure 6.2, where engineering stress is used. A linear relationship between σ and ε can continue up to a limited longitudinal extension, then deviations from the linearity will occur. This non-linear behaviour will be accelerated as stress further increases until a point where an increase in strain will not be followed by an increase in stress. After that, a sudden drop in stress normally occurs because of localized reduction in cross-section. This is known as 'necking'. Continuing increases in strain will not lead to further increases in stress, as new material will be drawn from the 'shoulder' of the 'neck' to develop the reduced cross-section. This process is known as 'cold-drawing'. Tensile yield stress σ_y is normally defined at the point where $d\sigma/d\varepsilon = 0$, i.e. the first point where $\sigma_y=\sigma_{max}$ on the σ-ε curve.

However, as shown in Figure 6.1, no maximum stress exists on the σ-ε curve for the modified Modar resin. Neither 'necking' nor 'cold-drawing' has ever appeared in the tensile tests for all the materials investigated in this research. Except for linearity in the initial part of σ-ε curve, the relationship between σ and ε changes simply from a higher to a lower slope. No well-defined yield stress as that discussed above can be obtained.

For this type of σ-ε relationship, there are two ways which may be used to obtain yield stress. In the first method, it takes the stress at the 'knee' on the curve as the yield stress (McCrum 1988). Alternatively, an offset procedure can be used to define yield stress (Ward 1983). For the later case, draw an initial slope on σ-ε curve then draw another line parallel to the slope by offsetting a specified strain, say 0.2% (which is suggested in tensile tests for metals). At the intersection of the second line with σ-ε curve is offset stress, which is considered to be yield stress.

The yield stresses of the materials investigated in this research were obtained based on these two ideas. This was achieved by choosing different offset strains and following the offset procedure mentioned above to find the one of offset strains which could give rise to an offset stress approximately on the 'knee' of σ-ε curve. In Figure 6.1, two lines with offset strains 0.2% and 0.5% were drawn. It appears that the offset strain 0.5% gives an offset stress approximately on the 'knee'. The offset stress defined by 0.2% offset strain appears to be a little bit smaller. Therefore, the offset stress defined by 0.5% offset strain is taken as yield stress in this thesis.

Modulus:

In order to get a reasonable elastic modulus E, all the values are obtained using the method of linear regression at strains between 0.1% and 0.5%. Within this region, a reasonable linear relationship between σ and ε can be guaranteed.

Poisson's Ratio:

Poisson's ratios (ν) were obtained by calculating each Poisson's ratios at longitudinal strains between 0.2 % and 1 % then taking the average of all of them as one Poisson's ratio for one specimen as shown in Figure 6.3. This is because ν can keep fairly constant for the chosen strains. At least 3 specimens were used for each test and the average of all the values measured was taken as one Poisson's ratio for one material.

Volume Strain:

Volume strains were calculated according to the following equation (Bucknall 1977):

$$\frac{\Delta V}{V} = (1+\epsilon_l)(1-\epsilon_t)^2 - 1 \qquad (6.1)$$

where ε_t and ε_l are transverse and longitudinal strains. One hypothesis is made here that the transverse strains in direction 2 and 3 (Figure 6.1) are equal. The volume strain calculated from Equation 6.1 is the total strain which includes all contributions from both elastic and non-elastic volume change (Further discussions will follow in Section 6.3).

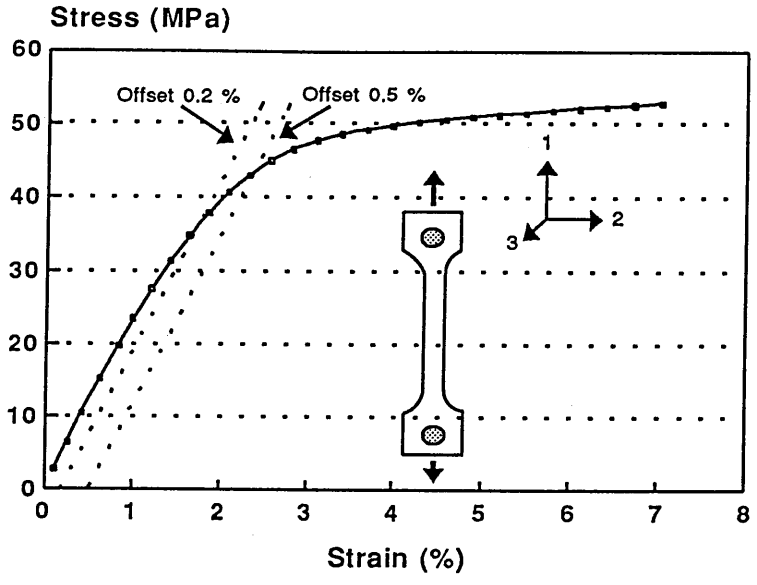

Figure 6.1 A Typical curve of stress against strain of one modified Modar 8035 resin.

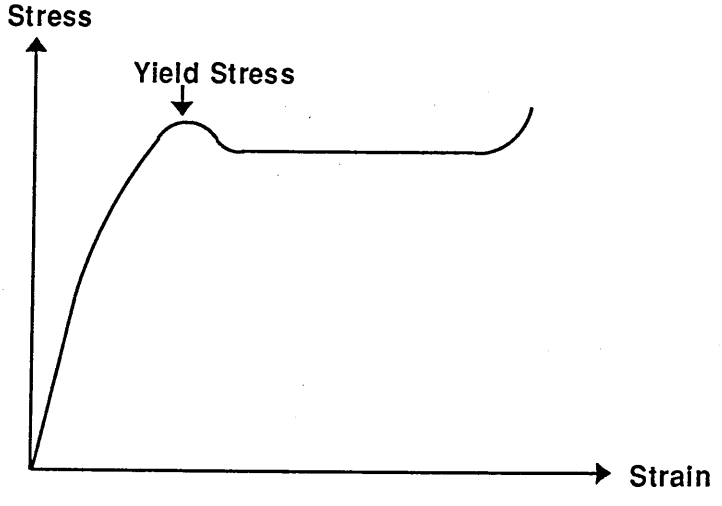

Figure 6.2 A typical curve of stress against strain of ductile plastics.

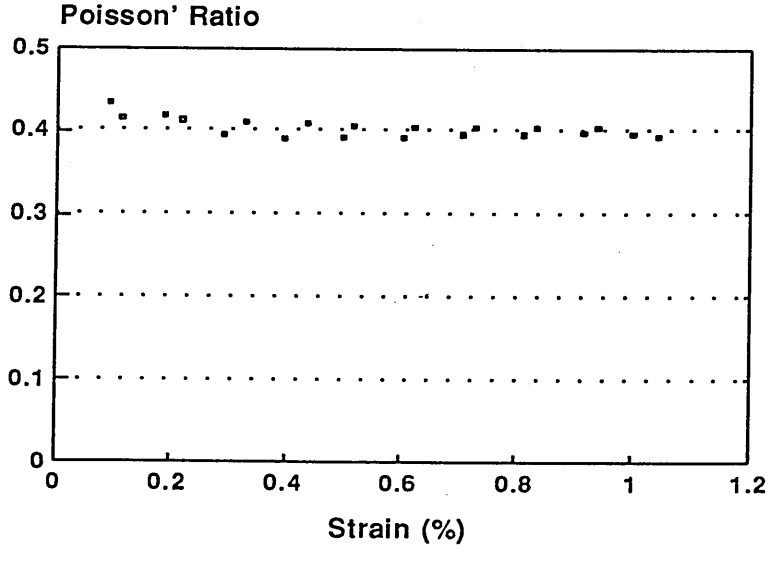

Figure 6.3 Poisson's ratio as function of strain of one modified Modar 8035 resin.

F002&5

6.2 Experimental Results

Experimental results covered in this chapter only concern the materials toughened by rubber Paraloid BTA 753 and the hybrid materials based on this rubber toughened material.

6.2.1 Modulus and yield stress

Tables 6.1 and 6.2 collect the basic mechanical properties of the materials investigated in this research, including modulus E, yield stress σ_y and Poisson's ratio, which will be used in this and the following chapters. The data in these two tables were measured at crosshead speed 0.5 mm min^{-1}. The specimens were left in an open laboratory at temperature 23°C for several months before testing. They are termed 'normal' specimens, comparing to those which were either fully dried or water saturated in this thesis.

The basic trends in the influence of additives on modulus and yield stress are shown in Figures 6.4 and 6.5. The rubber used effectively reduces yield stress and modulus of Modar 8035 resin while the filler silica XPF6 increases these two properties. For the former, modulus decreases from 3.24 to 2.33 GPa (Figure 6.4a) and yield stress falls from 62.6 down to 42.1 MPa (Figure 6.5a) after incorporation of 15 wt % rubber.

Contrary to the effect of rubber, filler increases both the modulus and the yield stress on the basis of the matrix toughened by 15 wt % rubber. Modulus more than doubles at the

Table 6.1 Mechanical properties of Paraloid BTA 753 toughened Modar 8035 resins

Materials	Modulus E (GPa)	Yield Stress σ_y (MPa)	Poisson Ratio ν
T00F00	3.24	62.6	0.34
T05F00	3.01	53.4	0.36
T10F00	2.62	46.7	0.38
T15F00	2.33	41.2	0.40

Data scatter: $E < \pm 0.06$ GPa; $\sigma_y < \pm 1$ MPa; $\nu < \pm 0.02$

Table 6.2 Mechanical properties of hybridized composites - Paraloid BTA 753/Silica XPF6/Modar 8035 resin

Materials	Modulus E (GPa)	Yield Stress σ_y (MPa)	Poisson Ratio ν
T15F00	2.33	41.2	0.40
T15F10	2.67	43.4	0.38
T15F20	3.03	44.7	0.37
T15F30	3.59	48.0	0.35
T15F40	4.10	49.4	0.34
T15F46	4.85	52.2	0.33
T00F50*	7.85	> 83.9	-

Data scatter: $E < \pm 0.06$ GPa; $\sigma_y < \pm 1$ MPa; $\nu < \pm 0.02$

* untoughened matrix with 50/50 Silica XPF6 to Modar 8035; 83.9 MPa is the stress at break as no intersection occurred by the procedure of offset strain 0.5%.

concentration 46 wt % of filler comparing to the modulus of the matrix, from 2.33 GPa to 4.85 GPa (Figure 6.4b). Yield stress increases from 41.2 to 52.2 MPa at the same time (Figure 6.5b).

In addition to the influence of additives, deformation rate also affects these two properties. Table 6.3 and Figure 6.6 are the results obtained at strain rates covering from 0.00013 to 0.23 s^{-1}. Three materials Modar 8035 resin T00F00, the rubber toughened T15F00 and the hybrid composite T15F46 were selected for the study. In order to get rid of the influence of moisture, all the specimens were fully dried under vacuum at 65°C for more than 4 days before testing. After that, they were gradually cooled down then kept in a desiccator at 23°C. Specimens made through this process are termed 'dry' ones.

It can be seen that reasonable linear relationships between logarithm strain rate ($\log\dot{\varepsilon}$) and modulus (E) and yield stress (σ_{yield}) have been obtained (Figure 6.6) for all the materials investigated. Both modulus and yield stress increase with increasing strain rate.

Table 6.3 The influence of strain rate on modulus and yield stress for Modar 8035 resin and the modified composites

$\dot{\varepsilon}$ (sec^{-1})	E (GPa)			σ_y (MPa)		
	T00F00	T10F00	T15F46	T00F00	T15F00	T15F46
0.00013	3.38	-	-	56.1	-	-
0.00032	3.48	2.33	4.62	58.1	38.0	46.2
0.0010	3.49	2.53	4.90	61.7	41.8	48.6
0.0032	3.65	2.54	4.92	65.8	44.9	50.4
0.010	3.71	2.62	5.03	69.0	46.5	52.2
0.032	-	2.70	5.33	-	49.4	55.0
0.10	-	2.77	5.38	-	51.9	57.9
0.23	-	2.94	5.55	-	54.4	59.5

Moisture also has an influence on these two properties for the same materials. Tensile specimens were left in distilled water at 100°C for 4 days then gradually cooled down and kept in distilled water at 23°C over 24 hours. Specimens made through this procedure are termed 'water saturated' ones in this thesis. The saturated concentrations of water measured at 100°C have been collected in a previous chapter (Table 5.1 in Chapter 5). They are 3.2 wt % for the materials T00F00 and T15F00 and 1.8 wt % for T15F46. After that, the edge of each specimen was sealed to stop water escaping from it, with the two faces of the specimen left open in order to achieve one dimensional desorption conditions. All the sealed specimens were placed in a desiccator and buried in dried silica gel at 23°C. Tensile tests were conducted at crosshead speed 0.5 mm min^{-1} at different intervals of time during the experiment.

Moisture concentrations M_t/M_s and the corresponding modulus and yield stress are collected in Tables 6.4 and 6.5. M_t/M_s was calculated according to Equation (5.5b) in Chapter 5, where diffusion coefficient of water desorption was assumed equal to that of absorption measured at 23°C and all the other data used in the calculation are also collected in Table 6.4.

The influence of desorption time of water on modulus and yield stress is shown in Figure 6.7.

The corresponding moisture contents are in Table 6.4. It appears that both modulus and yield stress increase with the time of desorption until day 43 when the moisture concentrations M_t/M_s are below 0.22 for T00F00 and T15F00 and 0.33 for T15F46. Considering M_s is 3.2 wt % for the former two and 1.8 wt % for the latter, the corresponding water concentrations M_t are 0.7 wt % and 0.6 wt %.

Table 6.4 Moisture concentration M_t/M_s and the time of water desorption of Modar 8035 resin and the modified composites

Materials	$2l^+$ (mm)	D^* ($\mu m^2\ s^{-1}$)	Time Days				
			0	8	43	72	∞
T00F00	2.47	0.21	1	0.65	0.22	0.10	0
T15F00	2.52	0.22	1	0.65	0.22	0.13	0
T15F46	2.70	0.18	1	0.71	0.33	0.17	0

+ 2l is specimen thickness.

* D is diffusion coefficient which was assumed to have the same value as that of absorption measured at 23°C (Table 5.1, Chapter 5).

Table 6.5 The influence of time of water desorption (moisture contents in Table 6.4) on modulus and yield stress for Modar 8035 resin and the modified composites

Time (Days)	E (GPa)			σ_y (MPa)		
	T00F00	T10F00	T15F46	T00F00	T15F00	T15F46
0	3.08	2.20	4.34	55.6	36.7	47.1
8	3.27	2.22	4.44	61.9	40.5	48.7
43	3.56	2.50	4.86	66.9	44.5	52.2
72	3.54	2.52	4.85	68.6	44.9	52.2
∞*	3.57	-	4.93	71.2	-	54.5

* Water saturated specimens were dried at full vacuum at 65°C for more than 7 days and the measured E and σ_y are taken as the data corresponding to infinite desorption time.

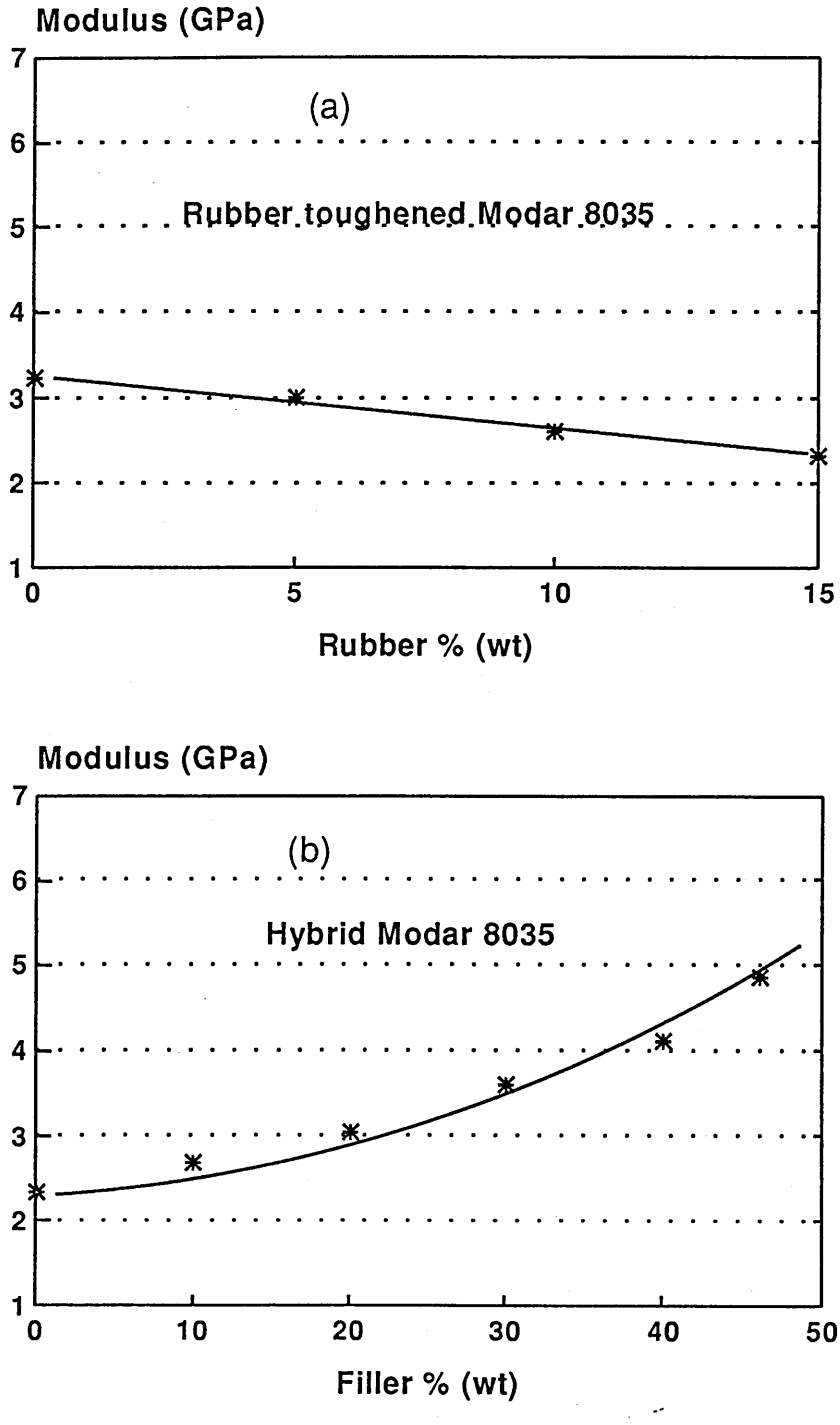

Figure 6.4 The influence of additives on modulus of modified Modar 8035 resins: (a) rubber toughened; (b) the hybrid composites all with 15 wt % rubber in the Modar matrix (23°C).

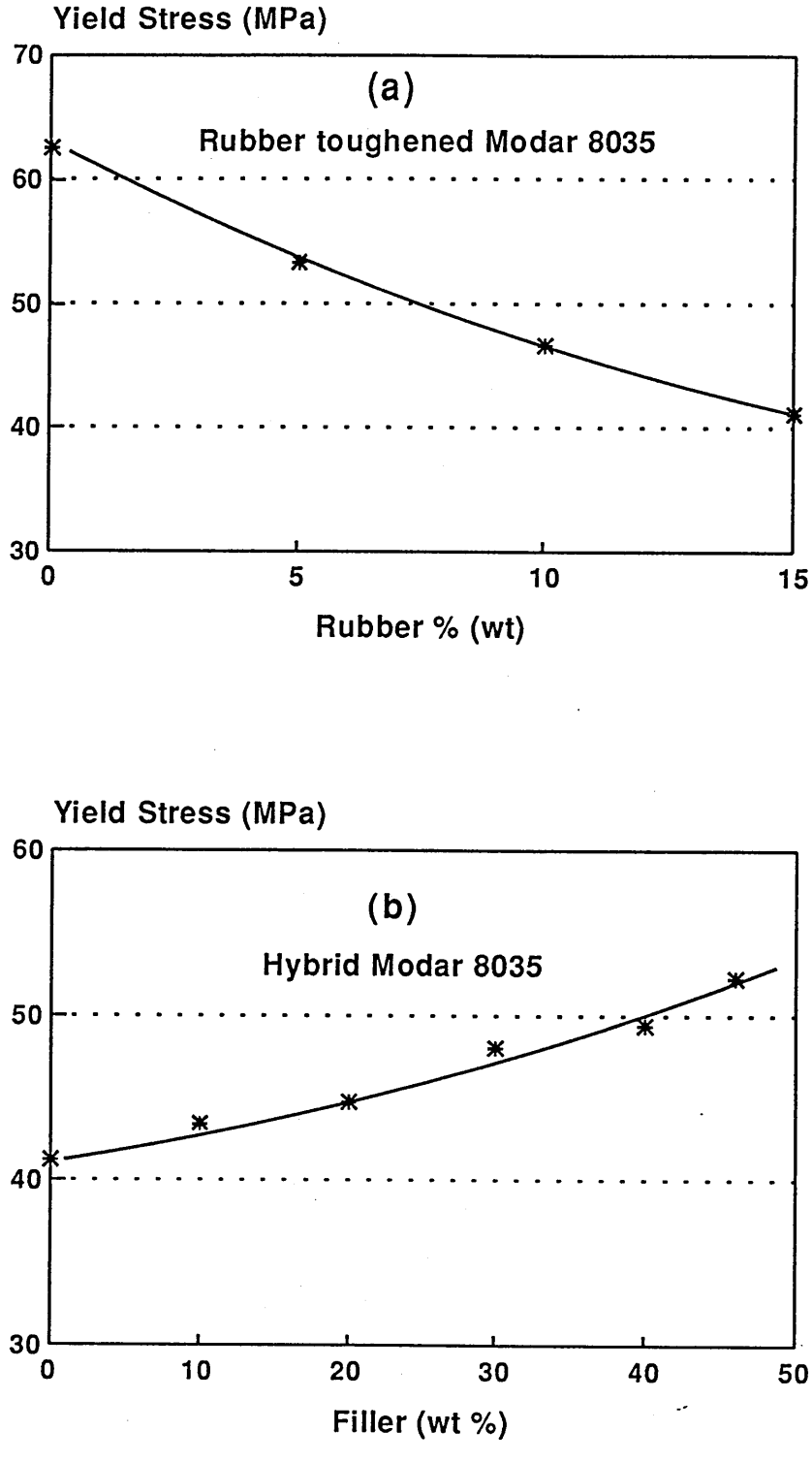

Figure 6.5 The influence of additives on yield stress of modified Modar 8035: (a) rubber toughened; (b) the hybrid composites all with 15 wt % rubber in the Modar matrix (23°C).

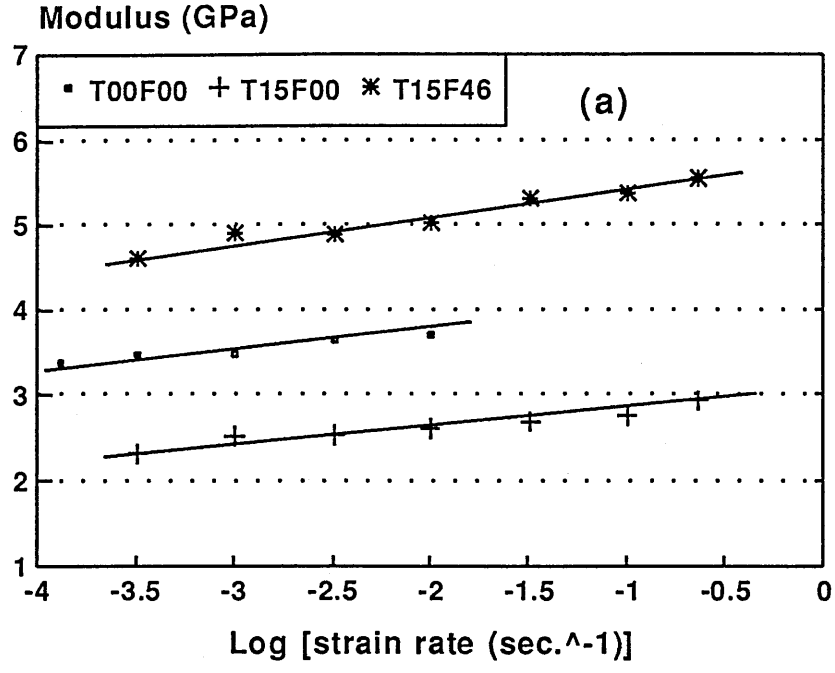

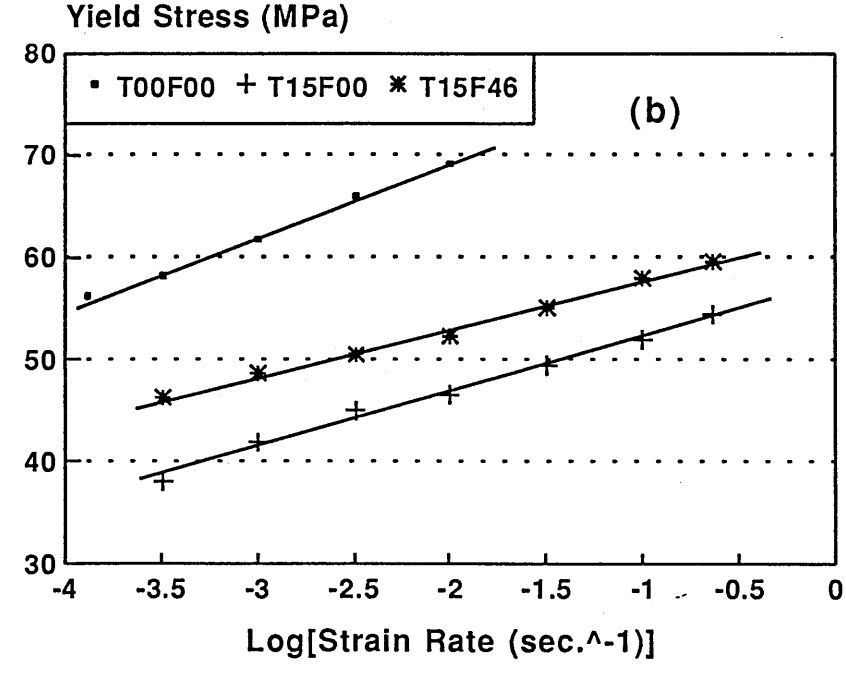

Figure 6.6 The influence of strain rate on (a) modulus and (b) yield stress (23°C).

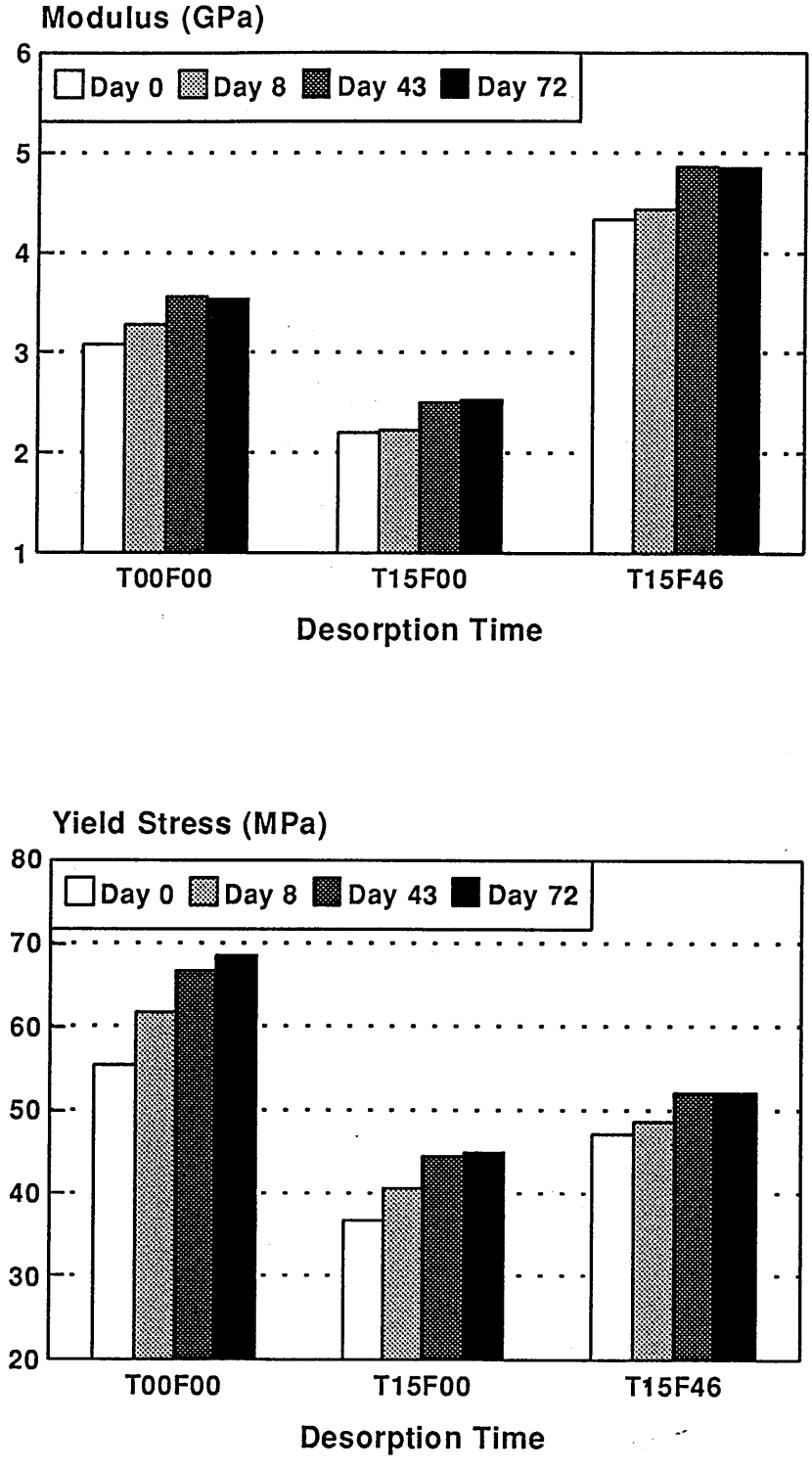

Figure 6.7 The influence of water desorption time on modulus (top) and yield stress (bottom).

It appears that there are no significant changes in either modulus or yield stress below these levels of moisture content although a little increase in modulus and yield stress has been obtained for materials which were dried under full vacuum at 65°C for more than 7 days (Table 6.5). After this process, modulus increased from 3.54 to 3.57 GPa and from 4.85 to 4.93 GPa and yield stress increased from 68.6 to 71.2 MPa and from 52.2 to 54.5 MPa for materials T00F00 and T15F46 repectively.

It is understood that water distribution within a specimen was not uniform, varying with the time during water desorption. Further discussions on the subject will follow in Section 6.3.

6.2.2 Volume change - elongation

Volume changes $\Delta V/V$ during tensile testing are shown in Figure 6.8, where $\Delta V/V$ was calculated according to Equation 6.1. Plot (a) is for the materials toughened with Paraloid BTA 753 rubber and (b) the hybrid composites. It can be seen that volume increases with increasing longitudinal strain for both systems. It appears that incorporation of rubber particles delays the process of material dilatation while filler accelerates it. The possible mechanisms involved in the process will be discussed in Sections 6.3 and 8.3.

6.2.3 Thermomechanical properties

Typical thermodynamic spectra are shown in Figures 6.9 and 6.10. Glass transition temperature T_g is defined as that shown in these two figures. The temperature corresponding to the peak point in tanδ in DMTA tests is taken as T_g and the middle point between onset and ending points of glass transition in DSC tests is regard as T_g. The results are collected in Tables 6.6 and 6.7 and Figure 6.11.

It can be seen that the glass transition temperature T_g of the dispersed rubber phase keeps constant for all compositions. It is about -72°C. However, the T_g of matrix increases unexpectedly with increasing rubber concentration. About 4°C increment has been found after incorporation of 15 wt % rubber (Table 6.7 and Figure 6.11). The reason for the increase is not very clear. It may caused by a slight increase in cross-link density because part of the monomer methyl methacrylate may be absorbed by rubber particles, which will produce a resin with a little higher cross-link density. More likely it may caused by removal of low molecular weight impurities (monomer etc.) from the cured matrix into rubber phase, which will also raise the glass transition temperature.

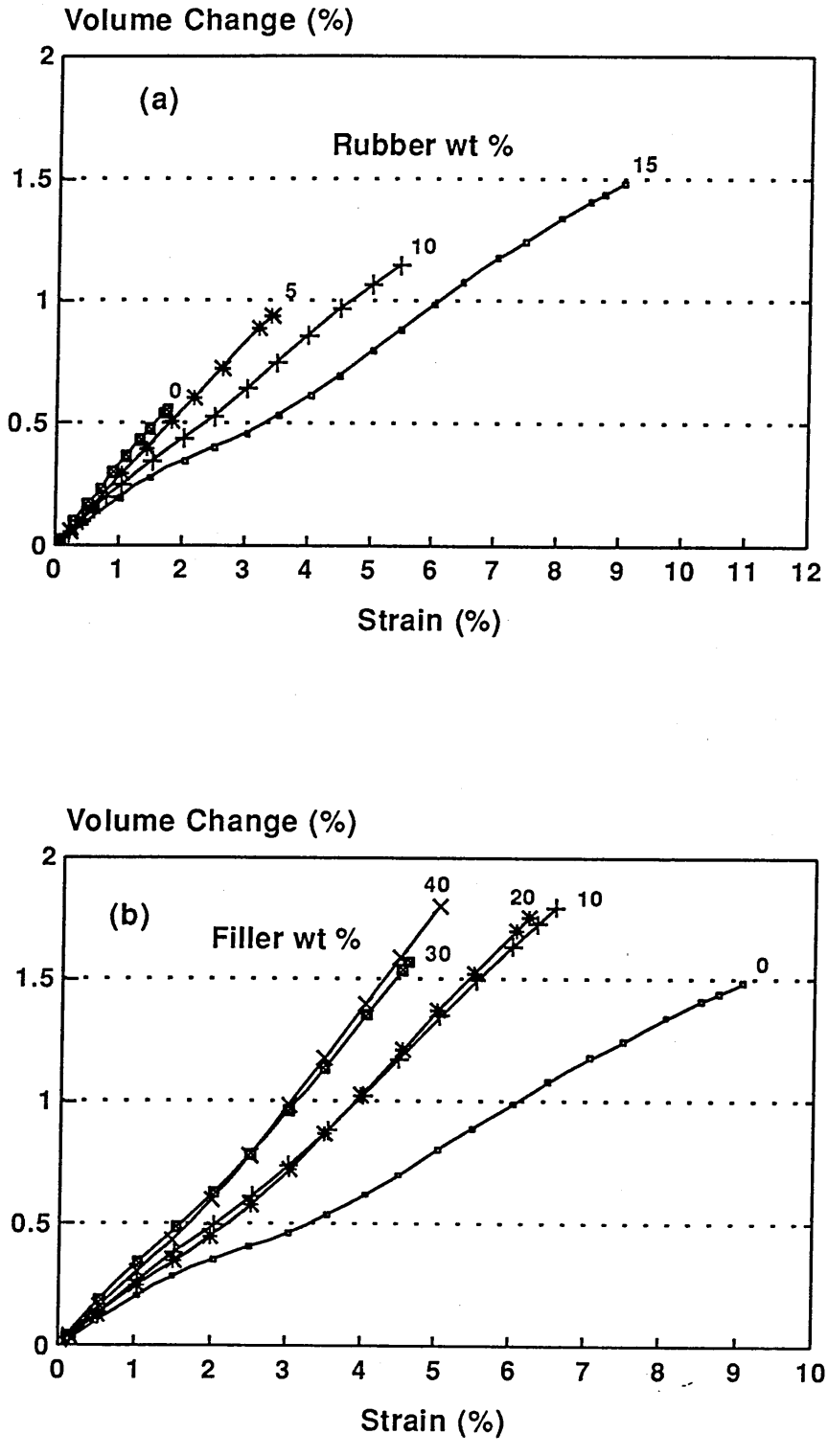

Figure 6.8 The influence of additives on volume deformation of modified Modar 8035: rubber toughened (top) and the hybrid composites all with 15 wt % rubber in the Modar matrix (bottom) (23°C).

Table 6.6 Glass transition temperature T_g of Modar 8035 and rubbers Paraloid BTA 753 and XC 37

Materials	DMTA (°C)	DSC (°C)
XC 37	-	-13
Paraloid BTA 753	-	-74
Modar 8035	151	145

Note: DSC data of XC 37 and Paraloid BTA 753 were provided by ICI measured at 10°C/min.

Table 6.7 Glass transition temperature T_g of matrix Modar 8035 and dispersed rubber phase Paraloid BTA 753 (DMTA)

Materials	T_g of Matrix (°C)	T_g of Rubber (°C)
T00F00	151	-
T05F00	153	-72
T10F00	154	-72
T15F00	155	-72

Note 1: T_g of matrix was measured at 10 Hz using thick specimen (about 2.5 mm thick); T_g of Paraloid BTA 753 measured at 1 Hz using thin specimen (about 1.5 mm thick).
Note 2: error $T_g < \pm$ 1°C.

Deformation rate will affect relaxation of glassy polymers. The glass transition shown in Figure 6.9 is normally termed α transition, which is a function of deformation rate. From the α peak is the T_g estimated here. So the T_g is also a function of the rate. This is shown in Table 6.8 and Figure 6.12 for three typical materials: Modar 8035 T00F00, the rubber toughened T15F00, and the hybrid composite T15F46. About a 20°C increment has been observed when deformation rate in terms of testing frequency changes from 0.1 Hz up to 30 Hz.

The glass transition can be expressed by Arrhenius equation:

$$\tau = \frac{1}{f} = Ae^{\frac{E}{RT_g}} \tag{6.2a}$$

$$Log\tau = Log(\frac{1}{f}) = LogA + \frac{E}{2.303R}\frac{1}{T_g} \tag{6.2b}$$

where τ is relaxation time, f frequency, E_a activation energy and R gas constant. A linear relationship between logτ and T_g^{-1} should be obtained if the hypothesis is correct.

Table 6.8 The influence of deformation rate on glass transition T_g (°C) of unmodified and modified Modar 8035 (DMTA)

Materials	Frequency (Hz)				E^* (kJ mol^{-1})
	0.1	1	10	30	
T00F00	134	142	151	156	370.8
T15F00	139	147	155	159	407.4
T15F46	141	148	155	160	449.7

* E is activation energy of glass transition

Figure 6.13 is the plot made according to Equation 6.2b. Good linear relationships do exist between log(1/f) and T_g^{-1} for the materials mentioned above. Activation energies E_a were calculated from the slopes and are collected in Table 6.8.

It was found that rubber and filler additives have a slight influence on the relaxation of matrix Modar 8035. This is reflected in the change of activation energy after incorporation of the additives. The activation energy E_a is 370.8 kJ mol^{-1} for pure Modar 8035 resin but 407.4 and 449.7 kJ mol^{-1} for the rubber toughened T15F00 and the hybrid composite T15F46 respectively.

Moisture has a strong influence on glass transition temperature T_g too. Table 6.9 gives the results obtained from DMTA tests for the materials in terms of normal, water-saturated and re-dried specimens. The specimens saturated by water were prepared as follows. They were

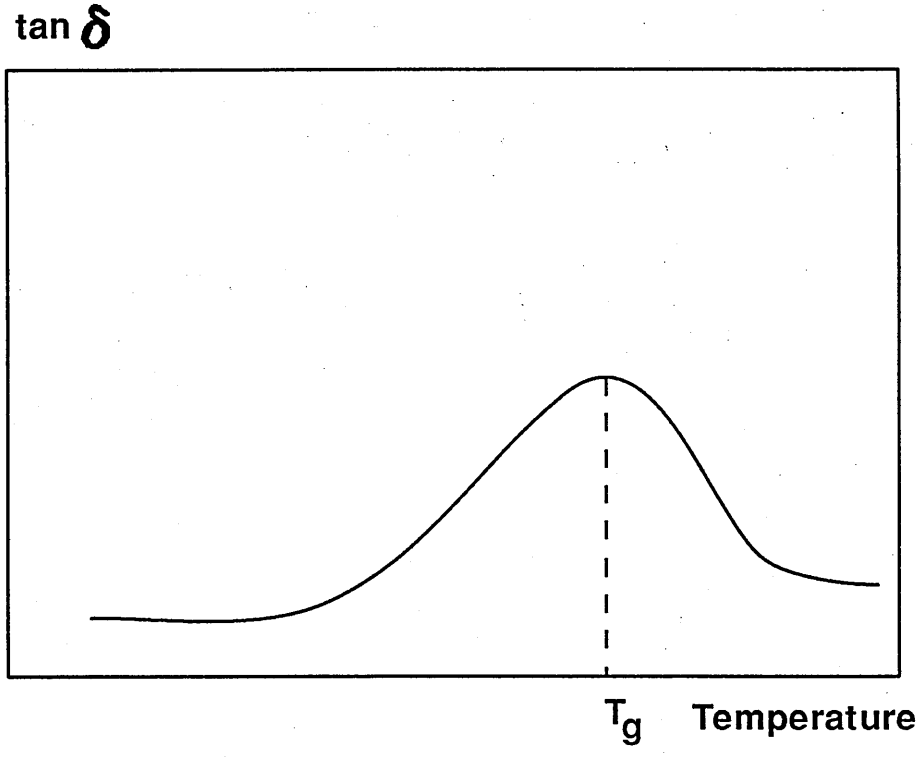

Figure 6.9 Schematic diagram of DMTA spectrum: temperature against tanδ.

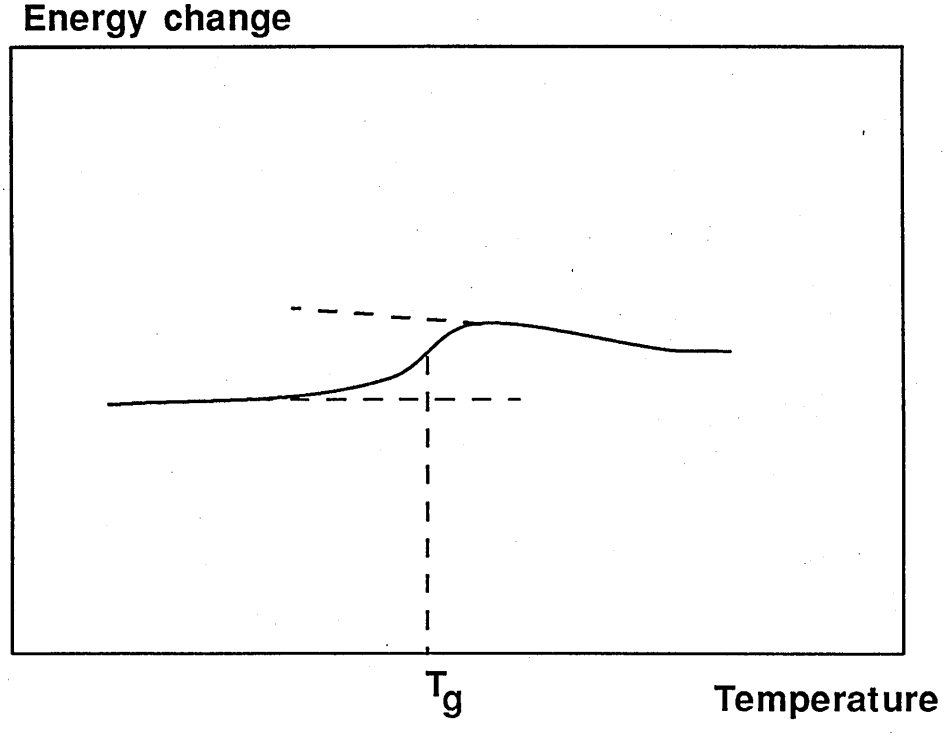

Figure 6.10 Schematic diagram of DSC spectrum: temperature against energy change.

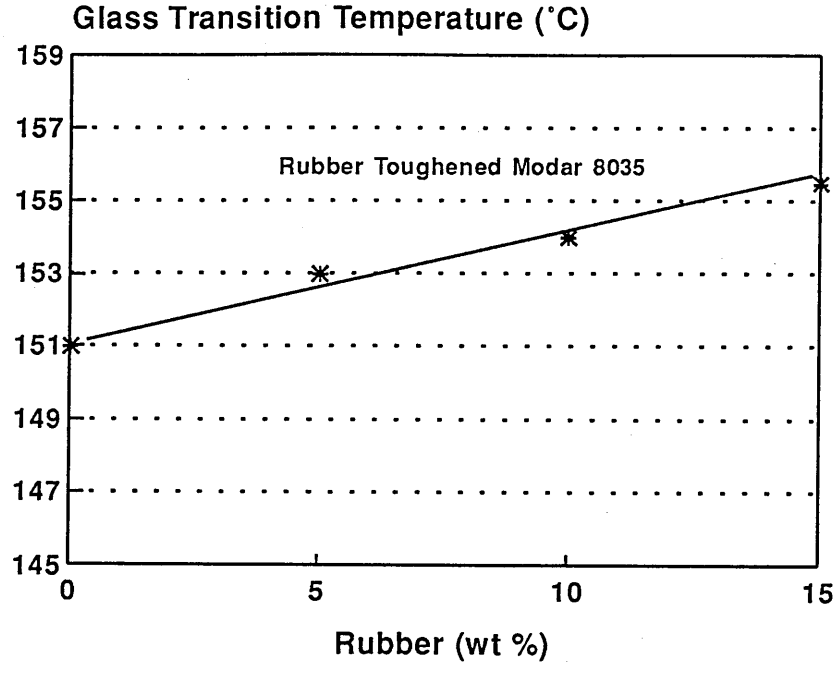

Figure 6.11 The influence of rubber on glass transition temperature of Modar 8035 resin

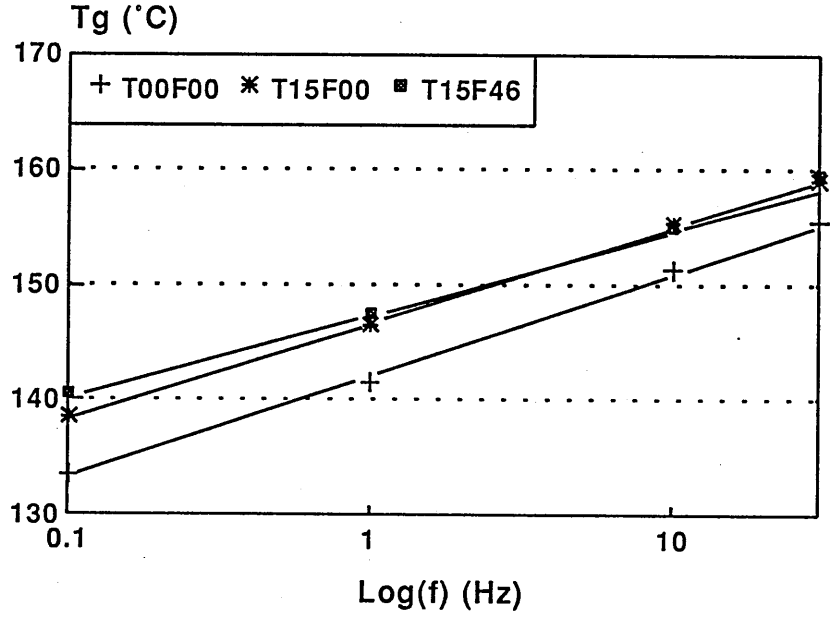

: f: frequency

Figure 6.12 The dependence of glass transition temperature on loading frequency of Modar 8035 resin and the modified composites.

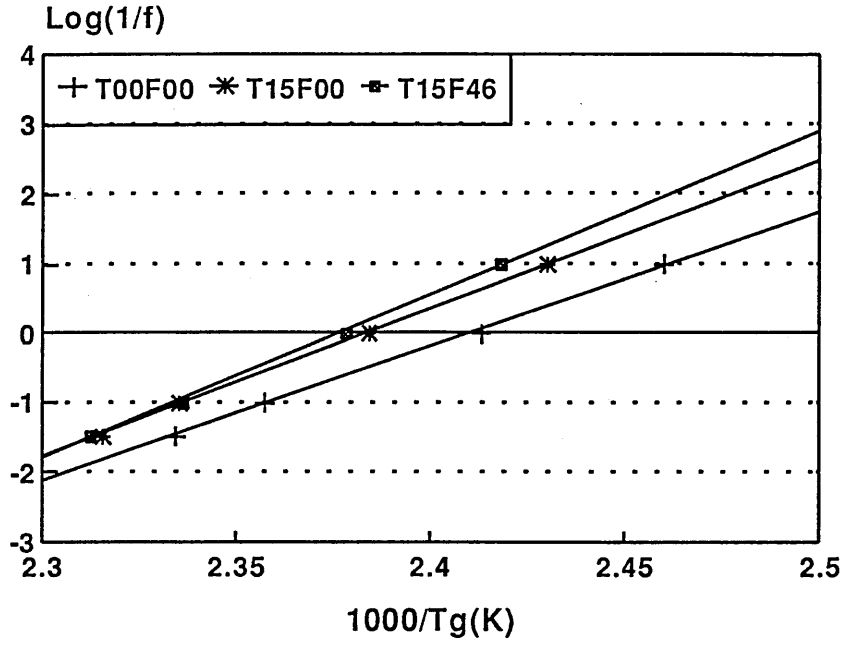

f: frequency (Hz)

Figure 6.13 Arrhenius equation fitted to experimental data on glass transition temperature Tg and loading frequency f.

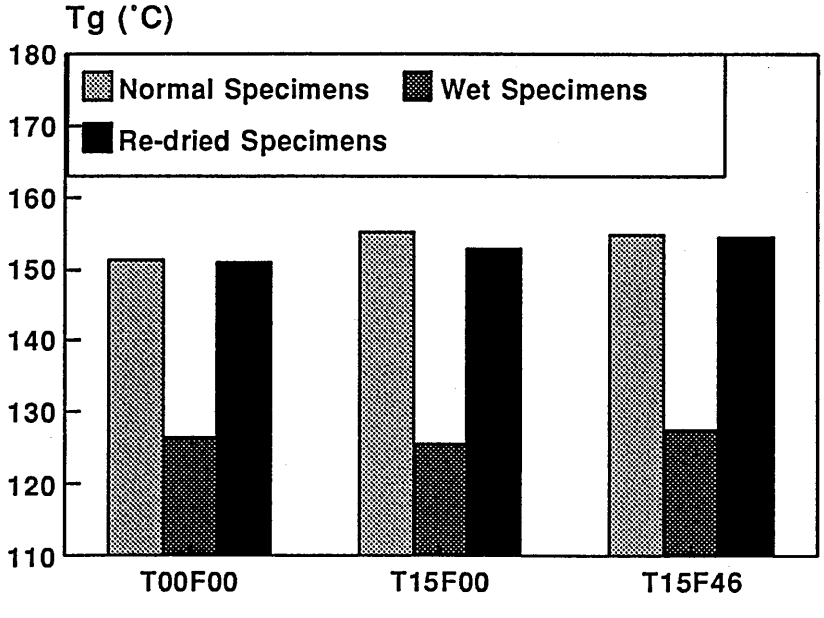

DMTA: 3 C / min, 10 Hz

Figure 6.14 The influence of moisture on glass transition temperature Tg of Modar 8035 resin and the modified composites.

kept in distilled water at 100°C for 20 days then left to stand in distilled water at 23°C for about one year. After that, they were either tested, as wet specimens, in the way mentioned in Chapter 4 or re-dried under full vacuum at 65°C for about 7 days then tested in the normal way as re-dried specimens. Comparison of T_g of normal specimens with that of water saturated and re-dried specimens are made in Figure 6.14. It is clearly shown that T_g has reduced by 25 to 30°C in the presence of water and that this is a reversible process. T_g can recover almost completely if water has been driven out of the materials.

Table 6.9 The inflence of moisture on glass transition temperature T_g(°C) (DMTA at 10 Hz)

Materials	T00F00	T15F00	T15F46
(a) Normal specimen	151	155	155
(b) Water saturated	127	125	128
(c) Re-dried after (b)	151	153	155

6.3 Discussions

6.3.1 Elasticity and yielding

As discussed previously, both modulus E and yield stress σ_{yield} are dependent on deformation rate (Table 6.3). Good linear relationships between these two properties and logarithm strain rate have been well demonstrated for materials Modar 8035 resin T00F00, the rubber toughened resin T15F00 and the hybrid composite T15F46 (Figure 6.6). These relationships can be, in general, expressed by the following equations:

$$E(GPa) = A_E + B_E Log\dot{\varepsilon} \tag{6.3}$$

$$\sigma_{yield}(MPa) = A_\sigma + B_\sigma Log\dot{\varepsilon} \tag{6.4}$$

where A_E and A_σ are constants and B_E and B_σ slopes, which are obtained by the method of linear regression and listed in Table 6.10. The unit of strain rate is $second^{-1}$

Elasticity

As discussed before, the modulus, which was obtained by the method of linear regression at strains between 0.1 % and 0.5 %, was assumed to stand for an elastic property. However, it is not quite true for the materials studied. This is reflected on the relationships of E and logarithm $\dot{\varepsilon}$. Modulus increases with increasing strain rate (Figure 6.6). So viscoelasticity still plays a role even at low strains, say below 0.5 %, although this influence is not so pronouced as that on the yield stress.

Table 6.10 Constants in equations (6.3) and (6.4)

Materials	A_E	A_σ	B_E	B_σ
T00F00	4.05	83.2	0.17	7.08
T15F00	2.99	57.2	0.18	5.26
T15F46	5.70	61.8	0.30	4.51

Note: The units used in Equations (6.3) and (6.4) are in GPa for modulus, in MPa for yield stress and in $second^{-1}$ for strain rate.

Yielding

Deformation rate has a strong influence on the yield behaviour of the materials investigated. This is reflected in the slope relating yield stress σ_{yiled} to logarithm strain rate $\log\dot{\varepsilon}$ as expressed by Equation 6.3. Yield stress increases with increasing strain rate. The dependence of σ_{yield} on $\log\dot{\varepsilon}$ is in the order T00F00 > T15F00 > T15F46. The slopes are 7.08, 5.26 and 4.51 MPa for the corresponding materials (Table 6.10). In order to reveal the underlying mechanisms, the yielding behaviour will be discussed with reference to the theories discussed in Chapter 2.

6.3.2 Comparison with yielding theories

Three theories have been introduced in Chapter 2. They are the Eyring, Argon and Chow theories. They are summarized in Equations (2.41), (2.47) and (2.52) respectively. In this section, it will first be considered whether they agree with the experimetal results obtained

in this research. Then discussions will follow on the meanings of some parameters relating to each of the corresponding theories in order to have a better understanding on yielding mechanisms.

It is obvious that Equations (2.41) of Eyring and (2.52) of Chow should give rise to a straight line if a plot is made of yield stress σ_{yield} against logarithm strain rate log$\dot{\varepsilon}$ for a given material at a given temperature. This is just what has been shown in Figure 6.6, where three straight lines were drawn with reference to experimental data. The general trend has been expressed by Equation (6.4) for the materials T00F00, T15F00 and T15F46.

However, it is not clear whether Equation (2.47) of Argon will give rise to a straight line using the same data as that of Figure 6.6. In order to make the equation applicable, some parameters should be changed first. Tensile yield stress σ_{yield} and tensile strain rate $\dot{\varepsilon}$ should be changed to shear yield stress σ_{sy} and shear strain rate $\dot{\gamma}$. In addition, shear modulus which appears in the equation should also be provided, which can be obtained from Young's modulus. All these properties are related by the following equations:

$$\sigma_{yield}=\sqrt{3}\sigma_{sy} \qquad \text{(Eq. 2.39)}$$

$$E=2(1+\nu)\mu \qquad (6.5)$$

$$\dot{\epsilon}_y=\frac{4}{\sqrt{3}}\dot{\gamma}_y \qquad (6.6)$$

Equation (6.6) is derived from the Levy-Mises equation:

$$\frac{d\epsilon_{11}}{\sigma'_{11}}=\frac{d\epsilon_{11}}{\sigma_{11}-\sigma_m}=\frac{d\epsilon_{12}}{\sigma_{12}} \qquad (6.7)$$

where σ_m is hydrostatic stress.

For uniaxial tension, $\sigma_m=\frac{1}{3}\sigma_{11}$. Equation (6.7) becomes:

$$\frac{d\epsilon_{11}}{\frac{2}{3}\sigma_{11}}=\frac{d\epsilon_{12}}{\sigma_{12}} \qquad (6.8)$$

$$\frac{\frac{d\epsilon_{11}}{dt}}{\frac{2}{3}\sigma_{11}} = \frac{\frac{d\epsilon_{12}}{dt}}{\sigma_{12}} = \frac{2\frac{d\gamma_{12}}{dt}}{\sigma_{12}} \tag{6.9}$$

Using σ_{yield} instead of σ_{11} and σ_{sy} instead of σ_{12}, Equation (6.9) becomes:

$$\frac{\dot{\epsilon}_y}{\frac{2}{3}\sigma_{yield}} = \frac{2\dot{\gamma}_y}{\sigma_{sy}} \tag{6.10}$$

where $\dot{\epsilon}_y$ is tensile strain rate and γ_y shear strain rate. Substituting $\sigma_{yield} = 3^{½}\sigma_{sy}$ into Equation (6.10) gives Equation (6.6).

It is emphasized that, because Argon's analysis is based on an elastic field of atomic dimensions, all the above equations are assumed applicable as approximations.

The data on shear strain rate γ, shear modulus μ and shear stress σ_{sy} are collected in Table 6.11, having been transformed from Table 6.3 according to the equations above. Figure 6.15 is the plot drawn according to Equation (2.47) of Argon using the data in Table 6.11. It can be seen that reasonable straight lines have been obtained for all three materials T00F00, T15F00 and T15F46. The general trend can be expressed by the following equation:

$$\left(\frac{\sigma_{sy}}{\mu}\right)^{\frac{5}{6}} = A_{Argon} + B_{Argon}\frac{1}{\mu}Log\left(\frac{\dot{\gamma}}{\dot{\gamma}_0}\right) \tag{6.11}$$

where A_{Argon} is constant and B_{Argon} the slope, which are listed in Table 6.12. $\dot{\gamma}_0 = 1x10^{13}$ was used in the calculation. It was found that $\dot{\gamma}_0$ is in the order about 10^{13} s^{-1}, which is applicable for most thermoplastics (Argon 1973, 1977). The same figure was also used for thermosets and their composites (Yamini 1980, Young 1986). The dependence of shear stress divided by shear modulus, raised to power (5/6), on logarithm shear strain rate divided by shear modulus is in the order T00F00 > T15F00 > T15F46 as shown in Figure 6.15. The slopes are 1.93, 0.91 and 0.69 $x10^{-6}$ N m^{-2} (Table 6.12) for each of the corresponding materials, and can be expressed by:

$$B_{Argon} = \frac{1.45 k_B T (1-\nu)^{\frac{1}{6}}}{\pi \omega^2 a^3} \qquad (6.12)$$

where k_B is Boltzmann constant and the rest of the parameters have the same meanings as defined in Chapter 2.

In general, experimental results agree well with the theories of Eyring, Argon and Chow. Now, it is time to consider each of the three theories separately, then the possible relationships between them will be discussed.

Table 6.11 The influence of strain rate on shear modulus and yield stress for Modar 8035 resin and the modified composites

$\dot{\gamma}$ (s^{-1})	μ (GPa)			σ_{sy} (MPa)		
	T00F00	T10F00	T15F46	T00F00	T15F00	T15F46
0.000056	1.263	-	-	32.4	-	-
0.000138	1.299	0.831	1.735	33.5	21.4	26.7
0.000433	1.301	0.903	1.842	35.6	24.2	28.1
0.00139	1.361	0.908	1.849	38.0	25.9	29.1
0.00433	1.385	0.935	1.892	39.9	26.8	30.1
0.0139	-	0.964	2.002	-	28.5	31.8
0.0433	-	0.989	2.023	-	30.0	33.4
0.0996	-	1.050	2.088	-	31.4	34.3

Table 6.12 The constants in Equation (6.11)

Materials	T00F00	T15F00	T15F46
$A_{Argon} x 10^2$	7.33	6.67	3.72
$B_{Argon} x 10^6$ ($N\ m^{-2}$)	1.93	0.91	0.69

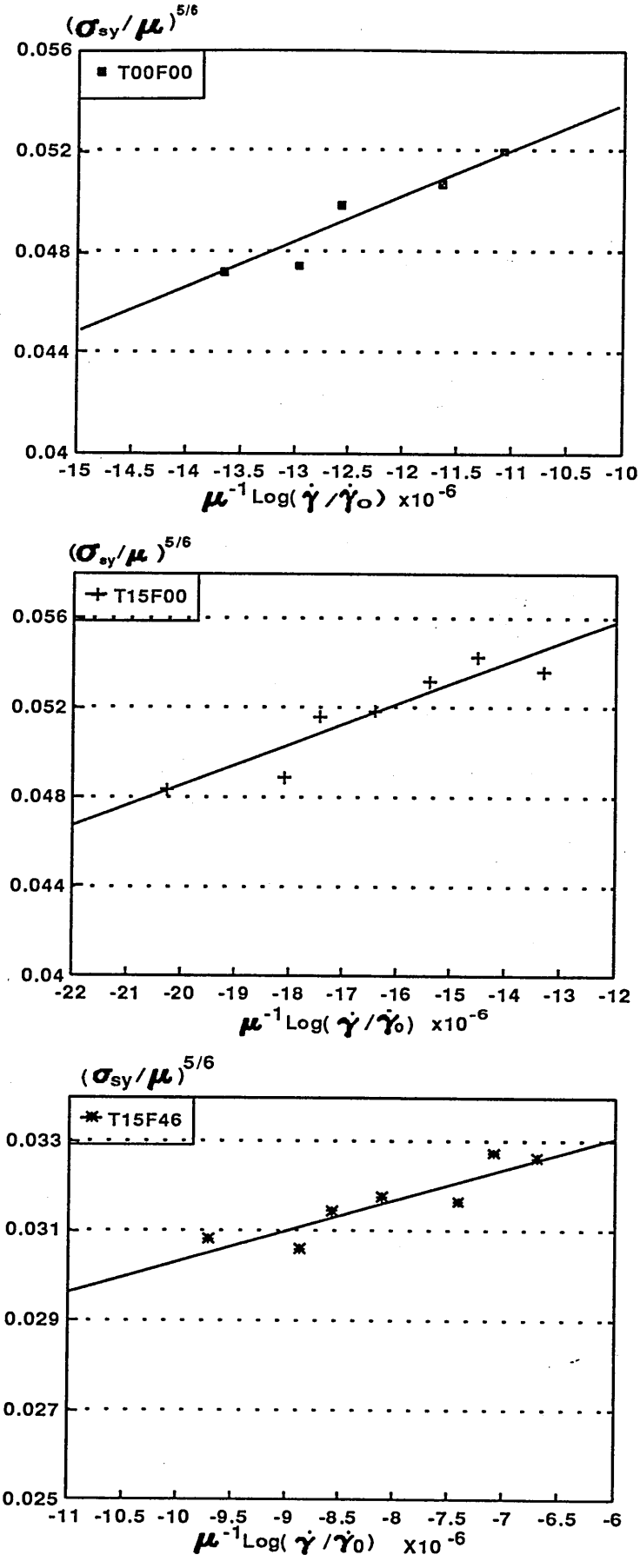

Figure 6.15 Argon equation fitted with experimental data: T00F00 (top); T15F00 (middle); T15F46 (bottom).

Argon's theory

In the theory of Argon, the shear activation volume V^* is not directly reflected in Equation (6.12b). So Argon (1973) defined his V^* from the view point of thermodynamics and assumed that it is equivalent to Eyring's activation volume V^*_{Eyring} (This is not true. Discussions follow later). His V^* is given by:

$$V^*_{Argon}=-\left(\frac{\partial \Delta G^*}{\partial \sigma_{sy}}\right)_{P,T} \tag{6.13}$$

Substituting Equation (2.43) for ΔG^* into Equation (6.13) gives:

$$V^*_{Argon}=1.59\pi\omega^2 a^3\left(\frac{\mu}{\sigma_{sy}(1-\nu)}\right)^{\frac{1}{6}} \tag{6.14}$$

As mentioned in Chapter 2, at absolute zero of temperature 0 K, shear stress depends only on elastic modulus and Poisson's ratio. Through Equation (2.47), it is related by the following Equation:

$$\left(\frac{\mu}{\sigma_{sy}(1-\nu)}\right)^{\frac{1}{6}}=8.5^{\frac{1}{5}} \tag{6.15}$$

Substituting this equation into Equation (6.14) gives:

$$V^*_{0,Argon}=2.45\pi\omega^2 a^3 \tag{6.16}$$

where subscript '0' means at temperature 0 K.

The other important parameters relating to molecule dimensions are 'a', the radius of effective polymer chain, and z^*, the length of the segment. They are expressed by Equation (2.44) (see below). At a temperature of absolute zero, substituting Equation (6.15) into (2.44) gives Equation (6.17) as follows:

$$\left(\frac{z}{a}\right)^*=\left(\frac{45}{8(1-\nu)}\frac{\mu}{\sigma_{sy}}\right)^{1/6} \qquad \text{Equation (2.44)}$$

$$z_0^*=2.05a \tag{6.17}$$

where subscript '0' means at temperature 0 K too. Now, all the parameters involved in

Argon's theory are obtainable through the equations above.

As mentioned in the introduction to Argon's theory (Chapter 2), polymer yielding is considered as a chain alignment process through a series of local rotations along the chain. If the rotating angle ω is taken as the angle fixed by the C-C backbone, it will be $\omega = 109.5°$, i.e. $\omega = 0.61\pi = 1.92$. $\omega \approx 2$ is used in this thesis. The same figure was used by Argon (1973, 1977), Yamini (1980) and Young (1986). In addition, it was found by these authors that 'a' is independent of temperature. z^* was assumed not to change significantly with temperature. The value at the temperature absolute zero (0 K) was chosen as the basis of their discussion. Here, the data on z^* are the values at both 0 K and 296 K (23°C).

Table 6.13 and 6.14 are the results obtained from Argon's theory for materials T00F00, T15F00 and T15F46. $\omega^2 a^3$ is determined from the slope of $(\sigma/\mu)^{5/6}$ against $[\text{Log}(\gamma/\gamma_0)]/\mu$, using Equation (6.12). The parameters 'a' and z^* are related by Equations (2.44) and (6.17), which defines the dimension of the polymer segment (see Figure 2.13, the model for wedge disclination loops), where $\pi a^2 z^*$ is the volume of the unit defined by 'a' and z^*. V^*_{Argon} is the activation volume defined by Equations (6.14) and (6.16).

For a real polymer chain, the length of one monomer unit and the radius of the chain can be estimated if the length and the angles of chemical bonds are known. Consider the material PMMA, which is the main component of Modar 8035 resin used in the research. When the polymer chain is drawn in plan with a syndiotactic configuration, the length of one monomer unit is about 0.23 nm and the radius 0.34 nm[1], which is the maximum radius compared with isotactic and atactic configurations. Compare these two figures with experimental values z^* 1.58 nm, and 'a' 0.61 nm for the unmodified Modar 8035 T00F00 (Table 6.13). It is found that one unit defined by 'a' and z^* contains about 14 monomer units in two polymer segments. This conclusion comes from $z^*/0.23 = 7$, the experimentally measured segment length divided by the length of one monomer unit of PMMA, and $'a'/0.34 = 2$, the measured radius divided by the maximum radius of the polymer chain, here only round numbers are allowed. This result is comparable to the findings of Argon (1977). His conclusion is that z^* (at 0 K) is 1 to 5 times the length of one monomer unit and 'a' is about 1 to 7 times radius of polymer chains for different materials. At 0 K, the z^*_0 is about 5 times of the length of one monomer of PMMA ($z^*_0 = 1.25$, $1.25/0.23 = 5$, the round number). However, this estimate takes only PMMA into account. Other components such as amide groups are also in the network of Modar 8035 resin (See the chemical structure shown in Figure 4.1). So, the conclusions made here are not accurate enough and only taken as approximations.

---

[1] Bond length: C-H 0.109 nm, C-C 0.154 nm; Bond angles: C-C-C 109.5°, C=C-C 122°, C-C-H 109.5°.

Table 6.13 Basic parameters of Argon theory measured from Modar 8035 resin and the modified composites

Materials		T00F00	T15F00	T15F46
ω^2a^3 (nm^3)	-	0.91	1.90	2.55
a (nm)	-	0.61	0.78	0.86
$(z/a)^*$	296 K	2.59	2.63	2.85
$(z/a)^*_0$	0 K	2.05	2.05	2.05
z^* (nm)	296 K	1.58	2.05	2.45
z^*_0 (nm)	0 K	1.25	1.60	1.76
$\pi a^2 z^*$ (nm^3)	296 K	1.85	3.92	5.69
$\pi a^2 z^*_0$ (nm^3)	0 K	1.46	3.05	4.10
V^*_{Argon} (nm^3)	296 K	10.29	21.82	31.76
$V^*_{0,Argon}$ (nm^3)	0 K	6.99	14.58	19.60

Note: (a) The data of $(z/a)^*$ at 296 K is the values corresponding to $\dot{\varepsilon}$ = 0.01 s^{-1} (See Table 14).
(b) $\omega \approx 2$ was assumed (ω = 109.5° = 0.61π)

Table 6.14 The influence of strain rate on Argon's parameter z^* and activation volume V^*_{Argon} for Modar 8035 resin and the modified composites (23°C).

$\dot{\varepsilon}$ (sec^{-1})	z^* (nm^3)			V^*_{Argon} (nm^3)		
	T00F00	T10F00	T15F46	T00F00	T15F00	T15F46
0.00013	1.61	-	-	10.49	-	-
0.00032	1.61	2.08	2.46	10.48	22.12	31.95
0.0010	1.59	2.07	2.47	10.38	22.07	32.00
0.0032	1.59	2.05	2.45	10.34	21.84	31.82
0.010	1.58	2.05	2.44	10.29	21.82	31.76
0.032	-	2.04	2.45	-	21.71	31.78
0.10	-	2.03	2.43	-	21.62	31.56
0.23	-	2.03	2.43	-	21.67	31.59

There are obvious anomalies in Table 6.13. The chain parameters differ from one material to another, although they are based on the same matrix. The radius 'a' and the effective segment length z^* increase in the order T00F00 > T15F00 > T15F46. For example at temperature 296 K (23°C), 'a' is 0.61, 0.78 and 0.86 nm and z^* 1.25, 1.60 and 1.76 nm for materials T00F00, T15F00 and T15F46 respectively. This variation should not occur. The radius of polymer chain cannot be changed by the additives rubber and filler. It is a constant no matter whether the additives are present or not. The reason for the anomaly is the effect of stress concentrations, which are induced by inclusions (Section 3.1 in Chapter 3). This effect has not been taken into account in all the calculations of Tables 6.13 and 6.14.

To overcome this problem, a stress concentration factor Γ must be introduced into Argon's theory. This can be done by substituting $\Gamma\sigma_{sy}$ for σ_{sy} into Equation (2.47). The same method has been used in dealing with Eyring theory (Bucknall 1977, 1982, 1984). It is given:

$$\left(\frac{\Gamma\sigma_{sy}}{\mu}\right)^{5/6} = \frac{1}{8.5(1-\nu)^{5/6}}\left[1+\frac{36.8k_BT(1-\nu)}{3\pi\mu\omega^2a_r^3}\log\frac{\dot{\gamma}}{\dot{\gamma}_0}\right] \tag{6.18}$$

$$\left(\frac{\sigma_{sy}}{\mu}\right)^{5/6} = \frac{1}{8.5(1-\nu)^{5/6}}\left[\Gamma^{-\frac{5}{6}}+\frac{36.8k_BT(1-\nu)}{3\pi\Gamma^{5/6}\omega^2a_r^3}\frac{1}{\mu}\log\frac{\dot{\gamma}}{\dot{\gamma}_0}\right] \tag{6.19}$$

Following the same procedure as before, the corresponding equations are:

$$V^*_{Argon} = 1.59\pi\Gamma^{5/6}\omega^2a_r^3\left(\frac{\mu}{\sigma_{sy}(1-\nu)}\right)^{\frac{1}{6}} \tag{6.20a}$$

$$V^*_{0,Argon} = 2.45\pi\Gamma\omega^2a_r^3 \tag{6.20b}$$

$$\left(\frac{z}{a}\right)^*_r = \left(\frac{45}{8(1-\nu)}\frac{\mu}{\Gamma\sigma_{sy}}\right)^{1/6} \tag{6.21a}$$

$$z_0^* = 2.05a_r \tag{6.21b}$$

where the subscript 'r' means true value after the correction by Γ and '0' the value at temperature 0 K.

Let $\Gamma^{5/6}$ in Equation (6.19) be inclined with $\omega^2 a_r^3$, i.e. $\Gamma^{5/6}\omega^2 a_r^3$. The measured values of $\Gamma^{5/6}\omega^2 a_r^3$ are the same ones as those of $\omega^2 a^3$ measured from the slope Equation (6.12), which has been collected in Table 6.13. Parallel results similar to those in Tables 6.13 and 6.14 are then obtained. They are collected in Tables 6.15 and 6.16, where $\Gamma = 1$ is assumed under conditions when no additives are involved.

Compare such pairs of parameters as 'a' and 'a_r', z^* and z_r^*, $\pi a^2 z^*$ and $\pi a_r^2 z_r^*$, and V^*_{Argon} and $V^*_{r,Argon}$ in Tables 6.13 and 6.15. After introduction of the stress concentration factor Γ into Argon's equation, the difference of these parameters from one material to another has reduced at temperature 23°C (296 K) and, eventually, vanished at temperature 0 K except for the activation volume defined by Argon (Equation 6.13). V^*_{Argon} and $V^*_{r,Argon}$ share the same values and still change from one material to another at temperatures both 296 K and 0 K. Therefore, Argon's activation volume cannot be equivalent to the activation volume of

Table 6.15 Basic parameters of Argon theory for Modar 8035 resin and the modified composites after correction by stress concentration factor (23°C).

Materials		T00F00	T15F00	T15F46
$\Gamma^{5/6}\omega^2 a_r^3$ (nm^3)	-	0.91	1.90	2.55
Γ	-	1	2.42	3.44
a_r (nm)	-	0.61	0.61	0.61
$(z/a)_r^*$	296 K	2.58	2.26	2.31
$(z/a)_0^*$	0 K	2.05	2.05	2.05
z_r^* (nm)	296 K	1.58	1.38	1.41
z_0^* (nm)	0 K	1.25	1.25	1.25
$\pi a_r^2 z_r^*$ (nm^3)	296 K	1.85	1.61	1.65
$\pi a_r^2 z_0^*$ (nm^3)	0 K	1.46	1.46	1.46
$V^*_{r,Argon}$ (nm^3)	296 K	10.29	21.82	31.76
$V^*_{0,Argon}$ (nm^3)	0 K	6.99	14.58	19.60

Note: (a) The data of $(z/a)^*$ at 296 K is values corresponding to $\dot{\varepsilon} = 0.01\ s^{-1}$ (See Table 16).
(b) $\omega \approx 2$ was used ($\omega = 109.5° = 0.61\pi$).

Table 6.16 The influence of strain rate on Argon's parameter z^* and activation volume V^*_{Argon} for Modar 8035 resin and the modified composites after correction by stress concentration factor(23°C).

$\dot{\varepsilon}$ (sec^{-1})	z_r^* (nm^3)			$V^*_{r,Argon}$ (nm^3)		
	T00F00	T10F00	T15F46	T00F00	T15F00	T15F46
0.00013	1.61	-	-	10.49	-	-
0.00032	1.61	1.40	1.42	10.48	22.12	31.95
0.0010	1.59	1.40	1.42	10.38	22.07	32.00
0.0032	1.59	1.38	1.41	10.34	21.84	31.82
0.010	1.58	1.38	1.41	10.29	21.82	31.76
0.032	-	1.37	1.41	-	21.71	31.78
0.10	-	1.37	1.40	-	21.62	31.56
0.23	-	1.37	1.40	-	21.67	31.59

Eyring V^*_{Eyring} as postulated by Argon. V^*_{Eyring} is a constant. It is independent of temperature provided that the same deformation mechanisms operate at temperatures studied. It is independent of additives employed after introducing Γ into Eyring's theory, (Bucknall 1982 and 1984; Ishai 1968).

The roles of stress concentrations become clear now, after introduction of Γ into Argon's equation. Γ is 2.42 and 3.44 for the materials T15F00 and T15F46 respectively. The concentration of rubber is about 18.5 vol % for the material T15F00 and, based on the rubber toughened matrix, the filler accounts for about 30 % volume for the hybrid material T15F46 (Tables 4.1 and 4.2 in Chapter 4).

Surprisingly, this stress concentration effect has not been observed by Young (1986) for simple compression tests using Argon's theory. As discussed in Section 3.4.1 (Chapter 3), the results obtained by Young give the conclusion that rubber and filler additives do not affect Argon's parameters 'a' and z^* (z^* was the values at temperature 0 K in the paper of the author). They remain unchanged for various compositions without considering the influence of stress concentrations. This is not the case for the materials studied in the present programme.

The reason for the above result is not clear. The results reported by Young (1986) were obtained under compressive conditions at fixed strain rate but at different levels of temperature. However, under the same compressive conditions but at a given temperature and with varying strain rate, the stress concentrations caused by voids (porous filler) were clearly demonstrated (Ishai 1968). The apparent increase in activation volume of Eyring was observed. The main reason for that was the effect of geometry. The cross section of matrix reduced in the presence of voids. After taking this effect into account, the same activation volume of Eyring was obtained for all concentrations of voids, using Equation (3.5) the stress concentration factor (Ishai 1968).

The difference between the system of Ishai and that of Young is that the former has real voids in the matrix and the latter is rubber particles. This perhaps is another reason why no effect of stress concentrations has been observed by Young under compressive conditions when Argon's theory was used. The function of rubber cannot be the same as voids. It can bear stress to a certain extent (Chapters 3, 8 and later in this chapter).

Another significant point is that, at 0 K, the radius 'a_r', the segment length z^*_0 and the volume $\pi a_r^2 z^*_0$ (defined by 'a_r' and z^*_0) are constants (Table 6.15). More important is that they are not significantly different from the values at 296 K (23°C). For example, z^*_0 is 1.25 nm at 0 K while z_r^* is 1.58, 1.38 and 1.41 nm at 296 K (23°C) for materials T00F00, T15F00 and T15F46 respectively. The difference is about one unit length of monomer (about 0.23 nm for C-C backbone). In addition, z_r^* is insensitive to the change of strain rate. When strain rate $\dot{\varepsilon}$ changes from 0.00013 to 0.23, z_r^* changes very little (Table 6.16).

Consider the fact that a_r is independent of temperature (Argon 1973, 1977; Yamini 1980; Young 1986) and strain rate (Argon 1973 and this research) and z^* is assumed insensitive to the change of temperature and strain rate because it is not significantly different from the values z^*_0 at 0 K, which always is a constant. Both a_r and z^*_0 may be taken as material constants. Physically, they stand for the effective dimensions of polymer segments in an activated state at yielding. Only these two values were reported in the literatures by other authors Argon (1973, 1977), Yamini (1980) and Young (1986) (Table 3.1).

Based on these considerations, such parameters as a_r and z^*_0 do not change from one material to another provided that the same matrix is used and a correction for stress concentrations is made (Equation 6.19). For example, a_r = 0.61 nm, z^*_0 = 1.25 nm and $\pi a_r^2 z_0^*$ = 1.46 nm^3 (see the model Figure 2.13) are applicable to all three materials studied, the Modar 8035 resin T00F00, the rubber toughened T15F00 and the hybrid composite T15F46. If the stress concentration factor Γ were not taken into account, however, these parameters would differ from one to another. For example z^*_0 is 1.25, 1.60 and 1.76 nm for T00F00, T15F00 and

T15F46 respectively (Table 6.13 the values at temperature 0 K).

As discussed previously, the rubber and filler additives do affect yield stress of Modar 8035 resin significantly (Figure 6.5) and so does the strain rate (Figure 6.6). However, the underlying mechanism does not change in the presence of rubber or filler or both. The same segment parameters such as a_r^* and z_0^* operate, regardless of the additives used. The deformation mechanism is shearing according to Argon's theory. The shear deformation is realized by polymer chain alignment through a series of rotations (Chapter 2). The reverse model of this process has been shown in Figure 2.13, assuming that a segment of polymer has diameter 'a' and length z^*.

The basic volume of this segment can be well defined by $\pi a_r^* z_0^*$, which accounts for the actual size of the segment which is assumed in the activated state at yielding. It differs from V^*_{Argon} defined by Equation (6.13). It is a constant while V^*_{Argon} is a variable even after considering the effect of stress concentrations (Table 6.15). So, V^*_{Argon} should not be equivalent to the activation volume of Eyring V^*_{Eyring} which is a constant for a given material provided that the same deformation mechanisms operate.

Physically, it is generally recognized that the movement of polymer chains, such as that at yielding, is in the form of segments rather than of monomer units. One segment can contain several monomer units, depending on the properties of polymer chain, in particular whether it is flexible or not. The length of the segment can be determined experimentally, normally through polymer solutions (liquid or solid). Argon's theory may provide a new method to measure this property. This perhaps is another significant point achieved by using Argon's theory.

Chow and Eyring Theories

Chow's theory is similar to Eyring's. They are discussed together now. In order to get more general equations, the stress concentration factor Γ should be taken into account first when composites are concerned. Following the principle outlined above, and substituting $\Gamma\sigma_{yield}$ for σ_{yield} in Equations (2.41) and (2.52) gives:

$$\sigma_{yield} = \frac{\sqrt{3}}{\Gamma V^*}(\Delta H^* + 2.303RT\log\frac{\dot{\varepsilon}_y}{\dot{\varepsilon}_0}) \qquad (6.22)$$

The corresponding slopes in relation to the lines of σ_{yield} against $\log\dot{\varepsilon}$ (Figure 6.6) are:

$$\sigma_{yield} = \frac{4.606 f \beta RT}{\Gamma \Omega_{11}} (\log \tau_0 + \log \dot{\varepsilon}_y) \tag{6.23}$$

$$B_{Eyring} = \frac{2.303\sqrt{3}RT}{\Gamma V^*_{Eyring}} \tag{6.24}$$

$$B_{Chow} = \frac{4.606RT}{\Gamma \frac{\Omega_{11}}{f\beta}} \tag{6.25}$$

The experimental results have already collected in Table 6.10 for materials T00F00, T15F00 and T15F46.

In the theory of Eyring, shear yielding is assumed to be a dominant mechanism and V^* is the corresponding activation volume. Now, V^* is termed V^*_{Eyring} in Equation (6.24) and still considered to have the same meaning.

In the theory of Chow, Ω_{11} has been defined as pressure activation volume of holes (free volume). The relationship between Ω_{11} and shear activation volume of holes Ω_{12} is given by (Chow 1984):

$$\Omega_{12} \approx 1.41\Omega_{11} \tag{6.26}$$

As discussed in Chapter 2, Ω_{11}/f stands for the pressure activation volume of polymer segments at yield, where f is free volume ($f \approx 0.025$ is an universal constant for most amorphous polymers). So, Ω_{12}/f is the corresponding shear activation volume.

Compare Equation (6.24) with (6.25). The activation volume V^*_{Eyring} is equivalent to the apparent activation volume $\Omega_{11}/(\beta f)$ of Chow. As mentioned before, ß is a constant which defines the shape of the relaxation spectrum by the following equation (Chow 1988, 1989):

$$\phi(t) = \exp[-(t/\tau)^{\beta}] \quad (0 < \beta \leq 1) \tag{6.27}$$

where, $\phi(t)$ is relaxation function, t time and τ relaxation time. The relaxation function is controlled not only by τ but also by ß. More interesting is that, when ß = 1, Equation (6.27) becomes the relaxation function which is normally used to accounts for linear viscoelastic behaviour (McCrum 1988, Ward 1983). So, when ß < 1, it accounts for non-linear viscoelasticity of polymer relaxation.

From this point of view, the apparent activation volume $\Omega_{11}/(\beta f)$ in Equation (6.25) reflects some non-linear viscoelasticity through the term ß, and accounts for the activation volume of polymer segments by the term Ω_{11}/f. So, Eyring's activation volume V^*_{Eyring} may have the same meaning as $\Omega_{11}/(\beta f)$ with reference to Equations (6.24) and (6.25).

Table 6.17 and 6.18 are the results obtained from the Chow and Eyring theories. The data on ΓV^*_{Eyring} and $\Gamma[\Omega_{11}/(\beta f)]$ are calculated using Equations (6.24) and (6.25). $\Gamma = 1$ is assumed when no additives are involved. The relationship between Ω_{11} and Ω_{12} is given in Equation (6.26).

Table 6.17 Activation volume of Eyring V^*_{Eyring} for Modar 8035 resin and the modified composites (23°C)

Materials	T00F00	T15F00	T15F46
B_{Eyring} (MPa)	7.08	5.26	4.51
ΓV^*_{Eyring} (nm^3)	2.30	3.10	3.62
Γ	1	1.35	1.57
V^*_{Eyring} (nm^3)	2.30	2.30	2.30

Table 6.18 Basic parameters of Chow theory for Modar 8035 resin and the modified composites (23°C)

Materials	T00F00	T15F00	T15F46
B_{Chow} (MPa)	7.08	5.26	4.51
$\Gamma[\Omega_{11}/(f\beta)]$ (nm^3)	2.66	3.58	4.17
$\Gamma[\Omega_{12}/(f\beta)]$ (nm^3)	3.75	5.05	5.88
Γ	1	1.35	1.57
$\Omega_{11}/(f\beta)$ (nm^3)	2.66	2.66	2.66
$\Omega_{12}/(f\beta)$ (nm^3)	3.76	3.76	3.76

The influence of stress concentrations can be seen in the results but it is not as big as that calculated from the slope of Equation (6.19) in Argon's theory. Here, the stress concentration

factor Γ is 1.35 and 1.57 for T15F00 and T15F46 respectively from Chow and Eyring's equations but it is 2.42 and 3.44 (Table 6.15) for the same materials from Argon's analysis. The reason for the difference may be in the theories themselves. With regard to Argon's theory, such material constants as shear modulus and Poisson's ratio are taken into account.

These two factors are not considered in Chow and Eyring theories, in which the same set of experimental data was used, resulting in the same figures of stress concentration factor (Tables 6.17 and 6.18).

Now, consider the shear activation volume of **polymer segments** (not the general activation volume V^*). This has been defined in terms of $\pi a_r^2 z^*_r$ in Argon's theory (see the model of Argon in Figure 2.13), where the radius a_r and the length z^*_r of polymer segments are available. Considering the results in Tables 6.17 and 6.18, it is not clear what types of polymer segments are involved in V^*_{Eyring} and $\Omega_{12}/(ßf)$. However, Ω_{12}/f, as discussed previously, is the activation parameter which has the same meaning as $\pi a_r^2 z^*_r$. The problem is ß, which is unknown.

Chow (1986, 1988, 1989) reported that ß = 0.5 is applicable for most thermoplastics and, it may be assumed, for lightly cross-linked thermosets. As a first approximation taking ß = 0.5, Ω_{12}/f can be calculated. It is 1.88 nm^3 (resulting from $\Omega_{12}/(ßf)$ x ß = 3.76 x 0.5). Surprisingly, this figure is not far away from the values of $\pi a_r^2 z^*_r$, which are 1.85, 1.61 and 1.65 nm^3 for materials T00F00, T15F00 and T15F46 respectively (Table 6.15). ß = 0.5 means that about half of the apparent activation volume $\Omega_{11}/(ßf)$ or $\Omega_{12}/(ßf)$ is contributed by polymer segments and the rest possibly by non-linear viscoelasticity in terms of ß.

This analysis may help in understanding the meaning of Eyring activation volume. As discussed above, the apparent activation volume $\Omega_{11}/(ßf)$ in Equation 6.25 and V^*_{Eyring} in Equation (2.64) seem to be equivalent. So, V^*_{Eyring} should also contain contributions partly from polymer segments and partly from non-linear viscoelasticity, provided that the meanings of $\Omega_{11}/(ßf)$ explained above are correct.

Comments

The three theories discussed above all agree with the experimental data. Eyring's equation gives the simplest form. The next is Chow's equation. Argon's equation is the most complicated one. Of primary importance is that they all characterize the viscoelasticity of polymers at yield.

Where the activation volume is concerned, the emphasis of this section is on a description of the polymer segments involved, with regard to atomic dimensions. This object has been achieved by using Argon's theory. The effective radius and length of polymer segments have been calculated. Compare the results in Table 6.15 with those in Table 3.1, obtained by other authors for diverse materials (the values of z^* in the table are the results at 0 K). 'a' and z^* are 0.61 and 1.46 nm for Modar 8035 resin. A range of 'a' from 0.37 to 0.58 nm and z^* from 0.74 to 1.16 nm are shown in Table 3.1. There are no significant differences between the values obtained in this research and those from other authors.

The parameters 'a' and z^* can help in understanding the mechanisms of deformation at yield. As described in Chapter 2, polymer segments in a random zig-zag fashion will be forced to line up along the primary force direction. The critical size in an activated state at yield has been characterized by z^* and 'a'. The unit of polymer chain segment is, therefore, defined by them in terms of $\pi a^2 z^*$. Based on the unit, polymer yielding is realized through a series of local rotations into an aligned state. More interesting is that all the local movement is carried out in an elastic field considered on an atomic scale (Li 1971) according to the theory.

The ratio of critical dimensions $(z/a)^* \approx 2.05$ (Equation 6.17) should be obeyed at yield according to Argon's theory. This is the value at 0 K. What was found in this research is that $(z/a)^*$ may greater than 2.05 at other temperatures although the difference is not very big. For example, at 296 K (23°C), $(z/a)^*$ is 2.58, 2.26 and 2.31 for materials T00F00, T15F00 and T15F46 respectively. In addition, the measured 'a' value is more than double the radius of a single polymer chain (Argon 1973, 1977). This agrees with the results obtained for Modar 8035 resin as discussed previously.

From Chow's theory, the dimension of the activation volume of polymer segments can also be calculated through the apparent activation volume in terms of $\Omega_{11}/(\beta f)$ or $\Omega_{12}/(\beta f)$ if the constant ß is known. However, such dimensions as the radius 'a' and the length z^* of polymer segments cannot be obtained. Interesting is the parameter ß, which may account for non-linear viscoelasticity as mentioned above. ß is involved in the apparent activation volume, together with stress concentration factor Γ, pressure activation volume of holes Ω_{11} and free volume in terms of 'f' (Equation 6.25). This probably implies that non-linear viscoelastic relaxation also plays a role at yield. The thing is that it is not clear whether ß is independent of additives such as rubber and rigid filler, a point which needs further exploration.

Compared with Chow's Equation (6.25), the Equation (6.24) of Eyring gives general activation volume at yield but less information than the latter.

The influence of stress concentrations has clearly been demonstrated when the stress concentration factor Γ is incorporated into the equations based on the three theories discussed above. The increase in apparent activation volume is assumed to be due to this effect. After the correction through Γ in the theories, such parameters as 'a' and z^* in Argon's theory and activation volume in Chow and Eyring theories are independent of additives used. This means that the basic deformation mechanisms of matrix do not change in the presence of additives. However, the activation volume defined by Argon (See Equation 6.13) is a variable as discussed previously (see Table 6.15).

The effect of stress concentrations caused by additives was not observed by Young (1986) for the systems studied: the epoxy resin, the rubber toughened resin and the filler filled/hybridized epoxies when Argon's theory are considered. The difference between this research and Young's lies in experimental procedures. Here, it was conducted under simple tension at a given temperature with varying strain rate. The procedure conducted by Young was simple compression at a given strain with varying temperature. This may imply that tension will facilitate stress concentrations but compression not.

6.3.3 Factors affecting deformation behaviour

In the previous section, yielding behaviour has been discussed based on Argon, Chow and Eyring theories. The purpose in the current section is to discuss the factors that affect deformation behaviour, especially with reference to additives used. The influence of moisture will be discussed too.

The influence of soft/hard inclusions

Yield stress σ_{yield}

As discussed before, additives (rubber or filler or both) will significantly affect yield stress. This has been illustrated in Figure 6.5. The underlying mechanisms are not clearly demonstrated by the plot. However, the change of yield stress of composites caused by inclusions can be considered as follows. Firstly, inclusions will reduce the effective cross-section of matrix. So, the contribution made by the matrix to the yield stress of composites will be reduced. Secondly, inclusions will influence the deformation behaviour of matrix. For the second factor, it was believed to be controlled mainly by the bonding conditions at interfaces formed between matrix and additives (Pukanszky 1988).

One semi-empirical equation to characterize the change of yield stress in the presence of fillers was proposed by Pukanszky (1988):

$$\sigma_{yield} = f_A \sigma_{m,y} \exp(B_P \phi) \tag{6.27a}$$

or

$$\Gamma_A \sigma_{yield} = \sigma_{m,y} \exp(B_P \phi) \tag{6.27b}$$

$$f_A = 1/\Gamma_A = (1 - \phi)/(1 + 2.5\phi) \tag{6.28}$$

where, f_A is the effective cross-section area of matrix, Γ_A the geometric stress concentration factor (Γ_A has the same meaning as that of Ishai in Equation (3.5) but the former is a little bit higher than the latter at a given concentration ϕ), $\sigma_{m,y}$ the yield stress of matrix, ϕ the volume fraction of filler and B_P a constant which is assumed to account for the property of interfaces.

$f_A \sigma_{m,y}$ is the first factor mentioned above, which accounts for the contribution made by the matrix to overall yield stress σ_{yield} in the presence of additives. The second factor is $\exp(B_P \phi)$ which accounts for the influence on the property of the additives. Equation (6.27) has been used successfully for diverse systems filled with rigid fillers by fitting the parameter B_P (Pukanszky 1988). It can be seen that σ_{yield} will be equal to $f_A \sigma_{m,y}$ when $B_P = 0$, i.e. the decrease in yield stress is simply caused by the reduction in cross-section area of matrix, the case like voids in the matrix (Ishai 1968). The bigger the B_P, the more influence of additives will be expected.

Equation (6.27a) can be re-arranged to the following form:

$$\sigma_{yield}/\sigma_{m,y} = f_A \exp(B_P \phi) \tag{6.29}$$

Figure 6.16 is drawn according to Equation(6.29), using the normalized yield stress $\sigma_{yield}/\sigma_{m,y}$ as a function of volume fraction of additives. It can be seen that $B_P = 3$ is a neutral figure at which $\sigma_{yield} = \sigma_{m,y}$, i.e. the yield stress of a composite is equal to that of the matrix. When $B_P \leq 3$, $\sigma_{yield} \leq \sigma_{m,y}$, additives have a negative influence. When $B_P \geq 3$, the reverse is true.

The thing is how to measure B_P for a given material. This can be done by re-arranging Equation (6.27b) to the following equation:

$$\mathrm{Ln}(\Gamma_A \sigma_{yield}) = \mathrm{Ln}(\sigma_{m,y}) + B_P \phi \tag{6.30}$$

If the proposed semi-empirical equation is correct, the left hand term of Equation (6.30)

against ϕ will give a straight line. In this research, it is intended to apply the semi-empirical equation to the systems of rubber toughened thermosets and the hybridized composites in order to account for the influence of additives.

Figure 6.17 is the plot according to Equation (6.30) for the rubber toughened Modar 8035 resins and the hybrid systems, using the data in Tables 6.1 and 6.2. The experimental results are well fitted to the equation. Good straight lines have been obtained for both systems.

However, the parameter B_P is different. It is 0.913 for the rubber toughened system but 3.804 for the hybrid one. As mentioned before, the influence of additives on yield stress will be determined by Pukanszky's parameter B_P, whether $B_P \leq 3$ or not. The results in Figure 6.17 show that rubber has a strong negative influence on the yield stress ($B_P = 0.913$) but filler has a positive effect ($B_P = 3.804$). These features are clearly shown in Figure 6.18, using Equation (6.29). The lower curve is the rubber toughened systems and upper one for the hybrid systems. Square and cross symbols are experimental data. The yield stress increases with increasing filler concentration but decreases with increasing rubber concentration.

However, the underlying mechanisms are still not clear, with regard to parameter B_P. For the materials filled with voids (porous filler) and rigid filler, Ishai (1968) argued that yielding was controlled mainly by the matrix, giving the same activation volume regardless of the presence of 'voids' or filler. He also concluded that, for the materials filled with rigid filler, the increase in yield stress is due to the increase in activation energy (see Equation 2.41 of Eyring and Figure 2.12). The last conclusion about the role of the filler may not be true. It seems contrary to the argument that additives will not alter the deformation mechanisms but can accelerate or retard the processes (Chapter 3). The apparent increase in the activation energy may be due to other factors relating to the resin matrix itself rather than the increase in activation energy.

One theory in Chapter 2 has touched on the problem. Chow's theory established the relationships between yield stress and filler concentration as indicated in Equation 2.59. This equation is based on the theory of free volume, which assumes rigid filler particles have no free volume which is contributable at yielding. The matrix is still considered a dominant factor. Good bonding at interfaces is assumed.

At a given strain rate and temperature, Equation (2.59) can be written as:

$$\sigma_{yield} = A + \frac{C\phi}{(1-\phi)} \tag{6.31}$$

where A and C are constants. A straight line will be expected if a plot is made of σ_{yield}

against $\phi/(1-\phi)$. This is the result shown in Figure 6.19, according to the equation fitted with experimental data in Table 6.2. Good agreement has been obtained. This implies that the increase in yield stress is due to the decrease in free volume for particulate composites. This kind of agreement of the theory with experiments was also made by Chow (1991).

Both the equations of Pukanszky and of Chow can be fitted well to the experimental data. One problem with Pukanszky's semi-empirical equation is the parameter B_P. It may not be a constant that accounts only for the properties at interfaces as originally explained by Pukanszky.

What was found in this research is that Pukanszky equations above can be used not only in characterization of yield stress but also for modulus (Figure 6.20) and strength (see next chapter). The difference between them is in parameter B_P. Two curves in Figure 6.20 are drawn according to Equation 6.30 with experimental data on modulus from Tables 6.1 and 6.2, resulting in $B_p = 1.332$ for the rubber toughened Modar resin and 5.42 for the hybrid composites. So, B_P cannot be a material constant. More exploration will be needed in order to get a better understanding of B_P. However, one conclusion at least can be drawn that it is an index which accounts for the influence of additives on such properties as yield stress σ_{yield}, modulus E and strength σ_b. The bigger the B_P, the more contributions from additives.

It is worthy of notice that, because of $B_P > 0$ for the rubber toughened system, rubber particles in Modar matrix must be stress bearers in elastic deformation ($B_P = 1.33$) and during yielding ($B_P = 0.91$). Also it is true that more contributions are made from rubber in elastic deformation than in yielding as B_P is bigger for the former than the latter. This because rubber cavitation deteriorates the ability as stress bearers (see Chapter 8 and next section).

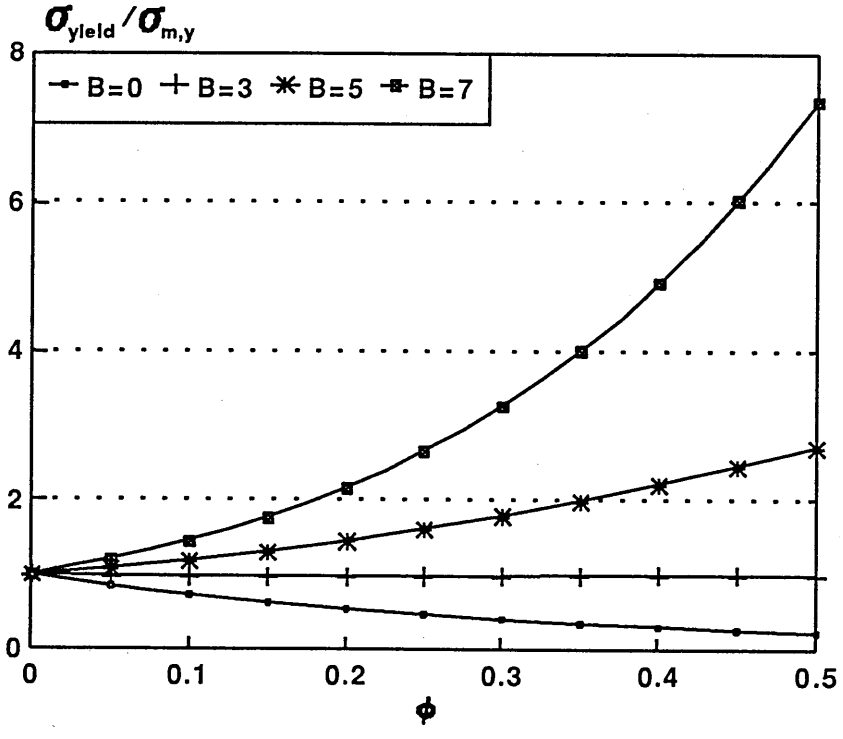

Figure 6.16 Normalized yield stress against volume fraction of additives using Pukanszky semi-empirical equation.

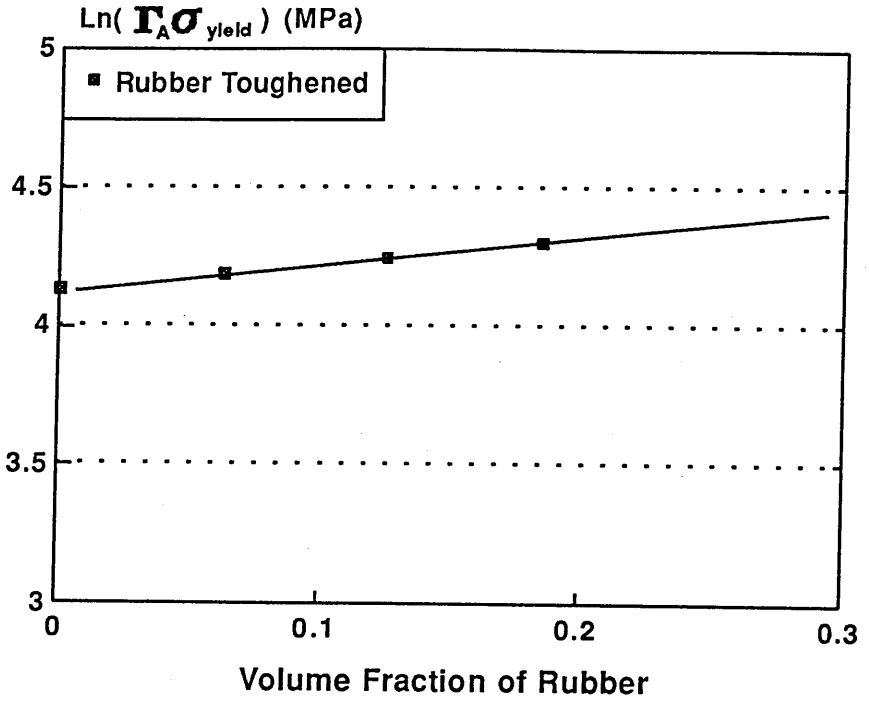

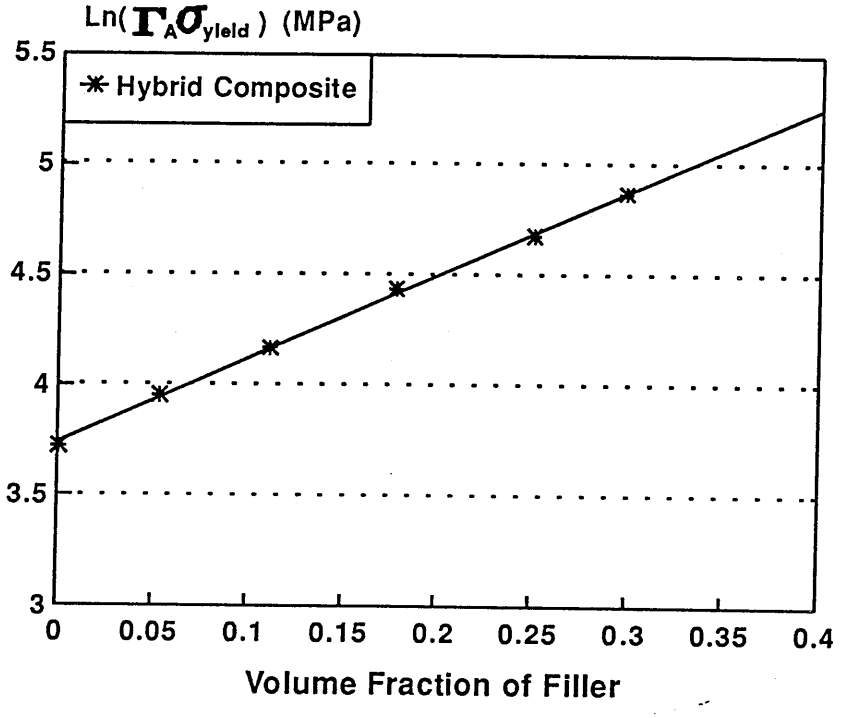

Figure 6.17 Effective yield stress as function of additives of rubber toughened Modar 8035 resin (top) and the hybrid composites containing 15 wt % rubber in the Modar matrix (bottom) (23°C).

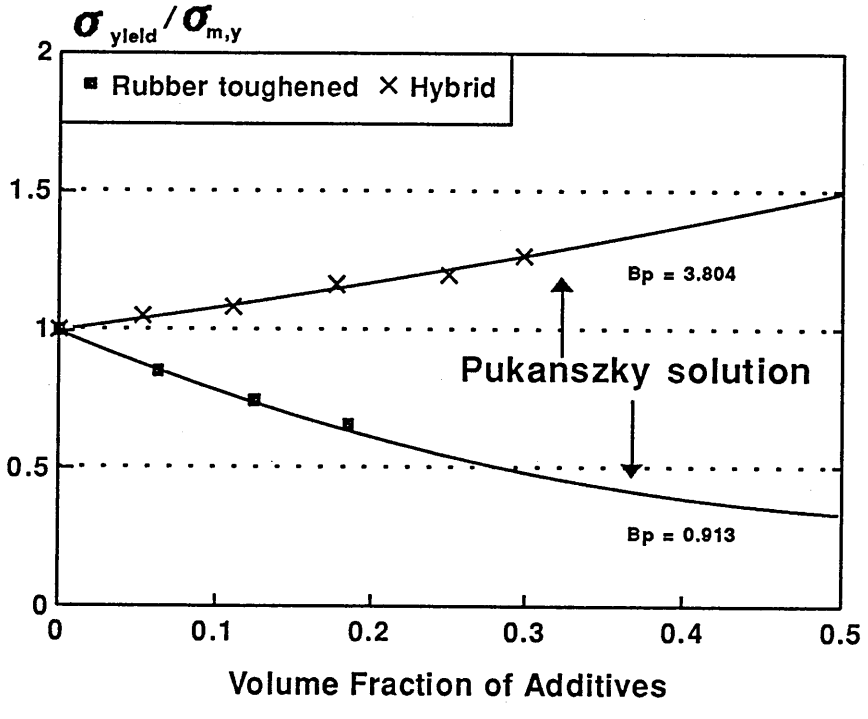

Figure 6.18 Normalized yield stress against volume fraction of additves using Pukanszky equation.

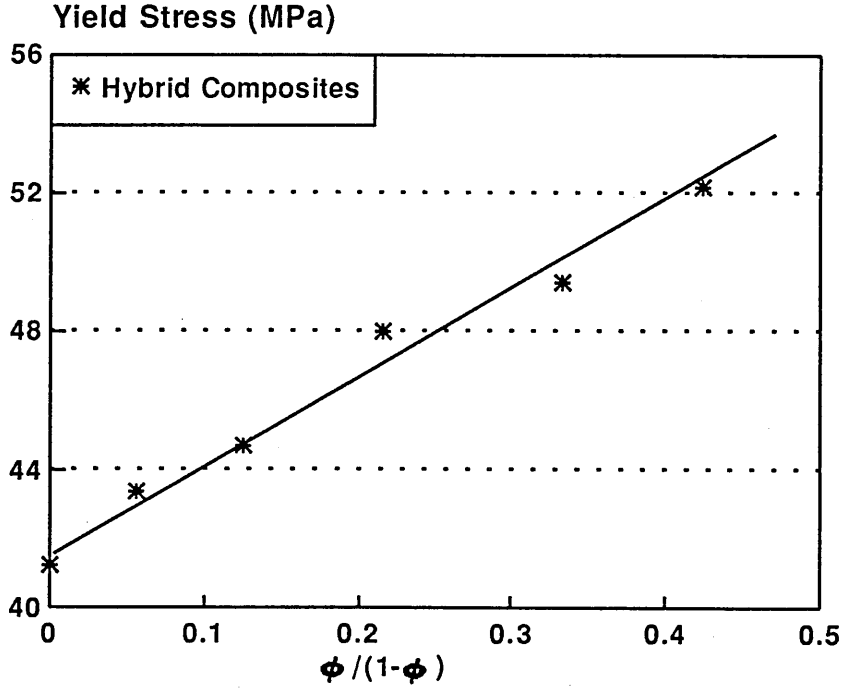

Figure 6.19 The influence of filler concentration on yield stress of modified Modar 8035 resins all with 15 wt % rubber.

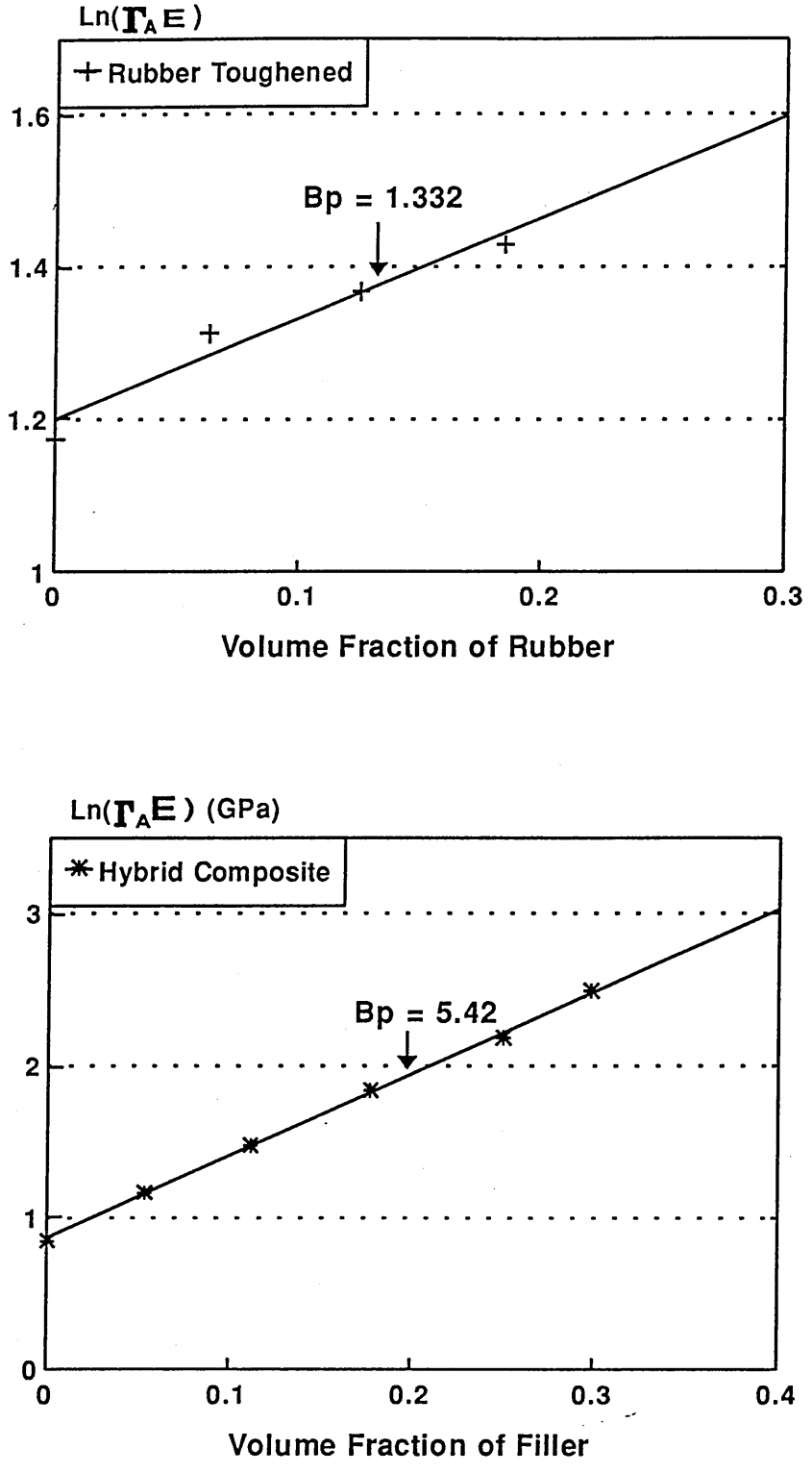

Figure 6.20 Effective modulus as function of additives of rubber toughened Modar 8035 (top) and the hybrid composites all with 15 wt % rubber (bottom).

Volume Strain ΔV/V

The experimental results of ΔV/V against longitudinal strain ε were presented in Figure 6.8 early in this chapter, which shows the general trend in the influence of rubber and filler additives on the volume change behaviour. However, the underlying mechanisms are not clearly revealed by Figure 6.8. The purpose of this section is to try to identify the deformation mechanisms, considering the following questions:

(a) how much volume increase is contributed by elastic dilatation and how much by plastic cavitation (evidence for rubber cavitation will be detailed in Chapter 8)?

(b) At what stress level will rubber start to cavitate?

(c) How much longitudinal strain is contributed by elastic deformation, shear deformation and cavitation of rubber particles?

The total volume strain expressed by Equation (6.1) can be considered to have two parts: elastic dilatation $(\Delta V/V)_{el}$ and plastic cavitation $(\Delta V/V)_{void}$. Equation (6.1) can be written as:

$$\frac{\Delta V}{V} = \left(\frac{\Delta V}{V}\right)_{el} + \left(\frac{\Delta V}{V}\right)_{void} = (1-\epsilon_l)^2(1+\epsilon_l) - 1 \qquad (6.32)$$

Consider simple tension. The elastic part can be expressed by:

$$\left(\frac{\Delta V}{V}\right)_{el} = (1-2\nu)\epsilon_{el} \qquad (6.33)$$

where ε_{el} is elastic strain.

One hypothesis made here is that ε_{el} is controlled by elastic modulus E as a function of true stress σ during elastic and plastic deformation i.e. $\varepsilon_{el} = \sigma/E$. Strictly speaking, this assumption is not correct. This is because elastic modulus will change before and after rubber cavitation. The question is whether the change is significant or not. The result from finite element analysis shows that the modulus of a composite will reach a lower limit when the modulus of the matrix is 3 orders of magnitude greater than that of the inclusions (Kinloch 1992). This means that further reduction in the modulus of the inclusions makes no difference to the modulus of the composite. The hypothesis made above is taken as an aproximation as the Young's modulus of rubber, say 2 MPa, is normally 3 orders less than that of matrix, say 3 GPa.

Substituting $\varepsilon_{el} = \sigma/E$ for ε_{el} into Equation (6.33) gives:

$$\left(\frac{\Delta V}{V}\right)_{el} = (1-2\nu)\frac{\sigma}{E} \tag{6.34}$$

Combination of Equations (6.32) and (6.34) gives:

$$\left(\frac{\Delta V}{V}\right)_{void} = (1-\epsilon_t)^2(1+\epsilon_l)-(1-2\nu)\frac{\sigma}{E}-1 \tag{6.35}$$

Now, it is possible to calculate the volume strain contributed by rubber cavitation (in this research, cavitation has been observed in the rubber, see Chapter 8).

As far as deformation mechanisms are concerned, the total longitudinal strain ε is made up of three parts: elastic ε_{el}, shear ε_{sh} and the part made by cavitation ε_{void}. This is expressed by:

$$\varepsilon = \varepsilon_{el} + \varepsilon_{sh} + \varepsilon_{void} \tag{6.36}$$

ε can be obtained from experiment and ε_{el} from σ/E as assumed above. If ε_{void} can be calculated, ε_{sh} is obtainable through Equation (6.36). The problem is how to get ε_{void}.

Consider a sphere of resin with a radius r_0, containing a single rubber particle in its centre. The sphere is chosen to have the same rubber volume fraction as that of the rubber toughened material as whole. Because of the cavitation of the rubber, the diameter of the sphere will increase from r_0 to 'r'. Then the volume strain of the sphere can be expressed by:

$$\left(\frac{\Delta V}{V}\right)_{void} = \frac{r^3-r_0^3}{r_0^3} = \left(\frac{r}{r_0}\right)^3-1 \tag{6.37}$$

$$\frac{r}{r_0} = \left[\left(\frac{\Delta V}{V}\right)_{void}+1\right]^{\frac{1}{3}} \tag{6.38}$$

Assuming the cavitation of the rubber particle takes place uniformly, the strain along any direction will be given:

$$\epsilon_{void} = \frac{r}{r_0}-1 \tag{6.39}$$

Substituting Equation (6.38) for r/r_0 into Equation (6.39) gives:

$$\epsilon_{void}=\left[\left(\frac{\Delta V}{V}\right)_{void}+1\right]^{\frac{1}{3}}-1 \tag{6.40}$$

So, ε_{void} can be calculated through $(\Delta V/V)_{void}$ (Equation 6.35) under the assumption that rubber particles cavitate uniformly.

Equations (6.35) and (6.36) will be used in the following discussions.

The same sets of experimental data as that used in Figure 6.8 are used here. Figure 6.21 is made by drawing $(\Delta V/V)_{void}$ against longitudinal strain ε for the rubber toughened Modar resins and the hybrid composites using Equation (6.35). Comparing this plot with Figure 6.8, it is found that elastic dilatation is the controlling factor only at the initial stage. After that, cavitation of rubber particles dominate the deformation.

It appears that rubber delays the onset of volume dilatation but filler accelerates it (Figure 6.21). The strain at which rubber cavitation starts increases with increasing rubber concentration but decreases with increasing filler. Borggreve (1989) used this strain as an indicator to compare the ability of diverse rubbers to cavitate.

This may not be correct because stress is a key factor controlling rubber cavitation (Chapter 3) rather than strain. If the plot is drawn as $(\Delta V/V)_{void}$ against stress σ, it is found that rubber cavitation starts at almost the same stress. This is shown in Figure 6.22. The cavitation starts at a stress of about 40 MPa. Consider the case of simple tension, the hydrostatic stress which is responsible for the cavitation is about 13 MPa (this subject will be discussed later in Chapter 8 when microstructure of rubber particle cavitation is presented).

One fact is clearly shown in Figure 6.22 that, at the later stage of the plastic deformation, the rate of void development is controlled mainly by the concentration of rubber particles. The higher the concentration of the rubber particles, the higher the rate. This conclusion can not be drawn from Figures 6.8 and 6.21, where the plot is made of volume strain against longitudinal strain which is commonly used in literature dealing with similar problems.

The role of filler particles in the deformation is also clearly demonstrated in Figure 6.22. Rigid filler does not accelerate the process of rubber cavitation as it appears in Figures 6.8 and 6.21, but delays the process to a certain extent. This is because the relative concentrations of rubber particles are reduced by increasing filler loadings. As discussed before, the dominant mechanisms are determined by the matrix. So, the basic deformation pattern does not change in the presence of filler particles. This is what has been shown in Figure 6.22.

When filler loading increases from 10 to 40, the volume change keeps the same trend for the hybridized composites.

Formation of voids during plastic deformation is obvious now. However, the subject of shearing deformation has not been touched yet. By using Equation (6.36), the shear strain can be estimated. Figure 6.23 is drawn for the purpose. The upper plot is for one rubber toughened Modar resin and the lower one for one hybrid composite. It is not surprised to find that the contribution made by rubber cavitation to the overall longitudinal strain accounts only for a small proportion. The majority of the strain is contributed from shear deformation. Elastic strain also contributes an important part to the overall strain, compared with that contributed from rubber cavitation.

However, the relationship between shear deformation of matrix and cavitation of rubber particles is not well demonstrated in Figure 6.23. As mentioned above, stress is a key factor which determines the cavitation of rubber. By drawing stress against strains ε_{el}, ε_{void} and ε, the relationship between shear deformation and rubber cavitation is reasonably revealed as indicated in Figure 6.24. The sharp increase in shear strain is always linked with the onset of rubber cavitation. It should be borne in mind that rubber concentration is small and the strain contributed by rubber cavitation is even smaller. It cannot be expected that rubber cavitation would contribute more to the overall plastic deformation and would be seen clearly in the early stage of the plastic deformation. So, the onset of rubber cavitation may be earlier than that shown in Figure 6.23 (See Figure 6.22). However, the development of the cavitation has been reasonably recorded in the later period of the plastic deformation.

It has generally been recognized that the key function of rubber particles is to facilitate plastic deformation through cavitation (See Chapter 3). The experimental results shown here do support the argument as indicated in Figures 6.22, 6.23 and 6.24. The main deformation mechanism of Modar resin is shearing. The rubber particles promote the process through cavitation. The filler used does not affect the deformation mechanism of the matrix toughened with rubber Paraloid BTA 753.

The influence of moisture

Glass Transition Temperature T_g

The change of glass transition temperature T_g caused by moisture has been presented in Figure 6.14 and Table 6.9 in Section 6.2. About 25 to 30°C reduction in T_g has been

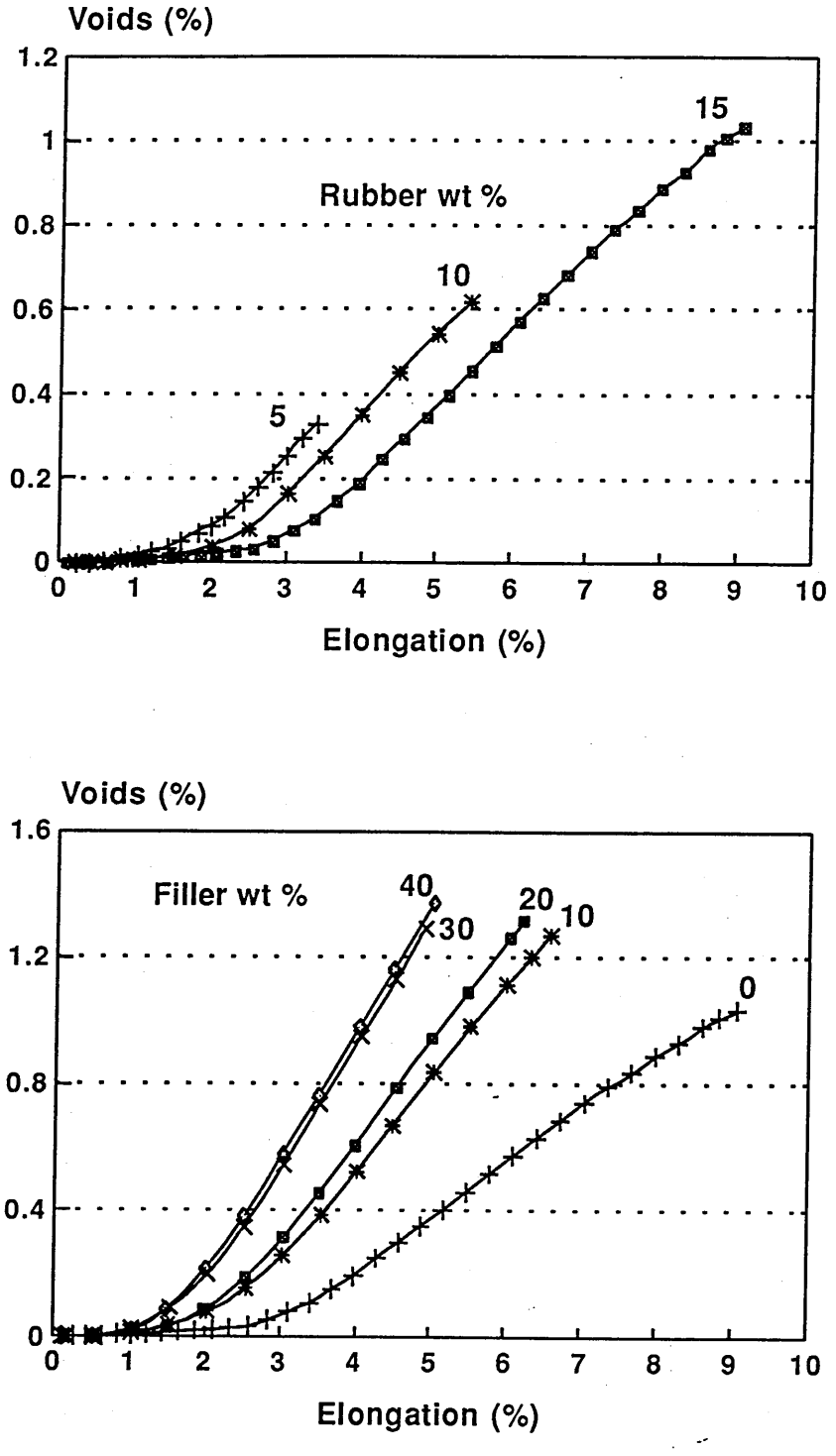

Figure 6.21 Voids change as function of additives of rubber toughened Modar 8035 resin (top) and the hybrid composites all with 15 wt % rubber in the Modar matrix (bottom) (23°C).

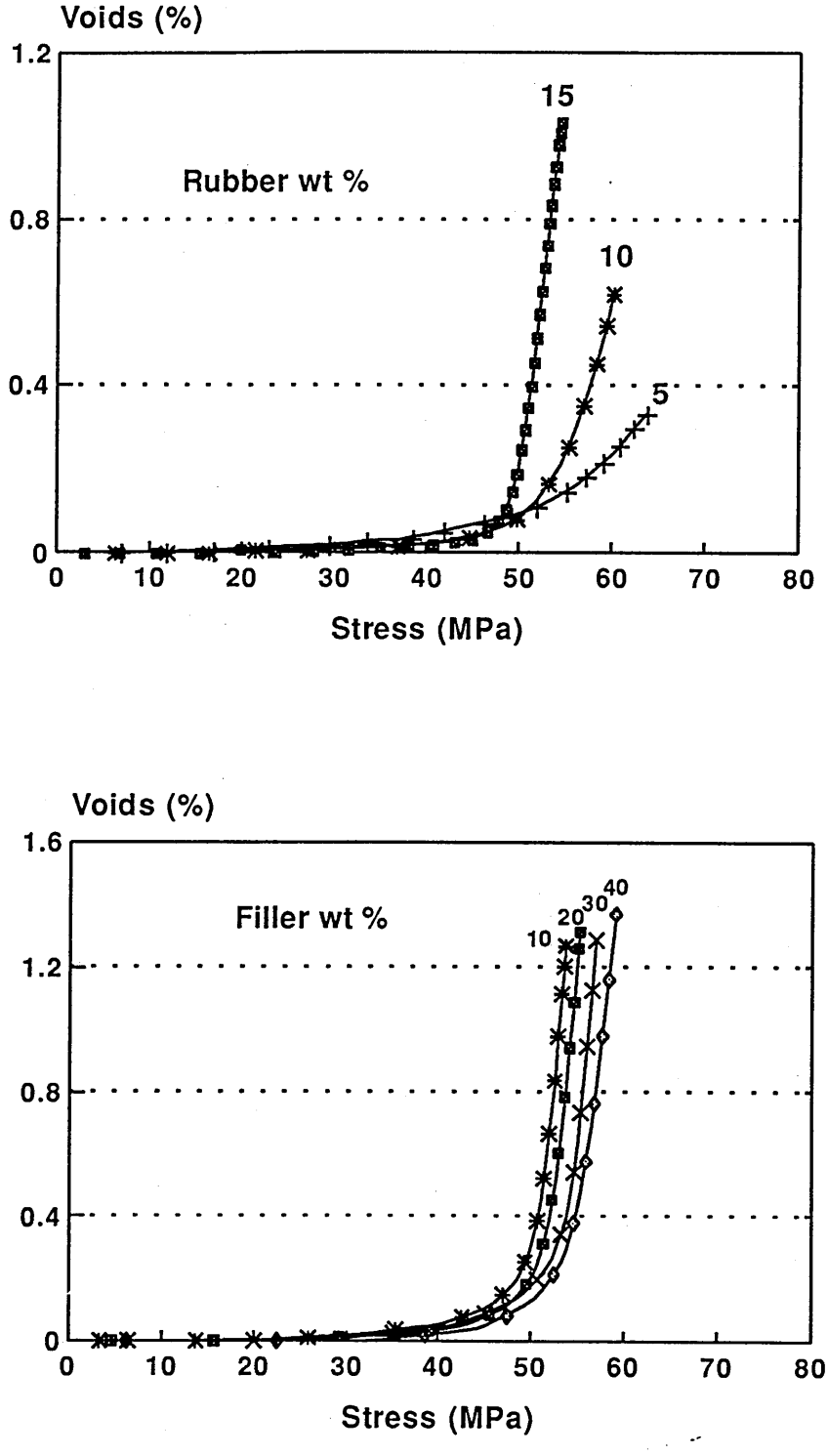

Figure 6.22 Voids change as function of tensile stress of rubber toughened Modar 8035 resin (top) and the hybrid composites all with 15 wt % rubber in the Modar matrix (bottom) (23°C).

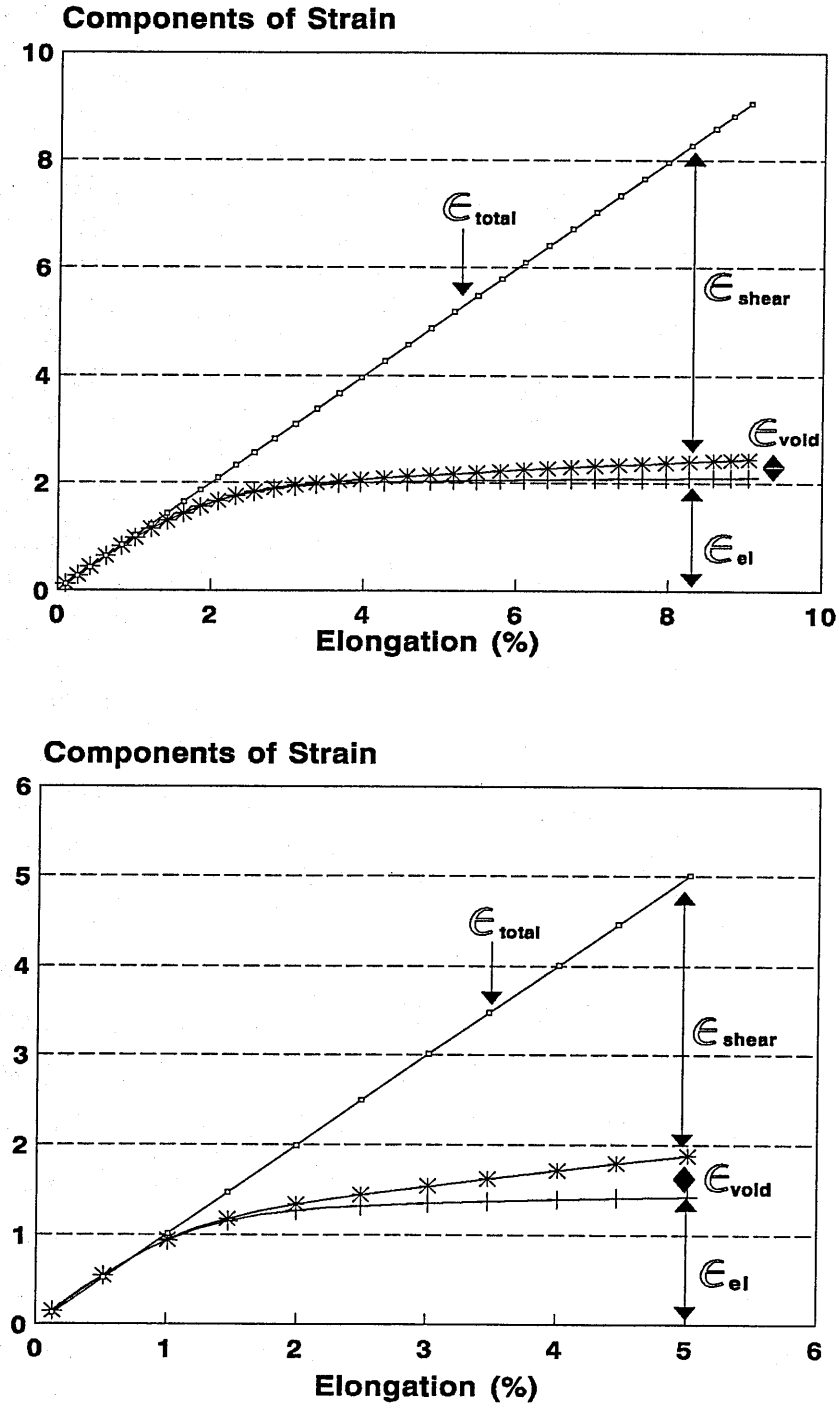

Figure 6.23 Strains contributed from elastic, shear and voids deformation of rubber toughened Modar 8035 (top) and hybrid composite containing 15 wt % rubber modifier (bottom) 23°C

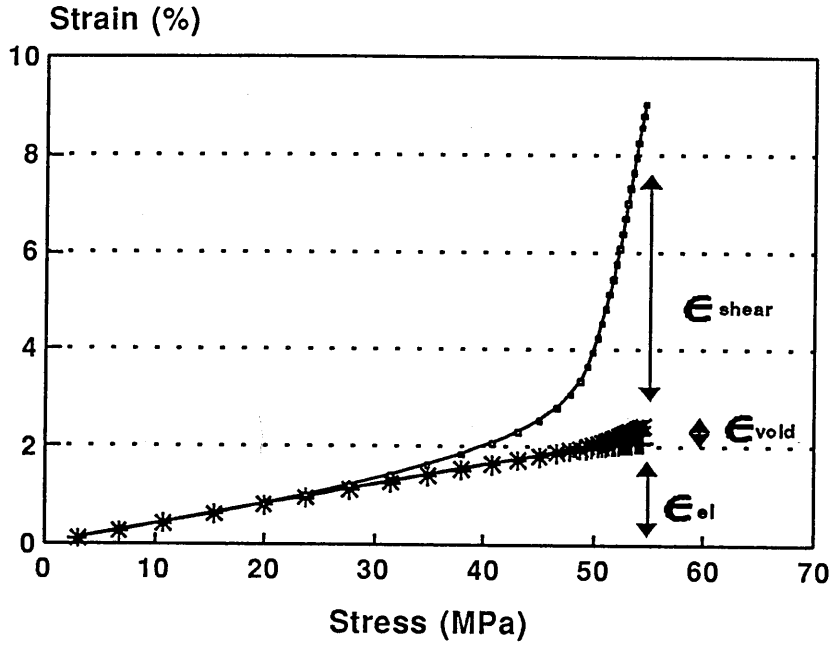

T15F00

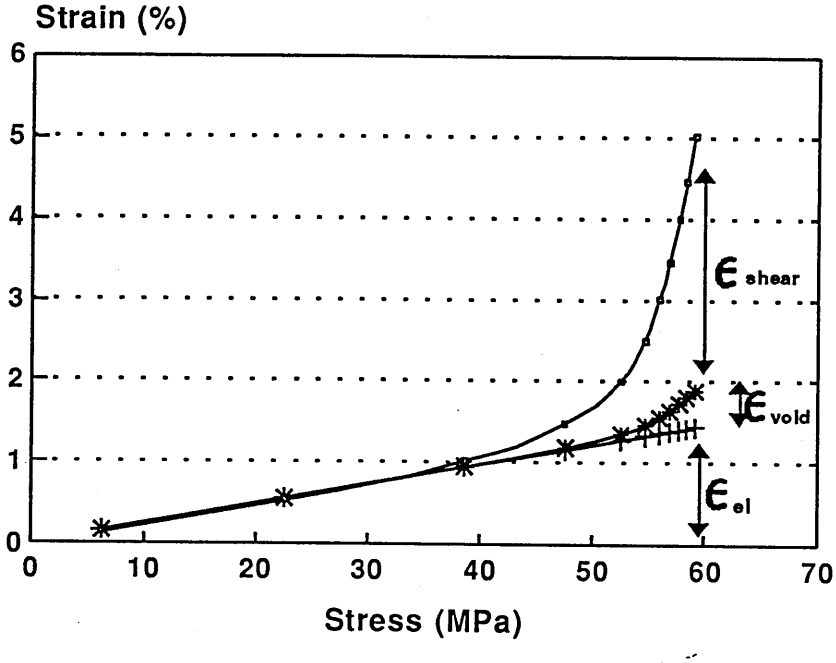

T15F40

Figure 6.24 Strains as function of stress of rubber toughened Modar 8035 resin (top) and the hybrid composite containing 15 wt % rubber in the Modar matrix (bottom) (23°C).

observed. The concentration of water for each of the corresponding materials is about 3.2 wt % for T00F00 and T15F00 and 1.8 wt % for T15F46. The interesting thing is that the influence of moisture is reversible. T_g can recover to its normal value in dry conditions if water has been driven out.

The results suggest that water acts as a plasticizer, which reduces glass transition temperature T_g of polymers. The main function of a plasticizer is to reduce secondary forces between polymer chains and to ease the resistance to chain segment movement. This will reduce the activation energy and the time τ for relaxation of polymer chains. For Modar 8035 and the modified resin composites, the primary role of water is probably to break down hydrogen bonds possibly formed by amide groups (See chemical structure of the Modar resin, Figure 4.1 in Chapter 4) and to enhance the mobility of polymer segments, resulting in the reduction in glass transition temperature T_g. After water has been driven out, T_g can recover to the normal value because those hydrogen bonds that were broken by water molecules can be restored in the absence of water.

Yield stress σ_{yield} and Modulus E

The influence of moisture on yield stress σ_{yield} and modulus E has been presented in Table 6.5 and Figure 6.7 early in Section 6.2. Both modulus and yield stress increase with decreasing water concentration. For example, E and σ_{yield} are 3.08 GPa and 55.6 MPa for the material T00F00 saturated by water but they are 3.57 GPa and 71.2 MPa after water has been driven out. The general profile of the influence can be seen in Figure 6.7, which shows E and σ_{yield} against desorption time. The materials used were saturated with water before desorption started.

The change in both modulus and yield stress appears to occur within 43 days. After that, little influence has been observed on extending the time of desorption. This is because the water concentration is very small. As mentioned before, the corresponding water concentration is about 0.6 - 0.7 wt % (Section 6.2).

The effect may be clearer when moisture distributions in the sheet of materials are taken into account. The distributions of a diffusing substance in the sheet varies with time. The general profile of the change is shown in Figure 6.25. It is drawn as normalized concentration (C/C_s) against position ($X = x/l$) in the sheet for the one dimensional case, according to Equation (5.5b) in Chapter 5, where the figures in the plot correspond to normalized time $T^* = Dtl^{-2}$. $X = 0$ is the centre of the sheet and $X = 1$ the surfaces. By using the data in Table 6.4, the estimated values of T^* are listed in Table 6.19, which correspond to the times at which the

materials T00F00, T15F00 and T15F46 were tested.

With reference to Table 6.19 and Figure 6.25, water distribution within the sheet of a material can be approximately estimated. The gradient of concentration decreases with increasing time. The difference between the concentrations at the surfaces and in the centre seems to be significant up to 43 days. So, what have been measured as E and σ_{yield} for Modar resins through simple tension tests are actually the average values, which represent the influence of moisture neither in the centre nor at the surfaces. However, the general trend is clear that the longer the time of desorption, the more uniform the concentrations. Again, it should be borne in mind that the concentrations of water are small. It will be expected that the influence of moisture is very small indeed after a certain time. Further change of E and σ_{yield} is hardly to be observed. This is what is shown in Figure 6.7.

Table 6.19 The relationships between the normalized time T^* and real time in water desorption for Modar 8035 resin and the modified composites

Time (days)	$T^* = Dtl^{-2}$		
	T00F00	T15F00	T15F46
0	0	0	0
8	0.09	0.08	0.07
43	0.51	0.41	0.37
72	0.85	0.68	0.61

Nevertheless, water does reduce yield stress and modulus. The reason for the reduction is probably the same as that in the case of glass transition temperature discussed above. Water acts as a plasticizer which can break hydrogen bonds possibly formed between amide groups, reducing secondary forces.

6.4 Conclusions

(1) The deformation mechanisms of Modar 8035 resin and the modified composites are shear-dominated. Rubber particles accelerate the deformation through cavitation. Filler particles have little influence on the mechanism.

(2) Viscoelasticity is apparent at yielding in the Modar resin and the modified composites. Increase in strain rate leads to an increase in yield stress. Elastic modulus measured through simple tension was also affected by strain rate to a certain extent.

(3) The yield stress of the Modar resin and the modified composites can be characterized by all three theories considered. They are Argon, Chow and Eyring theories. From Argon's theory, critical segment length z^* and effective diameter 'a' of polymer chains can be calculated. So can the activation volume of **polymer segment** in terms of $\pi a^2 z^*$. This activation volume can also be estimated through Chow's theory provided that the parameter ß is known. ß is a constant that probably characterizes non-linear viscoelasticity of polymer relaxation.

(4) Rubber particles as inclusions can effectively reduce yield stress of the Modar resin while filler particles increase it. The general influence of both rubber and filler on the yield stress can be well fitted to one semi-empirical equation proposed by Pukanszky (1988). This equation can also be used to characterize the change of modulus of the composites.

(5) Decrease in free volume is probably responsible for the increase in yield stress of the composites in the presence of rigid filler.

(6) Moisture in the Modar resin and the modified composites reduces such properties as yield stress, modulus and glass transition temperature. Its main role is apparently to act as a plasticizer, reducing secondary forces, possibly hydrogen bonds formed between amide groups in the Modar resins. This is a reversible process, i.e. all the properties can recover to their normal values in dry conditions after the moisture has been driven out of the system.

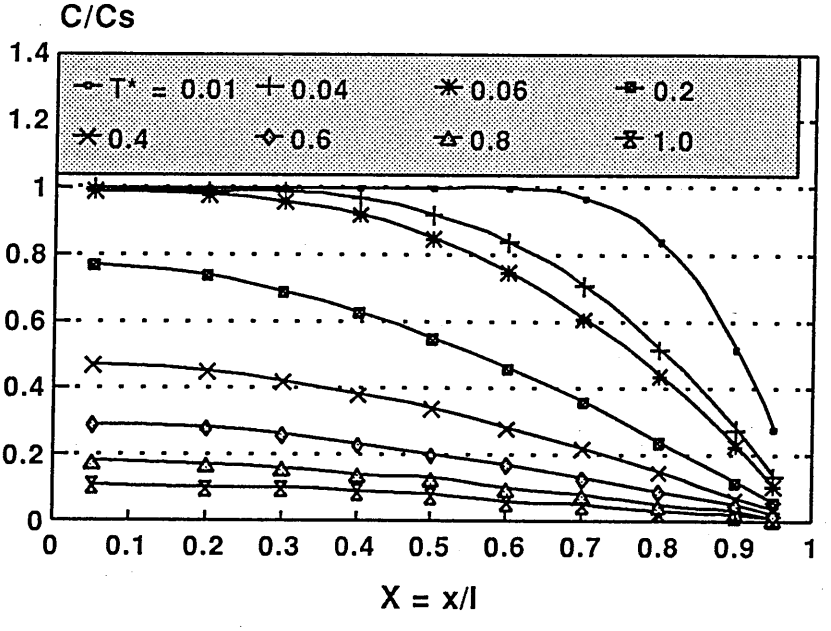

T* = Dt/l^2
Cs is saturated concentration of water

Figure 6.25 Moisture distribution in a sheet of Modar 8035 for the case of Fickian diffusion (23°C).

CHAPTER 7

FRACTURE

7.1 Introduction

Figure 7.1 is a typical diagram which shows the change of fracture strength σ_c of Modar 8035 caused by physical aging. σ_c can be as high as 91 MPa and as low as 26 MPa, depending on the aging time. The question is what is the key factor that determines the fracture behaviour of the Modar 8035 and the modified composites. As mentioned before, fracture prediction is of great importance to designers, engineers and materials scientists. Some theoretical aspects on the subject have been covered in Chapter two. Based on the theories, the current chapter is going to analyze experimental results, from which some mechanisms that cause failure of Modar 8035 resin and the modified composites will be discussed.

7.2 Experimental Results

7.2.1 Fracture strength σ_c

The experimental results of fracture strength σ_c of Modar 8035 resin and the modified composites are shown in Tables 7.1 and 7.2 and Figure 7.2. The rubber used is Paraloid BTA 753. All the hybrid composites are based on the matrix toughened with 15 wt % of rubber.

Table 7.1 Fracture strength σ_c of rubber toughened Modar 8035.

Materials	T00F00	T05F00	T10F00	T15F00
σ_c (MPa)	61 ± 10	59 ± 4	57 ± 1	50 ± 1

Table 7.2 Fracture strength σ_c of hybrid Modar 8035*.

Materials	T15F00	T15F10	T15F20	T15F30	T15F40	T15F46
σ_c (MPa)+	50	51	53	55	57	58

* all with 15 wt % rubber in the matrix.

\+ Data scattered: ± 1 MPa for all materials tested.

The materials were left to stand in an open laboratory at 23°C for several months before testing. Specimens made from these materials are termed 'normal' ones equilibrated with laboratory atmosphere at 23°C, comparing to those which were either fully dried or water saturated. For the latter two cases, the strengths of three typical materials - T00F00, T15F00 and T15F46 - are listed in Table 7.3 and the corresponding diagram is Figure 7.3.

Table 7.3 The influence of moisture on fracture strength σ_c (MPa) of Modar 8035 and the modified composites.

Materials	T00F00	T15F00	T15F46
Normal specimens	61 ± 10	50 ± 1	58 ± 1
Water-saturated	53 ± 10	46 ± 1	53 ± 1
Fully-dried	80 ± 10	59 ± 1	61 ± 1

Figure 7.2 shows that rubber reduces the strength σ_c while filler increases it. For example, σ_c decreases from 61 MPa to 50 MPa after incorporation of 15 wt % rubber in the Modar resin (Table 7.1). For the rubber toughened matrix, σ_c increases from 50 MPa to 59 MPa at 46 wt % filler loading (Table 7.2).

Moisture has a negative influence on strength as shown in Figure 7.3, where moisture concentrations are 3.2, 3.2 and 1.8 wt % (Table 5.1) for the wet materials T00F00, T15F00 and T15F46 respectively. 'Normal' specimens can contain moisture as high as 0.98, 0.84 and 0.50 wt % for the same materials. These values were obtained from the materials which were left to stand in an open laboratory about 18 months. No moisture is assumed for the dried materials which were dried under full vacuum at 65°C for 35 days in this case. In general, the fracture strength is in the order of: wet < normal < dried materials.

Another fact that needs to be emphasized is the data scattering for unmodified Modar 8035. The data scattered of fracture strength σ_c normally lies in ± 10 MPa. Sometimes it is bigger than that. This can be seen in Table 7.4, for tensile specimens of Modar 8035 aged in distilled water at 100°C from 0 to 46 days. All the aged specimens were dried under full vacuum at 65°C for about 7 days then gradually cooled down and kept in a desiccator at 23°C before testing. Figure 7.1, which was shown previously, is based on the data in Table 7.4. The fracture strength σ_c of the aged material decreases after a certain time. It is at this time when disc-like cracks start to develop (Figure 5.9 in Chapter 5). Further discussion on the subject will follow later.

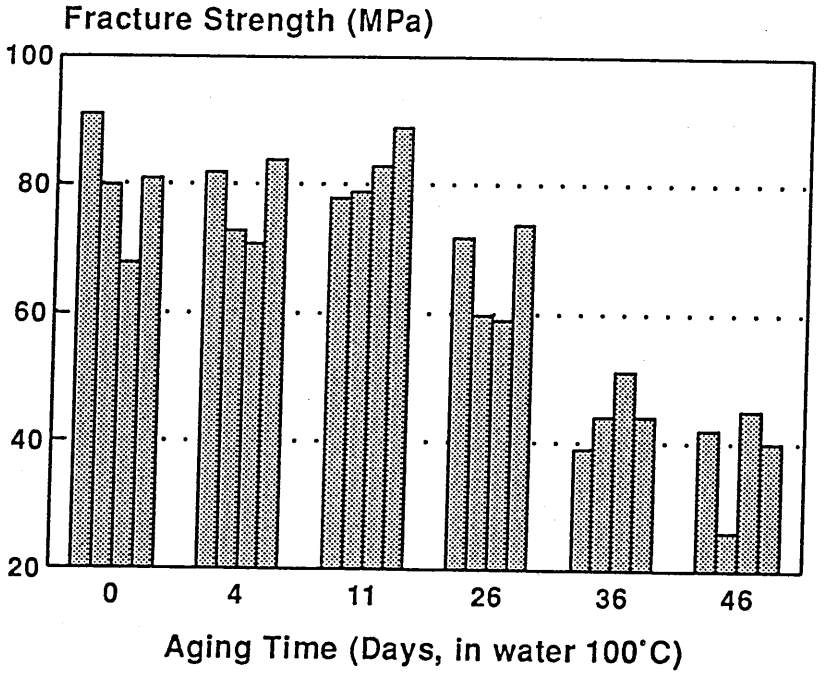

Figure 7.1 The influence of aging time on fracture strength of Modar 8035 resin (23°C).

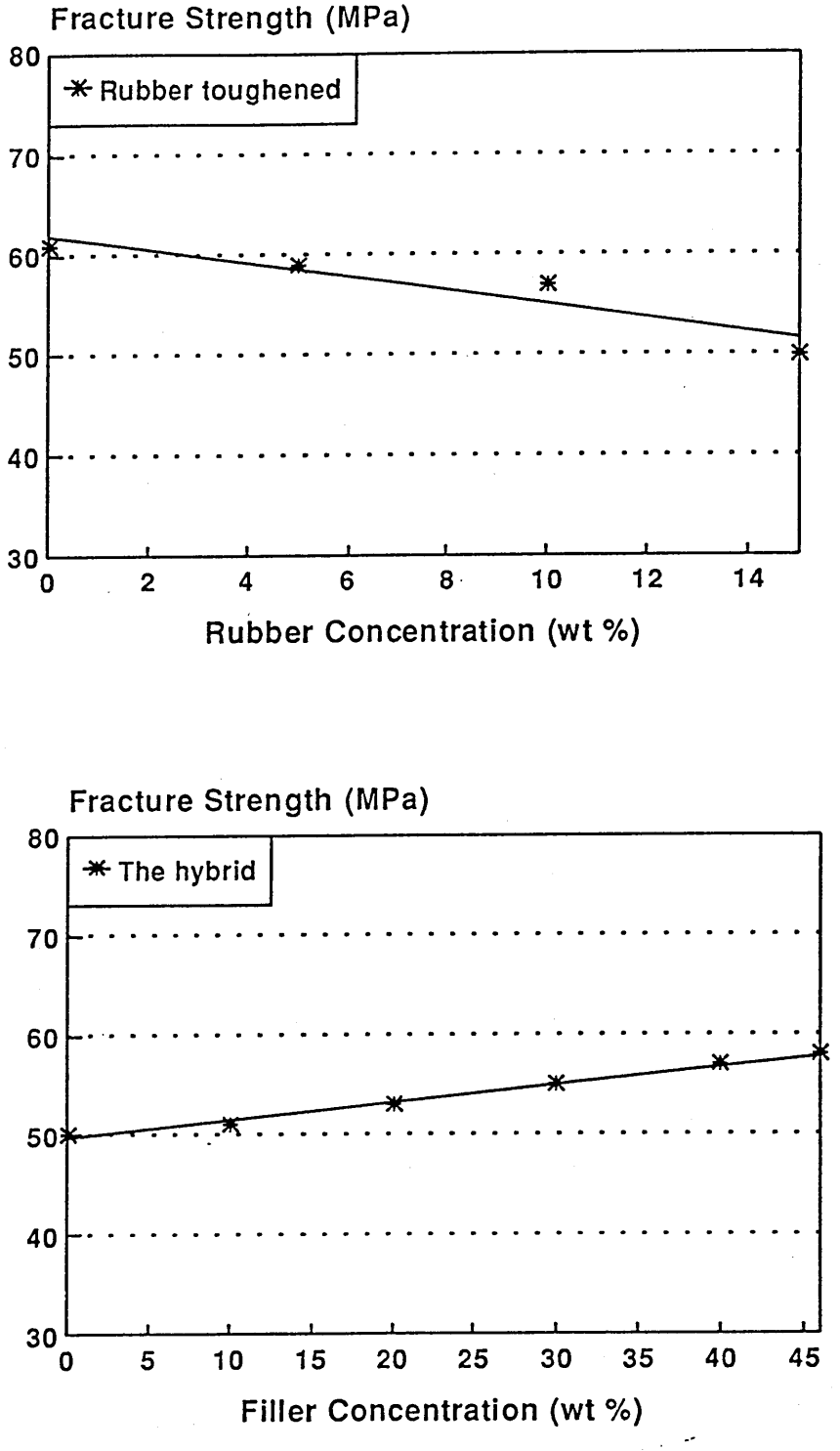

Figure 7.2 The influences of rubber and filler on fracture strength in rubber-modified Modar 8035 resins (top) and hybrid composites based on the matrix toughened by 15 wt % rubber (bottom) (23°C).

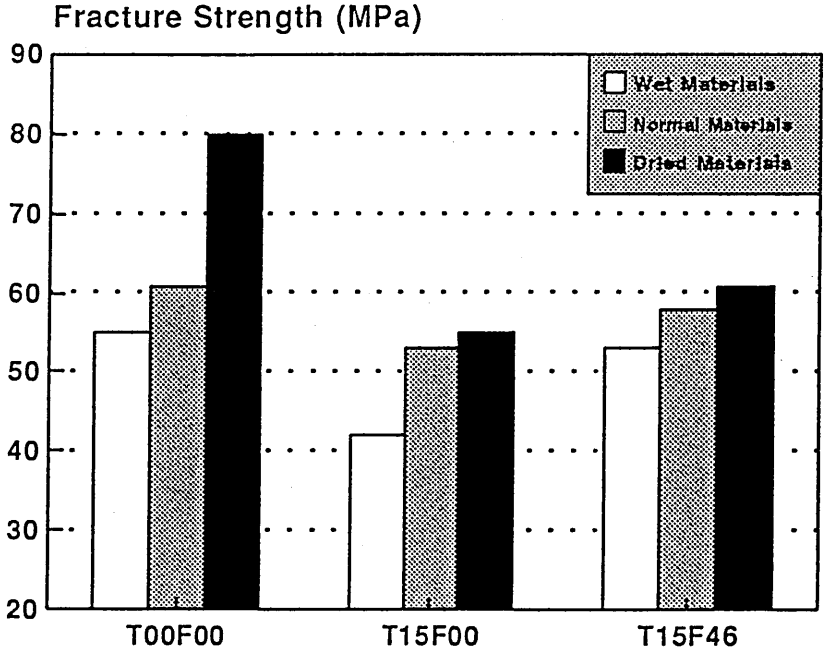

Figure 7.3 The influence of moisture on fracture strength of Modar 8035(T00F00), the rubber toughened (T15F00) and hybrid composites (T15F46) (23°C).

Table 7.4 Influence of aging time* on fracture strength σ_c (MPa) of Modar 8035 resin.

Specimen (No.)	Aging Time (Days)					
	0	4	11	26	36	46
1	91	82	78	72	39	42
2	80	73	79	60	44	26
3	68	71	83	59	51	45
4	81	84	87	74	44	40

* The tensile specimens were kept in distilled water at 100°C for the time indicated in the table then dried under full-vacuum at 65°C for about 7 days.

7.2.2 Fracture toughness K_{IC} and critical energy release rate G_{IC}

Fracture toughness K_{IC} and critical energy release rate G_{IC} of Modar 8035 resin and the modified composites are collected in Tables 7.5 and 7.6. The materials in Table 7.5 were toughened with Paraloid BTA 753 rubber. The hybrid composites in Table 7.6 were filled with silica flour XPF6, all based on the Modar matrix toughened by 15 wt % rubber. Those materials are termed 'normal' ones which were equilibrated with laboratory atmosphere at 23°C. The results of K_{IC} for dried materials are also listed in these two tables.

Table 7.5 Fracture toughness K_{IC} and critical energy release rate G_{IC} of Modar 8035 resins toughened by Paraloid BTA 753 rubber.

Materials	T00F00	T05F00	T10F00	T15F00
K_{IC} (MPa $m^{1/2}$)	0.50	1.06	1.22	1.52
	0.59*	0.90*	1.16*	1.34*
G_{IC} (kJ m^{-2})	0.07	0.33	0.49	0.83

* Fully-dried materials.

Note: (a) the data scattered of K_{IC} ± 0.05 MPa $m^{1/2}$; (b) G_{IC} is calculated from Equation (2.10b) using the E and ν data in Table 6.1 and the K_{IC} values above; (3) thickness of specimens: about 4 mm.

Table 7.6 Fracture toughness K_{IC} and critical energy release rate G_{IC} of hybrid Modar 8035 all with 15 wt % Paraloid BTA 753 rubber in the matrx.

Materials	T15F00	T15F10	T15F20	T15F30	T15F40	T15F46
K_{IC} (MPa $m^{1/2}$)	1.52	1.56	1.61	1.54	1.72	1.82
	1.34*	1.39*	1.48*	1.44*	1.53*	1.62*
G_{IC} (kJ m^{-2})	0.83	0.79	0.74	0.58	0.64	0.61

* Fully-dried materials.

Note: (a) the data scattered of K_{IC} ± 0.05 MPa $m^{1/2}$; (b) G_{IC} is calculated from Equation (2.10b) using the E and ν data in Table 6.2 and the K_{IC} values above; (3) thickness of specimens: about 4 mmm.

In general, fracture toughness K_{IC} increases with both rubber and filler concentration. These features are shown in Figure 7.4, where the upper plot is for the rubber toughened materials and the lower one for the hybrid composites. About a three times increase in K_{IC} has been obtained after incorporation of 15 wt % rubber. For example, K_{IC} of the unmodified resin is 0.50 MPa $m^{1/2}$. It increases to 1.52 MPa $m^{1/2}$ at 15 wt % rubber concentration. Based on the rubber toughened matrix, a further increase in K_{IC} has also been obtained by incorporation of filler. K_{IC} increases from 1.52 to 1.82 $MPa^{1/2}$ at 46 wt % filler loading.

Critical energy release rate G_{IC} increases with rubber concentration but decreases with filler. This is shown in Figure 7.5, where the upper plot is for the rubber toughened materials and lower one for the hybrid composites. G_{IC} increases from 0.07 kJ m^{-2} for the unmodified Modar resin to 0.83 kJ m^{-2} for the material toughened by 15 wt % rubber. Based on the rubber toughened Modar matrix, G_{IC} decreases with increasing filler concentration. At 46 wt % filler loading, G_{IC} reduces to 0.61 kJ m^{-2}.

Moisture has an influence on K_{IC} and G_{IC}. K_{IC} values of dried materials are systematically lower than those of non-dried materials as indicated in Figure 7.4 and Tables 7.5 and 7.6 except for the unmodified Modar 8035 resin.

Further evidence on the influence of moisture is shown in Table 7.7 and Figure 7.6 for three typical materials - T00F00, T15F00 and T15F46. SENB specimens of about 6 mm thick made from these materials were kept in distilled water at 100°C for about 20 days then gradually cooled down and kept in distilled water at 23°C for another 3 days before testing. In addition, some of the specimens were re-dried under vacuum at 65°C for about 7 days.

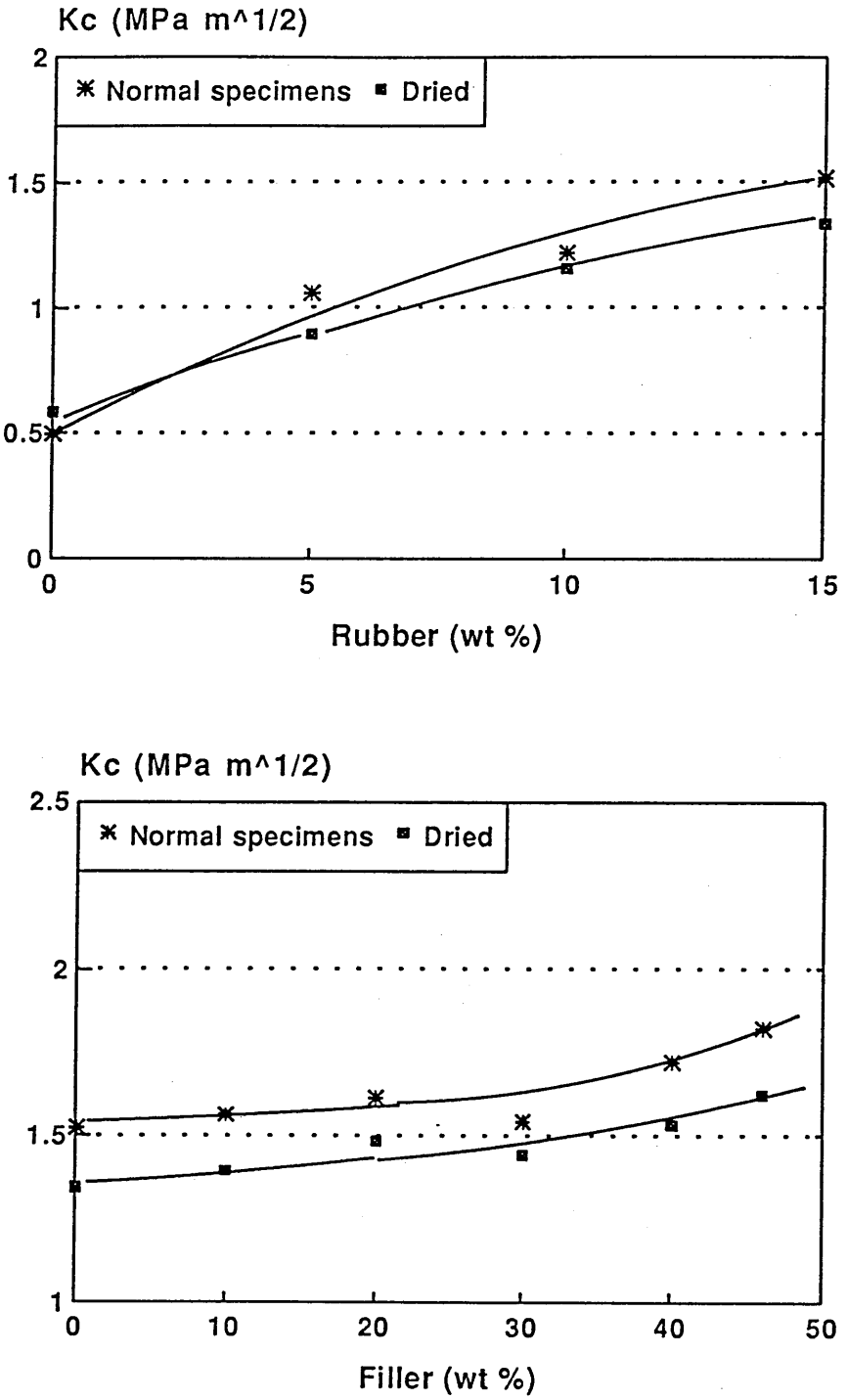

Figure 7.4 Fracture toughness of rubber-modified Modar 8035 (top) and the hybrid composites based on the Modar matrix toughened by 15 wt % rubber (bottom) (23°C)

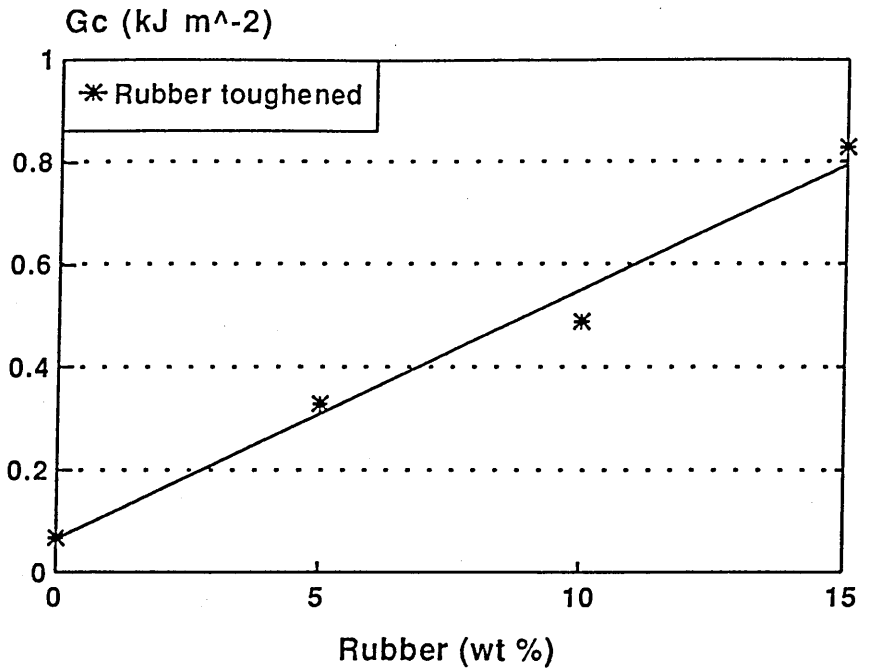

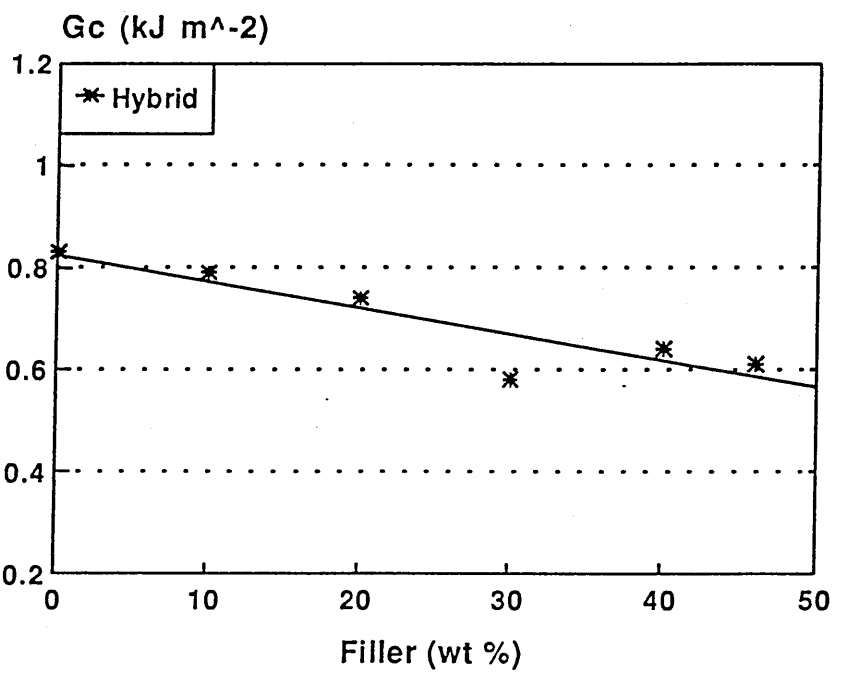

Figure 7.5 Critical energy release rate of rubber-modified Modar 8035 (top) and the hybrid composites all with 15 wt % rubber in the matrix (bottom) (23°C)

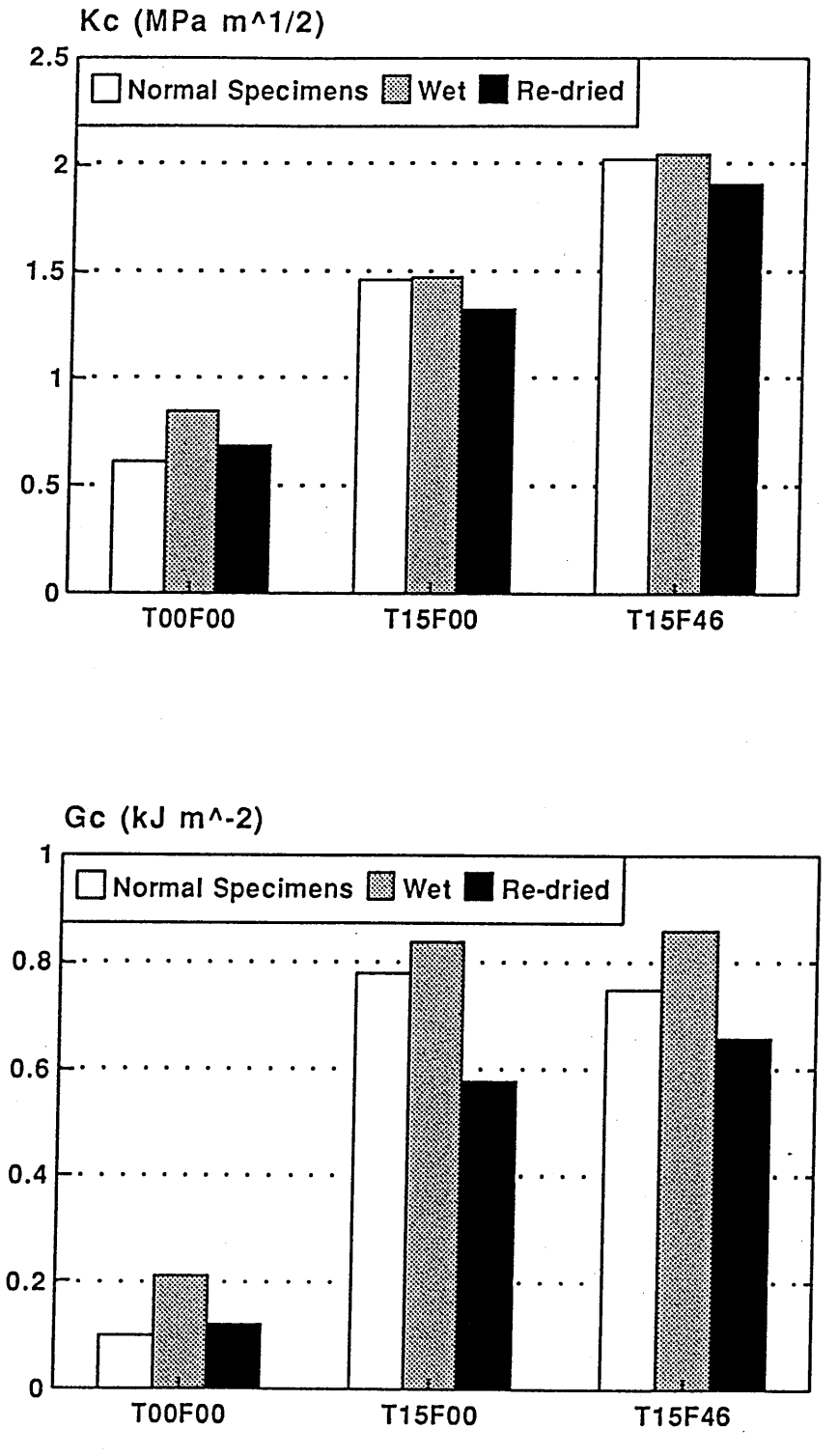

Figure 7.6 The influence of moisture on fracture toughness (top) and critical energy release rate (bottom) for Modar 8035 (T00F00), rubber-modified (T15F00) and the hybrid composite (T15F46) (23°C).

Table 7.7 The influence of moisture on fracture toughness K_{IC} (MPa $m^{1/2}$) and critical energy release rate G_{IC} (kJ m^{-2}) of Modar 8035 resin and the modified composites.

Materials	T00F00		T15F00		T15F46	
	K_{IC}	G_{IC}	K_{IC}	G_{IC}	K_{IC}	G_{IC}
Normal	0.61	0.10	1.47	0.78	2.03	0.75
Wet	0.85	0.21	1.48	0.84	2.05	0.86
Re-dried	0.69	0.12	1.32	0.58	1.91	0.66

Note: (a) The thickness of specimens used was about 6 mm. The values of K_{IC} differ from those in Tables 7.5 and 7.6 to a certain extent, especially for the material T15F46, where 4 mm thick specimens were used. (b) G_{IC} is calculated from Equation (2.10b) using the data in Tables 6.1, 6.2 and 6.5 and the K_{IC} above.

As shown in Figure 7.6, a considerable increase in K_{IC} with water absorption occurs only for the unmodified Modar resin. Little change can be observed for the modified resins T15F00 and T15F46 (the upper plot). However, a significant decrease in K_{IC} occurs for all the materials after moisture has been driven out of the systems. The value of K_{IC} is in the order of wet > dried > normal for the unmodified Modar resin. For the modified resins T15F00 and T15F46, it is in the order of wet ≈ normal > dried materials.

The change in G_{IC} has also been shown in Figure 7.6 (the lower plot). In general, the more the moisture, the higher the G_{IC}. The differences in G_{IC} between wet and dried specimens are 0.09, 0.26 and 0.20 kJ m^{-2} for materials T00F00, T15F00 and T15F46 respectively. Differences also exist between normal and dried specimens for T15F00 and T15F46 but T00F00. For the latter, G_{IC} is 0.10 kJ m^{-2} for normal specimens and 0.12 kJ m^{-2} for dried ones (Table 7.7).

The crack tip radius ρ affects fracture toughness K_{IC} too. The values of K_{IC} measured for different ρ are listed in Table 7.8. The Modar resin was toughened by two types of rubber, Paraloid BTA 753 and XC 37, both at 10 wt % concentration. The specimens were dried under full vacuum at 65°C for about 7 days. The change in K_{IC} with ρ is shown in Figure 7.7 using the data in Table 7.8. The plot is of K_{IC} against $\rho^{1/2}$. The upper plot is for the material toughened by Paraloid BTA 753 and the lower one by XC 37. The lowest value in the plot was obtained through the standard described in Chapter 4, where a sharp notch was

Table 7.8 The influence of the radius of the crack tip ρ (μm) on fracture toughness K_{IC} (MPa $m^{1/2}$) of Modar 8035 toughened by 10 wt % rubber.

Rubber	ρ (μm)				
	5*	50	500	750	1000
BTA 753	1.15	1.58	2.89	3.61	3.71
XC 37	1.15	1.56	2.70	3.66	3.92

* It is estimated under microcope. The sharp notch was made by the standard described in Chapter 4. Note: The rest of the notch ρ = 50 - 10000 μm was made by a cutter with the radius.

made with a new razor blade. The radius made in this way is estimated about 5 μm approximately. The rest of the K_{IC} values were measured according to the standard but using the specimens with different crack tip radius, which was made either with a V-shaped cutter or by drilling a hole with a specific diameter.

The results in Table 7.8 and Figure 7.7 have clearly demonstrated the strong influence of the crack tip radius on K_{IC}. A significant increase in K_{IC} has been obtained by increasing ρ. For example, K_{IC} is 1.15 MPa $m^{1/2}$ when the tip radius is about 5 μm. It increases to 3.6 MPa $m^{1/2}$ when ρ increases to 750 μm. The types of rubber used appear to have little influence on K_{IC} in the experiment. Paraloid BTA 753 is a 2-layer core-shell polymer while XC 37 is a 4-layer core-shell one (Figure 4.2 in Chapter 4). The glass transition temperature T_g is -74°C for the former and -13°C for the latter, which was measured by DSC at scanning rate 10°C min^{-1}. It should be borne in mind that those K_{IC} data with high crack tip radius do not meet the requirement as discussed in Chapter 4. They might be useful only in application of crack tip blunting theory (Kinloch and Williams 1980).

7.2.3 Fatigue crack propagation (FCP)

The experimental results of fatigue crack propagation (FCP) are shown in Figure 7.8. The plot is of logarithm FCP against logarithm ΔK. ΔK is stress intensity range (K_{max} - K_{min}) as defined in Chapter 4. The materials tested are Modar 8035 (T00F00), rubber toughened (T15F00) and the hybrid composite (T15F46). They were dried before testing. The rubber used is Paraloid BTA 753.

The hybrid composite T15F46 has demonstrated the best fatigue properties among the resins

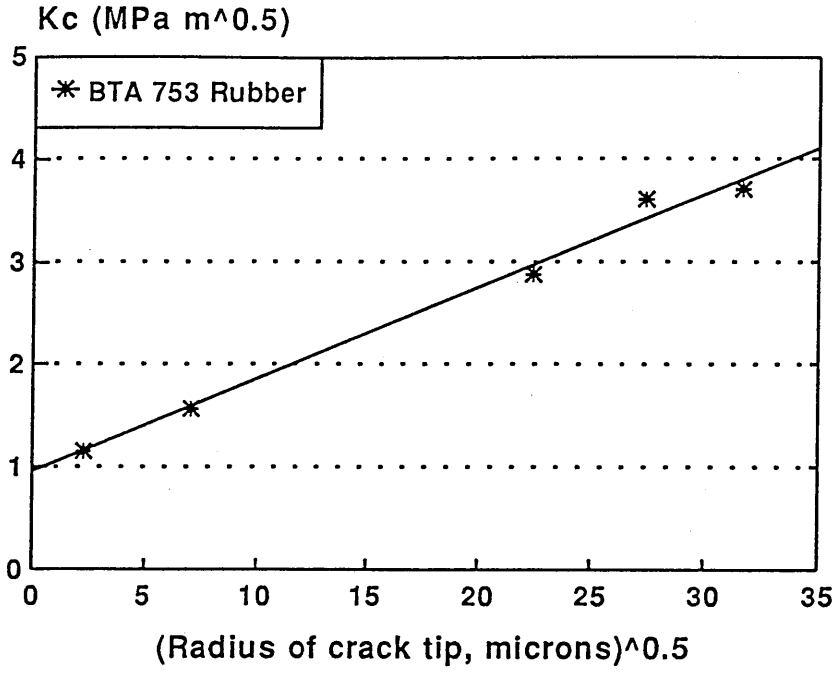

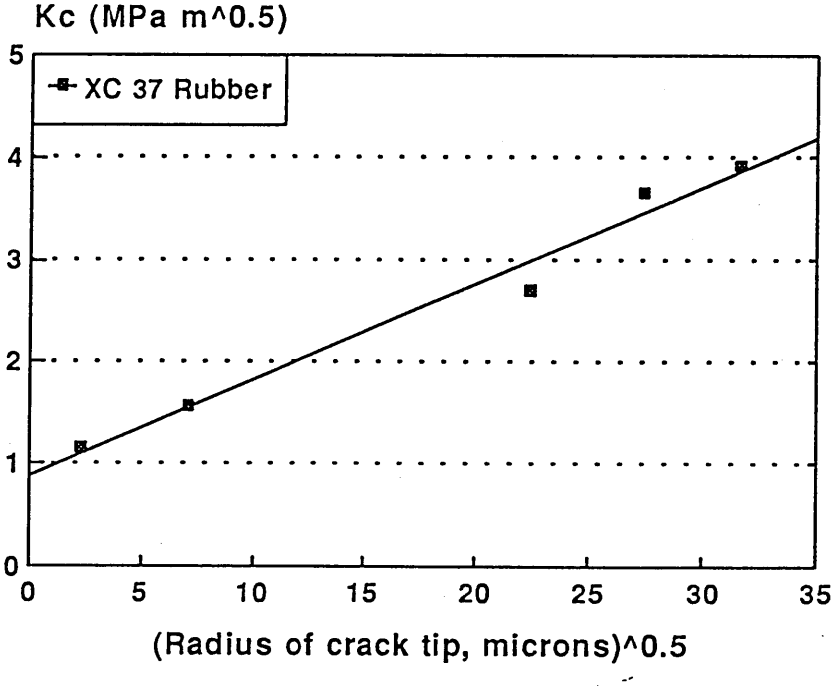

Figure 7.7 The influence of crack tip radius on fracture toughness of Modar 8035 toughened by 10 wt % rubber: Paraloid BTA (top) and XC 37 (bottom) (23°C).

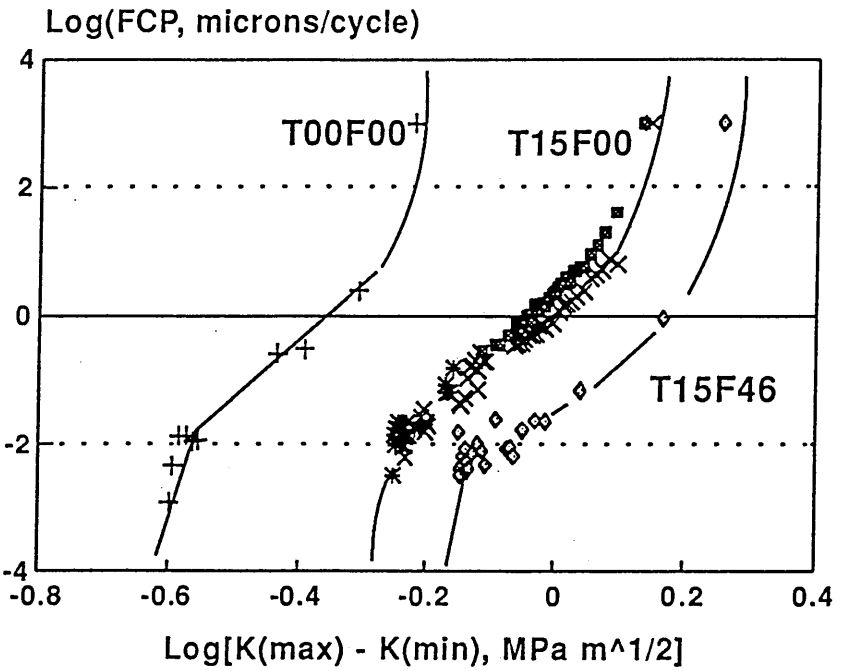

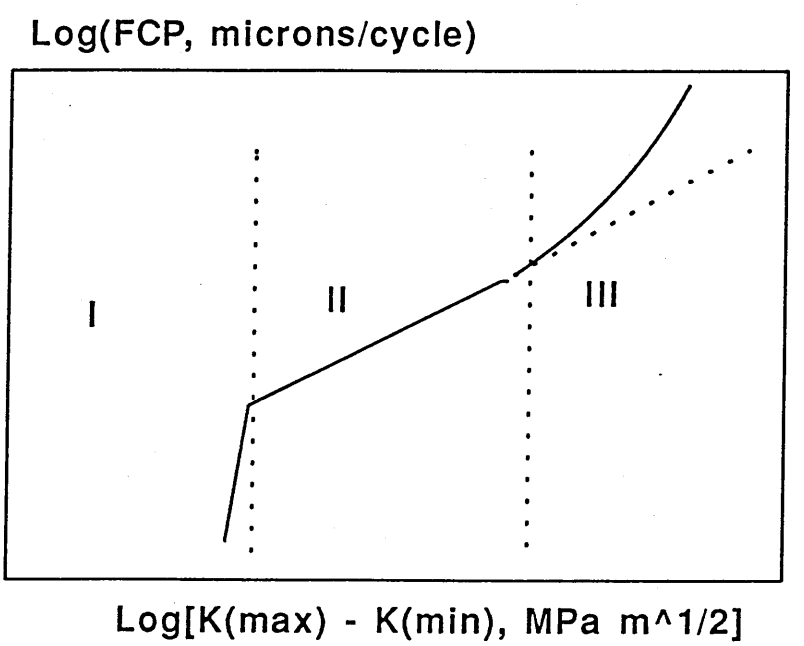

Figure 7.8 The relationships between fatigue crack propagation (FCP) and a range of stress intensity factor of Modar 8035 resin T00F00, rubber toughened T15F00 and hybrid composite T15F46 (23°C).

investigated. The next best is the rubber toughened T15F00. In Figure 7.8, the highest points of FCP are the values in the last fatigue cycling. They represent the critical stress intensity factor K_{IC} for the materials, which are 0.6, 1.4 and 1.8 MPa $m^{1/2}$ for T00F00, T15F00 and T15F46 respectively. They are very close to the values of K_{IC} measured by SENB tests as shown in Tables 7.5 and 7.6.

7.3 Discussions

7.3.1 Fracture of Modar 8035

For most solid materials, theoretical strength σ_{theo} is about one tenth of their Young's modulus, i.e.:

$$\sigma_{theo} \approx E/10 \qquad (7.1)$$

In fact, fracture strength is normally much less σ_{theo}, even for single crystal fibre of polymer. For example, the single crystal fibre of polydiacetylene has Young's modulus about 60 GPa (Kinloch and Young 1983). So, the theoretical strength should be about 6 GPa. The measured strength is about 2 GPa, three times less than theoretical one. For Modar 8035 resin, both Young's modulus, which is about 3 - 4 GPa (Tables 6.1, 6.3 and 6.5), and fracture strength are much less than these values. The highest fracture strength σ_c obtained in this research is 91 MPa (Table 7.4).

The factor that causes the fracture strength σ_c of real materials to be much less than σ_{theo} is the presence of flaws which naturally occur in materials during manufacturing or in service. In this research, it has been found that the fracture of Modar 8035 started either at defects occupied by impurities or at disc-like cracks developed in water environments in most cases. Of interest is the position from which fracture originates.

The probability that fracture starts from a corner or surface defect along the gauge portion of a tensile specimen (see Figure 6.1) is approximately 50 % for non-water-aged materials. The statistical result is based on 15 specimens fractured. None of them fractured at internal defects in the Modar resin.

Contrary to these findings, internal defects dominate the fracture behaviour after the Modar resin has been aged in distilled water at 100°C for more than 4 days. The probabilities that the Modar resin fractures from corner, surface and internal defects are listed in Table 7.9.

7.9 The probabilities (%) that fracture starts from corner, surface or internal defects of Modar 8035.

Defect	Aging Time (Days)					
	0	4	11	26	36	46
Corner	50	17	13	0	0	0
Surface	50	25	25	14	0	0
Internal	0	58	72	86	100	100

It can be seen that the probability that internal defects cause the material failure increases with increasing aging time. Eventually, they are the only factors that determine the fracture behaviour of the Modar resin. All failure of the material is caused by internal defects.

Two types of defects have been identified for Modar 8035 resin in this research. The first consists of aggregates of 'impurities' which are inorganic compounds containing elements Na, Al, Si, S, Cl, Ca, Cr etc as indicated in Figure 7.9. The second is in the form of disc-like cracks which develop from the impurity aggregates. This is shown in Figure 7.10, where the inorganic compounds are in the centre of the disc-like crack.

The relationships between the defect size and fracture strength have been discussed in Chapter 2. The critical stress intensity factor can generally be expressed by:

$$K_{IC} = Y\sigma_c\sqrt{\pi a} \tag{7.2}$$

For embedded defects, the geometric factor Y is (Ewalds 1986):

$$Y = C2/\pi \tag{7.3}$$

where C = 1, 1.12 and 1.2 for embedded circular disc defects, semi-circular surface defects and quarter-circular corner defects respectively.

Taking K_{IC} = 0.59 MPa $m^{1/2}$ for dried Modar 8035 (Table 7.5), the relationships between fracture strength σ_c and defect size are shown in Figure 7.11, according to Equations (7.2) and (7.3).

Two conclusions can be drawn from the plot. The first is that σ_c decreases with increasing

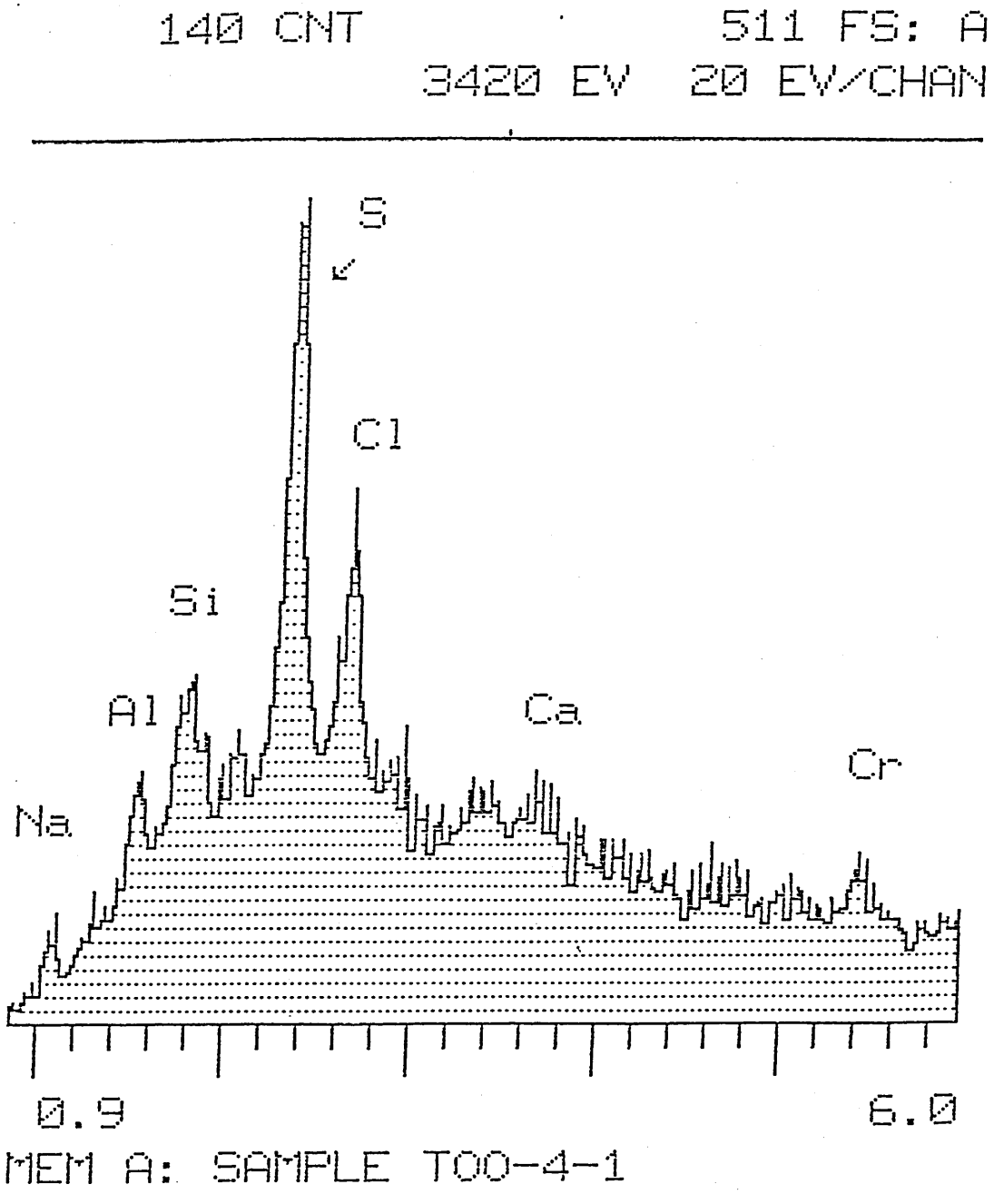

Figure 7.9 Chemical elements in the impurities in Modar 8035 resin.

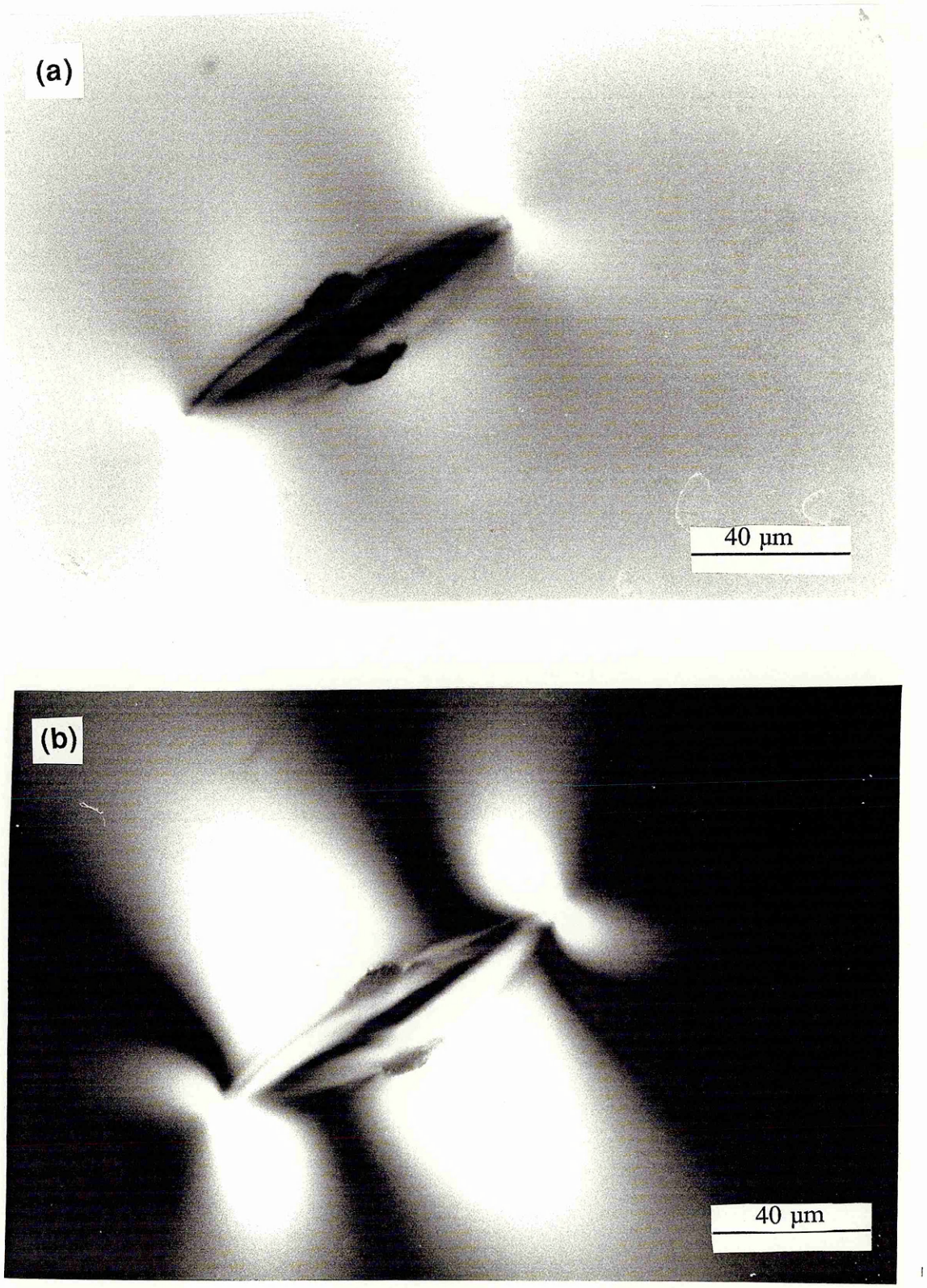

Figure 7.10 Disc-like crack originated from the impurities (in the centre of the crack) in Modar 8035 resin.

defect size. The second is that, for a given defect size, internal flaws give rise to the highest fracture strength. The next best is a surface flaw. Corner defects are the worst. This is why all fracture of non-water-aged Modar 8035 starts from either corner or surface defects.

As discussed previously, impurities are the main defects which occur in the Modar resin. The probability that these defects exist in the corners is smaller than in the surfaces along the gauge of a tensile specimen. Because corner defects are the worst, the probability that fracture starts from them increases and one of the worst corner defects would be enough to cause material failure. So, this may explain why the probabilities that fracture from corner defects and surface ones are approximately equal, as found in this research (Table 7.9).

For the Modar resin which was aged in distilled water at 100°C over 4 days, fracture strength σ_c varies with aging time as shown in Table 7.4 and Figure 7.1. σ_c can be as high as 91 MPa and as low as 26 MPa. However, the critical stress intensity factor remains almost the same, as calculated from the fracture strength σ_c (Table 7.4) and defect size in Table 7.10. The

Table 7.10 Aging time* and crack size (microns) from which fracture originated in Modar 8035 resin (corresponding to the fracture strength σ_b in Table 7.4).

Specimen	Aging Time (Days)					
(No.)	0+	4	11	26	36	46
1: 2a	-	75	75	100	350	450
2c	-	75	150	100	370	450
2: 2a	-	-	-	150	200	800
2c	-	-	-	150	480	800
3: 2a	-	65	125	80	200	330
2c	-	125	125	300	320	330
4: 2a	-	100	60	60	450	200
2c	-	100	110	225	450	460

* The tensile specimens were kept in distilled water at 100°C for the time as indicated in the table then dried under full-vacuum at 65°C for about 7 days.

\+ Fracture starts from either corner or surface defects for all the specimens tested.

defect sizes were measured from the fracture surfaces, assuming that they are embedded elliptical defects, no matter whether they are in the form of impurity aggregates or in the form of disc-like cracks (Figure 7.10). It should be borne in mind that the largest defects cause material failure. The specimen numbers in Table 7.10 correspond to the same numbers in Table 7.4.

Y factor for an embedded elliptical defect is (Ewalds 1986):

$$Y = \frac{(\sin^2\phi + \frac{a^2}{c^2}\cos^2\phi)^{\frac{1}{4}}}{\frac{3\pi}{8} + \frac{\pi}{8}\frac{a^2}{c^2}} \qquad (7.4)$$

where 'c' is half of the major axis, 'a' half of the minor axis and ϕ is the angle, a parameter normally used for elliptical equations as indicated in Figure 7.12. Taking the average value of the function $[\sin^2\phi + (a^2/c^2)\cos^2\phi]$ (in Equation 7.4) from $\phi = 0$ to $\phi = 2\pi$, it results in $(1 + a^2/c^2)/2$. Then Equation (7.4) becomes:

$$Y = \frac{\left(\frac{1}{2} + \frac{a^2}{2c^2}\right)^{\frac{1}{4}}}{\frac{3\pi}{8} + \frac{\pi}{8}\frac{a^2}{c^2}} \qquad (7.5)$$

Table 7.11 collects the results of K_{IC} calculated according to Equations (7.2) and (7.5) using the data of σ_c in Table 7.4 and 'a' and 'c' in Table 7.10. The average value of K_{IC} in the table is 0.59 MPa $m^{1/2}$. This result agrees very well with the value K_{IC} = 0.59 MPa $m^{1/2}$ (Table 7.5) measured from SENB test.

The fracture stress σ_c changes from 91 MPa to 26 MPa (Table 7.4 and Figure 7.1) and the defect size changes from 65 μm to 800 μm (Table 7.10). However, the corresponding K_{IC} remains almost constant. Figure 7.13 is the plot which shows the big difference in defect size but small deviations in K_{IC}, which varies about the average value 0.59 MPa $m^{1/2}$. This fact demonstrates the importance of the critical stress intensity factor K_{IC} and the success in applying fracture mechanics to the material Modar 8035 resin.

Based on these results, Equation 7.2 with the corresponding geometric factor Y can be used to relate the fracture behaviour of Modar 8035 resin to the defects in the material. From Figure 7.11, it can be estimated that the size of corner or surface defects in terms of radius,

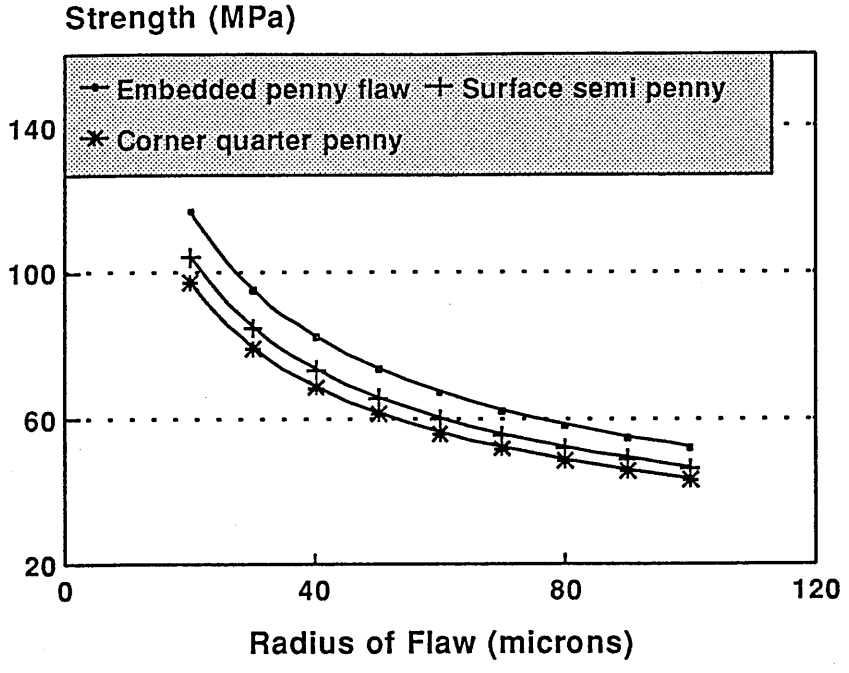

Figure 7.11 The influence of defect size on fracture strength.

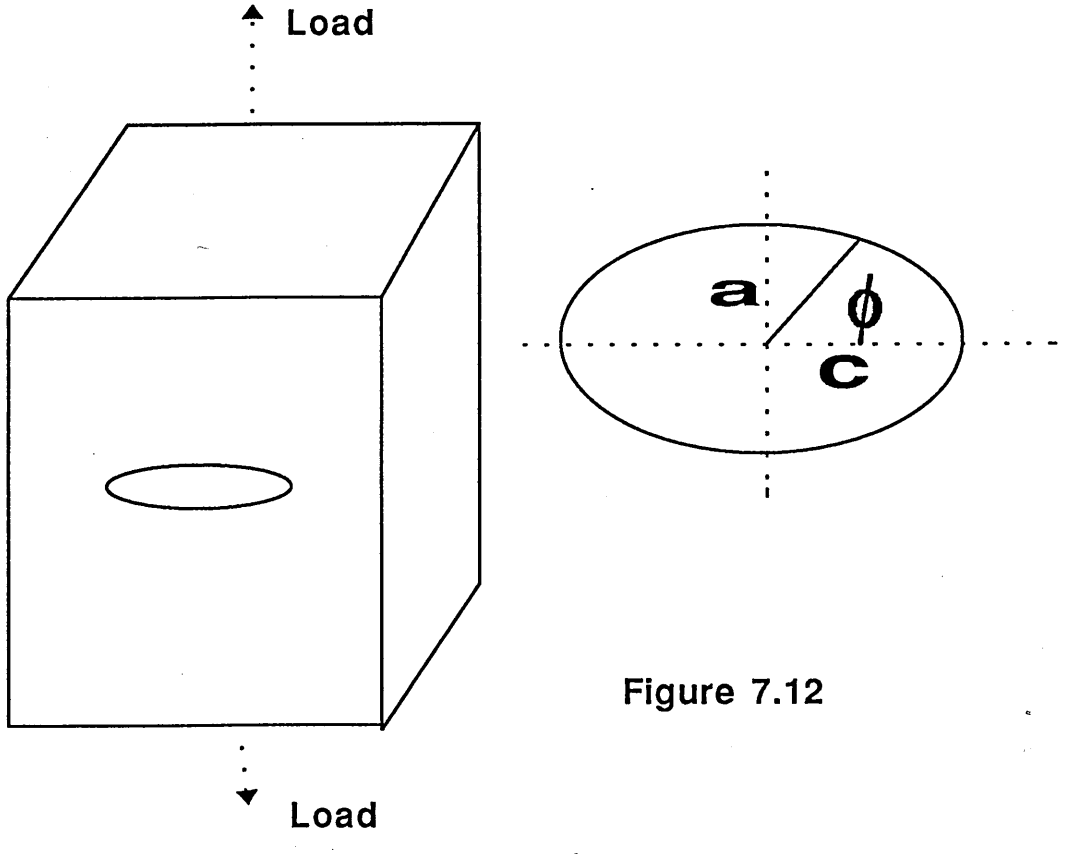

Figure 7.12

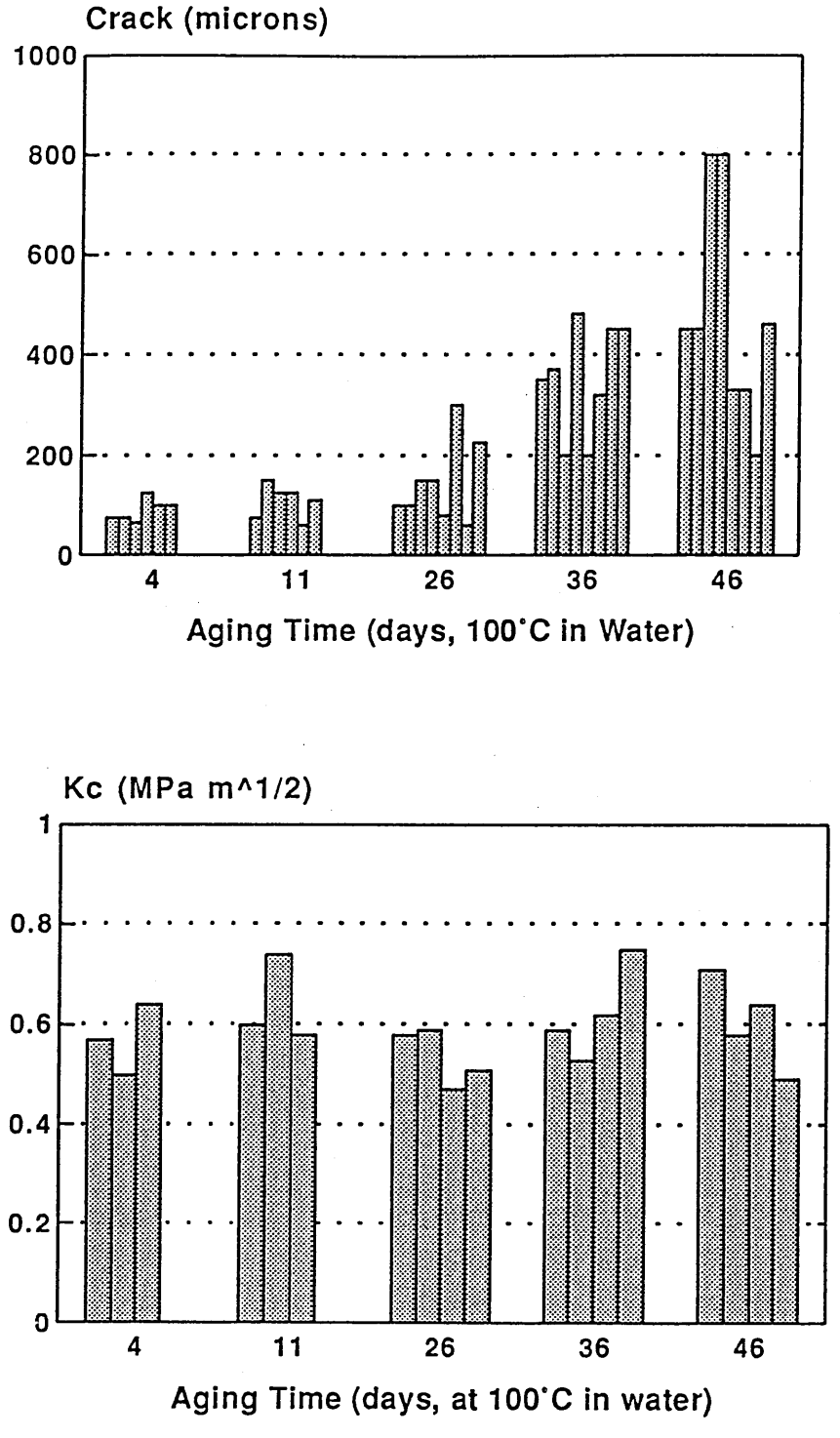

Figure 7.13 The influence of aging time on internal defect size (top) and fracture toughness (bottom) of Modar 8035.

Table 7.11 Influence of aging time* on fracture toughness K_{IC} (MPa $m^{1/2}$) of Modar 8035 resin.

Specimen	Aging Time (Days)					
(No.)	0+	4	11	26	36	46
1	0.57	0.57	0.60	0.58	0.59	0.71
2	0.61	-	-	0.59	0.53	0.58
3	0.55	0.50	0.74	0.47	0.62	0.65
4	0.59	0.64	0.58	0.51	0.75	0.49

* The tensile specimens were kept in distilled water at 100°C for the time indicated in the table then dried under full-vacuum at 65°C for about 7 days.

+ The results of SENB tests of 6 mm thick specimens dried under full-vacuum at 65°C for 35 days. The rest are calculated using the data in Tables 7.4 and 7.10.

responsible for the material failure, varies from about 20 μm to 40 μm for the dried but not water-aged Modar resin because the fracture strength σ_c is in a range from 70 to 90 MPa (Table 7.4). It may be assumed that the same defect sizes also exist within the material. After the material has aged in water but before disc-like cracks develop, the size of the defect may increase, especially inside the material because the probability that fracture starts from internal defects rises sharply (Table 7.9). The radius for an internal penny-shaped defect can be estimated from Equations 7.2 and 7.3. Consider the σ_c data on aging time 4 and 11 days in Table 7.4: the radius of the corresponding defects is in a range from 43 to 63 μm, i.e. about 80 to 120 μm in diameter. K_{IC} = 0.59 MPa $m^{1/2}$ (Table 7.5) of the dried Modar resin was used in the calculation. Again, it should be borne in mind that they are the maximum defect size.

As found in this research, the original defects are aggregates of impurities, the expansion of which eventually leads to the formation of disc-like cracks inside the material. The defect size increases dramatically as soon as disc-like cracks are formed as indicated in Figures 7.10 and 7.13.

What kind of internal force causes the formation of the disc-like cracks ? The internal stress which is needed to initiate disc-like cracks can be estimated as follows.

The expression for the stress intensity factor due to an internal stress σ acting on an internal crack of length 2a has the same form as that when the same stress is applied at infinity (Ewalds 1986, Williams 1980). This is illustrated in Figure 7.14. So Equation 7.2 is also applicable to the stress field. Here it is termed internal stress σ_c, using defect radius 'r' instead of half crack length 'a':

$$K_{IC} = \frac{2}{\pi}\sigma_c\sqrt{\pi r} \qquad (7.6)$$

for the case of embedded circular disc cracks.

The K_{IC} of water-saturated Modar 8035 is not known at 100°C. What has been found is that an increase in temperature will reduce K_{IC} a little bit for not in water-aged Modar 8035. For example, it is 0.61 MPa $m^{1/2}$ at 23°C but 0.46 MPa $m^{1/2}$ at 60°C for the normal 6 mm thick specimens. At 23°C and for the water saturated Modar 8035, K_{IC} is equal to 0.85 MPa $m^{1/2}$ (Table 7.7). At 100°C, it may be bigger or less than the value. If it is assumed that the K_{IC} of the water-saturated Modar resin is in the range from 0.50 to 1.0 MPa $m^{1/2}$, the critical internal stress σ_c can be estimated according to the equation above. This is shown in Figure 7.15.

As discussed above, the defect radius can be as big as 60 μm. However, many defect sizes in the Modar resin are much less than 60 μm. Disc-like cracks also develop from them (Figure 5.9). For a defect of radius 10 μm (Figure 7.10), the critical internal stress σ_c is estimated to be in the range 140 to 260 MPa, corresponding to K_{IC} from 0.50 to 1.0 MPa $m^{1/2}$ (Figure 7.15). The question is: where does the internal stress σ_c come from ?

7.3.2 Mechanisms of formation of disc-like cracks

Three factors are probably responsible for generation of internal stress which initiates internal disc-like cracks from the impurities in Modar 8035 resin. They include:

(a) Modar shrinkage during cure: there is no stress on impurities while Modar is soft but, as soon as the resin starts to harden, it compresses the impurities.

(b) Thermal contraction: both resin and impurities contract on cooling to room temperature after resin hardening, but Modar has a higher coefficient of thermal expansion. Again, the impurities are compressed.

Figure 7.14

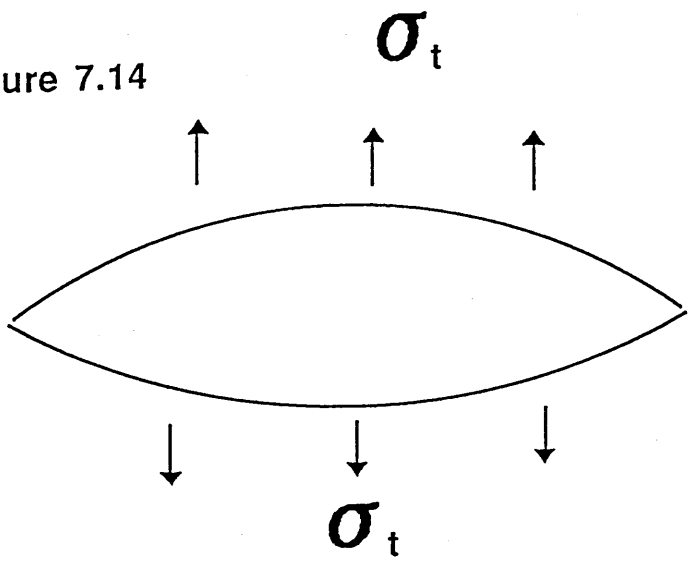

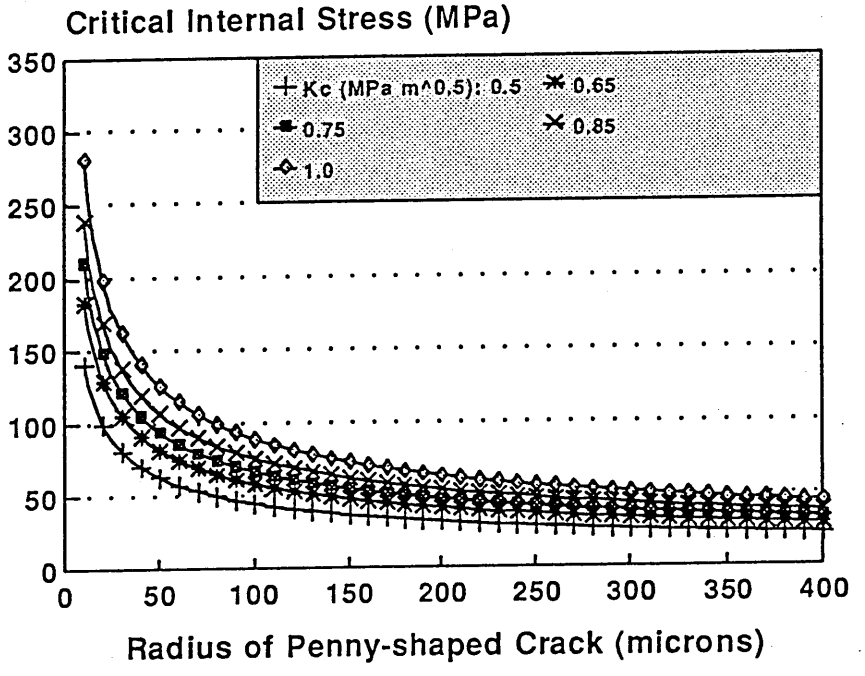

Figure 7.15 The relationships between critical internal pressure Pc and defect size for a range of fracture toughness from 0.5 to 1.0 MPa m^1/2.

(c) The impurities swelling in water: volume expansion of impurities produces extra internal pressure in addition to (a) and (b). Presumably, the Modar also swells, but to a lesser extent.

As a result, impurities will crack Modar if tangential stress at interfaces approaches the critical stress of the resin. The problem is how to calculate the stress.

In order to give a quantitative analysis about the stress field, factors (a) and (c) will be discussed in this section, neglecting factor (b). This is because only a small proportion of volume change may be caused by thermal contraction in the resin and in impurities, compared to the shrinkage of the resin which is about 11 %. As mentioned in Chapter 4, the Modar cured in a laboratory atmosphere at ambient temperature. The resin temperature may rise to 100°C for heat generation during polymerization (private communication with Dr M Orton, ICI). Taking the coefficient about 2 x 10^{-4} K^{-1} of PMMA as approximation, volume contraction of the resin is only 1.5 % when temperature changes from 100°C to 23°C. For metal compounds, their coefficients of thermal expansion are even much smaller than that of PMMA, in the order of 3 - 10 x 10^{-6} K^{-1} (Ref: Handbook of Chemistry and Physics, 72nd Edition, 1991-1992, CRC). Their volume change due to varying temperature is also negligible.

Shrinkage of Modar 8035 Resin

Consider a sphere of resin with a spherical aggregate of metal complexes in its centre. After cure, compressive pressure is expected to be built upon the aggregate.

If it is assumed that the aggregate of metal complexes were taken out, leaving a cavity in its place as indicated in Figure 7.16 (a). The cavity would become smaller after resin cure for volume shrinkage of the resin. Now, the aggregate is bigger than the space that would be occupied by the Modar that it displaced. In order to fit the aggregate back into the place from where it had been taken out, the cavity should dilate to the same dimensions as the metal compounds. To do so, an internal pressure was assumed to increase in the cavity until it approaches a value when the metal compounds could be fitted in. This internal pressure is approximately equal to the pressure on the impurity in the resin after cure.

The key point is to establish the relationship between the internal pressure and the volume change of the cavity. In addition, tangential stress at interfaces in the resin is also important, which is probably responsible for initiation of disc-like cracks when the stress is equal or greater than the critical stress of the resin. These problems are analyzed as follows:

Consider the resin sphere above as a spherical shell with internal and external radii 'a' and 'b' respectively as shown in Figure 7.16 (b), where 'r' is distance from the centre ($a \leq r \leq b$), σ_r and σ_t are radial and tangential stresses, P_a and P_b are internal and external pressures. Assuming this is an elastic stress field, the displacement 'u' and the tangential stress σ_t can be expressed by (Reismann and Pawlik 1980):

$$u = \frac{(P_a a^3 - P_b b^3)r}{3K(a^3 - b^3)} + \frac{(P_a - P_b)a^3 b^3}{4G(a^3 - b^3)r^2} \tag{7.7}$$

$$\sigma_t = \frac{P_a a^3 - P_b b^3}{(a^3 - b^3)} + \frac{(P_a - P_b)a^3 b^3}{2(a^3 - b^3)r^3} \tag{7.8}$$

where K and G are bulk and shear modulus, which can be expressed through Young's modulus E and Poisson's ratio ν by:

$$K = \frac{E}{3(1-2\nu)} \tag{7.9}$$

$$G = \frac{E}{2(1+\nu)} \tag{7.10}$$

In the stress field considered, $P_a > 0$ denotes tension and $P_a < 0$ denotes compression.

What needs to be solved is the problem at internal sphere surface, i.e. $r = a$. Also this analysis can be further simplified by assuming $b >> a$, i.e. external radius of the spherical shell is much bigger than internal one, which is applicable to the problem considered. So, Equations (7.7) and (7.8) become:

$$\frac{u}{a} = \frac{P_b}{3K} - \frac{P_a - P_b}{4G} \tag{7.11}$$

$$\sigma_t = P_b - \frac{P_a}{2} \tag{7.12}$$

where u/a represents strain. The relationship between u/a and the cavity volume change is:

$$\frac{u}{a} = (1+\frac{\Delta V}{V})^{\frac{1}{3}} - 1 \qquad (7.13)$$

assuming uniform dilatation of the cavity.

Taking E as 2 MPa and ν as 0.4, the results relating the relationships between internal pressure P_a, tangential stress σ_t and the cavity volume change are shown in Figure 7.17, using Equations (7.9) - (7.13). The influence of external pressure on the relationships is also shown.

Both internal pressure P_a and tangential stress at interface σ_t increase with volume expansion of the cavity. Now, it is possible to estimate the P_a and the σ_t due to shrinkage of the Modar. The reduced volume is about 13 %[1] after cure. So the cavity should increase volume by the same magnitude in order to fit the aggregate of impurities back into the cavity as discussed previously. The corresponding internal pressure P_a and tangential stress σ_t at interfaces are 119 - 196 MPa and 59 - 38 MPa respectively, for external pressure between 0 to 60 MPa applied at infinity, as indicated in Figure 7.17.

Assuming that there is a plane across a spherical aggregate of impurities from where a disc-like crack will be initiated as indicated in Figure 7.18 (a), if σ_t is a dominant factor that initiates the internal crack when $\sigma_t \geq \sigma_c$, the critical stress of the Modar, the problem might be treated as a penny-shaped defect embedded in the Modar resin as shown in Figure 7.18 (b).

The relationship between defect size and the critical internal stress σ_c has been shown in Figure 7.15 previously. For the stress σ_t in range from 38 to 59 MPa, as calculated above, it is impossible to form disc-like cracks in the Modar for defect size less than 40 μm which is the maximum defect estimated to exist in the Modar resin.

Therefore, extra work is required to increase σ_t to initiate disc-like cracks from the impurities. This extra work probably comes from impurities swelling in the presence of water.

---

[1] d = 1.08 before cure and d_0 = 1.22 after cure:

$$\frac{\Delta V}{V} = \frac{\frac{1}{d_0} - \frac{1}{d}}{\frac{1}{d_0}} = -13(\%)$$

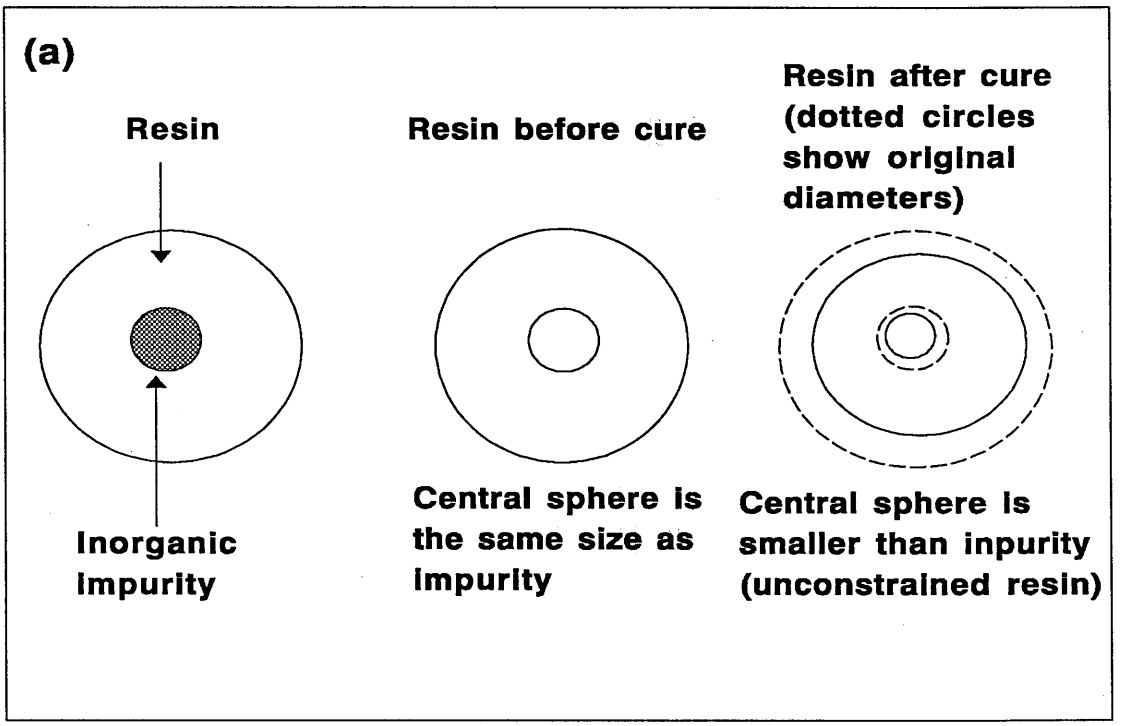

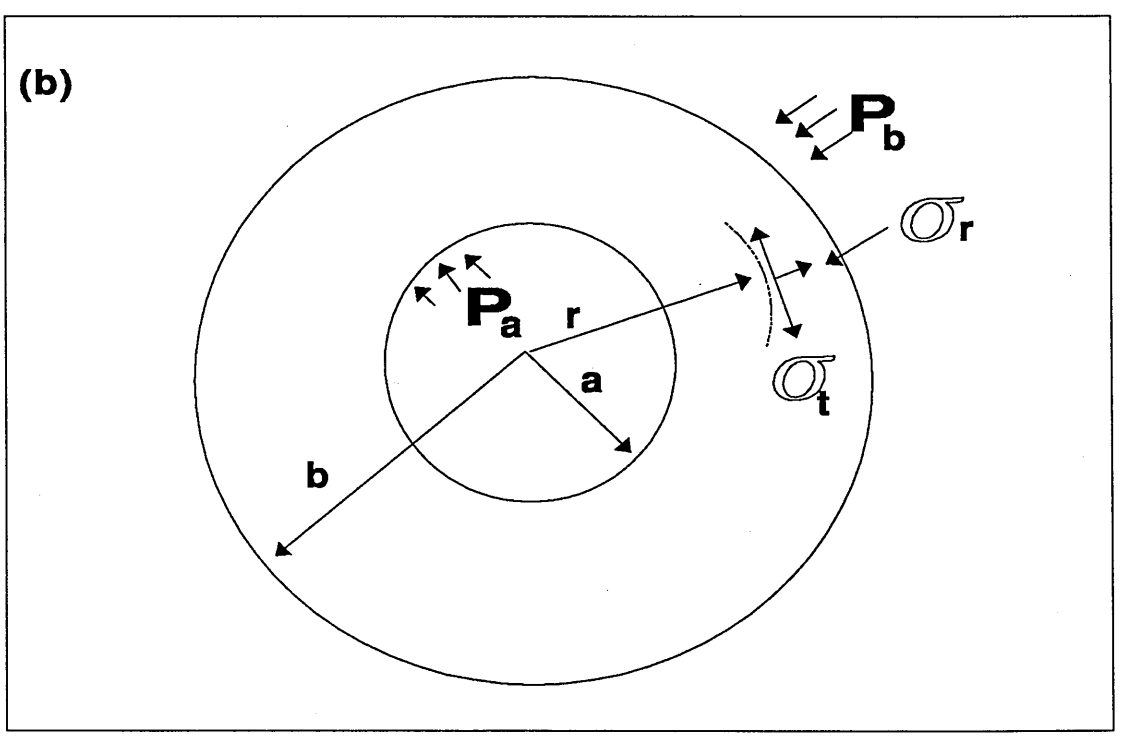

Figure 7.16 Schematic diagram of (a) resin contraction; (b) stress field of a sphere shell under internal and external pressure.

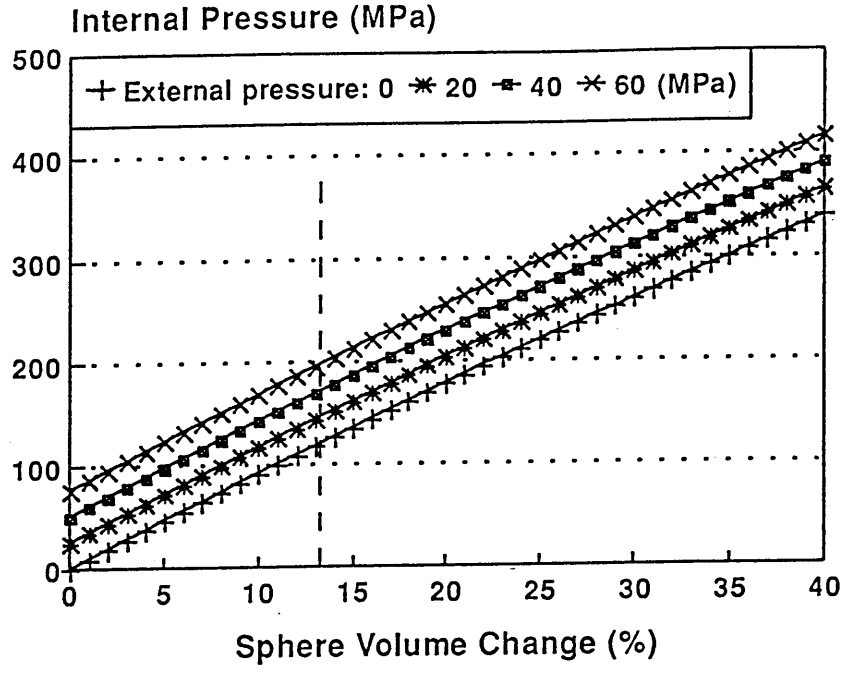

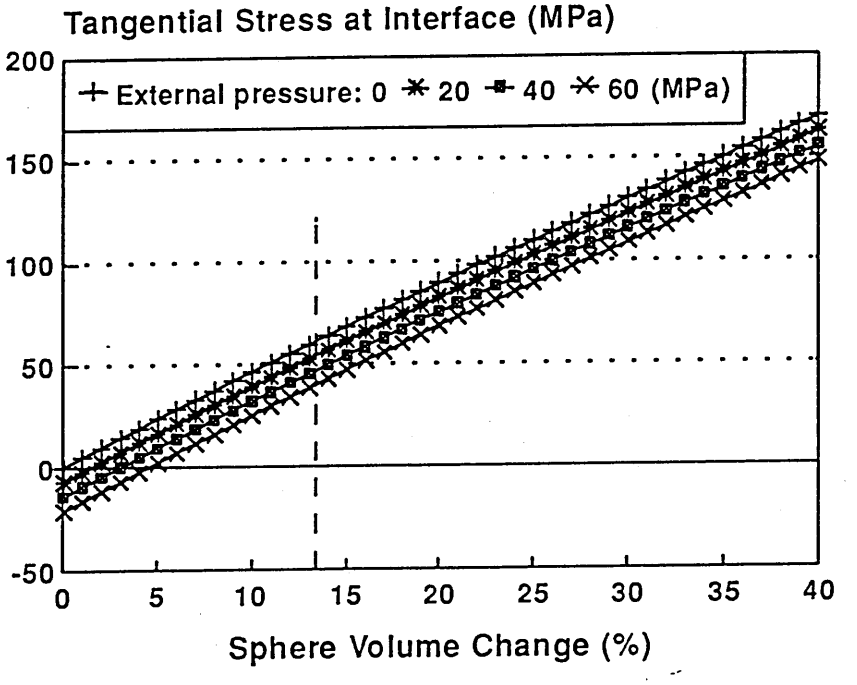

Figure 7.17 The relationships between cavity expansion and internal pressure (top) and tangential stress at interface (bottom).

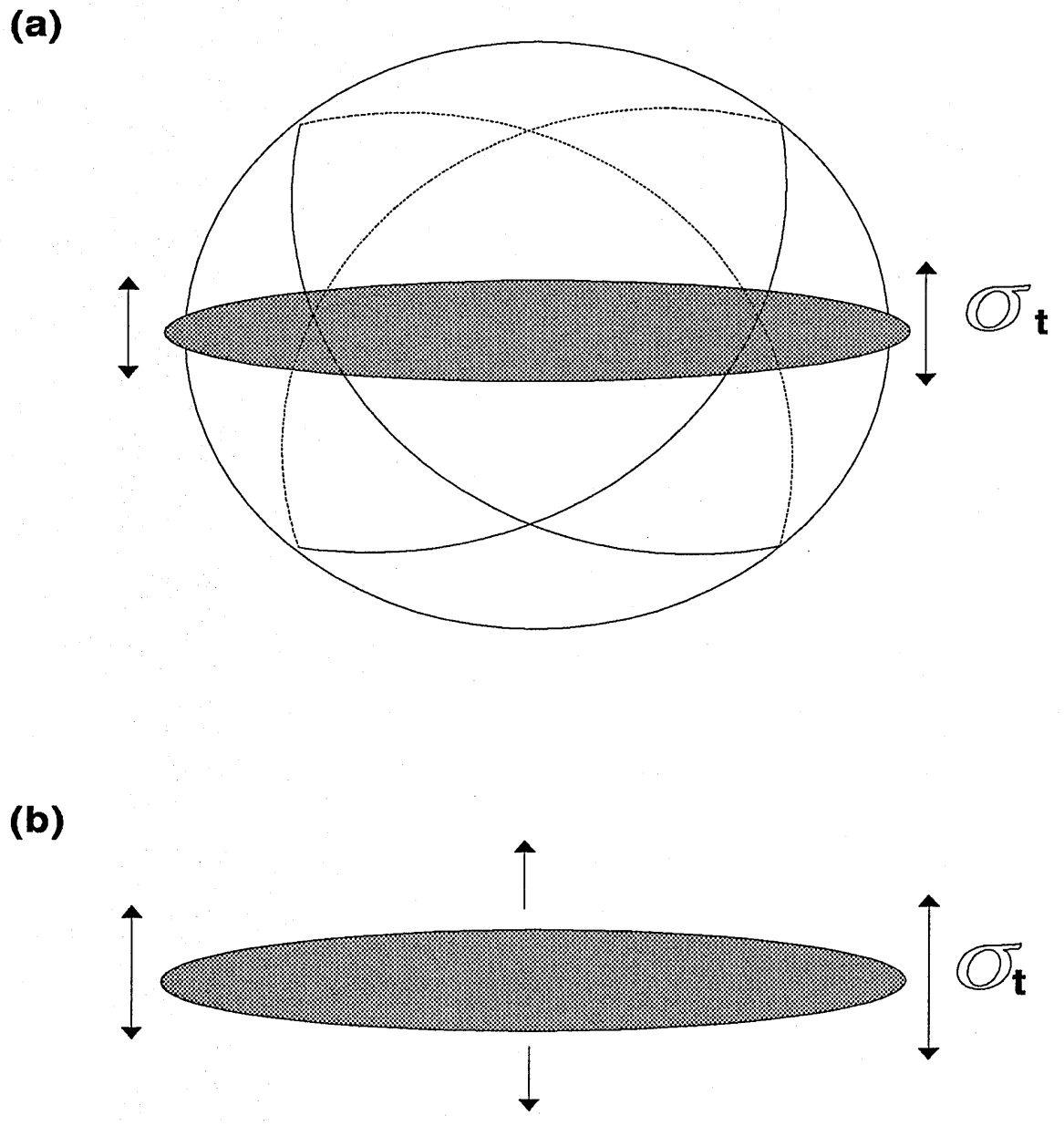

Figure 7.10 Schematic diagram of fracture plane across impurity sphere.

Water of Crystallization

The chemical composition of the impurities has been shown in Figure 7.9. They contain Na, Al, Si, S, Cl, Ca, Cr. In addition, elements Fe, K and Mg have also been found in the impurities by ICI (ICI internal report). They are probably in the form of inorganic salts, possibly sulphates and chlorides of these metals, such as $MgSO_4$, $Mg(ClO)_2$, $NaSO_3$, $Al_2(SO_4)_3$. These metal salts can form the hydrates in the presence of water.

There is plenty of evidence of the formation of hydrates of metal complexes in which water molecules associate with metal cations either in the solid state or in solution. Bivalent and trivalent metals form a very large number of complexes with 6 H_2O per metal atom, such as, alkaline earth complexes $[Ca(H_2O)_6]^{2+}$ and $[Mg(H_2O)_6]^{2+}$ and transitional metal complexes $[Cr(H_2O)_6]^{2+}$ and $[Fe(H_2O)_6]^{2+}$. Alkali metal cations can also form hydrates but with 4 H_2O per metal atom, for example $[Na(H_2O)_6]^{2+}$ and $[K(H_2O)_6]^{2+}$ (Emeleus 1943). The number of water molecules in each complex, say 4 and 6, is normally termed co-ordination number. The stereo-structures of these metal complexes are plannar when co-ordination number is 4 and octahedral when it is 6.

Formation of hydrates from metal salts will cause their structure to expand. This effect will lead to the formation of disc-like cracks in the Modar resin provided that the internal stress (caused by the structure expanding) approaches the critical stress σ_c needed to develop the cracks.

Table 7.12 collects results of volume expansion for some metal complexes after formation of hydrates, where the change in volume is calculated from molar weight M and density 'd' for each of the corresponding materials. Density data is in reference: Handbook of Chemistry and Physics, 72nd Edition, 1991 - 1992, CRC.

It can be seen that incorporation of water into metal complexes can give rise to an enormous increase in volume. Assume that a metal cation M^{n+} forms hydrates by taking water molecules one by one as follows:

$$[M(H_2O)]^{n+} \leftrightarrow [M(H_2O)_2]^{n+} \leftrightarrow [M(H_2O)_3]^{n+} \leftrightarrow [M(H_2O)_4]^{n+} \ldots$$

In each step, volume increase is approximately 21 % according to the results in Table 7.12.

Table 7.12 Relative volume increase after formation of hydrates for some metal complexes.

Materials	M (g)	d (g cm^3)	ΔV/V (%)
$Al_2(SO_4)_3$	342	2.71	-
$Al_2(SO_4)_3.18H_2O$	666	1.69	212
Na_2SO_3	158	2.50	-
$Na_2SO_3.12H_2O$	474	1.76	326
$Mg(ClO_4)_2$	223	2.21	-
$Mg(ClO_4)_2.8H_2O$	331	1.98	66
$MgSO_4$	120	2.66	-
$MgSO_4.H_2O$	138	2.45	25
$MgSO_4.7H_2O$	246	1.68	225

* M is molar weight and d density.

Recall Figure 7.17, dash lines in these two plots correspond to the stress state generated by resin shrinkage. If there is a further increase in volume by 20 % for formation of one monohydrate from one metal complex, the general increase in volume is 36 %[2], based on the cavity volume as discussed previously. Taking this value into account, the corresponding internal pressure P_a and tangential stress σ_t are about 308 and 154 MPa, neglecting the influence of external pressure P_b. This high stress might be enough to cause internal crack to start in the Modar from Modar/impurities interfaces when radius of defect is less than 40 μm (Figure 7.15).

---

[2] Assume V_a, V, and V_w are volumes of original cavity, after 13 % expansion of the cavity and after formation of monohydrate respectively. Because:

$$\frac{V_w - V}{V} = \frac{\frac{V_w}{V_a} - \frac{V}{V_a}}{\frac{V}{V_a}} = 0.2$$

and $V/V_a = 1.13$, so $V_w/V_a = 1.36$.

Comments

The model discussed above can predict the formation of disc-like cracks in Modar 8035 matrix in the presence of inorganic metal salts. The physical state of the hydrates is solid throughout the water aging process. This has been confirmed by keeping exposed aggregates of impurities in distilled water at 100°C for a few days. They remained in the solid state, and little change was observed. This does not mean that there are no species which are deliquescent. For example, Fe_2Cl_6 cannot form the hydrate $Fe_2Cl_6.H_2O$ at 100°C but can form solution with water (Roozeboom 1894, in Thorne 1948). The fact is that the majority of impurities are not deliquescent. So, swelling of impurities is believed play an important role for the formation of disc-like cracks in the Modar. These cracks are the main cause of the reduced the fracture strength of Modar 8035 (Table 7.4 and Figure 7.1).

Except for the cracks caused by inorganic compounds, hydrolysis of the Modar resin will also lead to further development of disc-like cracks if the aging time is extended up to about 2000 hours (in water at 100°C, unpublished information provided by ICI) in a sheet of 3 mm thick. The time when disc-like cracks occur is determined by the ability to resist hydrolysis in Modar resins. The stronger the resistance, the later the time when disc-like cracks occur.

The same phenomena were reported by Lee and co-workers (1992) in polyester resins. The formation of disc cracks is concluded to be caused by osmotic pressure due to formation of aqueous of hydrolysis products from the resin. The authors did not take further steps towards more theoretical exploration and did not consider the problem from a fracture mechanics point of view. Perhaps, the same principles, as discussed above, can be applied to the problem and, possibly, mathematical models can be derived.

7.3.3 Fracture of modified Modar 8035

Fracture Strength σ_c

As discussed previously, rubber reduces the overall fracture strength of Modar 8035 resins while filler increases it (Figure 7.2). In order to get better understanding of the fracture behaviour, the same ideas discussed in Section 6.3.3 in Chapter 6 will be used here. The reduction in cross-section of the Modar matrix in the presence of additives is taken into account in evaluation of overall fracture strength σ_c. So is the influence of additives on strength. Again, the semi-empirical equation proposed by Pukanszky (1988) (Equation 6.27a) and others forms discussed in Chapter 6 (Equations 6.27b, 6.29 and 6.30) are used in the

following discussions, but using σ_c instead of σ_{yield}. They are:

$$\sigma_c = f_A \sigma_{m,c} \exp(B_P \phi) \tag{7.14a}$$

$$\sigma_c/\sigma_{m,c} = f_A \exp(B_P \phi) \tag{7.14b}$$

$$\Gamma_A \sigma_c = \sigma_{m,c} \exp(B_P \phi) \tag{7.14c}$$

$$\mathrm{Ln}(\Gamma_A \sigma_c) = \mathrm{Ln}(\sigma_{m,c}) + B_P \phi \tag{7.15}$$

$$f_A = 1/\Gamma_A = (1 - \phi)/(1 + 2.5\phi) \qquad \text{Equa. (6.28)}$$

where, f_A is the effective cross-section area of matrix, Γ_A the geometric stress concentration factor, $\sigma_{m,c}$ the fracture strength of matrix, ϕ the volume fraction of additives and B_P a constant which is assumed to account for the properties of the interfaces (Pukanszky 1988). The term $f_A\sigma_{m,c}$ in Equation (7.18a) accounts for the contributions made by the matrix to overall fracture strength σ_c in the presence of additives and the factor $\exp(B_P\phi)$ the influence of additives on properties.

If the semi-empirical equation is approximately correct, the left hand term of Equation (7.15) against ϕ will give a straight line. This is shown in Figure 7.19 using the experimental data in Tables 7.1 and 7.2. The top plot is for the rubber toughened Modar resins and the lower one for the hybrid composites based on a Modar matrix toughened with 15 wt % rubber. Good straight lines are obtained, especially for the hybrid system. The data scatter for the rubber toughened system exists, which is due to the measurement variation of σ_c in unmodified Modar resin. This scatter can be as high as 10 MPa and some more than that as discussed previously. The corresponding slopes B_P are 2.17 and 3.54 for the rubber toughened and the hybrid composites respectively according to Figure 7.19.

Curves obtained by using Equation (7.14b) with $B_P = 2.17$ and 3.54 are shown in Figure 7.20 together with experimental data. It appears that data for the hybrid system fit the equation very well. For the rubber toughened system, there is some scatter. Nevertheless, the general trends are clear from this analysis. As discussed in Chapter 6, $B_P = 3$ is a neutral value. When $B_P = 3$, $\sigma_c/\sigma_{m,c} = 1$, i.e. additives have no influence on the fracture strength of the basic matrix. With regard to the above results, the rubber has a negative influence on σ_c ($B_P = 2.17$) while the filler a positive influence ($B_P = 3.54$) for the modified Modar resins.

Considering the extreme case when $B_P = 0$, Equation (7.14a) becomes $\sigma_c = f_A\sigma_{m,c}$. This

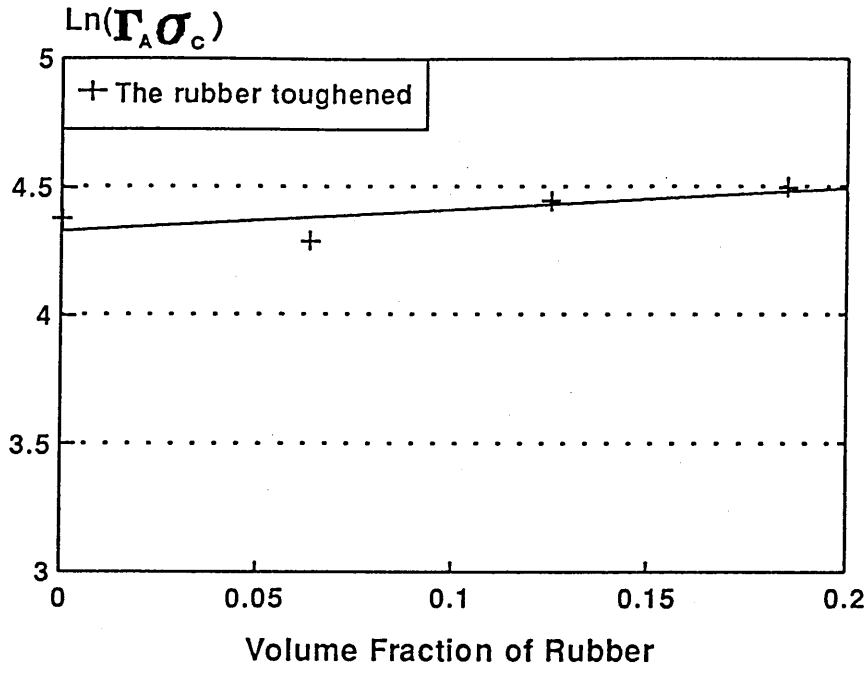

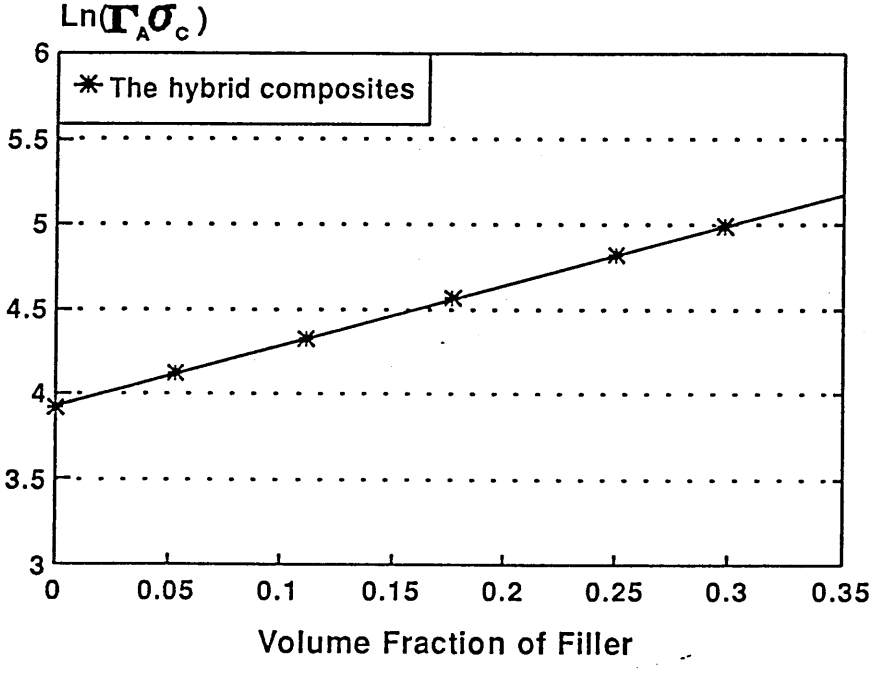

Figure 7.19 The effective fracture strength as a function of rubber and filler for rubber toughened (top) and the hybrid composites based on the Modar matrix toughened by 15 wt % rubber (bottom) (23°C).

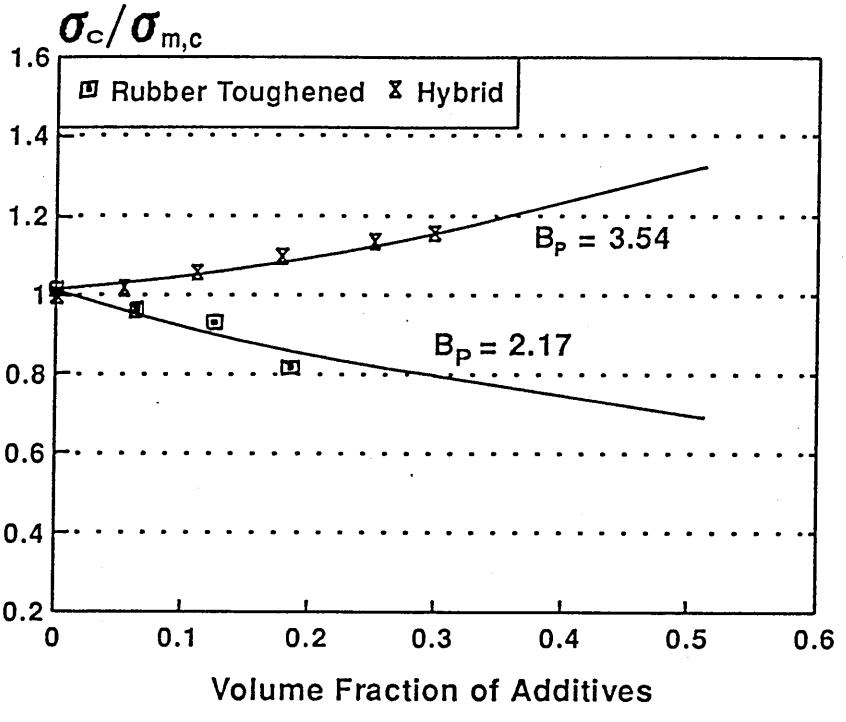

Figure 7.20 Normalized fracture strength as a function of additives according to Pukanszky semi-empirical equation.

means that the matrix alone dominates the fracture strength σ_c. The overall strength is equal to the effective strength of the matrix. So, the reduction in cross-section is the only factor that makes the reduction in overall strength σ_c. In fact, this is not true. B_P is not zero. For the rubber toughened system, it is about 2.17 . So, some contributions are made by rubber particles which affect the matrix behaviour although they have a negative influence on the overall fracture strength σ_c.

Fracture Toughness K_{IC} and Critical Energy Release Rate G_{IC}

Fracture toughness K_{IC} increases with increasing rubber concentration and, with a rubber toughened matrix, further increase in K_{IC} has been obtained by incorporation of rigid filler (Figure 7.4) to produce hybrid Modar resins. The critical energy release rate G_{IC}, however, increases with increasing rubber concentration but decreases with filler concentration (Figure 7.5).

It has been found that the increase in K_{IC} or G_{IC} is strongly linked with plastic deformation occurring before and during materials failure except in the unmodified Modar resin. It appears that the more the rubber, the more the plastic deformation. In fact, if the rubber is used effectively, it reduces the yield stress of the Modar resin (Table 6.1 and Figure 6.5a in Chapter 6) while filler increases it slightly (Table 6.2 and Figure 6.5b in Chapter 6). For example, at almost the same concentration, say rubber 18.5 vol % (T15F00) and filler 17.7 vol % (T15F30), the yield stress σ_{yield} reduces by about 34 % for the rubber toughened Modar resin (T15F00), compared with the yield stress of the Modar 8035 matrix. For the hybrid composite (T15F30), σ_{yield} increases by about 17 % comparing with the Modar matrix toughened by 15 wt % rubber.

Another factor that affects K_{IC} and G_{IC} is modulus E. The change of modulus with rubber and filler follows the same trend as σ_{yield} but the extent is different. For example, compared with the modulus of unmodified Modar resin, E decreases about 28 % at rubber concentration 18.5 vol % (T15F00). E increases by about 54 % at filler concentration 17.7 vol % (T15F30) based on the rubber toughened matrix.

The analysis above implies that rubber has a relatively stronger influence on yield stress than filler while filler has a relatively stronger influence on modulus than rubber. This consideration will help to understand the influence of rubber and filler additives on K_{IC} and G_{IC} for the systems studied.

It is generally recognized that rubber can effectively reduce yield stress, promote more plastic deformation and increase fracture toughness K_{IC}. Normally, the lower the yield stress, the higher the fracture toughness. This principle can be applied to plastics toughened by rubbers. However, this does not mean that an increase in yield stress will necessarily result in a decrease in K_{IC}. In fact, K_{IC} increases gradually with increasing yield stress for the hybrid Modar composites in this research; Figure 7.21 shows this. K_{IC} does increase with decreasing yield stress for the rubber toughened Modar resins (upper plot) but K_{IC} increases with increasing yield stress for the hybrid system which is based on the same Modar resin but toughened by 15 wt % rubber (lower plot). For the latter case, the change of modulus probably is responsible for the unexpected relationship between K_{IC} and yield stress.

As mentioned above, filler can effectively raise Young's modulus E of the hybrid composites. Of interest is that K_{IC} can increase with increasing E. This is shown in Figure 7.22, where two plots are made of K_{IC} against E. For the rubber toughened Modar resins (upper plot), an increase in E leads to a decrease in K_{IC}. For the hybrid composites (lower plot), the opposite is true.

As far as critical energy release rate is concerned, G_{IC} always increases with increasing rubber concentration but decreases with filler concentration (Figure 7.5). This general trend is also reflected in the relationship between G_{IC} and yield stress. This is shown in Figure 7.23. G_{IC} decreases with increasing yield stress. As discussed in Section 2.1.1 (Chapter 2), G_{IC} ($\approx \gamma_p$ the plastic work, true for most polymers) represents the extra work required to cause plastic flow at the crack tip. So, an increase in yield stress makes it more difficult to cause plastic flow at the crack tip, and therefore reduces fracture energy G_{IC}. Therefore, incorporation of rigid filler in a toughened matrix will cause a reduction in G_{IC} because yield stress increases (Figure 6.5b). This is what is shown in Figures 7.5 and 7.23 for the hybrid Modar composites.

Contrary to this conclusion, a maximum in G_{IC} exists for a hybrid composite at filler (glass bead) concentration about 10 vol % (Kinloch 1985, Maxwell 1986). This maximum in G_{IC} is probably due to the different dependencies of K_{IC} and E ($G_{IC} \approx K^2_{IC}/E$ used by Kinloch and Young) on concentration of rigid filler. E was measured under uniaxial compression. An important feature for their materials was debonding which always accompanied fracture. Most filler particles were exposed on fracture surfaces. This may be an important reason for a maximum in G_{IC}. Debonding between the toughened matrix and rigid filler particles will affect the dependencies of K_{IC} and E on filler concentration. For example, at 30°C for silane-coated glass beads, K_{IC} increased from 2.6 to 3.1 but E changed very little, from 2.55 to 2.60, up to filler concentration 12 vol % (Maxwell, Ph.D thesis 1986; the same data were used by

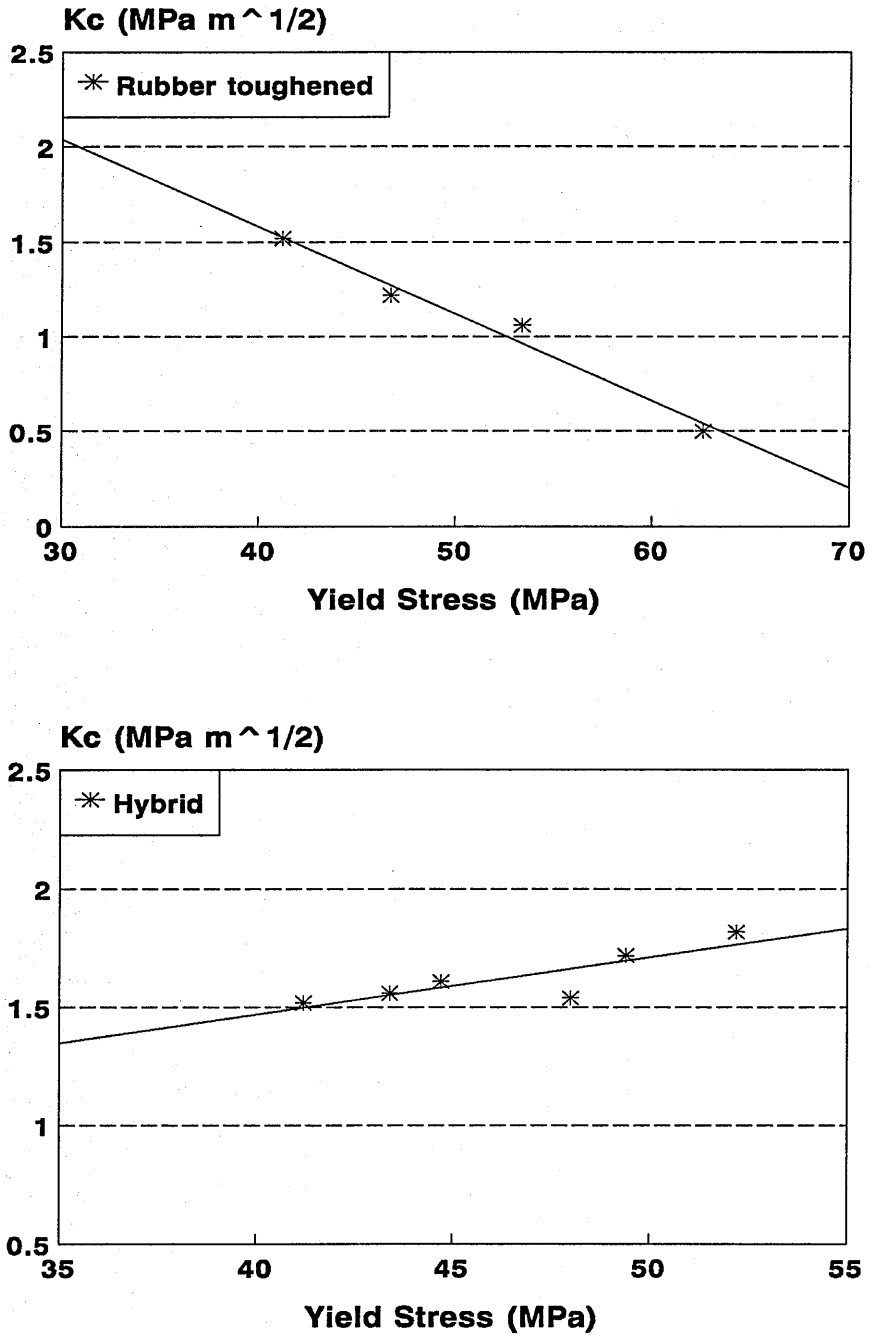

Figure 7.21 Fracture toughness as a function of yield stress for rubber-modified Modar 8035 resins (top) and hybrid composites all with 15 wt % rubber in the matrix (bottom) (23°C).

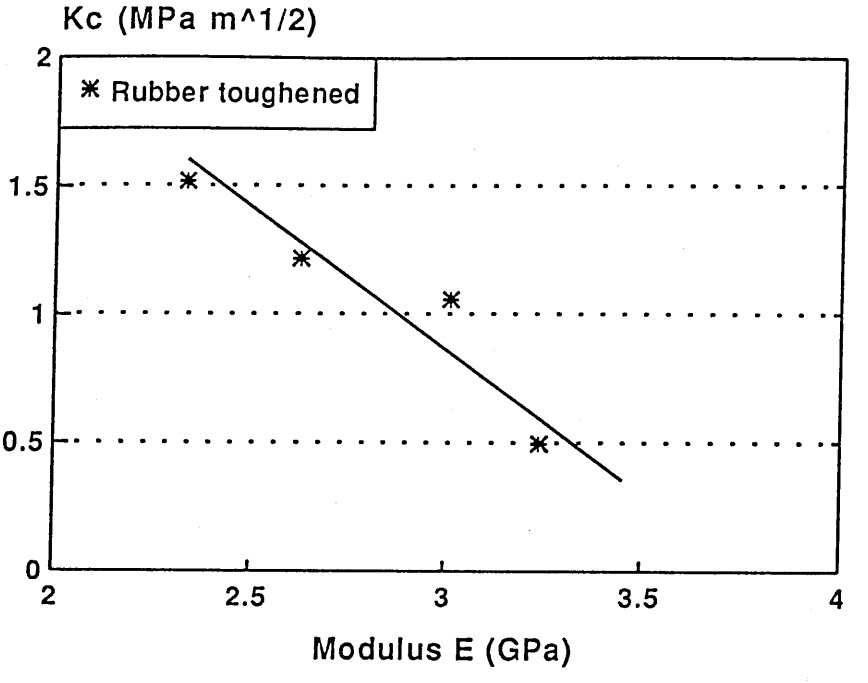

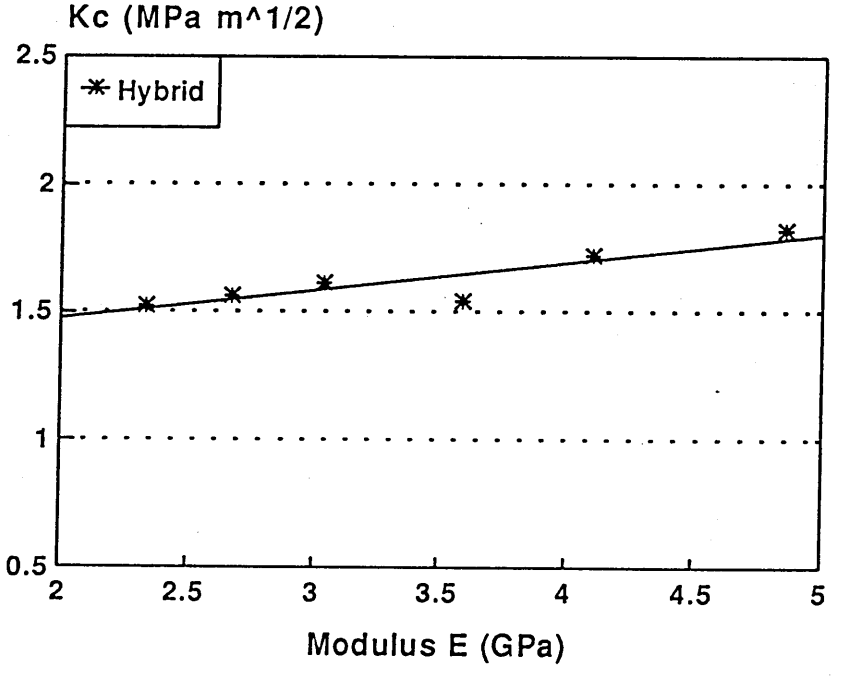

Figure 7.22 Fracture toughness as a function of Young's modulus for rubber-modified Modar 8035 resins (top) and hybrid composites all with 15 wt % rubber in the matrix (bottom) (23°C).

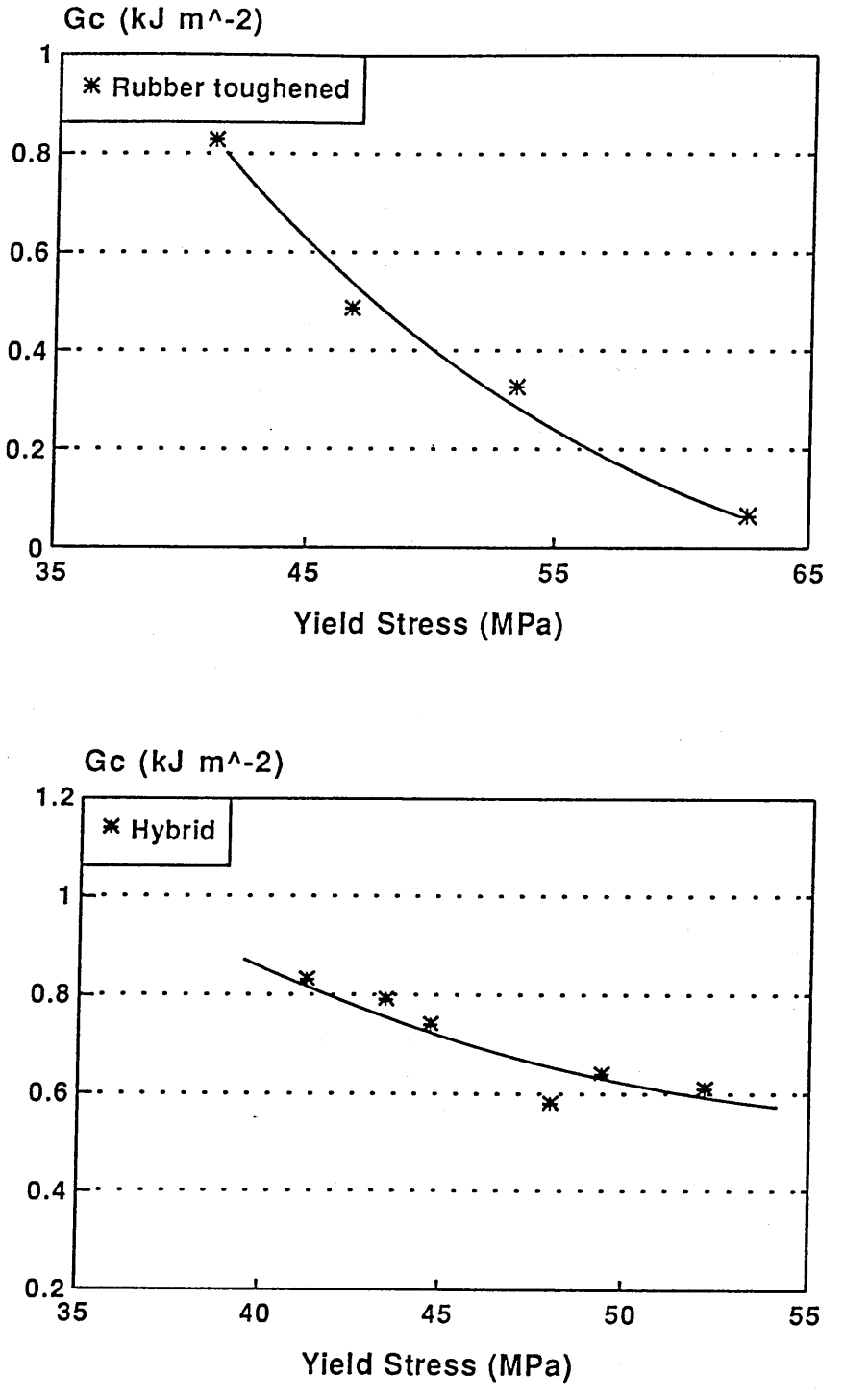

Figure 7.23 Critical energy release rate as a function of yield stress for rubber-modified Modar 8035 resins (top) and hybrid composites all with 15 wt % rubber in the matrix (bottom) (23°C).

Kinloch 1985). So, the initial increase in G_{IC} with increasing filler concentration is probably due to these effects.

In this research, however, debonding is rarely observed on fracture surfaces of the hybrid Modar composites. So, G_{IC} always decreases with increasing filler loading because yield stress increases. It is believed that good-bonding between the filler and the Modar matrix toughened by 15 wt % rubber is the main reason why the trends found in this research is different from those reported by other authors (Kinloch 1985, Maxwell 1986).

The functions of filler have been discussed in Chapter 3. No general conclusions have been drawn yet for composites based on the matrix toughened with rubber. It is recognised that the mechanism of crack front pinning caused by rigid filler functions only for a matrix dominated by the brittle failure mode (Section 3.2 in Chapter 3), in which it represents major contribution to the fracture resistance (Green 1977, Kinloch 1985, Maxwell 1986, Moloney 1983 and 1987). For the cases of non-brittle crack propagation, the role of filler particles is not clear.

In this research, what has been found is that filler can effectively increase Young's modulus of the hybrid composites (Figure 6.4 in Chapter 6). This effect is believed to be responsible for the increase in K_{IC} in the presence of filler (Figure 7.22). The decrease in G_{IC} is due to the influence of yield stress σ_{yield} (Figure 7.23), where G_{IC} always decreases with increasing σ_{yield}. In general, the dependencies of E and σ_{yield} on filler concentration will affect K_{IC} and G_{IC}.

Crack Tip Blunting Theory

Blunting of the crack tip under loading was suggested to be the main mechanism responsible for the increase in fracture resistance for rubber toughened plastics (Kinloch 1983) and hybrid composites (Kinloch 1985, Maxwell 1986). The theory about crack tip blunting has been discussed in Chapter 2. The theory is summed up in Equation (2.30).

Consider the case when the radius of the crack tip ρ is much greater than the critical distance r_c, i.e. $\rho >> r_c$. Equation (2.30) becomes:

$$K_{IB} = \frac{1}{2}K_{tc}\left(\frac{\rho}{2r_c}\right)^{\frac{1}{2}} = 0.35K_{tc}\left(\frac{\rho}{r_{tc}}\right)^{\frac{1}{2}} \qquad (7.16)$$

where $K_{tc} = \sigma_{tc}(2\pi r_c)$; σ_{tc} and r_c are constants over a wide range of temperature and strain rates (Kinloch 1983, 1985; Maxwell 1986). It has also been found that r_c is about a few microns (Maxwell 1986).

Equation (7.20) can be re-written in another form:

$$LogK_{IB} = A + \frac{1}{2}Log\rho \qquad (7.17)$$

where A is a constant. If the theory is correct, the slope of $LogK_{IB}$ against $Log\rho$ will be 0.5.

However, the slope obtained for two rubber toughened Modar resins is about 0.30 as indicated in Figure 7.24 using the data in Table 7.8, where Modar 8035 resin was toughened by 10 wt % rubber - Paraloid BTA 753 and XC 37. Linear regression was used to get the slopes for the two rubber toughened Modar resins. These results show that the slopes are less than that predicted by the theory. If the exponent in Equation (7.20) is not always equal to 0.5, the fitting data σ_{tc} and r_c obtained by Kinloch (1983, 1985) and Maxwell (1986) will change to a certain extent.

However, the message obtained from Figure 7.24 does support the theory, i.e. an increase in the crack tip radius will result in an increase in fracture toughness K_{IB}. The problem is the exponent in the equations above. It may not be always equal to 0.5. The actual values for different materials should be determined experimentally.

7.3.4 Fatigue of Modar 8035 and the modified composites

One theory of fatigue has been discussed briefly in Chapter 2. The theory is summarized in Equation (2.31), which is known as the Paris law. Strictly speaking, it is a semi-empirical theory. Fatigue crack propagation (FCP) rates which were proportional to the range of stress intensity factor ΔK raised to power 4 were obtained experimentally - crack growth data of aluminium alloy (Paris 1963). The exponent is not always equal to 4, but varies from one material to another. Of importance is that many polymeric materials obey the Paris Law (Hertzberg 1980, review; Bucknall 1985, 1991; Michel 1991) in a certain range of ΔK, which may be different from one material to another.

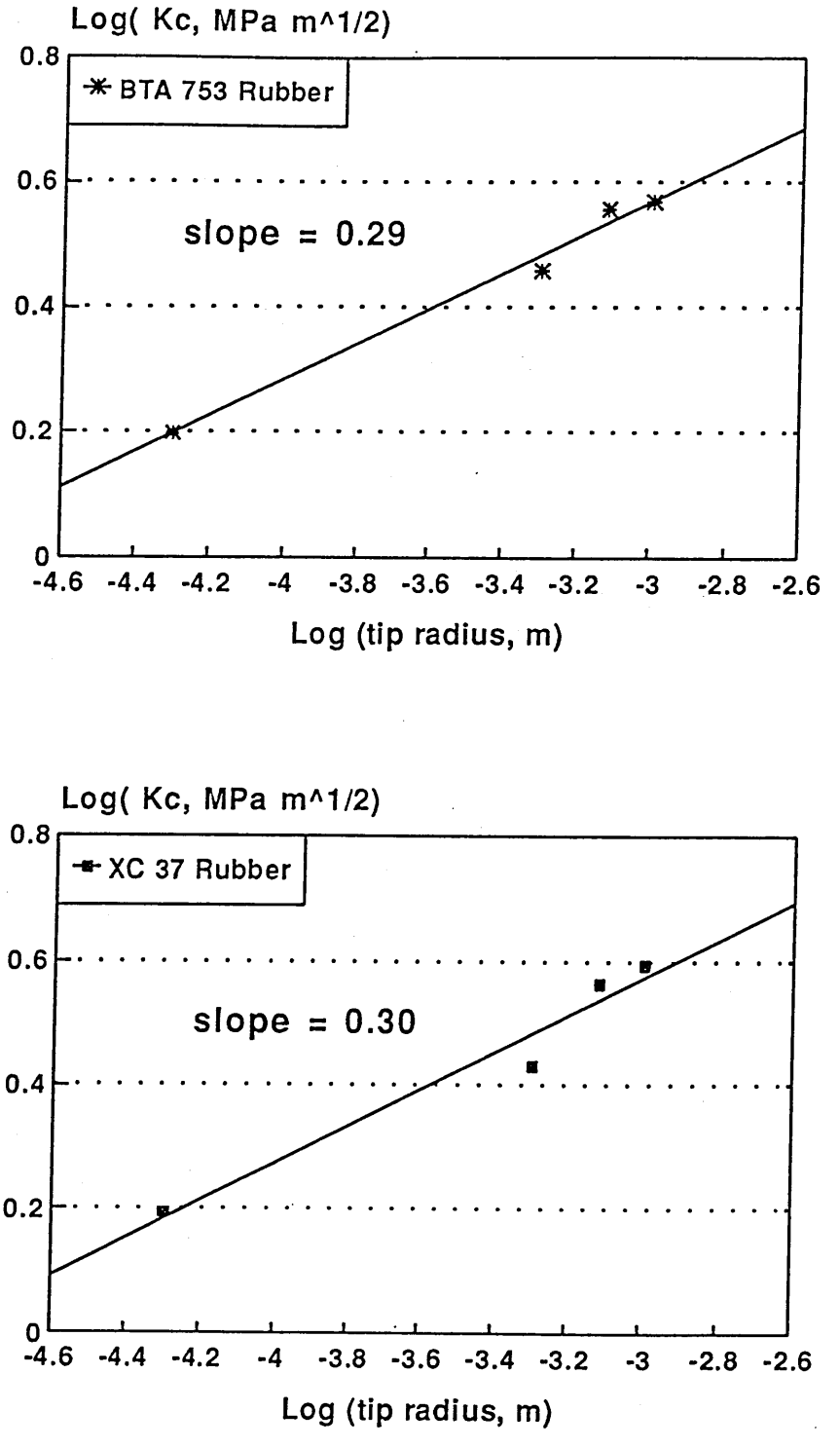

Figure 7.24 The influence of crack tip radius on fracture toughness of Modar 8035 toughened by 10 wt % rubber: Paraloid BTA 753 (top) and XC 37 (bottom) (23°C).

Another form of Paris' equation (2.31b) is:

$$Log\left(\frac{da}{dn}\right) = LogA + m Log\Delta K \tag{7.18}$$

A straight line will be expected in a plot of Log(da/dn) against Log(ΔK).

The results from fatigue experiments have been shown in Figure 7.8 for Modar 8035 T00F00 and the modified resin composites T15F00 and T15F46 early in this chapter. It has been clearly shown that there is a region of FCP in which these materials obey the Paris law. This region is about from 0.01 μm/cycle to 5 μm/cycle for the materials investigated, where the exponent in the Paris equation is about 8 to 9. Below this region and above it, FCP does not obey the Paris law. When FCP is below 0.01 μm/cycle, there is a transitional region in which ΔK appears to approach a threshold value ΔK_{th}, below which cracks do not propagate. For instance, there seemed to be no signs of crack propagation in the material T15F46 after a few days experiments at different loading levels corresponding to values of stress intensity factor range ΔK (= K_{max} - K_{min}) from about 0.3 to 0.7 MPa $m^{1/2}$. Another region, when FCP is above 5 μm/cycle, also shows transitional behaviour, in which the materials do not obey the Paris law. Catastrophic failure will occur during one fatigue cycle within this region. The corresponding K_{IC} at the last cycle is also indicated in Figure 7.8. The three different regions, termed I, II, and III, are shown schematically in Figure 7.8.

One fact is that most of the fatigue time is consumed in Region I and early stage of Region II. It can be approximately considered Region I as a crack initiation period and Region II as a crack propagation period. In Region III, failure behaviour is similar to static mode because failure will occur in a few cycles.

As far as fatigue life is concerned, the question is what are the key factors which determine the fatigue life. This problem can be considered from two aspects. The first is what is the driving force which makes the crack propagate. The second is what are the resistance factors which retard the propagation.

With reference to Figure 7.8, the factor (ΔK - ΔK_{th}) can be taken as a driving force. The bigger the difference, the higher the driving force. The converse is true. When ΔK = ΔK_{th}, the crack no longer propagates. The problem is resistance factors. The difference between the critical stress intensity factor K_{IC} and the maximum stress intensity factor K_{max} might be one factor. When K_{max} is much less than K_{IC}, FCP rate is low. When K_{max} approaches K_{IC}, it will be higher and catastrophic failure will occur. One equation which takes these factors above into account was proposed by Michel (1991). It is expressed as:

$$\frac{da}{dn} = D[\Phi(\Delta K)]^m \tag{7.19a}$$

$$Log\left(\frac{da}{dn}\right) = LogD + mLog[\Phi(\Delta K)] \tag{7.19b}$$

where

$$\Phi(\Delta K) = \frac{(\Delta K - \Delta K_{th})^4}{K_{IC}^2 - K_{max}^2}$$

where m is the exponent and K_{max} is equal to $\Delta K/(1 - R)$, ($R = K_{min}/K_{max}$).

Figure 7.25 is made according to Equation (7.19b) using the same data as Figure 7.8. The values of ΔK_{th} 0.2, 0.5 and 0.7 MPa $m^{1/2}$ and K_{IC} 0.6, 1.4 and 1.8 MPa $m^{1/2}$ for materials T00F00, T15F00 and T15F46 respectively were used in the calculations.

Figure 7.25 appears to represent a master curve, where crack propagation seems to start from the same point at which $\Phi(\Delta K)$ is approximately equal to $1x10^{-4}$ [$(MPa)^2$ m]. Below this point is the period of crack initiation, corresponding to Region I in Figure 7.8. Above this point is the period of crack propagation, where linear relationships between log(da/dn) and $log[\Phi(\Delta K)]$ operate. The exponent 'm' measured from the slopes is in a range from 0.6 to 0.8, which agrees with the values between 0.5 to 1 as proposed by Michel (1991). One advantage of Equation (7.23) is that the transition between Regions II and III shown in Figure 7.8 vanishes.

Again, the importance of fracture mechanics is demonstrated, especially the usefulness of the stress intensity factor K, which can be successfully applied to polymer materials and composites in characterization of subcritical crack growth such as fatigue.

7.4 Factors Affecting Fracture Resistance

The previous section has discussed fracture and fracture resistance of Modar 8035 resin and the modified composites, particularly with reference to the additives used. The current section will discuss some other factors such as cross head speed, specimen thickness and moisture that affect the fracture resistance of Modar resins.

7.4.1 The influence of cross head speed of testing on K_{IC}

The cross head speed affects fracture toughness. This is shown in Figure 7.26. The materials employed are unmodified Modar 8035 resin T00F00, 15 wt % rubber toughened resin T15F00, and, based on the rubber toughened Modar matrix, the hybrid composite with 46 wt % filler T15F46. The rubber used is Paraloid BTA 753.

In general, an increase in cross head speed will lead to a decrease in fracture toughness K_{IC}. The reason for the decrease is probably the increase in yield stress σ_{yield}. Another factor which can affect K_{IC} is Young's modulus E. As discussed in the previous section, an increase in E can lead to a decrease in K_{IC} for the rubber toughened Modar resins but an increase in K_{IC} for the hybrid composites. The reason for the differences is the different dependencies of σ_{yield} and E upon rubber and filler (Figures 7.21 and 7.22; see discussion in Section 7.3.3). What was found in this research is that the influence of strain rate on yield stress in considerably greater than that on modulus E (Figure 6.6, referring to Equations (6.3) and (6.4) and Table 6.10). So the major influence of cross head speed on fracture toughness K_{IC} is through the yield stress σ_{yield}. An increase in σ_{yield} results in a decrease in K_{IC}.

7.4.2 The influence of specimen thickness on K_{IC}

The influence of specimen thickness on K_{IC} is shown in Figure 7.27. All sizes used in the investigation met the requirement set by the standard for SENB tests as mentioned in Chapter 4 (Equation 4.2). It can be seen that little thickness effect can be seen in the rubber toughened Modar 8035 (T15F00), some effect in T00F00 and a stronger effect in T15F46. The variations in the hybrid Modar composite are not due to data scatter in the experiments. This has been confirmed by repeating the experiments. The values of K_{IC} for T15F46 are 1.80 ± 0.06, 1.82 ± 0.09 and 2.05 ± 0.08 MPa $m^{1/2}$ and the corresponding thicknesses are 3, 4.4 and 6.2 mm. The ranges quoted here are the maximum deviations within each group of specimens tested, and normally, the data scatter is less than that quoted.

The critical stress intensity factor K_C normally decreases with increasing specimen thickness until K_{IC} where a further increase in the thickness will not lead to a decrease in K_C, i.e. K_{IC} = constant where plain strain conditions dominate. What is found for K_{IC} in material T15F46 is exactly contrary to the prediction, as shown in Figure 7.27. This problem needs further exploration.

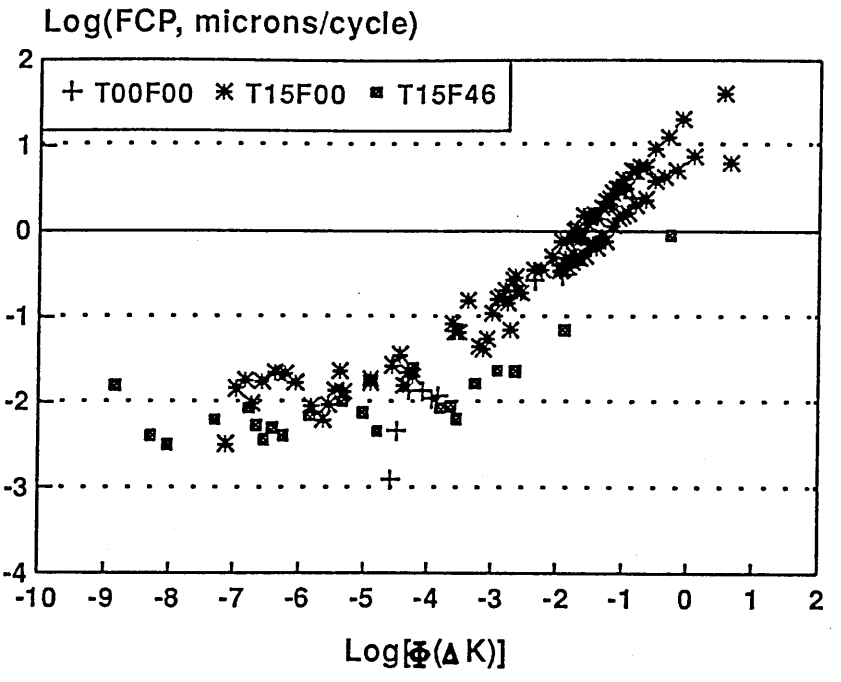

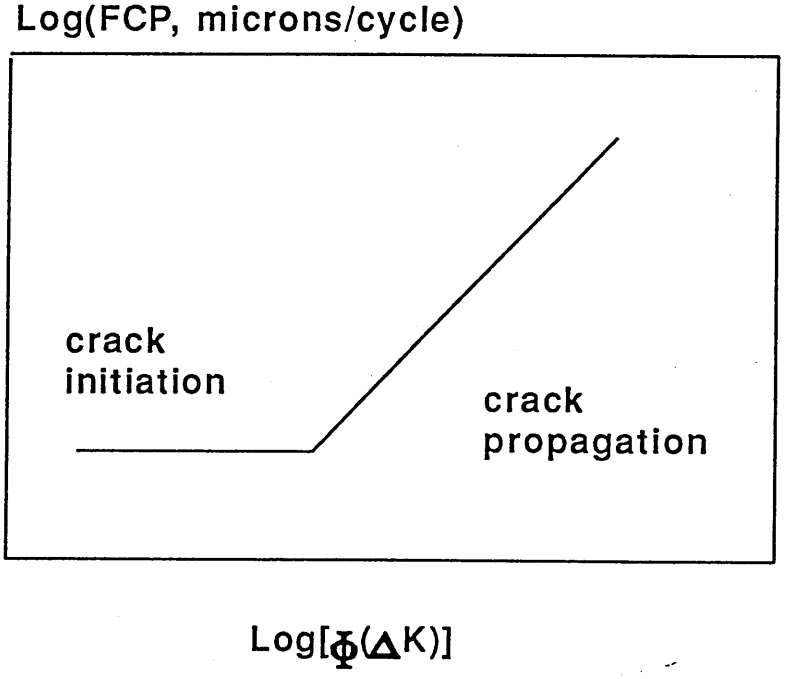

Figure 7.25 Fatigue crack initiation and propagation of Modar 8035 (T00F00), the rubber-modified (T15F00) and the hybrid composite (T15F46) using Equation (7.23) (23°C).

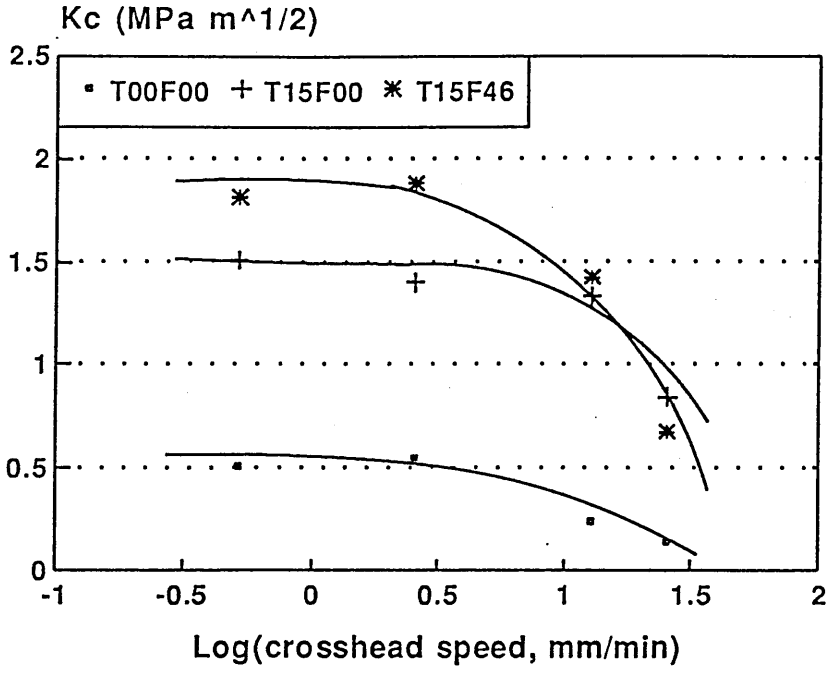

Figure 7.26 The influence of cross head speed on fracture toughness of Modar 8035 (T00F00), the rubber-modified (T15F00) and the hybrid composite (T15F46) (23°C).

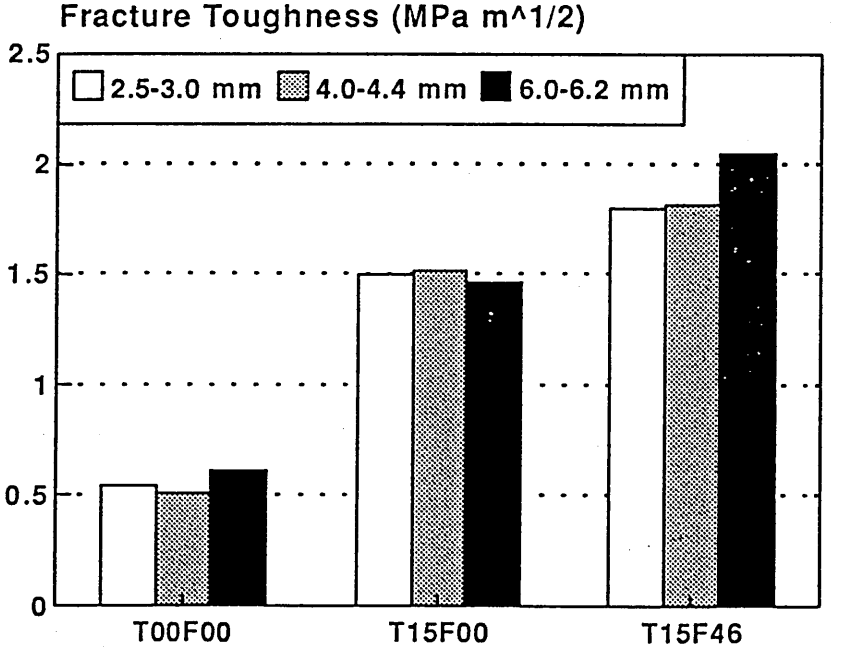

Figure 7.27 The influence of specimen thickness on fracture toughness of Modar 8035 (T00F00), the rubber-modified (T15F00) and the hybrid composite (T15F46) (23°C).

7.4.3 The influence of moisture on σ_c, K_{IC} and G_{IC}

The influence of moisture on fracture strength σ_c, K_{IC} and G_{IC} has been shown in Figures 7.3 and 7.6 in Section 7.2 previously. Moisture reduces fracture strength σ_c (Figure 7.3) but increases G_{IC} (Figure 7.6), especially in unmodified Modar resin. For example, comparing the same material but with different moisture concentrations - water-saturated, re-dried and normal materials which were equilibrated with the laboratory atmosphere, the corresponding σ_c is 53, 80 and 61 MPa (Table 7.3). Even when experimental data scatter is taken into account, normally ± 10 MPa, the effect of moisture concentration on the strength of unmodified Modar resin is obvious.

The change in K_{IC} appears differently. Comparing the three specimens - water-saturated, re-dried and normal materials, the smallest values in K_{IC} are in materials which were fully dried, except for unmodified Modar resin T00F00 (Table 7.7 and Figure 7.6). For instance, K_{IC} is 1.48 MPa $m^{1/2}$ for T15F00 and 2.05 MPa $m^{1/2}$ for T15F46 when these materials were saturated by water (wet specimens). It reduces to 1.32 and 1.91 MPa $m^{1/2}$ after the moisture has been driven out for the same materials (the re-dried specimens). For the unmodified Modar resin, K_{IC} is in the order: wet > re-dried > normal materials. The values are 0.85, 0.69 and 0.61 MPa $m^{1/2}$, i.e. the smallest in K_{IC} is not the material which was fully dried but the material containing a small fraction of moisture - less than 1 wt %.

The reduction in fracture strength σ_c caused by moisture is probably due to breaking down of hydrogen bonds, possibly formed by amide groups in the Modar resin, which weakens the intermolecular forces, so that σ_c decreases. The change in fracture toughness K_{IC} caused by moisture is probably due to the same reason: Chapter 6 discusses the way in which yield stress σ_{yield} and Young's modulus E are affected by moisture. The higher the moisture content, the lower the σ_{yield} and E (Table 6.5 and Figure 6.7). The influence of σ_{yield} and E upon K_{IC} has been discussed previously. This will help the understanding on the change in K_{IC} caused by moisture as shown in Figure 7.6.

The decrease in σ_{yield} will lead to an increase in K_{IC} but the decrease in E will cause a decrease in K_{IC}. Whether K_{IC} increases or decreases will be decided by the combined effect of σ_{yield} and E. This is why the change in K_{IC} does not follow the same trend. Compared with normal specimens, a big increase in K_{IC} for the unmodified Modar resin saturated by water is probably due to more plasticity at the crack tip resulting from reduction in yield stress. This effect is not so pronounced for the rubber-modified and the filled, rubber-modified Modar resins.

7.5 Conclusions

(1) The fracture mechanisms of Modar 8035 resin are defect-dominated. These defects are inorganic impurities which are probably metal salts. The sizes of the defects from which tensile fracture originate are in a range from 40 to 80 μm in diameter.

(2) Disc-like cracks are generated from the impurities in Modar 8035 if the material is aged in water at 100°C for a certain time which is determined by the thickness of specimens tested. The thicker the specimens, the longer the time needed.

(3) The mechanisms of formation of disc-like cracks are probably:

(a) swelling of solid impurities, which forces internal microcracks to occur when internal tangential stress at interfaces $\sigma_t \geq$ the critical fracture stress σ_c of Modar 8035 resin. Water of crystallization is probably responsible for the swelling of solid impurities;

(b) osmotic pressure due to formation of aqueous solutions of impurities and of hydrolysis products from the resin.

(c) contraction of the Modar resin during cure.

(4) Rubber reduces tensile fracture strength but filler increases it. The influence of both rubber and filler can be characterized by a semi-empirical equation proposed by Pukanszky.

(5) Rubber significantly increases K_{IC} and G_{IC}. Filler increases K_{IC} slightly but reduces G_{IC} gradually with increasing filler concentration. The increase in K_{IC} for the latter case is due to the effect of Young's modulus. Filler has a stronger influence on Young's modulus than yield stress for the hybrid Modar composites.

(6) An increase in radius ρ of the crack tip leads to an increase in K_{IB} (the critical stress intensity factor for a blunted crack tip). The slope $(\partial \text{Log}K_{IB}/\partial \text{Log}\rho)$ is about 0.3 for the rubber modified Modar 8035 resins rather than 0.5 as expected from the crack tip blunting theory.

(7) An increase in cross head speed will lead to a decrease in K_{IC}.

(8) Moisture reduces fracture strength but increases K_{IC} and G_{IC}.

(9) Fatigue crack propagation (FCP) obeys the Paris law for FCP rates approximately between 0.01 to 5 μm/cycle in the Modar 8035 resin, rubber modified and hybrid composites studied. Outside this region, the Paris law does not work.

(10) One modified Paris equation proposed by Michel has been used successfully to characterize the fatigue behaviour of Modar resins in one master curve. Fatigue crack initiation and propagation have been clearly exhibited.

CHAPTER 8

MICROMECHANISMS OF DEFORMATION

8.1 Introduction

Yielding and fracture of rubber modified and hybrid Modar 8035 resins have been discussed in the two previous chapters. From the microstructural point of view, the roles of rubber, filler and matrix, the morphology of plastic deformation, and the micromechanisms have not been touched yet. The current chapter will discuss these issues in the light of observations on deformed Modar resins, in order to get better understanding of the toughening mechanisms possibly involved in these materials.

8.2 Basic Deformation Models

8.2.1 Deformation in rubber particles

The role of rubber particles in toughened plastics is still a controversial issue. Most arguments are focused on whether it is essential for a rubber particle to cavitate. Discussion on the subject has been covered in Section 3.2.3 (Chapter 3) and further discussion will follow later in this chapter. In the current section, deformation patterns of rubber particles observed in this research will be discussed first.

(a) cavitation in rubber particles

The rubber studied is Paraloid BTA 753, which consists of a two-layer rubber particles with diameters about 0.1 - 0.2 μm. For such small particles, even if there is cavitation in the rubber, it is difficult to see unless the deformation is large enough and the rubber is kept in the cavitated state after unloading.

Fortunately, cavitation in such small particles is observed. In addition to it, another type of rubber cavitation is also observed. For the latter case, cavitation occurs within aggregates of rubber particles. These features are shown in Figure 8.1. The rubber phase shows black in the micrograph. The holes in rubber particles are the voids formed after rubber cavitation. The deformation took place ahead of the crack tip in SENB tests under conditions of triaxial tensile stresses, i.e. plane strain conditions.

(b) shearing in rubber particles

Also under plane strain conditions but in a compressive stress state, rubber particles deform in shear. This is shown in Figure 8.2, where rubber particles show in black. It appears that large-scale shear deformation has taken place in both the resin and rubber particles.

8.2.2 Deformation in Modar 8035 matrix

The role of matrix has been discussed in Chapter 3. Two types of matrix deformation have been generally recognized: crazing and shearing. For the Modar resin studied in this research, there is no evidence showing the presence of crazes. Shear deformation is believed to be the dominating mechanism.

Figure 8.3 shows the basic pattern of deformation in the Modar matrix. The deformation was carried out under tension in a thin sample with a thickness of about 60 μm. The upper picture was taken under normal light and the lower one under crossed polars. The arrows on the photomicrographs indicate the direction of tension. It can be seen that the rubber domains act as stress concentrators. All the deformation seems to originate from them and to take place around them in the matrix. Shear-band-like deformation around rubber domains is clearly shown in the lower micrograph in Figure 8.3. The angle of these bands is about 65° to the tensile direction rather than 45° as for 'ideal' shear bands.

There are two features which are worthy of notice. Firstly, matrix shearing originates from equators of rubber domains and develops from them into the matrix. Secondly, shear bands develop through the centre of rubber domains.

In addition, another interesting phenomenon is also worth noticing. It seems that some kind of cooperation exists between neighbouring rubber domains during tensile deformation. Shear deformation zones interact with one another. A typical pattern which exhibits this interaction is shown in Figure 8.4. An intensified and enlarged shear deformation zone appears in the form of circle, which develops between two neighbouring rubber domains. This localized shear deformation is in the region around the equators. Enhancement in plastic deformation of this or similar kind, which induces more plasticity between neighbouring rubber particles, especially at equators of rubber particles, is of great importance.

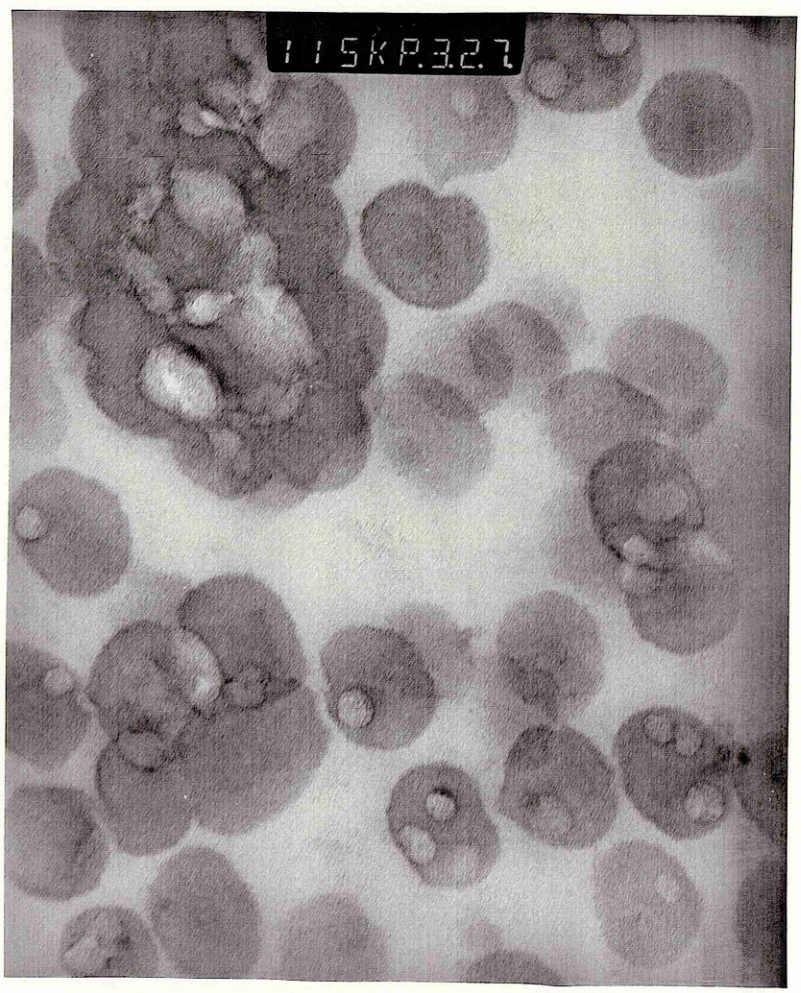

Figure 8.1 Cavitated rubber particles ahead of the crack tip in rubber-modified Modar 8035 in SENB test (23°C).

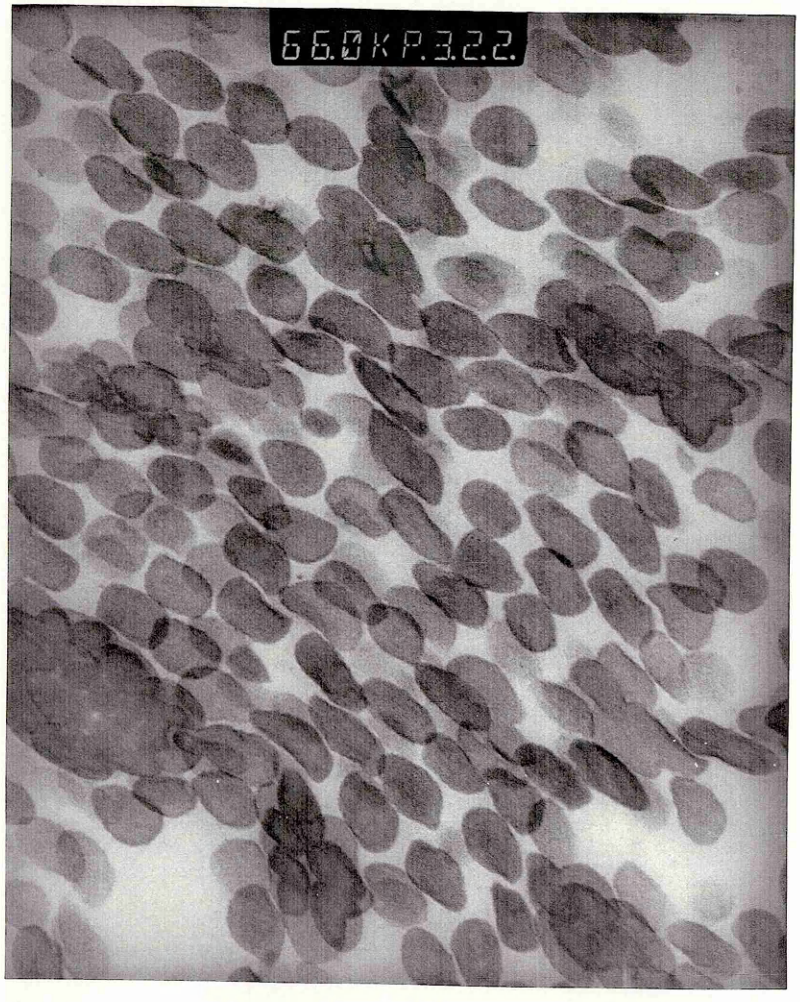

Figure 8.2 Shear-deformed rubber particles in rubber -modified Modar 8035 under compressive plane strain conditions (23°C).

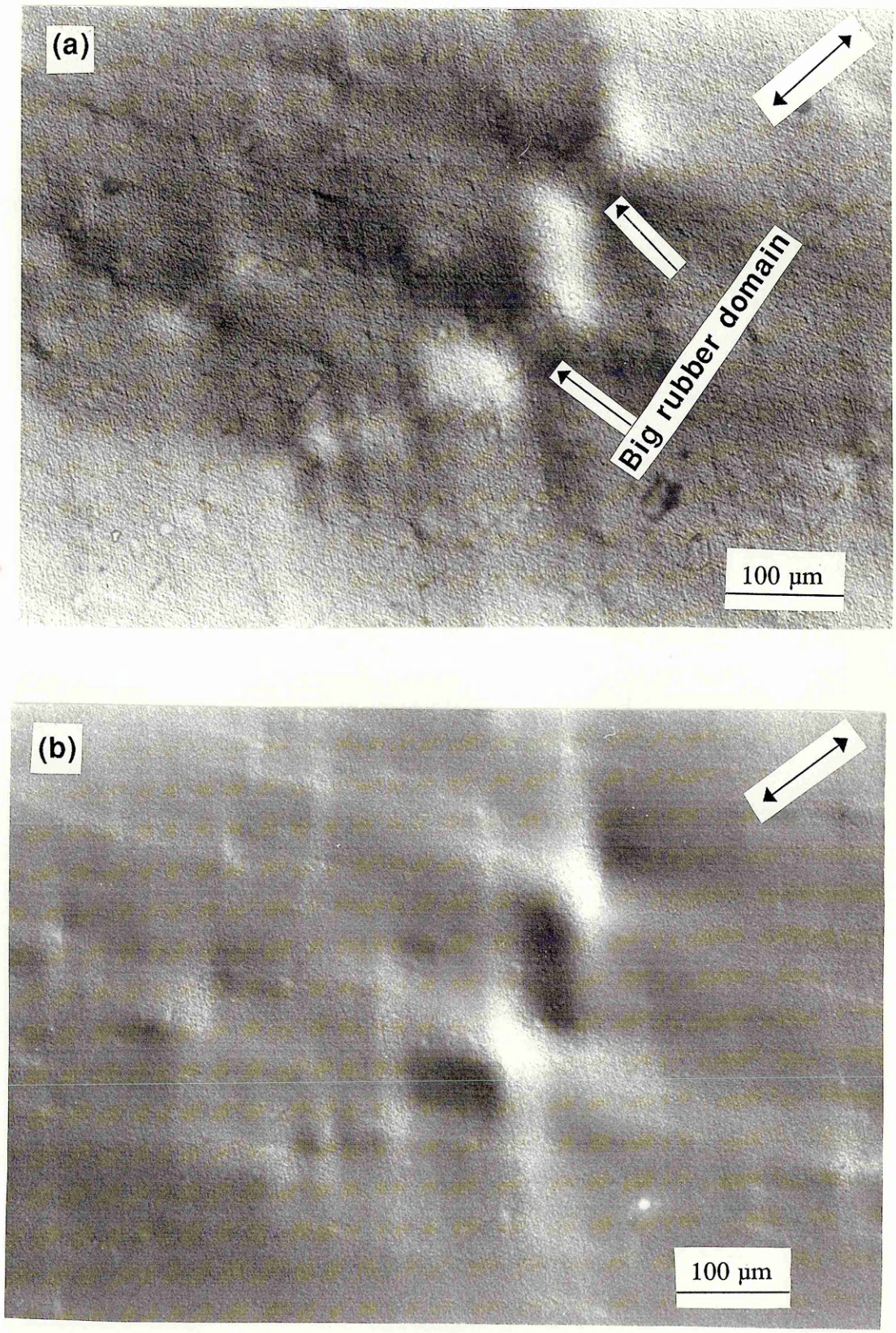

Figure 8.3 Shear-deformation pattern in thin sample of rubber-modified Modar 8035 under uniaxial tension: (a) normal light; (b) crossed polars (23°C).

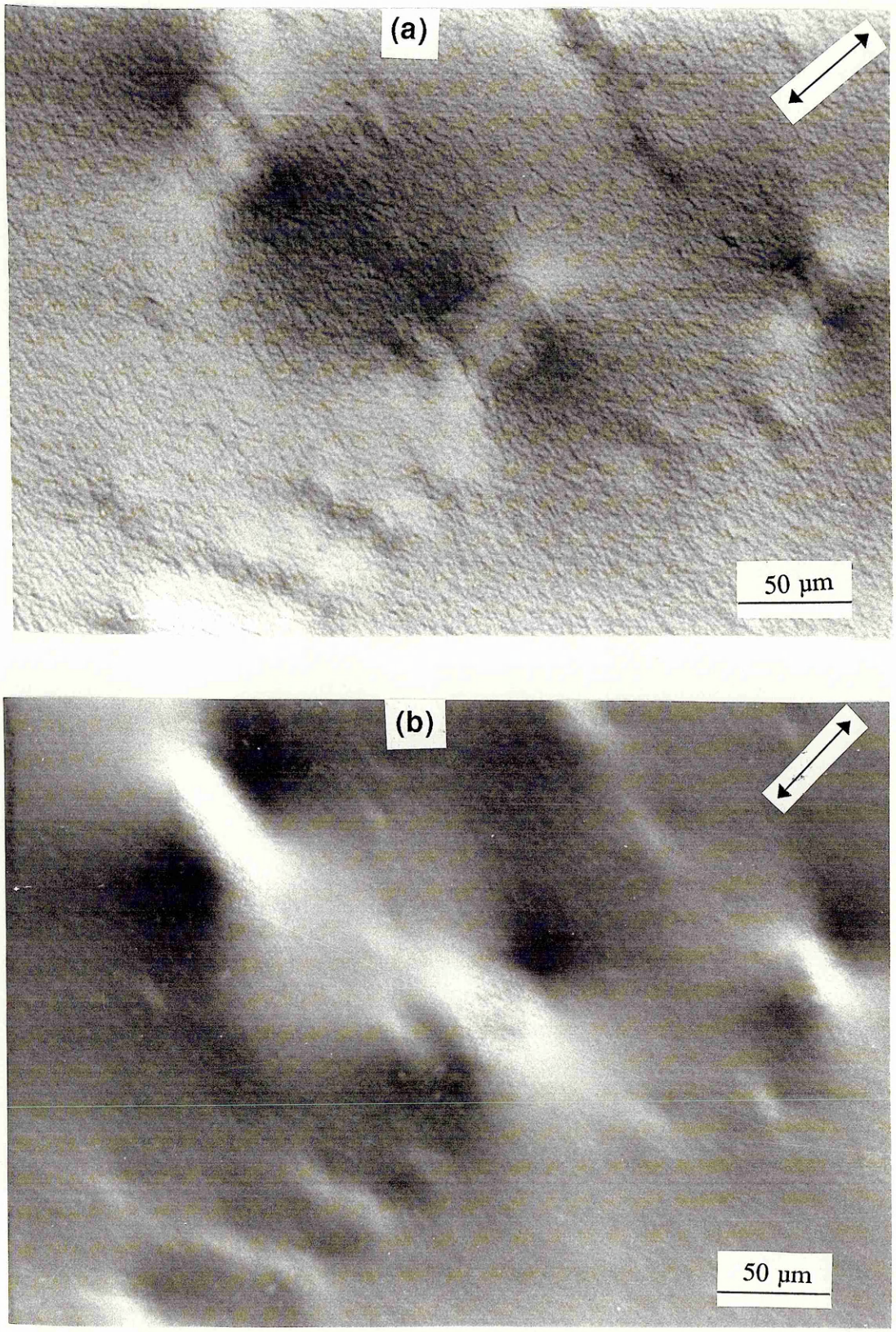

Figure 8.4 Intensified shear zone between two neighbouring rubber domains in thin sample under uniaxial tension: (a) normal light; (b) crossed polars (23°C).

8.3 Crack Tip Whitening Zone (CTWZ)

For a thick plate with a powerful sharp crack such as the sharp notch made in SENB specimens (Figure 4.4), triaxial stress will be generated ahead of the crack tip when tensile stress is applied perpendicular to the crack. These stresses have been derived in Chapter 2 and expressed in Equation (2.12) in terms of principal stresses. For materials which obey the Von Mises yield criterion (Equation 2.14), the ideal shape of plastic zone ahead of the crack tip has been shown in Figure 2.9, which shows that the plastic zone size is much bigger under plane stress conditions (at the two surfaces) than that under plane strain conditions (towards the centre). This kind of plastic zone is called a Von Mises plastic zone in the discussion later.

However, what has been found in this research appears to be opposite to this prediction of Von Mises plastic zone. The crack tip whitening zone (CTWZ), which is always generated ahead of the crack tip in rubber toughened Modar resins before fracturing, is much bigger in the central region than that at the surfaces. These features are shown in Figure 8.5. Photograph (a) is one deformed (a2) and fractured (a1) SENB specimen which shows a CTWZ, where sphere-like whitening zone indicates the rubber cavitation region. Photographs (b) and (c), which were made from (a2), were taken under transmitted light using thin sections from one deformed specimen of SENB. The specimen was placed under a load below that required to fracture it and kept for a certain time. The whitening zone shown in photograph (a) appears black in (b) and (c) under transmitted light because of cavitation of rubber particles in the region. Micrograph (b) is adjacent to the surface and (c) in the central region. It is clearly shown that the plastic zone in (c) is much bigger that in (b).

The question is why the shape of plastic zone in rubber toughened Modar resins is different from Von Mises plastic zone.

8.3.1 Cavitation zone

The reason for the difference is cavitation of the rubber particles. This factor was not considered in the treatment previously (Equation 2.23, using Von Mises yield criterion). The dependence of plastic deformation on cavitation of rubber should be taken into account for the materials studied. It is understood that there is a smaller hydrostatic stress in the surfaces than in the central region, where triaxial stresses will be generated ahead of the crack tip under tensile loading. Therefore, the size of cavitation zone should be bigger in the central region than that in surfaces. This is what has been observed in rubber modified Modar resins

[Figure 8.5 (b) and (c)].

Let σ_h stand for the hydrostatic stress. For a triaxial stress field, σ_h can be expressed by:

$$\sigma_h = (\sigma_1 + \sigma_2 + \sigma_3)/3 \tag{8.1}$$

where σ_i is principal stress in the 'i' direction.

Substituting Equation 2.12 for σ_i into Equation (8.1) using r_h instead of 'r' gives:

$$\sigma_h = \frac{2(1+\nu)K_I}{3\sqrt{2\pi r_h}}\cos\frac{\theta}{2} \tag{8.2}$$

$$r_h = \frac{2}{9\pi}\left(\frac{K_I}{\sigma_h}\right)^2(1+\nu)^2\cos^2\frac{\theta}{2} \tag{8.3}$$

In order to make r_h comparable with Von Mises plastic zone, the same method is adopted here as that used in Equation (2.23) in Chapter 2, using normalized plastic zone:

$$\frac{r_h}{r_p} = \frac{4}{9}(1+\nu)^2\left(\frac{\sigma_{yield}}{\sigma_h}\right)^2\cos^2\frac{\theta}{2} \tag{8.4}$$

where

$$r_p = \frac{1}{2\pi}\left(\frac{K_I}{\sigma_{yield}}\right)^2$$

r_p is the first approximation for the plastic zone size [Equation (2.15)] ahead of the crack tip when $\theta = 0$ under plane stress conditions and the rest of the parameters have the same meanings as defined in Chapter 2.

If it is assumed that σ_h represents cavitation stress and is a constant for a given rubber, the cavitation zone r_h ahead of the crack tip can be estimated using normalized zone size r_h/r_p against θ according to Equation (8.4).

Comparisons of cavitation zones using Equation 8.4 with Von Mises plastic zones (referring

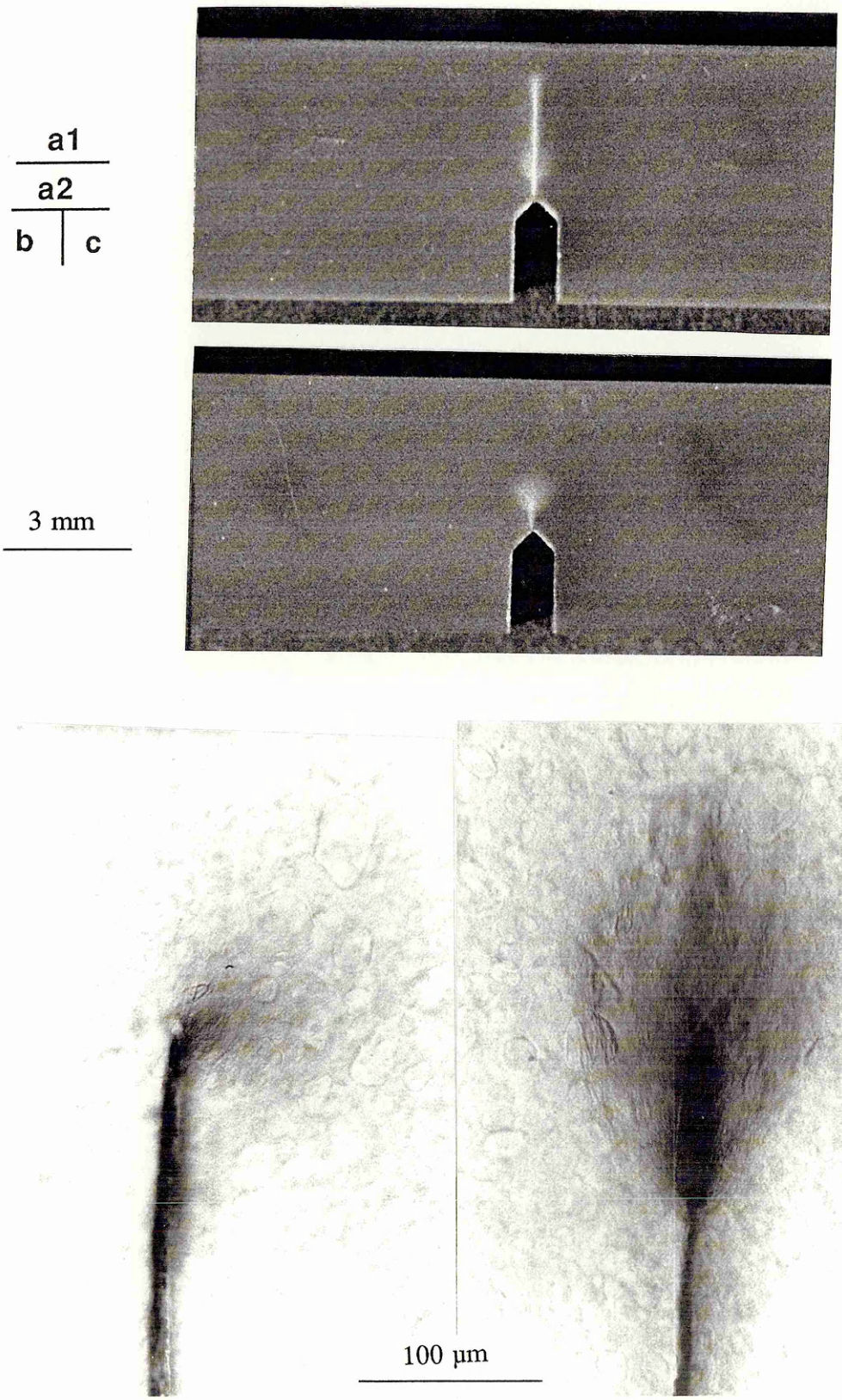

Figure 8.5 Plastic deformation ahead of the crack tip in rubber-modified Modar 8035: (a1) and (a2) crack tip whitening zone; (b) adjacent to the surface; (c) in the central region.

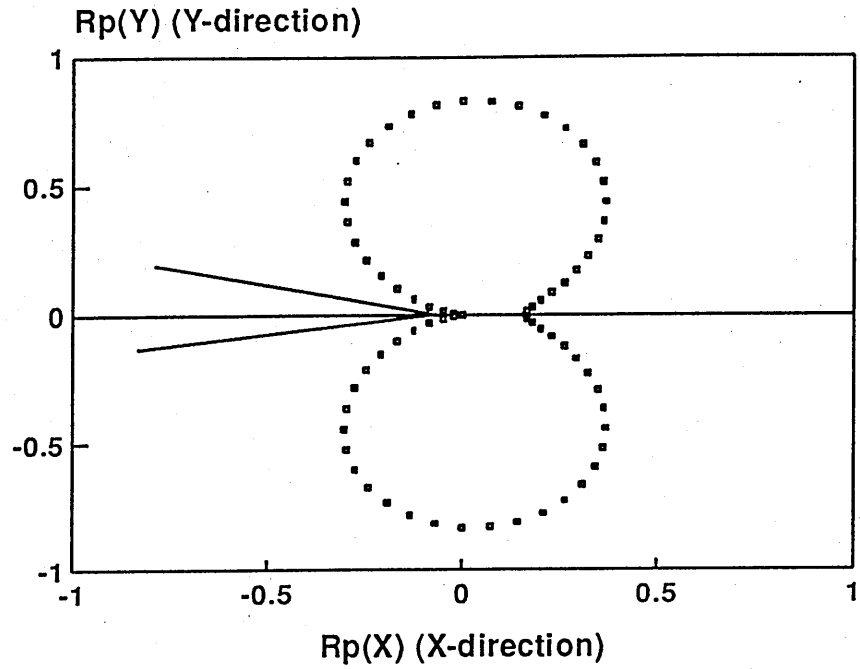

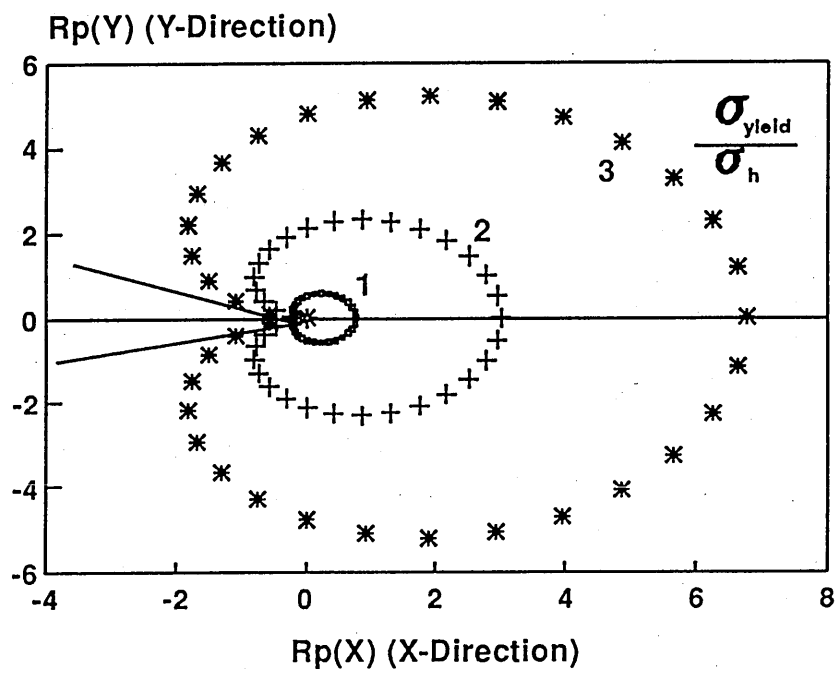

Figure 8.6 Comparisons of Von Mises plastic zone (top) with cavitation zone (bottom) under plane strain conditions.

to Equation 2.23) are made in Figure 8.6, where $\nu = 0.3$ is used in the calculation. Both size and shape are different from each other. The maximum in r_h is at $\theta = 0$ when hydrostatic stress state is considered (bottom plot). When $\theta = 0$, however, the Von Mises plastic zone r_p approaches a minimum (top plot). Also it can be seen that the general size is considerably bigger for the former than the latter for a given stress field when $\sigma_{yield} \geq \sigma_h$.

Of particular importance is the observation that the cavitation zone is strongly influenced by the ratio of yield stress σ_{yield} to cavitation stress σ_h. When the ratio changes from 1 to 3, the cavitation zone length increases 9 times.

What has been shown in Figure 8.5 supports the argument that cavitation in rubber particles or in rubber domains (Figure 8.1) is of importance in facilitating shear deformation in matrix (Figure 8.3 and 8.4). In addition, the shape of plastic deformation zone predicted by Equation (8.3) agrees well with experiment [Figure 8.5 (c)] when cavitation stress is taken into account. This means that Equation (8.3) is more suited to rubber toughened plastics (at least for brittle matrices) than Equation (2.23) when the Von Mises yield criterion is considered.

8.3.2 Cavitation stress

Now it is also possible to estimate the critical hydrostatic stress $\sigma_{c,h}$ at which rubber will start to cavitate if the size of cavitation zone r_h is known.

It is realized that the value of r_h at $\theta = 0$ is not easy to be measured because slow stable crack propagation may occur before catastrophic failure. However, it is not difficult to measure the maximum in $r_{h,y}$ which is the value of r_h along Y-direction. For a given material of K_{IC} and for a given rubber of $\sigma_{c,h}$, r_h is a function of angle θ only, so is $r_{h,y}$. It is calculated that the maximum in $r_{h,y}$ is at $\theta = 70°$ using Equation (8.3).

From Figure 8.5 (a), it is estimated the maximum in $r_{h,y}(70°) \approx 0.4$ mm. So $r_h(70°) = r_{h,y}(70°)/\sin(70°) = 0.4/0.94 = 0.43$ (mm). Taking this value together with $K_{IC} = 1.5$ MPa $m^{1/2}$ and $\nu = 0.4$ into Equation (8.2) gives $\sigma_{c,h} \approx 22$ MPa. This value is higher than the cavitation stress 13 MPa estimated through uniaxial tensile experiments in Section 6.3.3.

However, the difference is not very significant because the results are from different experiments with different geometry of specimens. As discussed in Chapter 6, massive matrix shear deformation appears to be linked with cavitation of rubber (Figure 6.24). If matrix deformation does depend on cavitation of rubber particles under tensile loading, it will be

expected that the size of plastic deformation zone ahead of the crack tip should be larger in the central region than in surfaces for a thick specimen. This is observed in SENB specimens (Figure 8.5). With reference to the basic pattern of shear deformation in Figure 8.3, it is believed that the plastic deformation shown in Figure 8.5 (b) and (c) is mainly shearing but induced by rubber cavitation (more discussion will follow soon).

8.4 Deformed Microstructure

As discussed in Section 8.2, the deformation mode in rubber particles depends on the stress state. Under tensile plane strain conditions, rubber can cavitate (Figure 8.1) but, under compressive plane strain conditions, rubber deforms in shear (Figure 8.2). The following discussions will consider different conditions relating to rubber and matrix deformation.

8.4.1 Uniaxial tension

The general deformation behaviour has been covered in Chapter 6 for rubber modified and hybrid Modar 8035 resins. Volume increases due to formation of voids has been shown in Figures 6.21 and 6.22. The question is: where do the voids come from? from rubber? matrix or both?

Figure 8.7 illustrates the microstructure of undeformed and deformed tensile specimens, observed under the optical transmission microscope using thin sections from these specimens. The material employed is Modar 8035 toughened with 10 wt % Paraloid BTA rubber. Microraph (a) is of the undeformed structure and (b) the deformed, where the left image is under normal light and the right under polarized light. These dispersed phases with irregular shapes in micrographs (a) and (b) are rubber domains. The arrow in the graphs indicates the direction of tension.

Comparing micrograph (a) with (b), it is found that severe deformation occurred in the rubber domains. Darkened areas inside the rubber domains, in micrograph (b) on the left, are caused by cavitation of rubber and, possibly, shear deformation in the rubber domains because large amount of shear-band-like fine structure also appears in the darkened areas. With reference to the basic deformation pattern of the thin sample shown in Figure 8.3, shear-band-like deformation around rubber domains did not develop so well in the tensile specimen (Figure 8.7 (b) on the right) as in the thin sample (Figure 8.3 (b)). This is because of the greater elastic constraint in thick tensile specimens. However, this does not mean that no shear

deformation occured. In fact, a major contribution to tensile deformation is from shear deformation, as discussed in Chapter 6 (referring to Figures 6.23 and 6.24). The problem lies in the technique adopted here, which cannot reveal this fact well.

Nevertheless, this technique does reveal the plastic deformation which occurs in the rubber domains. Of importance is that the darkened regions, in the form of irregular bands in the rubber domains, occur perpendicular to the loading direction and appear to line up from one rubber domain to another. This fact raises the probability that fracture probably starts from these darkened regions where coalescence and linkage of cavitated rubber might occur (more details will follow).

The advantage of this deformation mechanisms is that stress concentrations caused by sharp cracks or defects, which are the main factors causing failure in the unmodified Modar resin (see Chapter 7), will be released by rubber domains through cavitation and/or other forms of plastic deformation. Shear deformation in the matrix will be induced and intensified (referring to Figures 6.23 and 6.24). Therefore, an increase in fracture resistance is expected (Chapter 7).

Evidence for rubber cavitation in the tensile specimens is shown in Figure 8.8, comparing two micrographs taken by TEM. Micrograph (a) shows cavitation in aggregates of rubber particles and (b) in individual rubber particles. The dark areas are rubber. The white holes in the rubber are voids formed by rubber cavitation. The rest of the field is the Modar matrix. There is no evidence for the existence of voids in the matrix. This conclusion is drawn not only from this experiment but also from SENB tests after examination of deformed specimens (see Figure 8.1 and next section).

It is expected that rubber cavitation will be detrimental to some mechanical properties such as Young's modulus E: E should be bigger before rubber cavitation than after it. This has been verified by tensile experiments in cycling loading at different levels of stress. The experimental results are shown in Figure 8.9, where the two materials represented are rubber toughened (T10F00) and hybrid (T15F30) Modar 8035 resins. It appears that rubber cavitation starts at a stress between 40 - 50 MPa. This is because Young's modulus changes very little before the applied stress approaches 40 MPa but decreases sharply after the stress exceeds greater than 50 MPa. Again, here is demonstrated the fact that rubber particles act as stress bearers before cavitation and, probably, afterwards (as expected).

Combining these results with those in Figure 6.22, it is clear that voids do start to increase at a stress about 40 - 50 MPa and develop at a higher stress. Of importance is that it is in

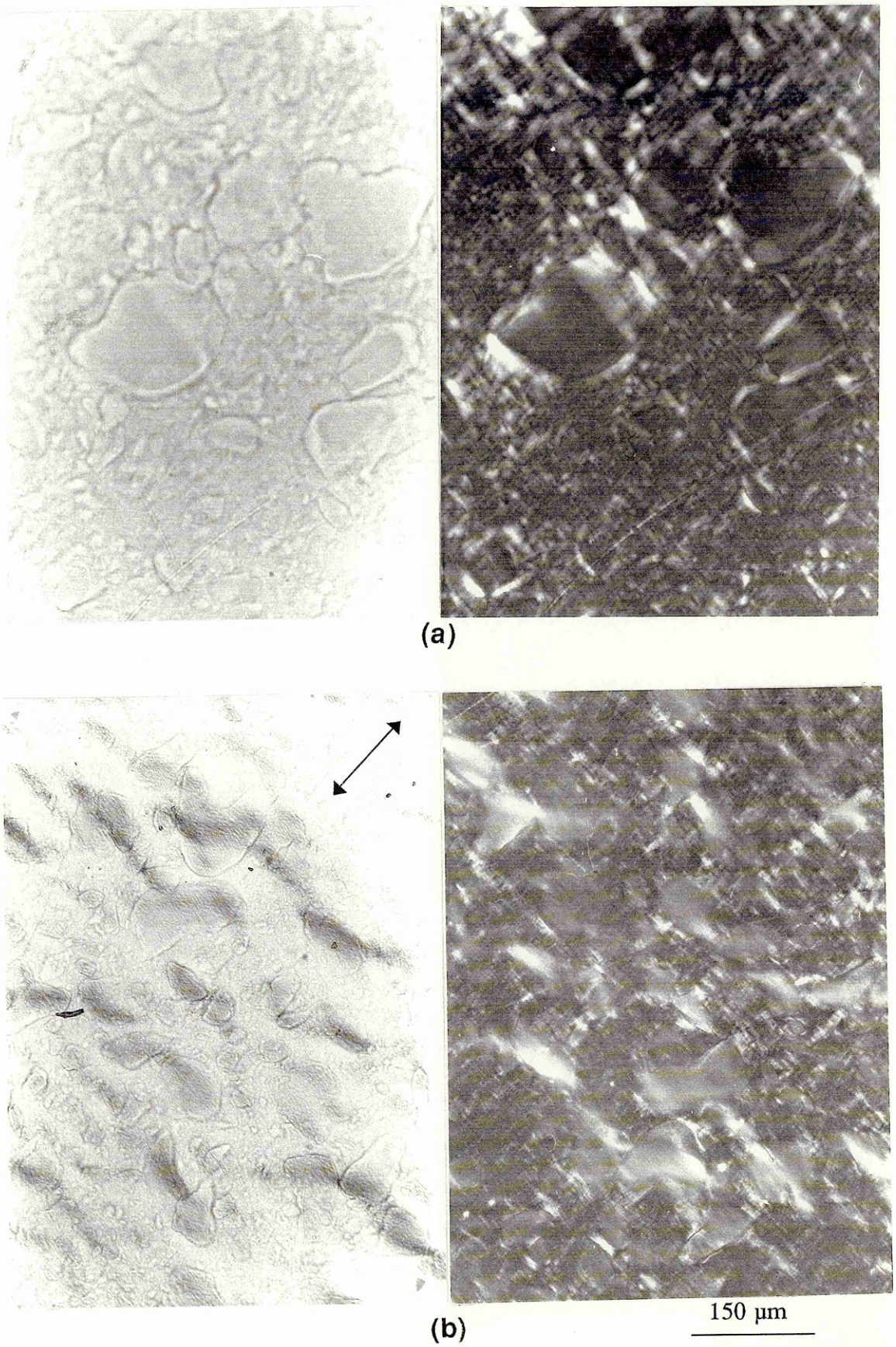

Figure 8.7 Thin section of tensile specimens of rubber-modified Modar 8035: (a) undeformed; (b) deformed. The left image is under normal light and the right crossed polars.

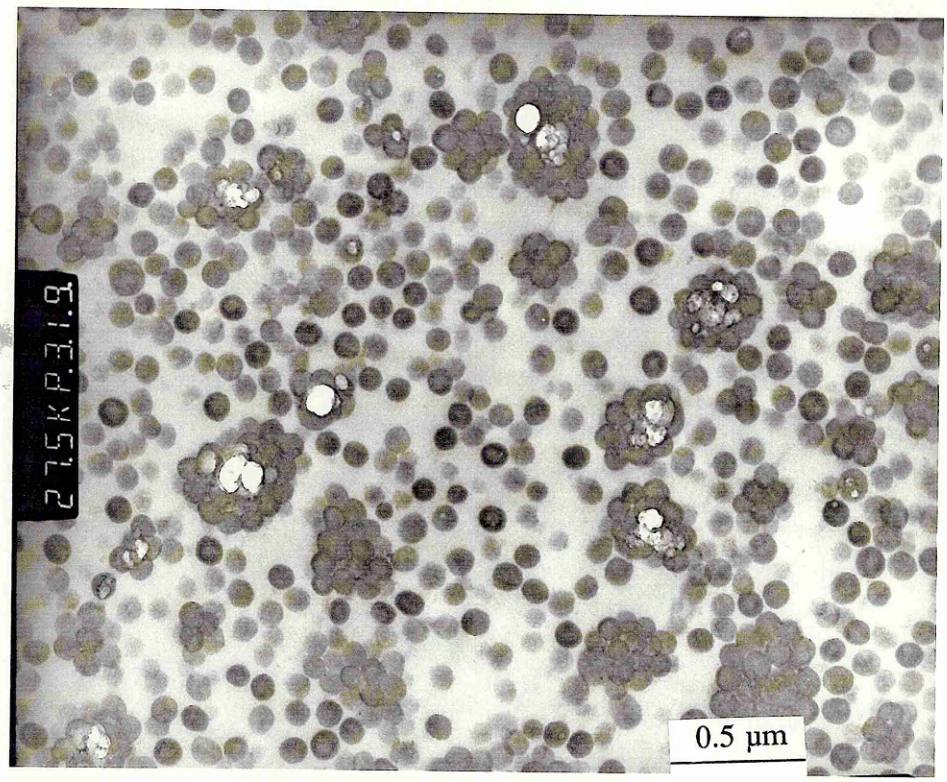

(a)

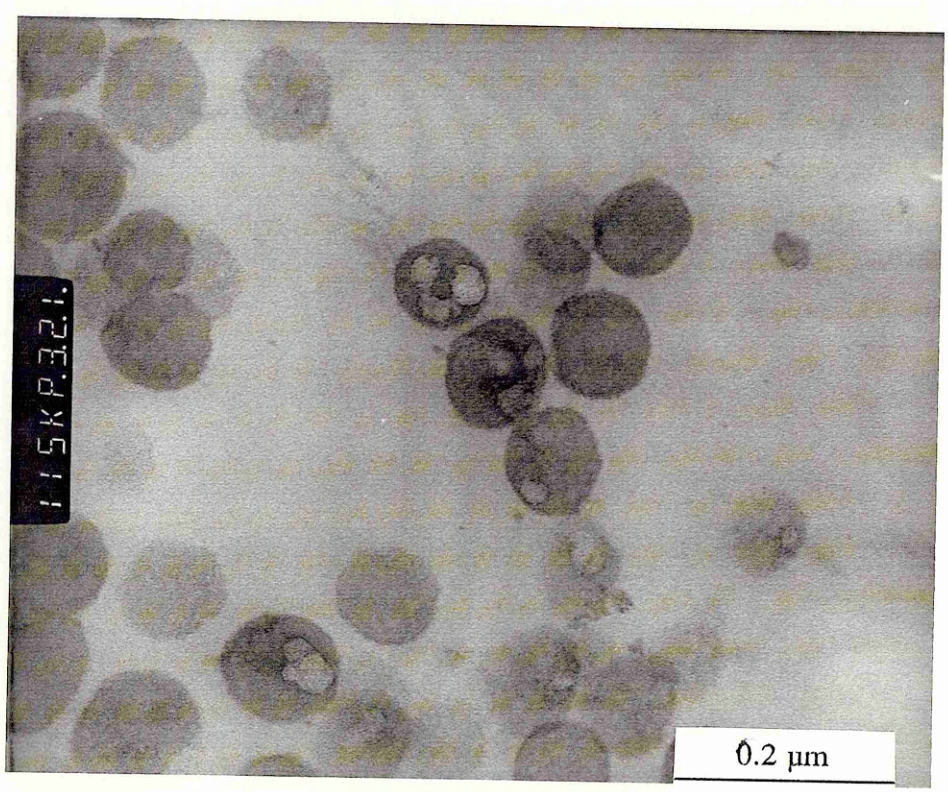

(b)

Figure 8.8 Cavitated rubber in tensile deformed specimen: (a) in aggregates; (b) in individual particles (23°C).

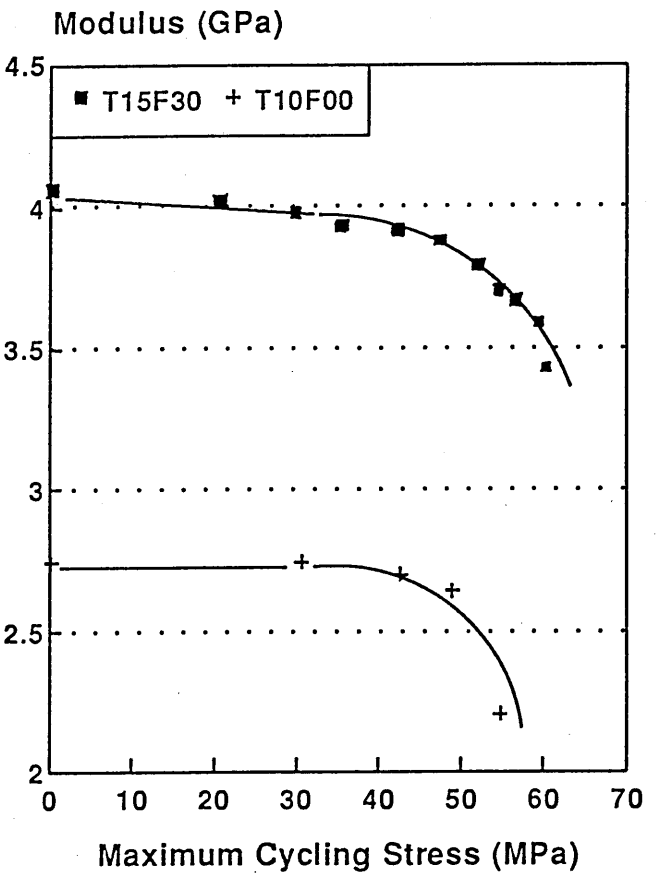

Figure 8.9 Modulus as a function of maximum cycling stress for rubber-modified Modar 8035 resin (T10F00) and the hybrid composite (T15F30) based on the matrix toughened by 15 wt % rubber (23°C).

this region of stress where yield is about to occur for rubber toughened and hybrid Modar 8035 resins (Chapter 6). This implies that rubber cavitation does induce shear deformation in the Modar matrix studied in this research. The importance of rubber cavitation in rubber toughened plastics (at least for brittle thermosetting matrices) is therefore demonstrated. This experimental result also supports the argument that rubber cavitation occurs prior to matrix shearing (Chapter 3). It is very likely that matrix shear deformation occurs immediately after rubber cavitation in the rubber toughened Modar resins.

Here the importance of stress field is also emphasized . It is necessary to in tension rather than compression to have rubber cavitate. Under compressive conditions, both rubber and matrix deform in shear.

8.4.2 Plane strain compression

Under compressive plane strain conditions, the material under loading is forced to move along one direction as indicated in Figure 4.3. Rubber particles act as stress concentrators and induce shear deformation in the matrix. Rubber deformation in shear has been shown in Figure 8.2 previously. Shear deformation in a rubber toughened Modar is shown in Figure 8.10, where coarse shear bands are clearly seen. However, the angle of those shear bands is about 30° to the loading direction rather than 45° as for 'ideal' bands. In addition, large amount of 'fine' shear bands appear within the coarse bands. Those fine bands are probably similar to the shear bands shown in Figure 8.3, where rubber domains act as the centres of shear deformation.

In a compressive stress field, the central role of a rubber particle or a rubber domain in the Modar matrix is to act as a stress concentrator and induce shear deformation in the matrix adjacent to the rubber particle, especially at its equator.

8.4.3 Single edge notch bending (SENB)

A crack tip whitening zone (CTWZ) is always generated ahead of the crack tip in rubber toughened Modar 8035 resin as shown in Figure 8.5 (a) previously. In the central region ahead of the crack tip, plane strain conditions are satisfied. The deformation pattern in the region is shown in Figure 8.5 (c). It is believed that rubber cavitation and matrix shearing occur in the darkened region in Figure 8.5 (c). In the surface, on the other hand, limited plastic deformation occurs as indicated in Figure 8.5 (b), where the plastic zone is adjacent

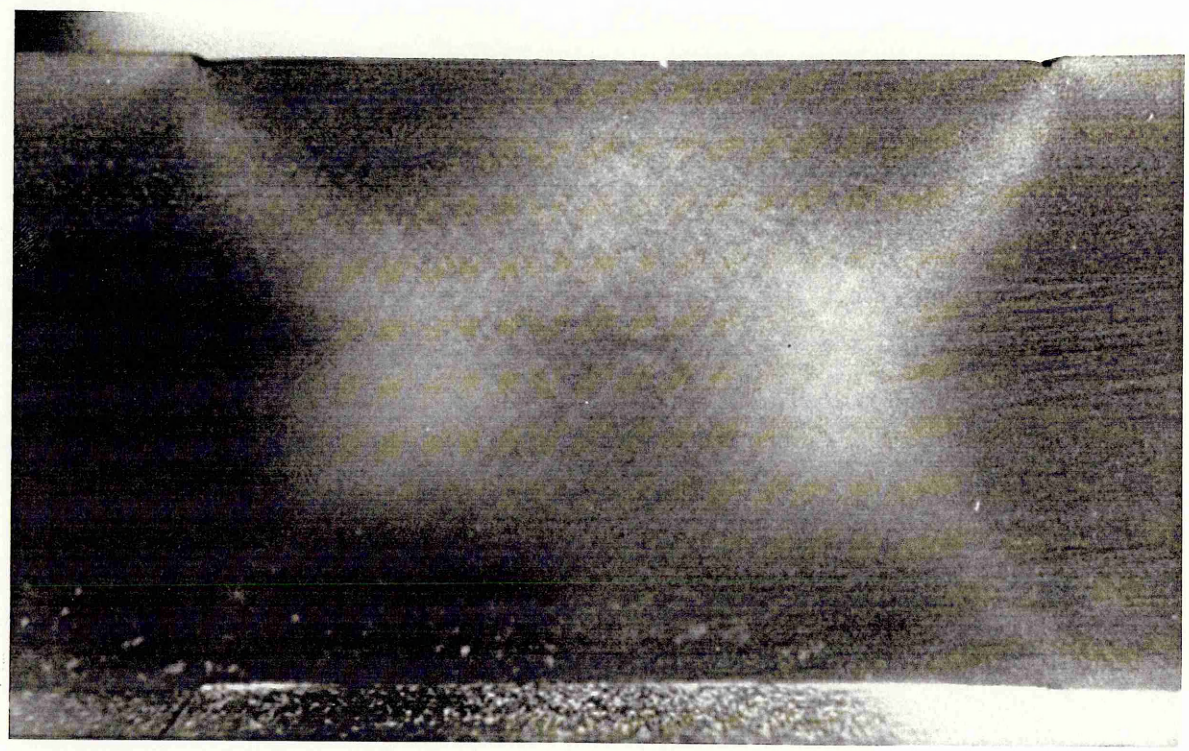

Figure 8.10 Shear bands in rubber-toughened Modar 8035 resin under compressive plane strain conditions (23°C).

to the surface. The following discussions will cover deformed microstructure in different regions.

In surfaces (plane stress conditions)

Figure 8.11 shows the micrographs ahead of the crack tip on the surfaces of SENB specimens, perpedicular to loading direction (they are not fracture surfaces), where the material employed is Modar 8035 toughened by 15 wt % Paraloid BTA 753 rubber. Photomicrograph (a1) shows a sharp crack in the surface before loading and (a2) the same area as (a1) but deformed under standard SENB testing conditions, unloading immediately after initial crack propagation. Little plastic deformation prior to crack propagation can be observed ahead of the crack tip in the surface. This conclusion is also obtained by examination of sections by optical transmission microscope under normal light and between crossed polars [referring to Figure 8.5 (b)].

However, if a SENB specimen is strained at a load just below the load required for fracture and allowed to undergo stress relaxation for a certain time, considerable plastic deformation will occur in and beneath the surfaces. This is also shown in Figure 8.11, where the specimen in micrograph (b) was loaded and allowed by stress relaxation for 14 hours. The corresponding stress intensity factor K_I changed from 1.5 MPa $m^{1/2}$ to 1.4 MPa $m^{1/2}$ from the beginning of the test to the end. Those dispersed phases with irregular shapes are rubber domains.

Comparisons of graph (a) with (b) demonstrate that considerable plastic deformation occurs after loading and stress relaxation. The interesting thing is the difference between micrographs (b1) and (b2), which were taken at the same time and in the same area. (b1) was focused on the surface while (b2) shows the area beneath the surface. What is found is that more darkened spheres are clearly visible in micrograph (b2) that are not seen in micrograph (b1). These darkened spheres are the cavitated rubber domains.

As discussed previously, whether the rubber cavitates or not is determined by the hydrostatic stress state. So more rubber cavitation should occur beneath the surface of the specimen than at the free surface because triaxial stress fields do not exist in surfaces.

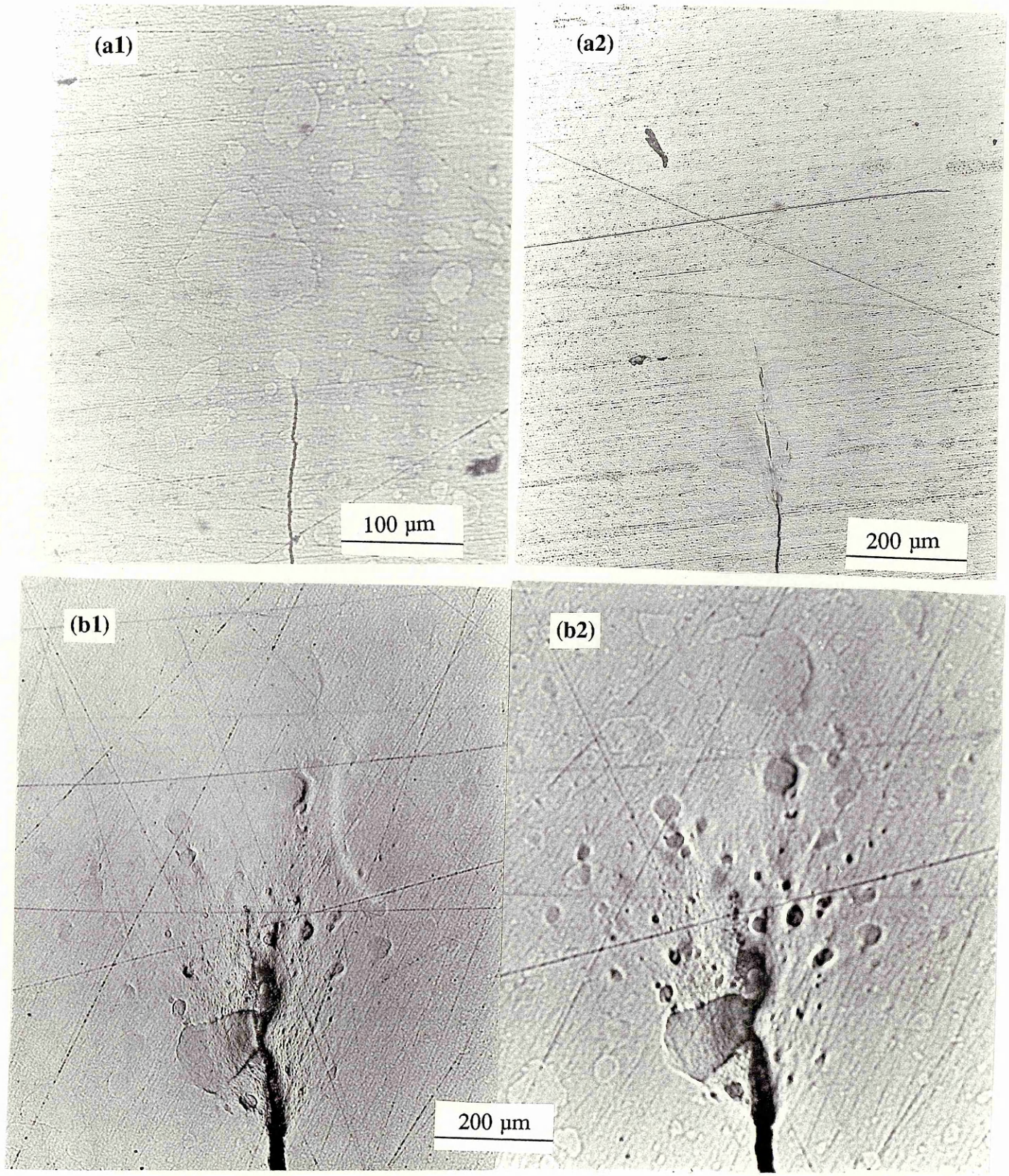

Figure 8.11 Microstructure of the crack tip in rubber-modified Modar 8035: (a1) undeformed; (a2) deformed; (b) deformed and stress-relaxed, where micrograph-1 is focused on the surface and micrograph-2 beneath it (23°C).

In the central region

The basic deformation pattern in the central region ahead of the crack tip does not corespond to the Von Mises plastic zone but to a criterion where deformation is assumed to be controlled by cavitation of rubber (Figures 8.5 and 8.6), as discussed previously. Cavitation in rubber will release hydrostatic stress and promote shear deformation in the matrix. Under tensile plane strain conditions, it is very difficult to have the material yield without rubber cavitation. This is because rubber has a high bulk modulus and can bear stress to a certain extent. So a triaxial stress state generated ahead of the crack tip will reduce the extent of yield occurring (Equation 2.14).

However, as soon as cavitation of rubber starts, plane strain conditions no longer hold. Thin matrix ligaments between cavitated rubber regions are probably in plane stress and shear deformation will occur in them and in the cavitated rubber particles. Typical cavitated rubbers have been shown in Figure 8.1 previously. More features are shown in Figure 8.12. The dark dispersed phases is Paraloid BTA 753 rubber. The micrograph was taken by TEM. The heavily shear-deformed rubber particles, some of which not only change in shape but are also torn into two parts due to shearing, strongly imply great possibility that cavitation occurs prior to shear deformation and the former induces the latter. As a result, stress concentrations at the crack tip are released and fracture resistance increases (Chapter 7).

Based on the facts observed above, it appears very likely that the whole deformation pattern ahead of the crack tip shown in Figure 8.5 (c) is formed by the same mechanisms. This is because (a): rubber cavitation-dominated plastic zone is bigger in the central region than in the surfaces because of high hydrostatic stresses towards the centre; and (b): there is no evidence showing other voiding mechanisms such as crazes in the deformed Modar matrix. Shear deformation in Modar matrix is responsible for the change in shape of the rubber particles.

In fracture surfaces

Cavitation in rubber domains is also observed in fracture surfaces of rubber toughened Modar resins. Figure 8.13 shows SEM micrographs taken in the central region ahead of the crack tip, which illustrate the typical morphology of rubber domains. (a) is a cold fractured surface (undeformed) and (b) is the SENB fractured surface within the crack tip whitened zone (CTWZ). It is clearly seen that a large amount of free space was generated in the deformed material in micrograph (b), compared with the undeformed in micrograph (a). These enlarged

holes in (b) are due to cavitation of rubber particles.

The general features in fracture surfaces of unmodified Modar resin and the rubber-modified are shown in Figure 8.14. The SEM micrograph in (a) is a fracture surface of Modar 8035, where the arrow shows the crack propagation direction. A few short white lines in the micrograph are due to electronic charge on edges. The formation of these edges occurs because cracking does not start from exactly the same planes, and disappears as soon as the crack fronts reach the same plane. The micrograph (b) was taken within a CTWZ in the Modar resin toughened with 15 wt % Paraloid BTA rubber. Comparisons of (a) with (b) reveal that a large amount of plastic deformation has taken place ahead of the crack tip in the rubber toughened material. Very limited plastic deformation occurred in the unmodified material, forming a mirror-like fracture surface.

In addition, one interesting phenomenon appears within most rubber domains. This is shown in Figure 8.15, where a river-like marking occurs, which developed along the crack propagation direction. Recall Figures 8.5 (c) and 8.7 (b). It has been found that microcrack-like (non-through thickness cracks) features always appear in each of the rubber domains around the crack tip and they are perpendicular to the loading direction. Because of the limited focus depth of the optical microscope used, these features are shown only in about two rubber domains in Figure 8.5 (c). In Figure 8.7 (b), darkened regions form in a wide strip within rubber domains, also perpendicular to the loading direction, where heavy cavitation is believed to occur. The microcrack-like features in Figure 8.5 (c) and the darkened regions in Figure 8.7 (b) are probably due to the coalescence and linkage of cavitated rubbers, for the development of voids (Referring to Figures 6.21 and 6.22) and possibly collapse of some thin ligaments between cavitated rubber particles, from there major crack will be originated. What is observed on fracture surfaces (Figure 8.15) in rubber domains are the 'tails' formed after fracturing, which probably developed from these microcrack-like features during fracture.

Details of these microcrack-like features are not known. However, sections of deformed rubber domains do not show these features but rubber cavitation under TEM. So, it is very likely that coalescence and linkage of holes generated from cavitated rubber particles occurs before fracture. The TEM microstructure shown in Figure 8.12 does support this possibility, where some boundaries between individual rubber particles disappear (also Figure 8.8 (a) shows enlarged holes due to cavitation) and shear deformation occurs.

The enlarged part of the river-like marking in Figure 8.15(a) is shown in (b), where big holes within rubber domain suggests the possibility of coalescence of cavitated particles.

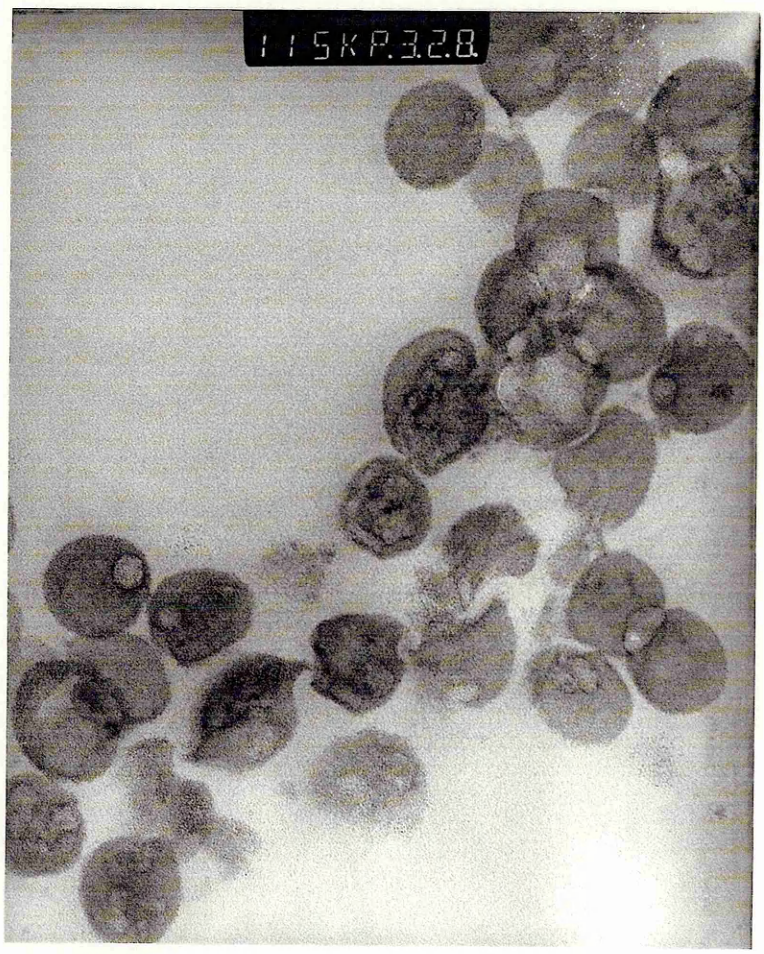

Figure 8.12 Plastic deformation ahead of the crack tip in the central region of SENB specimen in rubber-modified Modar 8035 resin (TEM).

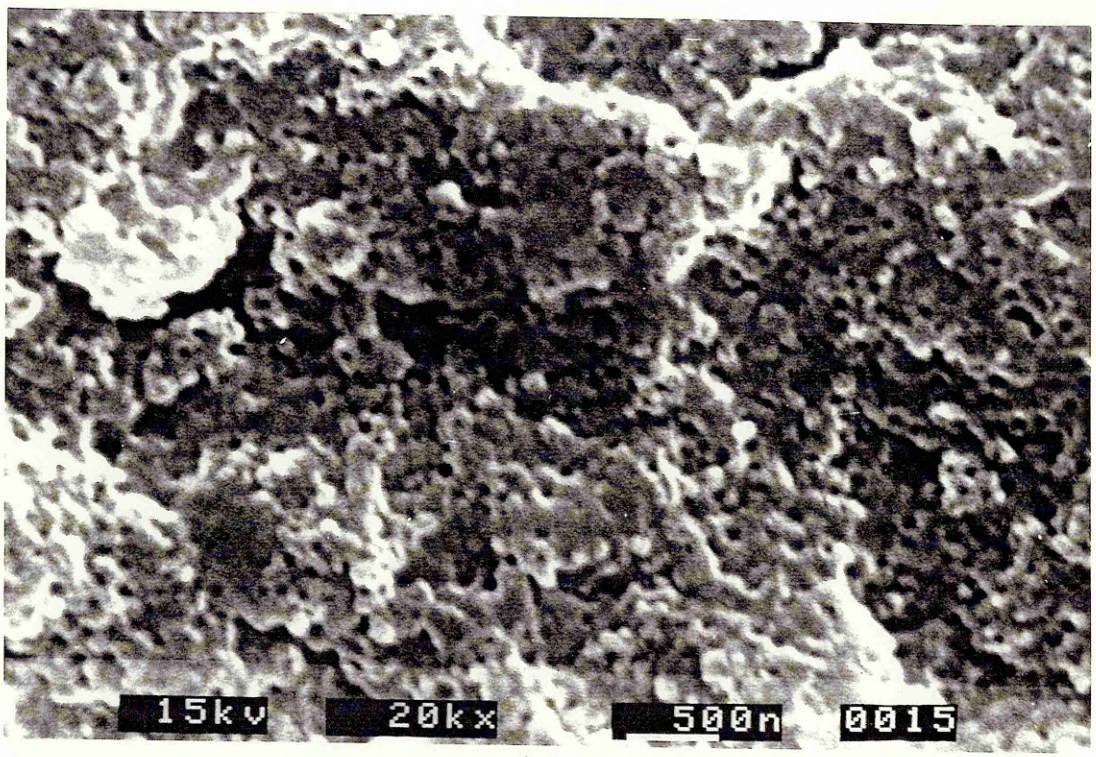

(a)

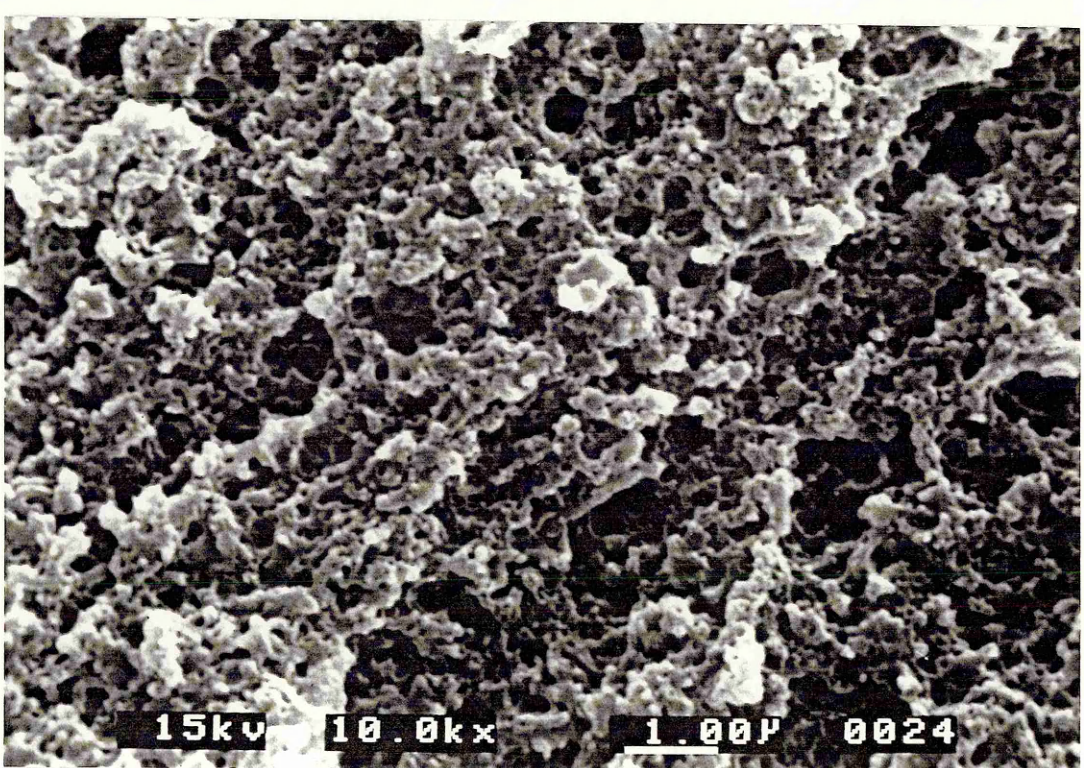

(b)

Figure 8.13 Microstructure in rubber domain: (a) undeformed; (b) deformed ahead of the crack tip in SENB specimen in rubber-modified Modar 8035 (SEM).

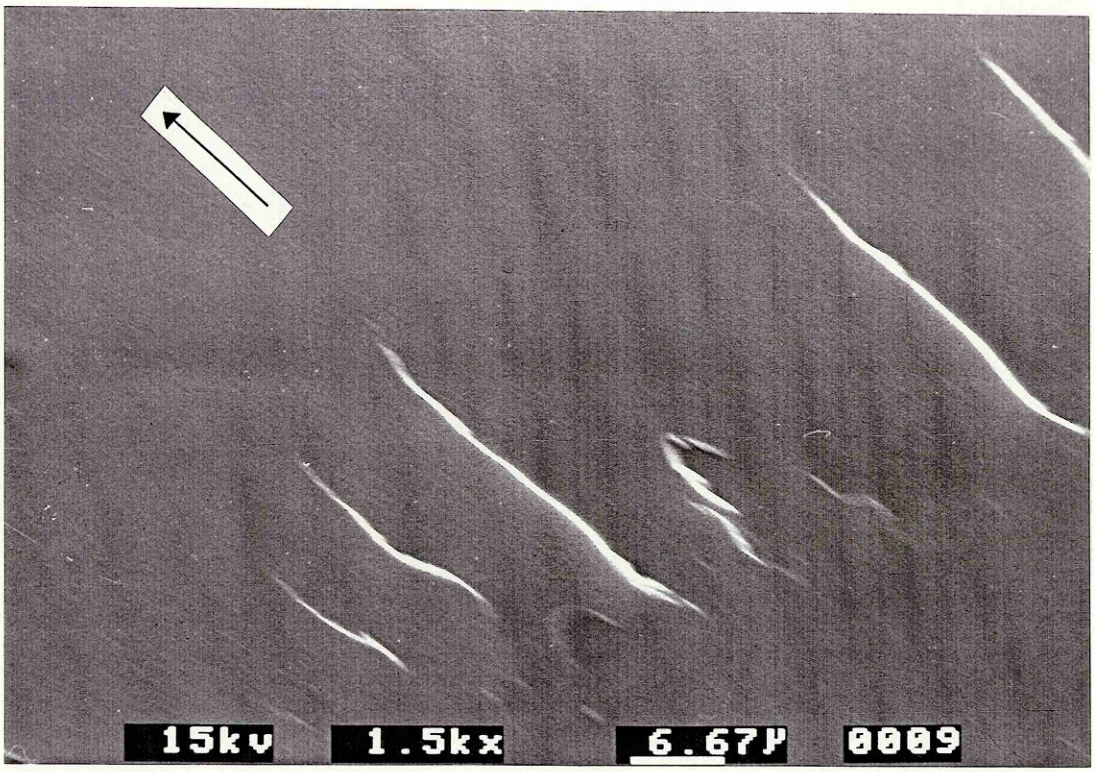

(a)

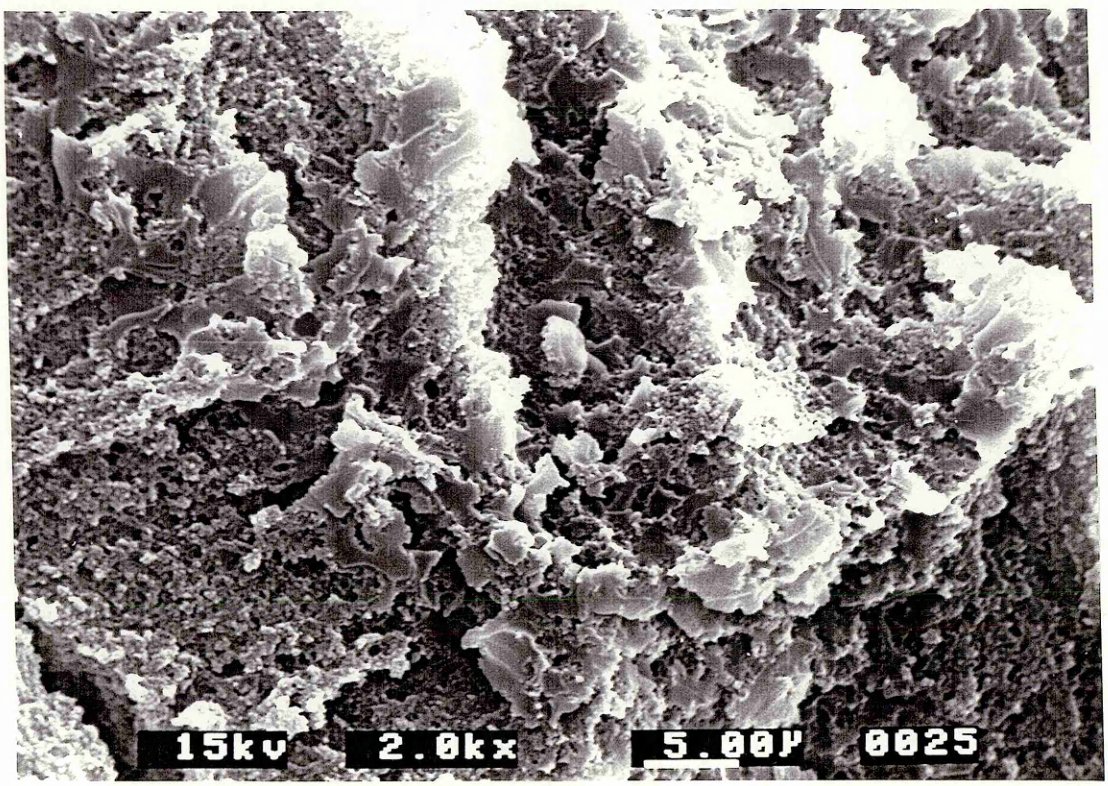

(b)

Figure 8.14 Fracture surface ahead of the crack tip in SENB specimen of Modar 8035 resins: (a) unmodified; (b) rubber-modified (SEM).

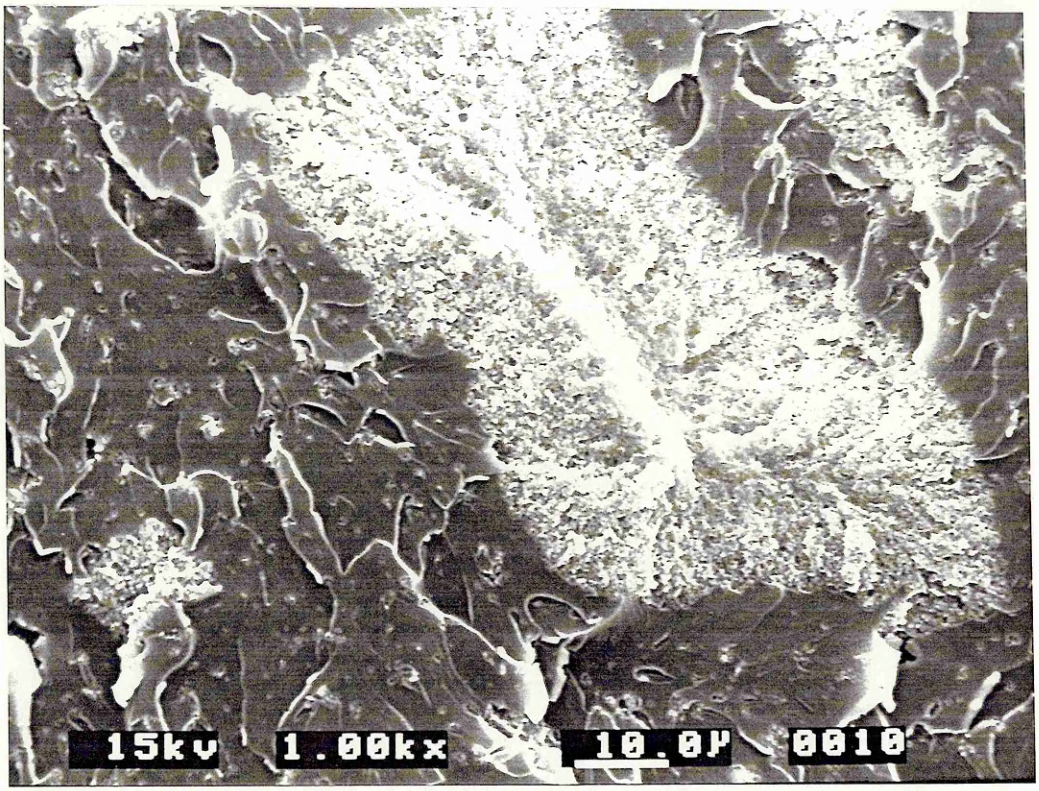

(a)

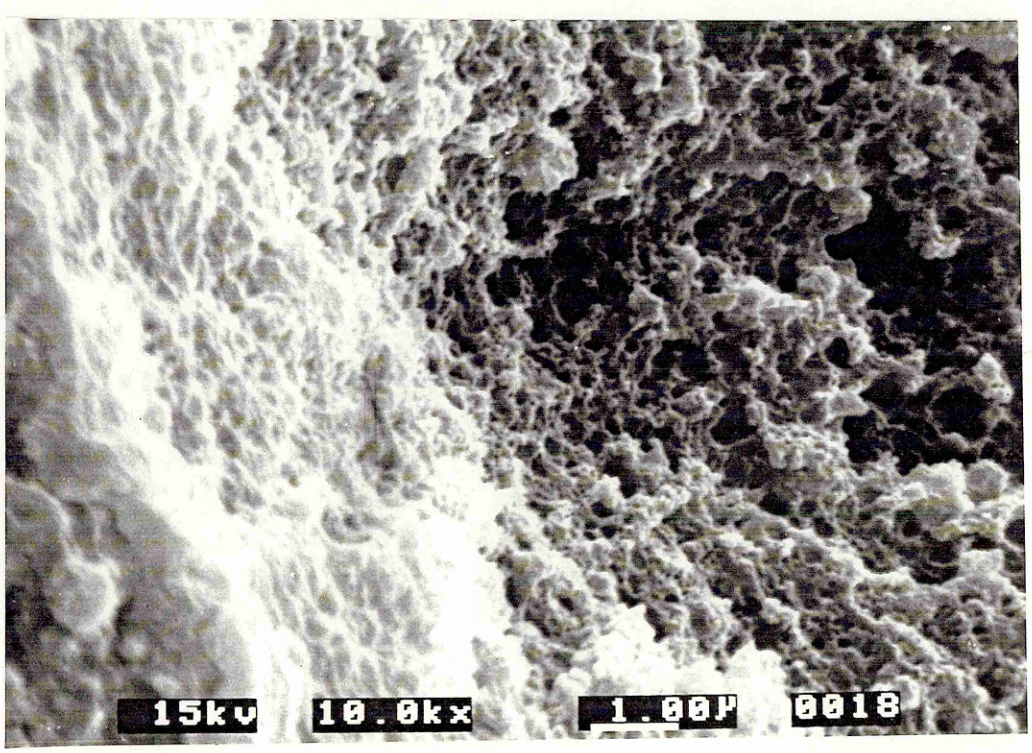

(b)

Figure 8.15 River-marking in rubber domain: (a) the whole image; (b) the enlarged part of (a) (SEM).

8.5 Coatings on Filler Particles

The influence of filler on yield stress and fracture resistance has been discussed in the two previous chapters, where good-bonding conditions between filler particles and Modar matrix was assumed. The current section will prove this assumption, and discuss the morphology of microstructure relating to the filler used. One fact found in this research is that filler particles are always covered with Modar resin on fracture surfaces.

A typical filler morphology is shown in Figure 8.16. However, it is hard to find them on fracture surfaces in hybrid Modar 8035 resins, which are based on the Modar matrix toughened with 15 wt % Paraloid BTA rubber. Almost all of filler particles were covered by the resin matrix to some extent no matter whether they are in the crack tip whitening zone (CTWZ) or beyond this region such as in the fast crack propagation area.

These features are shown in Figure 8.17. This is a micrograph within the CTWZ revealed by SEM with elemental analysis. The left micrograph is a normal SEM image and the right one is the X-ray intensity distribution map (also called EDAX - energy dispersive X-ray analysis) of filler silica, in which those whitened areas with irregular shapes are filler particles. It can be seen that matrix coatings exist on the filler particles. These coatings are also present in the matrix which is not rubber-modified but they are very thin as shown in Figure 8.18, where material is filled with 50 wt % filler (T00F50) without rubber modification.

Comparing of Figure 8.17 with 8.18, it appears that more plastic deformation occurs in the matrix which was toughened by rubber than in the same matrix without rubber modification. It is also appears that the coating on the silica is thicker for the former than the latter.

In fact, the plasticity of the matrix affects the coating thickness. Although the absolute value of the thickness is difficult to determine, the relative thickness can be estimated. This is shown in Figure 8.19. X-ray intensities reflected from the silica particles are recorded in terms of counts per second. The voltage used was 10 kV. The depth, within which X-ray emission is detectable, is about 4 μm in this experiments. The X-ray intensity is a function of thickness. The greater the depth, the less the X-ray intensity. Therefore, the intensity shown in Figure 8.19 reflects the relative thickness of coatings on filler particles. The two materials used in this experiment are T15F46, which contains 46 wt % filler based on the Modar matrix toughened with 15 wt % rubber, and T00F50, which is a filled neat Modar resin with 50 wt % filler.

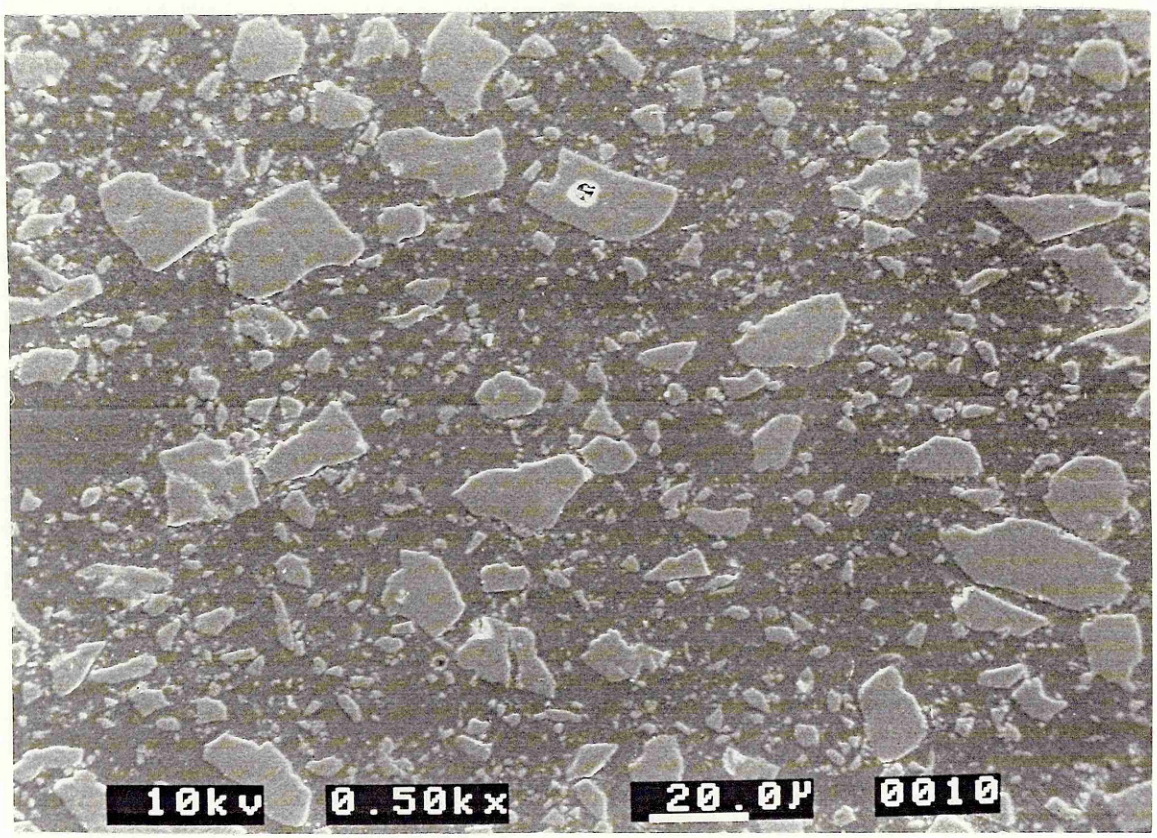

Figure 8.16 Microstructure of filler particles (SEM).

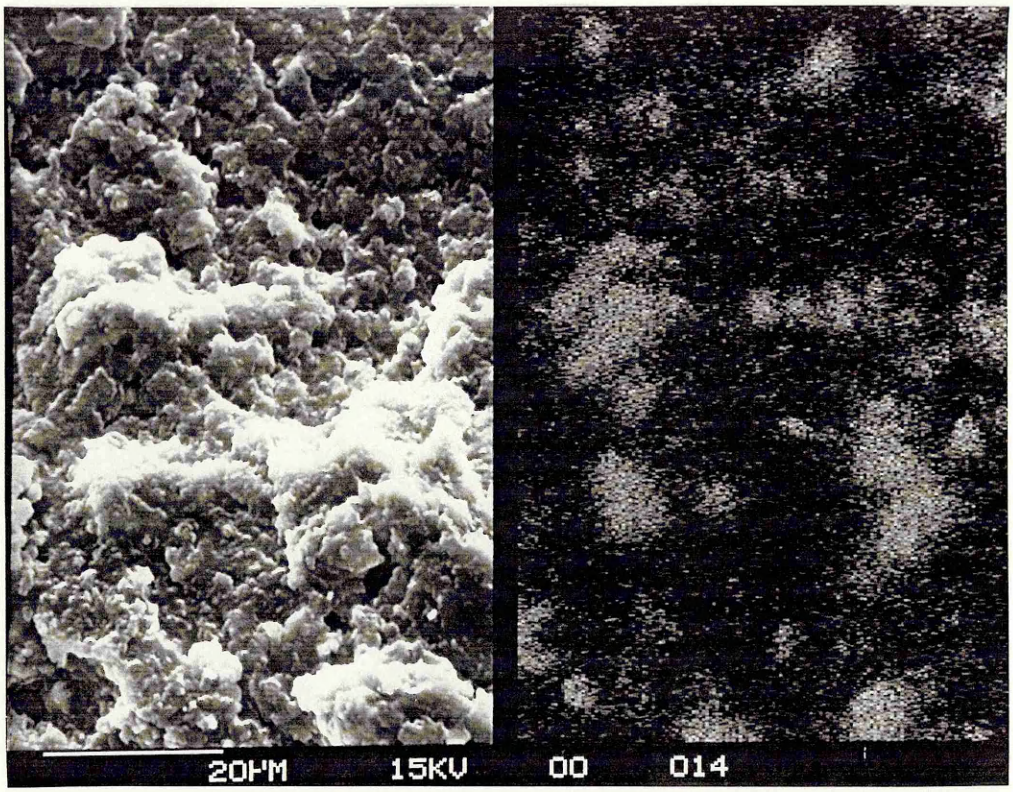

Figure 8.17 Coatings on filler particles in rubber-modified Modar 8035 matrix: the left is SEM image and the right EDAX image of silica filler.

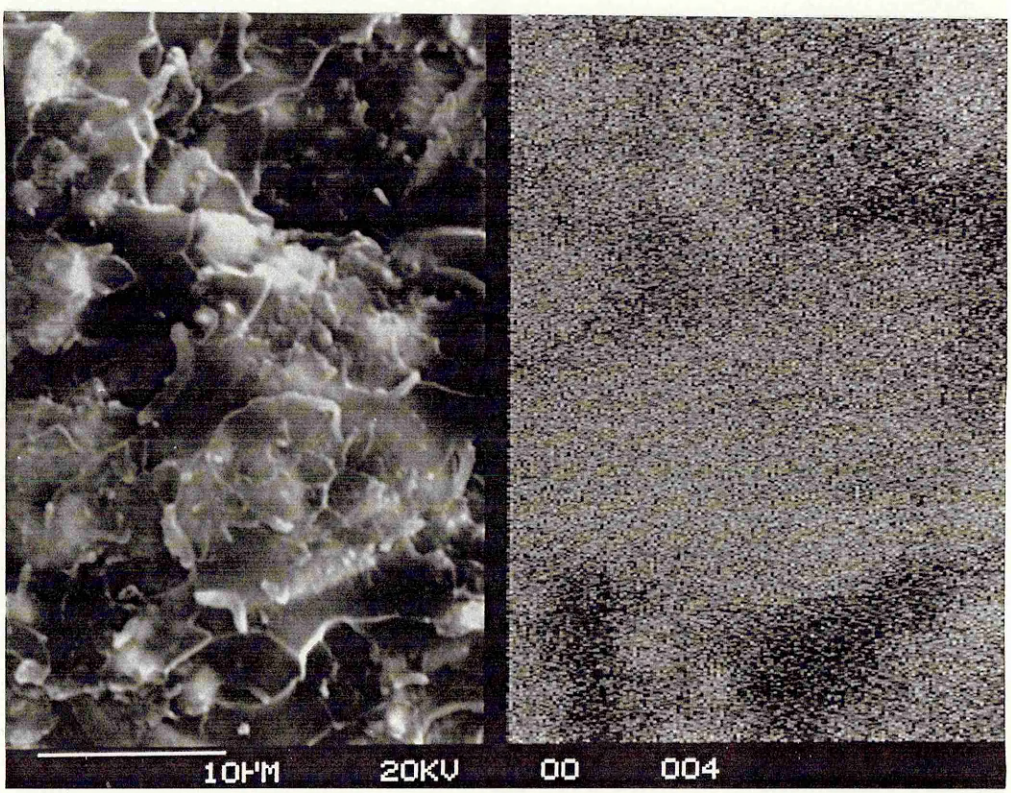

Figure 8.18 Coatings on filler particles in unmodified Modar 8035 matrix: the left is SEM image and the right EDAX image of silica filler.

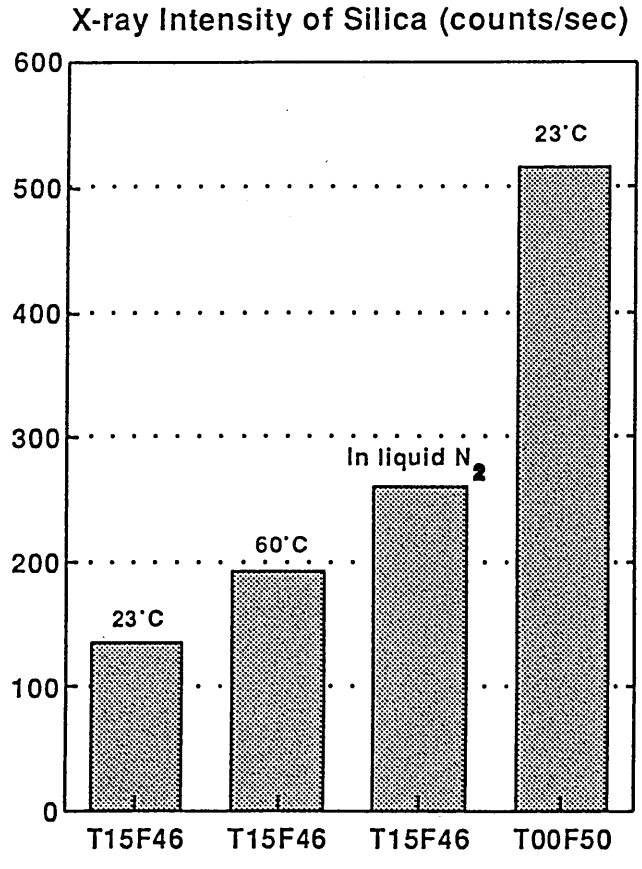

Figure 8.19 X-ray intensity in fracture surfaces for 50 wt % filled Modar 8035 (T00F50) and hybrid composite (T15F46) based the Modar matrix toughened by 15 wt % rubber.

For material T15F46, fracture at different temperatures gives different thicknesses of coating. The lower the temperature, the higher the X-ray intensity. This implies that the thickness of coating increases with material plasticity because more plastic deformation will occur at a higher temperature than at a lower one. For material T00F50 fractured at 23°C, the X-ray intensity is the strongest among the resin specimen investigated. This is because very thin layers of coating are present on the filler particles (Figure 8.18).

8.6 Discussions on Toughening Mechanisms

Up to 13 toughening mechanisms have been proposed for rubber-modified and particulate polymer composites, as summarized by Garg and Mai (1988). Several mechanisms may be involved in one toughened material, and each of them makes a contribution, more or less, to the total fracture resistance. However, the whole picture described by Garg and Mai involving these 13 mechanisms does not help the understanding of the key factor that controls deformation mechanisms in the matrix, which is believed the main source of fracture energy dissipation, no matter whether it deforms by crazing or shearing (Bucknall 1977).

In order to have a better understanding of toughening mechanisms in cross-linked thermosets, it is necessary to study what roles being actually played by dispersed rubber/filler particles and by resin matrices.

8.6.1 Functions of rubber particles

Rubber cavitation

A dispersed rubber particle can act as a stress concentrator (Section 3.1 and Section 6.3). In addition to this effect, cavitation of rubber has been considered to play an important role in rubber-modified thermosets (Kinloch 1983 and 1986; Chan 1984; Shah 1984; Yee 1983, 1986, 1989 and 1991; Sue 1991, Borggreve 1989). The direct evidence on rubber cavitation provided by these researchers is based on enlarged rubber particles in fracture surfaces or beneath them. The indirect evidence is volume dilatation in uniaxial tensile tests. However, the direct TEM evidence of cavitated rubber particles (with holes) in thin sections has not been published yet.

Rubber cavitation plays a key role in rubber-toughened Modar resins in this research. Cavitated rubber particles have been observed directly. For example, Figure 8.8, which has

been shown previously, has two types of cavitated rubber particles: one is in the aggregates of rubber and another in individual particles. Indirect evidence of rubber cavitation has also been obtained. One piece of evidence is the mechanical damage caused by rubber cavitation as indicated in Figure 8.9, where Young's modulus is higher before rubber cavitation than after it. Another is the formation of voids during uniaxial tensile tests as indicated in Figures 6.21 and 6.22. It can be concluded that voids generated during tensile tests are contributed from rubber cavitation. This is because (a) cavitated rubber has been directly observed and (b) no voids or crazes have been found in the Modar matrix yet.

This conclusion may also apply to the hybrid Modar composites since almost all fracture occurs in the rubber-modified matrix rather than at interfaces between filler and the matrix. So, the matrix should be responsible for the formation of voids (referring to Figures 6.21 and 6.22). According the discussion above, it is rubber cavitation that causes the formation of voids. So the increase in volume in hybrid composites should also be due to rubber cavitation. One filler particle with matrix coatings is shown in Figure 8.20, where sphere-like particles in the coatings are probably the cavitated rubber.

Rubber shearing

In addition to cavitation, it is also possible that rubber deforms in shear if the stress state allows it to do so.

Figure 8.21 shows shear deformation in some of rubber particles adjacent to a blunted crack tip as shown in micrograph (a), which is a deformed SENB specimen. Stress distribution is also schematically shown in (b). It is understood that stress σ_x is zero ($\sigma_x = 0$) at the surface of the blunted crack tip. This stress will increase to a maximum along the X-direction then fall afterwards as expected. Another stress component σ_z is also expected, which is approximately equal to $\nu(\sigma_x + \sigma_y)$. So, a triaxial stress state is not set up at or very adjacent to the surface. Therefore, it is very possible that the rubber deforms in shear with matrix. The thin matrix ligaments between rubber particles deform in shear together with rubber particles.

Figure 8.21 does not show cavitated rubber particles, but it is believed that there should be some. Even if there is cavitation, it is difficult to keep particles in their cavitated state after unloading, because only a small area about the crack tip deforms plastically in SENB specimens and the rest does not, so elastic and viscoelastic recovery are inevitable (These recovery processes have been observed after stress relaxation in SENB specimens).

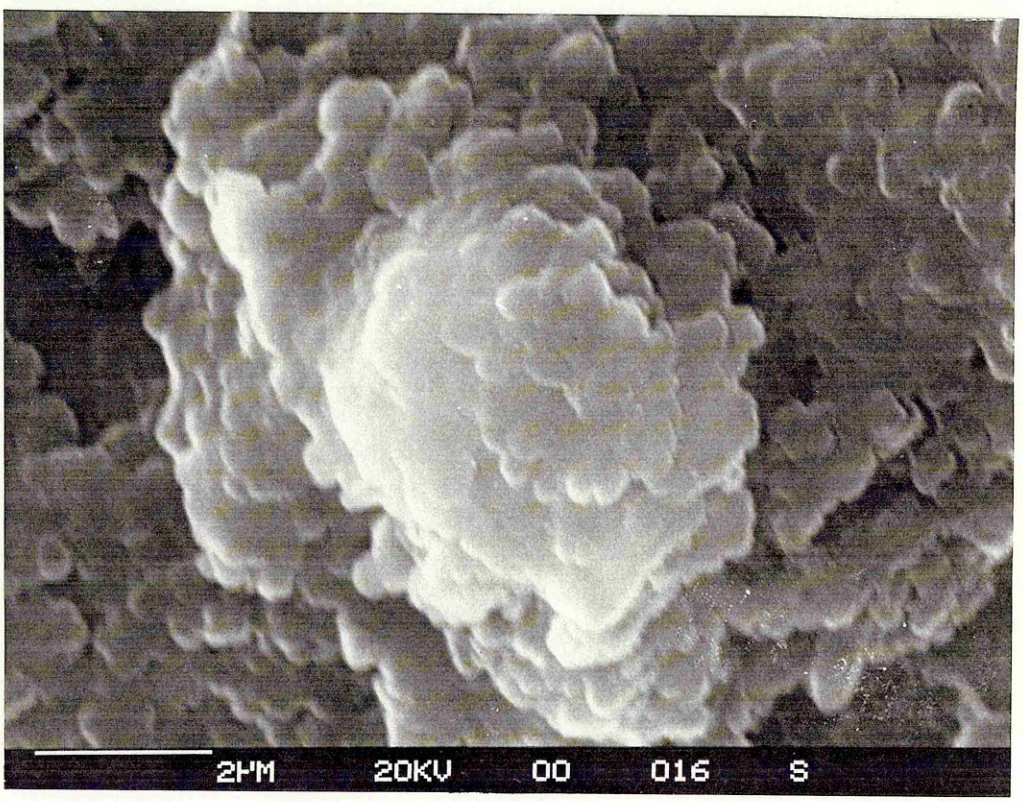

Figure 8.20 Coatings on one of filler particle in fracture surface in rubber-modified Modar 8035 matrix (SEM).

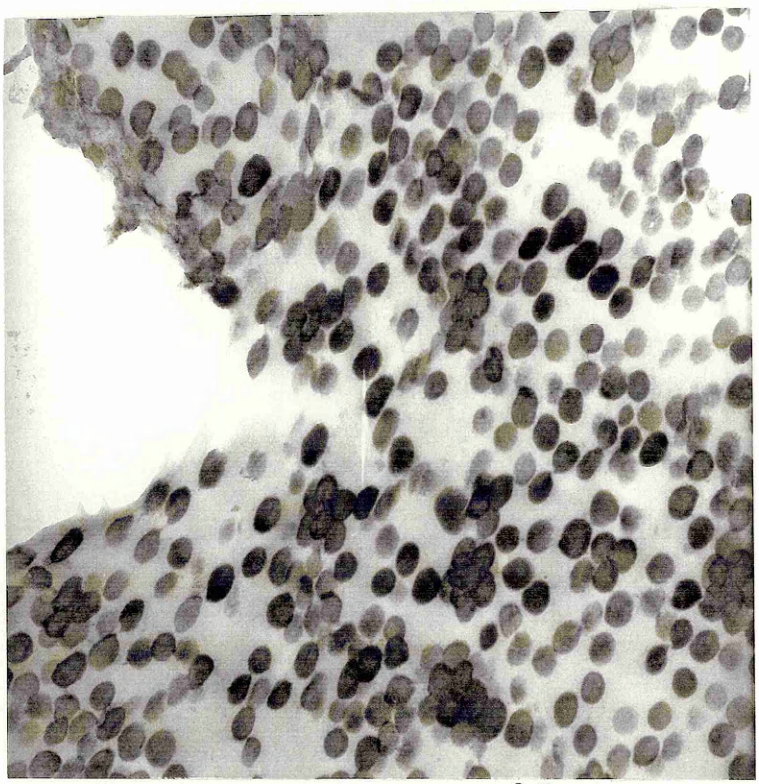

(a)

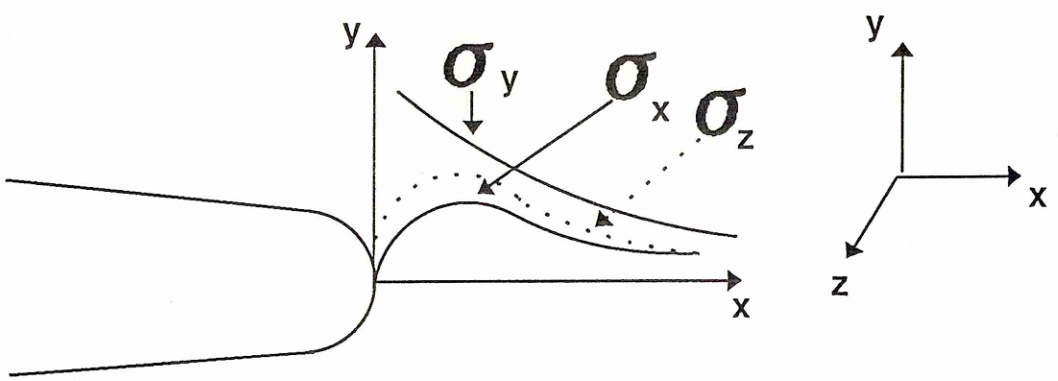

(b)

Figure 8.21 Plastic deformation adjacent to the crack tip of rubber modified Modar 8035 (top) and stress distribution (as expected) ahead of the crack tip (bottom).

Aother experiment which supports this argument comes from tensile-deformed specimens. Rubber cavitation is much easier to detect in these specimens than in SENB ones (referring to Figure 8.8), because a large scale of plastic deformation occurs along the whole gauge length of tensile specimens. The cavitated state can remain after material fracture.

8.6.2 Functions of filler particles

Crack front pinning is believed to be the main mechanism responsible for increase in fracture toughness in particulate composites (Moloney 1983, 1987) and hybrid composites (Kinloch 1985) provided that crack propagation is dominated by the brittle failure mode (referring to Chapter 3).

The basic idea of this theory, which has been outlined in Chapter 3, is shown in Figure 8.22. The line tension, which is originated from the crack front bowing between a pair of impenetrable obstacles, is responsible for the increase in fracture toughness, because extra energy will be required for crack propagation. The analytic results on the theory are listed in Table 8.1 (Green 1977, 1979). Figure 8.23 shows the relationships between normalized fracture toughness and inter-particle space using the data in the table. Two types of filler geometry are considered here: rectangular and circular.

The experimental results for hybrid Modar 8035 resins are listed in Table 8.2 and also shown in Figure 8.23. The inter-particle spacing and particle size in a crack plane (two dimensional rather than three dimension as required by the pinning theory) were measured with an image analyzer, Mini-Magiscan/IAS25/IV25 (Reference: Image Analyzer 1989). The measurement was based on micrographs taken from polished surfaces.

The side length of filler particle measured in a reference plane (not true particle dimensions) is about 14 μm, assuming rectangular geometry, or the diameter is 12 μm, assuming circular geometry (only the former value is used in Table 8.2 because the difference between them is not significant). These values are calculated from the average value of filler particle area exposed in the plane measured.

The average inter-particle spacing D_{space} in a reference plane is calculated according to the following equation (Reference: Image Analyzer 1989):

$$D_{space} = (1 - V_f) / n_i \qquad (8.5)$$

where V_f is volume fraction of filler and n_i the number of particles intersected per unit length in the plane measured by the image analyzer. The n_i values in Table 8.2 are the average ones, which were obtained by scanning in the plane along pixels, which are set by the instrument, vertically and horizontally.

Table 8.1 Interparticle spacing and K_C (Evans' theory)

r_0/D_{space}	$K_C/K_{C,m}$ (1)	$K_C/K_{C,m}$ (2)
0	1	1
0.25	2.16	2.02
0.5	2.72	2.52
1.0	3.48	3.05
1.25	3.81	3.25
2.0	4.52	3.75

* (1) Rectangular filler; (2) Circular filler.

Table 8.2 Interparticle spacing and K_C (Experimental results)

V_f (%)	$K_C/K_{C,m}$ +	n_i (numbers/μm) (x1000)	D_{space} (μm)	$2r^*/D_{space}$
5.3	1.03	5.72	165	0.04
11.1	1.06	1.47	61	0.12
17.7	1.01	2.98	28	0.25
25.0	1.13	5.02	15	0.47
29.8	1.20	5.81	12	0.58

+ The values used here are in Table 7.6 in Chapter 7.

* r used here is 7 μm which is the average value measured in polished surfaces from image analysis.

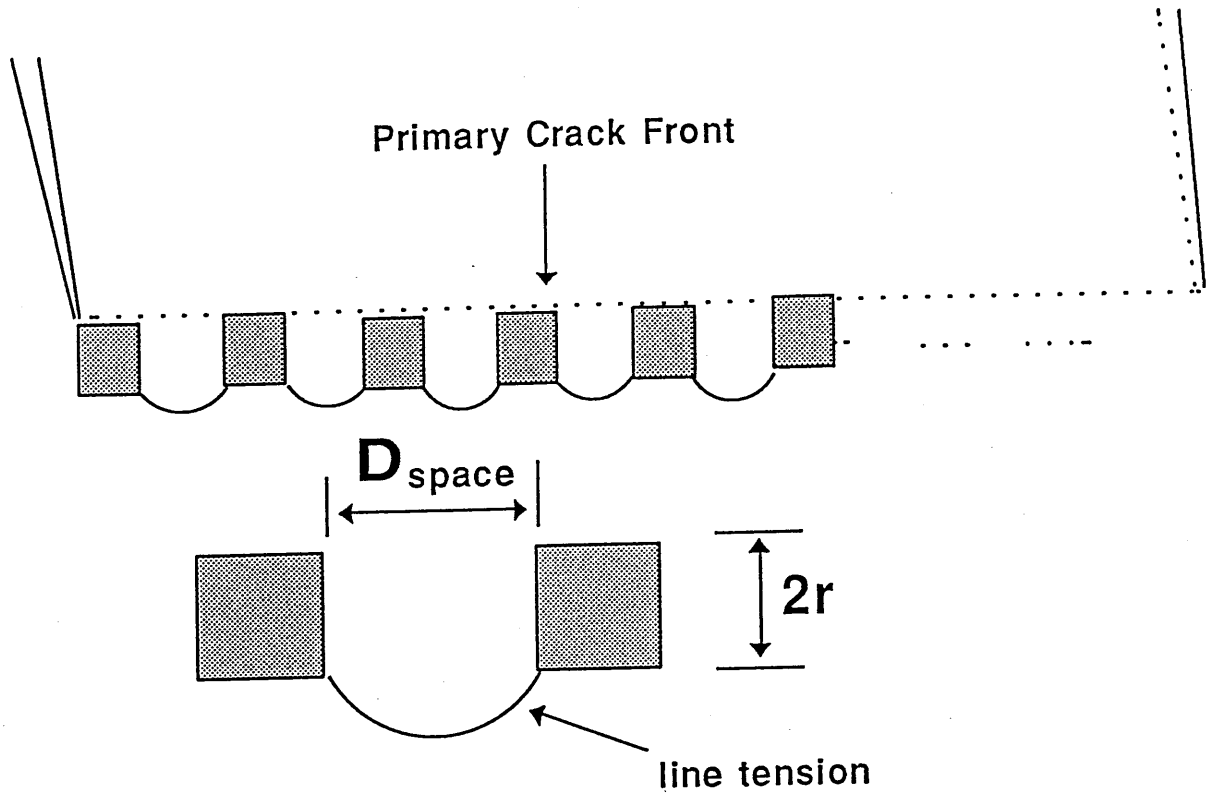

Figure 8.22 Schematic of crack front pinning for impenetrable obstacles.

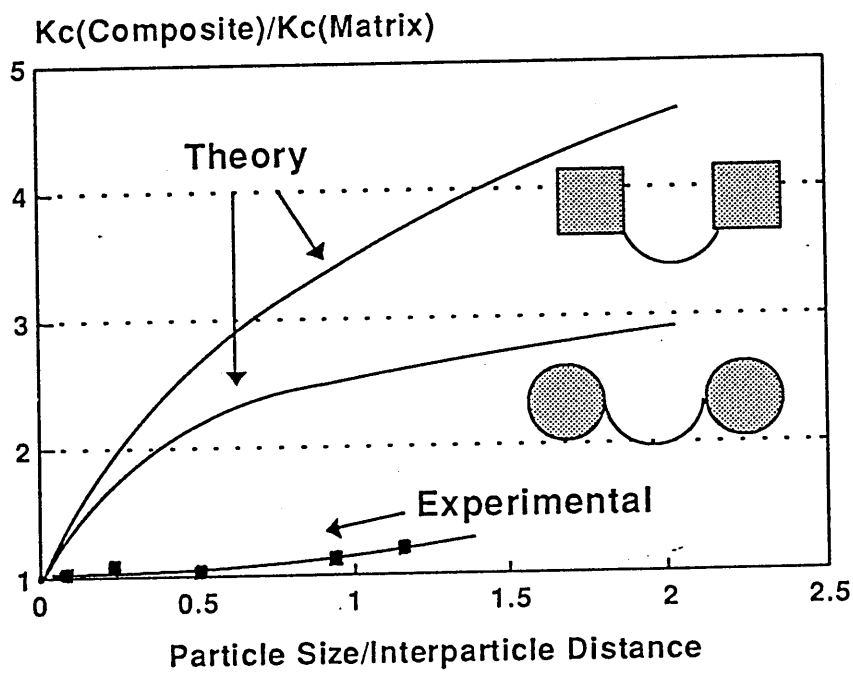

Figure 8.23 Theoretical prediction and experimental results of normalized fracture toughness for hybrid Modar 8035 resins based on the matrix toughened with 15 wt % rubber (23°).

From Figure 8.23, an important conclusion is that the hybrid Modar resins toughened with 15 wt % rubber do not show the pinning effect. A very big difference is found between the theory and experimental results when the rubber-modified material is taken as the reference primary matrix. If there is some pinning effect, it is restricted to high filler loadings, i.e. small inter-particle spacings because some increase in fracture toughness occurs at high filler loadings as indicated in Figure 8.23.

This analysis rules out crack front pinning as a major mechanism responsible for the increase in fracture toughness for hybrid composites unless brittle slow stable crack propagation dominates fracture, for example at low temperatures (Kinloch 1985, Maxwell 1986). The pinning effect may play a secondary role at high filler loading but this is difficult to verify because other factors can also affect fracture resistance. They include:

(a) Forming debonded zones around filler particles: these are the potential areas from where plastic deformation will take place, especially in the case of poor interfacial bonding, where enhanced plastic deformation will occur at equators of the particles. However, this effect might not be important in hybrid Modar resins because good interfacial bonding has been proved, as discussed previously. In this case, the maximum in stress concentration occurs on and above the poles of filler particles rather than at their equators (Section 3.1).

(b) Stepping on fracture surfaces: matrix coatings on and above the poles provide direct evidence, as shown in Figures 8.17 and 8.20. Crack fronts prefers to pass over filler particles rather than through them, especially in the case of well-bonded interfaces.

(c) Deflecting crack front: crack fronts will be deflected in the presence of filler particles as complex stress fields around them make crack growth select the routes of most highly concentrated stresses. These occur on and above the poles of filler particles.

(d) Bridging crack front: a filler particle could act as a bridge point where possible, especially at the stage of crack initiation. Uneven fracture surfaces and fewer fractured filler particles imply the involvement of the effect in the hybrid Modar resins in this research (comparing Figures 8.14 (a) with 8.17).

8.6.3 Functions of matrix

Shear deformation makes the largest contribution to the overall plastic deformation in both rubber toughened Modar resins and the hybrid ones, as discussed in Chapter 6 (Figures 6.23

and 6.24). The current chapter, from microstructure point of view, has shown that shear deformation in the matrix is the only mechanism functioning, because no crazes have been observed in any deformed matrix in this research, even with the aid of transmission electron microscope (TEM).

It is believed that shear deformation occurs in the matrix ligaments between cavitated rubber particles, where plane stress conditions are possibly met. Under other stress states such as compressive stresses, shear deformation can also be induced in Modar matrix in the presence of rubber. Stress concentrations at equators of rubber particles are probably the driving forces in the initial stage to start shear in both matrix and rubber phases.

8.6.4 Fracture

Matrix fracture mechanisms vary depending on stress state. What has been found in this research is that:

(a): Flat fracture surfaces are always generated in rubber toughened Modar resins under tensile loading, such as in uniaxial tensile tests or SENB tests;

(b): Slanted fracture surfaces occur under compressive plane strain conditions for the same materials, where most fracture starts from the edge of the die (Figure 4.3) along the plane outside the primary shear bands (Figure 8.10).

It is very likely that rubber domains are the places where fracture will originate under tensile loading conditions. The possible coalescence and linkage of cavities at rubber particles will increase the size of 'defects' and eventually lead to fracture when the applied stress σ is greater than the critical stress σ_c (referring to the deformed microstructures in Figures 8.1, 8.5 (c), 8.7 (b), 8.8, 8.11 (b), 8.12). This is why the tensile fracture strength of rubber-modified and hybrid Modar resins is lower than that of the unmodified Modar (Chapter 7).

As mentioned previously, every rubber domain around the crack tip shows microcrack-like features. The advantage of these features is that the concentrated stresses ahead of the crack tip can be eased and spread away through plastic deformation in the rubber domains and matrix. Fracture resistance therefore increases. The disadvantage of these features is that they might cause early fracture. So, the balance between the advantage and the disadvantage needs further exploration in order to get better toughened materials, especially from brittle thermosets.

The fracture mechanisms under compressive plane strain conditions are probably shear-dominated, because no flat fracture surfaces could be seen. The problem is that the slanted fracture planes did not follow the primary shear planes but lay outside them. Other mechanisms may operate in addition to shearing.

Under mode I loading conditions which are most concerned, crack tip blunting would be a general result, no matter which plastic deformation mechanism occurs (referring to Figure 8.21). This is the main cause of unstable crack propagation and should make a contribution to an increase in fracture resistance. However, whether it is a dominating mechanism or not remains in question. This is because the radius of the blunted crack tip is much less than the size of plastic deformation zone [Figures 8.21 and 8.5 (c)]. It is doubtful that such a small increase in the crack tip radius will cause more than a 10 times increase in fracture resistance for the Modar 8035 resin after rubber modification (Table 7.5 and Figure 7.5). Other mechanisms such as massive plastic deformation ahead of crack tip are probably responsible for the major increase in fracture resistance.

8.7 Conclusions

(1) Rubber particles deform in two ways. Under a tensile stress state, especially in a triaxial stress field, the rubber cavitates, either within a single particle or in the aggregates of the particles. Under a compressive stress state, the rubber deforms in shear.

(2) A plastic deformation zone is always generated ahead of the crack tip in rubber toughened Modar resins. The size of the zone is determined by the hydrostatic stress, which facilitates rubber cavitation, and is much bigger in the central region than in the surfaces for a thick specimen.

(3) The shape of plastic zone can be described in terms of cavitation stress and stress intensity factor by Equation (8.3), which agrees with the experimental results. The Von Mises plastic zone does not match the results. The size of cavitation zone is determined mainly by the ratio of yield stress σ_{yield} to cavitation stress σ_h. It increases with the ratio raised to power 2.

(4) Modar 8035 deforms in shear. No crazes have been found in the deformed matrix.

(5) Cavitation of rubber probably plays a key role in inducing shear deformation in the Modar matrix because the cavitation stress of rubber approximately matches the yield stress

of rubber-modified and hybrid Modar resins.

(6) Coalescence and linkage of voids initiated inside rubber particles within rubber domains probably occurs before catastrophic fracture, and is the cause of final fracture.

(7) Crack front pinning is not a major mechanism responsible for increase in fracture resistance in hybrid Modar composites at ambient temperature.

(8) The most highly concentrated stress locates on and above the poles of well-bonded filler particles, so they are always covered with a layer of the matrix.

(9) The thickness of matrix coatings on filler appears to vary with the ductility of the Modar matrix. The greater the ductility, the thicker the coatings.

(10) Massive shear deformation ahead of the crack tip, which is induced by cavitation of rubber particles, is the major mechanism for the increase in fracture resistance in rubber modified and hybrid Modar 8035 resins.

CHAPTER 9

GENERAL CONCLUSIONS

9.1 Toughening Mechanisms

Fracture mechanisms of Modar 8035 resin are defect-dominated. The relationships between defect size and fracture strength are characterized through the critical stress intensity factor K_{IC}. Low fracture toughness and high crack sensitivity of the unmodified resin is due to lack of plastic deformation that is needed to ease concentrated stress at the tip of a sharp crack, whatever reason for its presence.

A 10 times increase in fracture resistance in the Modar has been achieved through rubber modification. Main reason for the improvement is that intensive plastic deformation is induced in the Modar matrix after rubber modification, which effectively eases stress concentrations and spread them away from the crack tip.

Deformation mechanisms in the rubber-modified Modar are shear-dominated. Cavitation of rubber plays a key role in inducing shear deformation in the Modar matrix. Scales of plastic deformation are determined by the ability of rubber cavitation. The lower the cavitation stress, the larger the extent of shear deformation.

Fracture processes in the rubber-modified Modar possibly start from coalescence and linkage of voids initiated inside rubber particles within rubber domains, which leads to final fracture in the Modar matrix.

Crack front pinning is not a major mechanism in hybrid Modar composites when a rubber-modified Modar is taken as the primary reference matrix. Toughening mechanisms in these materials are probably the same as that in the rubber-modified resin.

9.2 Suggestions for Future Work

This research shows the importance of rubber cavitation in toughening Modar 8035 resin, which appears to be a decisive step towards massive shear deformation in the Modar matrix. What is not clear is the relationships between rubber cavitation and matrix ductility. It is also not clear whether cavitation stress of rubber will affect fracture resistance significantly, especially in highly cross-linked thermosets. Further research on the subjects is needed in order to understand these relationships, which will be beneficial to the development of better rubber toughenes suit to different ductility of thermosets.

ACKNOWLEDGEMENTS

I would like to express my appreciation to my supervisor Professor Clive B Bucknall for the help and guidance he has given to me over the last three years. His teaching in scientific disciplines that I have gained will benefit me for the rest of my life. I would also like to thank Mrs A Bucknall for the friendship shared with my family. Several unforgotten occasions she organized added more colours into the life at Cranfield.

I am thankful to the Committee of Vice-Chancellors and Principals of the Universities of the United Kingdom for my Overseas Research Students Award and to ICI for full financial support of the research. Special thanks are given to Dr M Orton, Dr G Jackson and Dr J Stoddart of ICI for their useful discussions and help in ICI and at Cranfield during the research work.

Thanks are also given to Mr P Logan and Mr D Woolnough for their help in experimental work and for the friendship shared with them and all the other students in the Polymer Engineering Group. Thanks are given to Val Emsley and Lynne White for their help in typing my reports to ICI. I appreciate the time working in this helpful, cheerful and friendly group over the last three years.

Finally, I am especially thankful to my wife Yong and my daughter Qian for their full support. There were many times that I should have spent with them and responsibilities that I should have undertaken. Only they know the hardships they have endured.

REFERENCES

Argon A S (1973) Phil. Mag., **28**, 839.

Argon A S (1977) Polym. Eng. Sci. **17**, 174.

Bandyopadhyay S
Silva V M
Low I M
Mai Y W
(1988) Plast. Rubb. Proc. Appl., **10**, 193.

Broutman L J
McGarry F J
(1965) J. Appl. Polym. Sci. **9**, 589.

Borggreve R J M
Gaymans R J
Luttmer A R
(1988) Makromol. Chem. Macromol. Symp. **16**, 195.

Borggreve R J M
Gaymans R J
Schuijer J
(1989) Polymer, **30**, 71.

Borggreve R J M
Gaymans R J
Schuijer J
(1989) Polymer, **30**, 78.

Breuer H
Haaf F
Stabenow J
(1977) J. Macromol. Sci.-Phys. **B14**, 387.

Bucknall C B
(1977) Toughened Plastics, Applied Science, London.

Bucknall C B
Page C J
(1982) J. Mater. Sci., **17**, 808.

Bucknall C B
Dumpleton P
(1985)
Plastics and Rubber Processing and Application, **5**, 343.

Bucknall C B
Partridge I
Ward M V
(1984)
J. Mater. Sci., **19**, 2064.

Bucknall C B
(1988)
Makromol. Chem., Macromol. Symp., **16**, 209.

Bucknall C B
(1990)
Makromol. Chem., Macromol. Symp. **38**, 1.

Bucknall C B
Faitrouni T
(1991)
Deformation Yield and Fracture of Polymers,
8th Inter.Conf., Churchill College, Cambridge,
UK, 8-11 Apr. 1991, paper No. 30/1.

Chan L C
Gillham J K
Kinloch A J
Shaw S J
(1984)
Adv. Chem. Ser., **208** (Rubber-Modified Thermosets
Resins), pp261-279.

Chow T S
(1984)
~~Polymer, 32, 29.~~ Polym Eng Sci, 24, 915

Chow T S
(1987)
J. Polym. Sci., Part **B**: Polym. Phys.,
Vol.25, 137.

Chow T S
(1988)
in 'Cross-linked Polymers: Chemistry,
Properties and Applications' (ed. by R J Dickie et al.)
ACS Symp Ser. 1988, pp124-135

Chow T S
(1989)
Macromolecules, **22**, 701.

Chow T S
(1991)
Polymer, **32**, 29.

Crank J
(1957)
The Mathematics of Diffusion, Oxford, Clarendon Press.

Emeleus H J
Anderson J S
Modern Aspects of Inorganic Chemistry,
George Routledge & Sons Ltd., London, 1943.

Evans A G (1972) Phil. Mag., **26**, 1327.

Evans A G (1974) J. Mater. Sci. **9**, 1974, 1145.

Ewalds H L Wanhill RJH (1986) Fracture Mechanics, ch.2&3, pages 33-34 and pages 64-65, 3rd.Ed., pub.by Edward Arnold.

Eyring H (1936) J. Chem. Phys. **4**, 283.

Gent A N Wang C (1991) J. Mater. Sci. **26**, 3392.

Glad M D Kramer E J (1991) J. Mater. Sci. **26**, 2273.

Goodier J H (1933) J. Appl. Mech. Trans. ASME, **55A**, 39.

Green D J (1977) Ph.D Thesis, McMaster University, Canada.

Green D J (1979) J. Mater. Sci. **14**, 1657.

Guild F J Young R J (1989) J. Mater. Sci., **24**, 298 (Part 1), 2454 (part 2).

Haward R N Thackray G (1968) Proc. Roy. Soc. **A 302**, 453.

He M J Cheng W X Dong X X (1981) in Chapter 7, 'Polymer Physics', Fudan University Publication.

Henkee C S Kramer E J (1984) J. Polym. Sci., Polym. Phys. Edn, **22**, 251.

Image Analyzer (1989) Principles & Practice, published by Joyce Loebl Ltd.

Ishai O (1968) J. Composite Materials, **2**, 302.

Kinloch A J Williams J G (1980) J. Mater. Sci., **15**, 987.

Kinloch A J Young R J (1983) Fracture Behaviour of Polymers, Applied Science, London.

Kinloch A J Tod D A Hunston D L (1983) Polymer, **24**, 1341.

Kinloch A J Tod D A Hunston D L (1983) Polymer, **24**, 1355.

Kinloch A J Maxwell D L Young R J (1985) J. Mater. Sci., **20**, 4169.

Kinloch A J Hunston D L (1986) J. Mater. Sci. Lett., **5**, 901.

Kinloch A J Hunston D L (1986) J. Mater. Sci. Lett., **5**, 1207.

Kinloch A J Hunston D L (1987) J. Mater. Sci. Lett., **6**, 137.

Kinloch A J Huang Y (1992) J. Mater. Sci., **27**, 2735.

Kocanda S (1978) Fatigue Failure of Metals, Wydawnictwa Naukowo-Techniczne, Warsaw, Poland.

Kramer (1975) J. Polym. Sci. (phys.) **13**, 509.

Kramer E J (1984) Polym. Eng. Sci., **24**, 761

Kunz S C Beaumount P W R Ashby M F (1978) Toughening Plast., Int. Conf., [Prepr.], Paper No. 15, Plast. Rubber Inst., London, England.

Kunz-Douglass S Beaumont P W R Ashby M F (1980) J. Mater. Sci., **15**, 1109.

Lange F F (1970) Phil. Mag., **22**, 983

Lange F F Radford K C (1971) J. Mater. Sci., **6**, 1179.

Lee Sang-Baek Rockett T J Hoffman R D (1992) Polymer, **33**, 2353.

Li J C M Gilman J J (1970) J. Appl. Phys., **41**, 4248.

Lin Y G Pascault J P (1986) Polym. Compos., Proc., Microsymp. Macromol., 28th Meeting, 1985, Edited by B Sedlacek. De Gruyter: Berlin, Fed. Rep. Ger.

Low I M Mai Y W Bandyopadhayay S Silva V M (1987) Mater. Forum, **10**, 241.

Low I M
Mai Y W
(1988) Compos. Sci. Tech. **33**, 191.

Garg A C
Mai Y W
(1988) Compos. Sci. Tech. **31**, 179.

Low I M
Mai Y W
Hewitt G
Foley C
(1989) Compos. Sci. Tech. **34**, 267.

Margolina A
Wu S
(1988) Polymer, **29**, 2170.

Maxwell D L
(1986) Ph.D thesis, University of London,
Queen Mary College London.

McGarry F J
Ming K T
(1986) Sci. Tech. Areosp. Rep. **24** (11),
Abstr. No. N86-20563.

McCrum N G
Buckley C P
Bucknall C B
(1988) Principles of Polymer Engineering, Oxford Science Publications

Michel J C
Manson J A
Hertzberg R W
Widmaier J M
(1991) Deformation Yield and Fracture of Polymers,
8th Inter.Conf., Churchill College, Cambridge,
UK, 8-11 Apr. 1991, paper No. 121/1.

Miller P
Buckley D J
Kramer E J
(1991) J. Mater. Sci., **26**, 4445.

Moloney A C
Kausch H H
Stieger H R
(1983) J. Mater. Sci. **18**, 208.

Moloney A C
Kausch H H
Kaiser T
(1987)
J. Mater. Sci. **22**, 381.

Paris P C
Erdogan F
(1963)
J. Basic Eng. Trans. ASME Ser. **D 85**, 528 (Dec. 1963)

Paris P C
(1964)
In ' Fatigue an Interdisciplinary Approach', pp107-132
Ed. Burke et al., Syracuse University Press.

Pukanszky B
Turcsanyi B
Tudos F
(1988)
J. Mater. Sci. Lett., **7**, 160.

Reismann
Pawlik
(1980)
Elasticity Theory and Application, A Wiley Interscience Pub.

Rowe E H
(1978)
Toughening Plast., Int. Conf., [Prepr.],
Paper No. 23, Plast. Rubber Inst., England 1978

Sayre J A
Kunz S C
Assink R A
(1984)
Adv. Chem. Ser., **208** (Rubber-Modified Thermosets
Resins), pp215-235

Schwier C E
Argon A S
Cohen R E
(1985)
Phil. Mag. **52**, 581.

Shah D N
Attalla G
Manson J A
Hertzberg R W
(1984)
Adv. Chem. Ser., **208** (Rubber-Modified Thermosets
Resins), pp117-135

Sue H J
(1991)
Polym. Eng. Sci., **31**, 270.

Sue H J
(1991)
Polym. Eng. Sci., **31**, 275.

Sue H J (1991) Deformation Yield and Fract. Polym. 8th Int. Conf. Churchill College, Cambridge, UK, 8-11 April 1991 paper No. 63/1-4.

Thomas N Windle A H (1978) Polymer, **19**, 255.

Thorne P C L Roberts E R Inorganic Chemistry, Gurney and Jackson, London, 1948.

Truong V-T (1990) Polymer, **31**, 1669.

Ward I M (1983) Mechanical Properties of Solid Polymers, 2nd Ed., John Wiley & Sons, 1983.

Weber I A (1990) Int. Conf. for Vehicle Industry 'Plastics on the Road 1990', Paper 2, 4-5 December 1990, Plast. Rubber. Inst.

Williams J G (1980) Stress Analysis of Polymers, ch.7, pages 350-352, 2nd Ed., Ellis Horwood Limited, London (UK)

Wood, A S (1990) Mod. Plast. Int. Nov. 1990, 52.

Wu S (1985) Polymer, **26**, 1855.

Wu S (1988) J. Appl. Polym. Sci., **35**, 549.

Yamini S Young R J (1980) J. Mater. Sci., **15**, 1814.

Yee A F Pearson R A (1983) Polym. Mater. Sci. Eng., **49**, 316.

Yee A F Pearson R A (1983) NASA Contractor Report 3718

Yee A F
Pearson R A
(1984)
NASA Contractor Report 3852

Yee A F
Pearson R A
(1986)
J. Mater. Sci., **21**, 2462.

Yee A F
Pearson R A
(1986)
J. Mater. Sci., **21**, 2475.

Yee A F
Pearson R A
(1989)
J. Mater. Sci., **24**, 2571.

Yee A F
Pearson R A
(1991)
J. Mater. Sci., **26**, 3828.

Young R J
Maxwell D L
Kinloch A J
(1986)
J. Mater. Sci., **21**, 380.